Piotr Dzwiniel

Modulation of Visual Information Processing in the Human Nervous System Using Non-Invasive Electrical Stimulation

Doctoral Dissertation
Completed in the Laboratory of Neurobiology of Emotions,
under the guidance of **Prof. Wioletta Waleszczyk**†
and in the Laboratory of Neurobiology of Vision
of the Nencki Institute of Experimental Biology
of the Polish Academy of Sciences

Supervisor:

Ewa Kublik, Ph.D., D.Sc.

Warsaw, 2024

Author's Declaration

I, the undersigned Piotr Dzwiniel, consent to the storage and release of my dissertation, titled: "Modulation of Visual Information Processing in the Human Nervous System Using Non-Invasive Electrical Stimulation" by the Library of the Nencki Institute of Experimental Biology of the Polish Academy of Sciences (PAS), in printed form, in a reading room, and as a part of interlibrary loans, on the basis of free use.

At the same time I grant the Nencki Institute of Experimental Biology PAS a free non-exclusive license to use the aforementioned work without time and territorial limitations in the following fields of use:

1. placing the content of the thesis as a PDF file together with metadata in the digital repository RCIN (*Digital Repository of Scientific Institutes*, collection: *Institute of Experimental Biology PAS / Dissertations*) located at the following address: https://rcin.org.pl/dlibra/collectiondescription/121
2. digital multiplication of the work (digitalisation of the work if it is necessary to scan the printed version).

Warsaw, Poland, 2025-01-23 Signature: ………………………………………

Acknowledgements

I am grateful to the people listed below for their invaluable assistance throughout PhD studies, as well as for their guidance in the world of science:

Ewa Kublik, Ph.D., D.Sc., who never refused to help me,

Prof. Wioletta Waleszczyk†, who invited me into the world of science,

Ida Raciborska, Ph.D., for her assistance in preparing participants for the studies,

People from both laboratories, for the friendly and inspiring atmosphere at work,

My Parents, who have always been and believed,

The Universe, for the favorable arrangement of all fields and particles.

My work was financially supported by statutory funding from the Nencki Institute of Experimental Biology of the Polish Academy of Sciences, the National Centre for Research and Development grant REVIS ERA-NET NEURON/08/2012, and the National Science Centre grant Preludium 12 (2016/23/N/HS6/02346).

NCBR
National Centre for Research
and Development

NATIONAL
SCIENCE
CENTRE

Contents

Abstract

Noninvasive current stimulation is increasingly used to support the brain function and recovery from trauma or disease. The dissertation focused on the stimulation paradigm aimed to concentrate the effect within initial stages of the visual system. Periorbital pulsed current stimulation (pPCS) in the form of single biphasic pulses of sinusoidal waveform applied with electrodes below and above the eyes were tested with simulation approach and during in vivo experiments with healthy volunteers. The specific aims of the dissertation were to evaluate the concentration of induced electric field (IEF) in the brain, to characterize the behavioral and electrophysiological (EEG) responses to visual and electric stimulation, and to analyze the potential of pPCS in modulating information processing in the visual system in a paired pulse stimulation (PPS) paradigm, in which a current pulse is applied prior to a visual stimulus, allowing its effects on excitability and neural processing to be assessed.

Computer simulations have shown that pPCS with electrodes located above and below the eyes concentrates the IEF mainly within the eyeballs, minimizing the impact on the optic nerves and other areas of the brain. In comparison, a configuration with electrodes over the eyes and one electrode placed on the occipital area generates a more diffuse IEF, covering also the optic nerve and the occipital cortex. IEF analyses indicated that the electric field concentration at the electrode's edges depended on current density and curvature of the electrode edge. The simulations also showed that the default tissue conductivity values used in SimNIBS – popular software used to model IEF, are inaccurate. The Swiss ITIS Foundation database was proposed as more accurate.

In the in vivo experimental study a periorbital electrodes' arrangement was tested. The current pulses were shown to effectively induce phosphenes of retinal origin, with a detection threshold (of about 5%) at about 10 ms at an amplitude of 300 µA and cortical electrically evoked potentials (EEP). The increase of the pulse amplitude and duration resulted in nonlinear increase of phosphene detection and EEP amplitude, which were described using a customized three-factor Naka-Rushton model, taking into account the total pulse charge, amplitude and duration. The model revealed that the effect of total charge on the response decreases with increasing pulse intensity and length, leading to a saturation effect. The importance of parameters such as total charge, amplitude and pulse duration in the induction of phosphenes and the characteristics of the responses given was also highlighted.

The second experimental study used the pPCS protocol, in which pulses of different lengths and amplitudes were applied before a checkerboard pattern reversal (CPR) visual stimulus. It was found that in the experimental group, current stimulation reduced the amplitude of early visual evoked potential (VEP) components, such as P1N1 and P1N2, compared to the placebo group, indicating its potential inhibitory effect on visual cortex excitability. This effect was cumulative over time, such that no differences in the strength of the effect were observed depending on the parameters of the stimulus, and its effect also extended to trials in which CPR was not preceded by the application of a current pulse. In addition, the effect of the stimulation increased with time, and clearly disappeared after its termination.

In conclusion, the simulation and experimental studies conducted indicate that it is possible to precisely induce an electric field in the eyeballs using single biphasic sinusoidal current pulses applied in a periorbital configuration. This makes it possible to study phosphenes at both the behavioral and electrophysiological levels, and to apply this method to modulate information processing in the visual system of healthy humans. These results open up prospects for the potential use of pPCS in the neurorehabilitation of known deficits of the visual system, and provide a basis for further research into elucidating the mechanisms of action of currently used stimulation methods in clinical practice.

Keywords: neuromodulation, visual information processing, periorbital pulsed current stimulation, phosphene perception, eeg, visual evoked potential

Streszczenie

Nieinwazyjna stymulacja prądowa jest coraz częściej wykorzystywana do wspierania funkcji mózgu i powrotu do zdrowia po urazie lub chorobie. W rozprawie skoncentrowano się na paradygmacie stymulacji mającym na celu skoncentrowanie efektu w obrębie początkowych etapów układu wzrokowego. Okołooczodołowa pulsacyjna stymulacja prądowa (ang. periorbital pulsed current stimulation, pPCS) w postaci pojedynczych dwufazowych impulsów o przebiegu sinusoidalnym aplikowanych za pomocą elektrod poniżej i powyżej oczu była testowana w podejściu symulacyjnym oraz podczas eksperymentów in vivo z udziałem zdrowych ochotników. Konkretnymi celami rozprawy były ocena stężenia indukowanego pola elektrycznego (ang. induced electric field, IEF) w mózgu, scharakteryzowanie behawioralnych i elektrofizjologicznych (EEG) odpowiedzi na stymulację wzrokową i elektryczną oraz analiza potencjału pPCS w modulowaniu przetwarzania informacji w układzie wzrokowym w paradygmacie sparowanej stymulacji impulsowej (ang. paired pulse stimulation, PPS), w którym impuls prądowy jest stosowany przed bodźcem wzrokowym, umożliwiając ocenę jego wpływu na pobudliwość i przetwarzanie neuronalne.

Symulacje komputerowe wykazały, że pPCS z elektrodami umieszczonymi powyżej i poniżej oczu koncentruje IEF głównie w gałkach ocznych, minimalizując wpływ na nerwy wzrokowe i inne obszary mózgu. Dla porównania, konfiguracja z elektrodami nad oczami i jedną elektrodą umieszczoną w okolicy potylicznej generuje bardziej rozproszone IEF, obejmujące również nerw wzrokowy i korę potyliczną. Analizy IEF wykazały, że koncentracja pola elektrycznego na krawędziach elektrody zależy od gęstości prądu i krzywizny krawędzi elektrody. Symulacje wykazały również, że domyślne wartości przewodności tkanek stosowane w SimNIBS - popularnym oprogramowaniu używanym do modelowania IEF, są niedokładne. Szwajcarska baza danych fundacji ITIS została zaproponowana jako bardziej dokładna.

W badaniu eksperymentalnym *in vivo* przetestowano układ elektrod okołooczodołowych. Wykazano, że impulsy prądowe skutecznie indukują fosfeny pochodzenia siatkówkowego, z progiem detekcji (około 5%) przy około 10 ms przy amplitudzie 300 µA i korowe potencjały wywołane elektrycznie (ang. electrically evoked potentials, EEP). Wzrost amplitudy i czasu trwania impulsu spowodował nieliniowy wzrost detekcji fosfenu i amplitudy EEP, które zostały opisane za pomocą niestandardowego trójczynnikowego modelu Naka-Rushtona, uwzględniającego całkowity ładunek impulsu, amplitudę i czas trwania. Model ujawnił, że wpływ całkowitego ładunku na odpowiedź maleje wraz ze wzrostem intensywności i długości impulsu, prowadząc do efektu nasycenia. Podkreślono również znaczenie parametrów takich jak całkowity ładunek, amplituda i czas trwania impulsu w indukcji fosfenów i charakterystyce odpowiedzi.

W drugim badaniu eksperymentalnym wykorzystano protokół pPCS, w którym impulsy o różnych długościach i amplitudach zastosowano przed bodźcem wzrokowym w postaci odwrócenia wzorca szachownicy (ang. checkerboard pattern reversal, CPR). Stwierdzono, że w grupie eksperymentalnej stymulacja prądem zmniejszyła amplitudę wczesnych komponentów wzrokowego potencjału wywołanego (ang. visual evoked potential, VEP), takich jak P1N1 i P1N2, w porównaniu z grupą placebo, co wskazuje na jej potencjalny hamujący wpływ na pobudliwość kory wzrokowej. Efekt ten był kumulatywny w czasie, tak że nie zaobserwowano różnic w sile efektu w zależności od parametrów bodźca, a jego działanie rozciągało się również na próby, w których CPR nie było poprzedzone zastosowaniem impulsu prądowego. Ponadto, efekt stymulacji zwiększał się wraz z upływem czasu i wyraźnie zanikał po jej zakończeniu.

Podsumowując, przeprowadzone badania symulacyjne i eksperymentalne wskazują, że możliwe jest precyzyjne indukowanie pola elektrycznego w gałkach ocznych za pomocą pojedynczych dwufazowych sinusoidalnych impulsów prądowych stosowanych w konfiguracji okołooczodołowej. Umożliwia to badanie fosfenów zarówno na poziomie behawioralnym, jak i elektrofizjologicznym, a także zastosowanie tej metody do modulowania przetwarzania informacji w układzie wzrokowym zdrowych ludzi. Wyniki te otwierają perspektywy potencjalnego wykorzystania pPCS w neurorehabilitacji znanych deficytów układu wzrokowego i stanowią podstawę do dalszych badań nad wyjaśnieniem mechanizmów działania obecnie stosowanych metod stymulacji w praktyce klinicznej.

Słowa kluczowe: neuromodulacja, przetwarzanie informacji wzrokowej, stymulacja impulsowym prądem okołooczodołowym, percepcja fosfenu, wzrokowy potencjał wywołany, elektroencefalografia

List of Abbreviations

AC	alternating current
ACS	alternating current stimulation
AMD	age-related macular degeneration
BDNF	brain-derived neurotrophic factor
CDM	current density magnitude
CPR	checkerboard pattern reversal
CSF	cerebrospinal fluid
DBS	deep brain stimulation
DC	direct current
EEG	electroencephalography
EEP	electrical evoked potential
EFM	electric field magnitude
EP	evoked potential
ERG	electroretinogram
FEF	frontal eye fields
FEM	finite element method
FFT	fast fourier transform
FIR	finite impulse response
FOV	field of view
GABA	gamma-aminobutyric acid (neurotransmitter)
GM	gray matter
ICA	independent component analysis
IEF	induced electric field
IIR	infinite impulse response
IPI	inter-pulse interval
IPL	inferior parietal lobule
ipRGC	intrinsically photosensitive retinal ganglion cell
ISI	inter-stimulus interval
ITC	inferior temporal cortex
K cells	small bistratified retinal ganglion cells (koniocellular pathway)
K pathway	koniocellular pathway
KDE	kernel density estimation

KHFAC	kilohertz frequency alternating current
LED	light-emitting diode
LFP	local field potential
LGN	lateral geniculate nucleus
LTD	long-term depression
LTP	long-term potentiation
M cells	parasol retinal ganglion cells (magnocellular pathway)
M pathway	magnocellular pathway
MEG	magnetoencephalography
MR-EPT	magnetic resonance electrical tomography
MRI	magnetic resonance imaging
NMDA	N-methyl-D-aspartate (receptor)
OPN	olivary pretectal nucleus
P cells	midget retinal ganglion cells (parvocellular pathway)
P pathway	parvocellular pathway
PAS	paired associative stimulation
PCA	principal component analysis
pCS	periorbital current stimulation
PCS	pulse current stimulation
PFC	prefrontal cortex
PPC	posterior parietal cortex
PPS	paired pulse stimulation
PSD	power spectral density
PSP	postsynaptic potential
RGC	retinal ganglion cell
RMS	root mean square
ROI	region of interest
RP	retinitis pigmentosa
rtACS	repetitive transorbital alternating current stimulation
SC	superior colliculus
SCN	suprachiasmatic nucleus
SD	standard deviation
SEM	standard error of the mean
SPL	superior parietal lobule
SR	stochastic resonance

SSP	signal-space projection
tACS	transcranial alternating current stimulation
tDCS	transcranial direct current stimulation
tES	transcranial electrical stimulation
TES	transcorneal electrical stimulation
TI	temporal interference stimulation
TMS	transcranial magnetic stimulation
TON	traumatic optic neuropathy
tRNS	transcranial random noise stimulation
UV	ultraviolet
V1	primary visual cortex
V2	secondary visual cortex
V3	tertiary visual cortex
V4	area located in the ventral part of the occipital lobe and extending into the the temporal lobe; part of the ventral visual stream
V5/MT	middle temporal area; located in the dorsal part of the extrastriate cortex in the temporal lobe; part of the dorsal visual stream
VEP	visual evoked potential
VRT	vision restoration therapy
WM	white matter

Introduction

The human nervous system is among the most complex and mysterious structures in the known universe. It comprises probably a few hundred billion specialized cells, each forming thousands of connections with similar cells, enabling vast networks for processing and transmitting information. It remains enigmatic because we still do not fully understand the connection between this intricate information processing and the subjective experiences we each have, though several hypotheses have been proposed (Hameroff, 2007; Havlík, 2017; Ward and Guevara, 2022). Despite its complexity and the mysteries that surround it, the nervous system is fundamentally a biological system, with its functions largely defined by the structure and cellular, biochemical and biophysical mechanisms. Any anomaly to this complex system can lead to compromised functional capabilities, often as a result of injury, disorder, or disease.

While impairments to any part of the nervous system should be avoided, the sense of sight is considered particularly crucial for humans, who largely rely on it to effectively navigate the environment. Vision is the most-studied and best-understood sense to date, both in terms of the anatomy and physiology of the visual system and the deficits that can affect it. This is due in part to its highly hierarchical and structured organization, which also influences how information is processed (Joukal, 2017). This structured design aids in understanding the mechanisms underlying specific visual deficits and how their localization within the visual system results in distinct functional impairments.

The fields of visual system deficits and neuro-ophthalmology are vast and encompass a wide range of issues (Miller et al., 2005), as do the methods for prevention, treatment, and rehabilitation (Kreutzer et al., 2017). This is primarily because there is no clear boundary between ophthalmology and neurology; the visual system spans both fields, leading to a broad spectrum of potential anatomical and physiological deficits that can impact its function at various stages. The complexity and variety of these deficits make understanding and addressing them a significant challenge. However, given that the biochemical activity of the nerve cells forming the core of the visual system is intricately linked to electromagnetic phenomena, there has long been interest in exploring whether electrical stimulation methods could be utilized in the rehabilitation of visual impairments. Neuronal activity relies on communication through neurotransmitters, the release of which depends on the flow of ionic currents within the neuron. These neurotransmitters, once released, alter the ionic currents in the target cells. Ionic currents, much like electric currents, are inherently tied to the presence of an electric field. Therefore, by influencing the electric field, one can also affect its sources. This understanding underpins the use of electrical stimulation to alter the electric fields within targeted tissues, thereby stimulating those tissues. Through the stimulation, it becomes possible to modify the physiology and function of the nervous system, which holds potential for both rehabilitation and also the enhancement of cognitive and sensory functions in healthy individuals.

Electrical stimulation is a well-understood method utilized not only in academic research but also actively in the rehabilitation of certain nervous system disorders (Antal et al., 2022). It is considered a relatively safe, cost-effective, and easy-to-use technique for both neurorehabilitation and neuroenhancement. However, two fundamental challenges arise when using electrical stimulation: the problem of specificity and the problem of understanding the relationship between stimulation parameters and outcomes.

The specificity challenge refers to the difficulty in confining the area affected by the electric field induced by electrical stimulation to a very small, precise region within the brain. With current knowledge, solutions, and technology, achieving such precise targeting with non-invasive techniques is challenging. Interestingly, temporal interference stimulation (TI), proposed by Grossman et al. in 2017, is an innovative non-invasive technique that enables the stimulation of deep brain structures without the need for implanted electrodes. While TI offers better targeting than traditional surface stimulation methods, its spatial precision remains lower compared to the direct implantation of electrodes in specific brain regions. Nevertheless, the technique holds great promise for refining the focality of the induced electric fields, making it a compelling approach for future research and applications. Although deep brain stimulation (DBS) offers high specificity, it is an invasive technique. Even with DBS, which offers a more localized approach by implanting electrodes directly into a specific brain region, the radius of the electric field generated still depends on its intensity, thus limiting the precision.

The issue of understanding the relationship between stimulation parameters and outcomes stems directly from this lack of spatial but also cellular specificity. If we are unable to isolate a sufficiently small and specific area of the brain during stimulation, it becomes challenging to determine precisely how different stimulation parameters relate to the expected or observed effects, both in the short and long term. This limitation complicates the development of reliable stimulation paradigms that can predictably and reproducibly achieve specific goals in modifying the function of the nervous system in both healthy and diseased states. As it stands, our ability to control and predict these effects is restricted to relatively large scales, making fine-tuned, targeted interventions challenging.

Despite these challenges, there are viable pathways forward. One approach is to limit the influence of the electric field to the smallest, most well-understood neuronal structures, ensuring more precise targeting. Another strategy involves carefully selecting stimulation parameters that have already known, specific effects on certain neuronal populations, structures, physiological processes, and functions. By focusing on these approaches, we can begin to develop more precise and effective neuromodulation techniques, even within the constraints of current technology and knowledge.

In the context of the visual system, we can address the problem of specificity by focusing the electric field on the eyeballs, which serve as the starting point of the visual pathway. The eyeballs effectively act as focal points for the electric field vector created by current applied through electrodes positioned on the facial surface near the eyes (Laakso and Hirata, 2013; Schutter, 2016). In simpler terms, the current from these electrodes flows directly through the eyeballs and into the visual system. This approach not only resolves the issue of specificity but also addresses the challenge of understanding the relationship between stimulation parameters and their effects. By confining the induced electric field to the eyeball, its impact is primarily limited to the structures within the eyeball itself - most notably the retina and the nerve cells that constitute it.

As the introduction to this dissertation I will briefly remind the structure and function of the visual system, and describe the electrical stimulation techniques currently used (or tested) in humans for a therapy of visual dysfunctions.

Visual System Anatomy and Function

Visual system consists of the eye - a visual sensory organ serving the function of a *camera obscura,* and dedicated elements of the central nervous system, coding and processing the information. The two stages overlap at the retina - neuronal tissue layer at the fundus on the eye.

Eye

The eye's structure can be divided into three principal layers: the outer (fibrous), middle (vascular), and inner (nervous) layers (Snell and Lemp, 1998). Each layer contains essential components that function collectively to capture, initially process, and transmit visual information to the brain.

The outermost layer of the eye is composed of the cornea and the sclera. The sclera, an opaque, white part of the eye provides structural support and protection for the inner components of the eye and an attachment point for the extraocular muscles, which control eye movements (Nishida et al., 2017). The cornea is the transparent, dome-shaped surface that covers the front of the eye. The transparency and curvature of the cornea are essential for maintaining clear vision. The carrier of visual information are photons, or corpuscular-wave components of electromagnetic waves. When the photons reach the surface of the eye, thanks to the refraction process within a cornea and a lens they change direction and can be focused onto the retina. This process of focusing light is similar to how a camera captures a sharp image (Hejtmancik et al., 2017). Most refraction occurs at the cornea's anterior surface, where light transitions from air to the denser corneal tissue. The lens provide additional refraction (Navarro, 2009) to fine-tune focus; and since its shape (curvature) can be changed it ensures the eye's ability to maintain clear vision at various distances, a process known as accommodation (Ovenseri-Ogbomo and Oduntan, 2015; Zhang et al., 2023a). The lens is suspended by zonule fibers, which are also known as suspensory ligaments, and which connect it to the ciliary body. These fibers serve to maintain the position of the lens and facilitate alterations in its shape during the accommodation process. Not all light from the outside world reaches the retina. The process is subject to regulation by the iris, working like an aperture, while another factor is the structure of the cornea and lens which are not transparent across the entire electromagnetic spectrum. They absorb electromagnetic waves primarily in the ultraviolet (UV) range, which can, with high or prolonged exposure, cause damage to the cornea (photokeratitis, a type of sunburn of the corneal tissue (Delic et al., 2017) and accelerate degenerative processes in the lens, leading to cataract formation over time (Taylor et al., 1988). In contrast, the cornea and the lens are largely transparent to visible light (approximately 400-700 nm) and infrared light, allowing these wavelengths to pass through to the deeper structures of the eye.

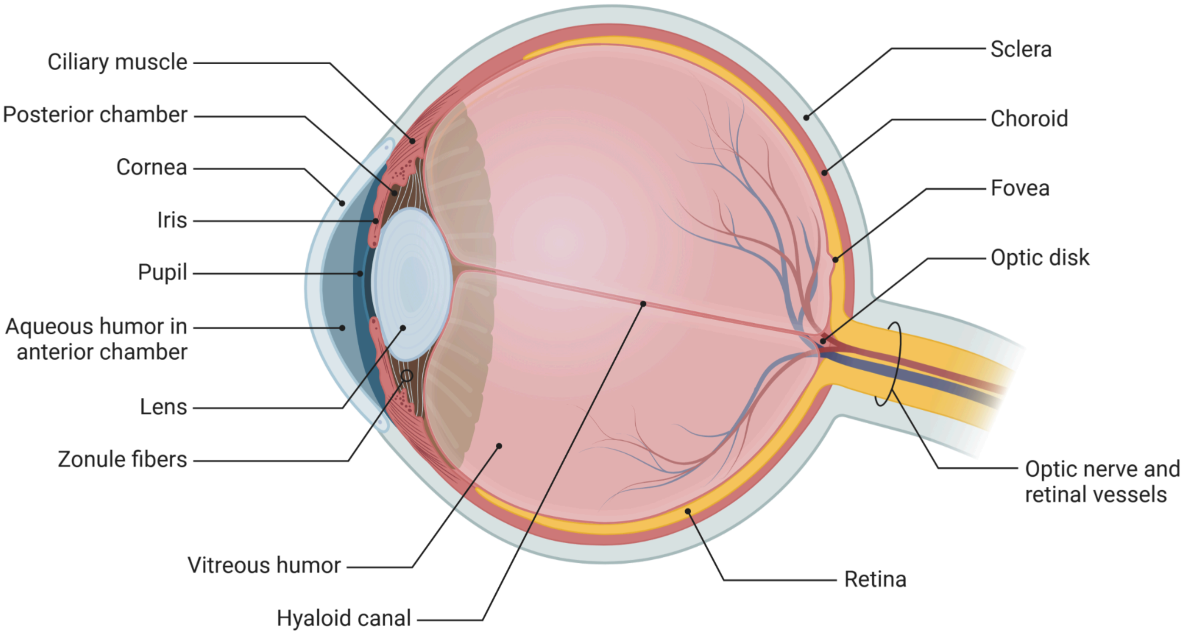

Figure 1-1. *Anatomy of the human eye. This diagram illustrates the key structures of the human eye, including the sclera, choroid, retina, optic nerve, and retinal vessels. The cornea, iris, pupil, and lens are shown at the front of the eye. The aqueous humor fills the anterior chamber, while the vitreous humor fills the larger posterior segment. The diagram also highlights the zonule fibers that support the lens and the hyaloid canal within the vitreous body. The fovea (macula), located in the retina, is the point of highest visual acuity. The optic disk, where the optic nerve exits the eye, is also known as the blind spot. Adapted from "Anatomy of the Human Eye" template, by BioRender.com (2024).*

The middle layer of the eye, also referred to as the uvea (derived from lat. *uva* meaning “grape”), encompasses the iris, ciliary body, and choroid. The iris is the colored portion of the eye that surrounds the pupil and contains muscles that adjust the size of the pupil in order to regulate the amount of light entering the eye. This process, known as the pupillary reflex, serves to safeguard the retina from excessive light and to enhance visual acuity under conditions of varying illumination (Kawasaki, 1999). The ciliary body, situated posterior to the iris, comprises the ciliary muscle and ciliary processes (Li et al., 2024). The ciliary muscle is responsible for adjusting the shape of the lens, thereby facilitating accommodation and enabling the eye to focus on objects at varying distances. The ciliary processes, meanwhile, produce aqueous humor, a fluid that nourishes the eye and maintains intraocular pressure. The choroid is a vascular layer situated between the sclera and the retina (Belden, 2002). It is responsible for supplying the outer layers of the retina with oxygen and nutrients, as well as regulating the temperature of the eye (Lejoyeux et al., 2022). Additionally, its pigmented cells reduce light scatter within the eye, thereby enhancing visual clarity (Hu et al., 2008).

The vitreous humor, a transparent, gelatinous substance occupying the space between the lens and the retina, serves to maintain the shape of the eye and acts as a conduit through which light can reach the retina. It accounts for about 80% of the volume of the eyeball (Azhdam et al., 2020). The vitreous humor is traversed by the hyaloid canal, a narrow channel that extends from the optic disc to the posterior surface of the lens. During fetal development, the hyaloid artery is present and supplies blood to the developing lens. In adults, the vitreous is typically devoid of fluid and is considered a rudimentary structure. The aqueous humor, a clear fluid produced by the ciliary body, circulates through the anterior and posterior chambers of the eye, providing nutrients to the avascular structures of the cornea and lens and maintaining intraocular pressure.

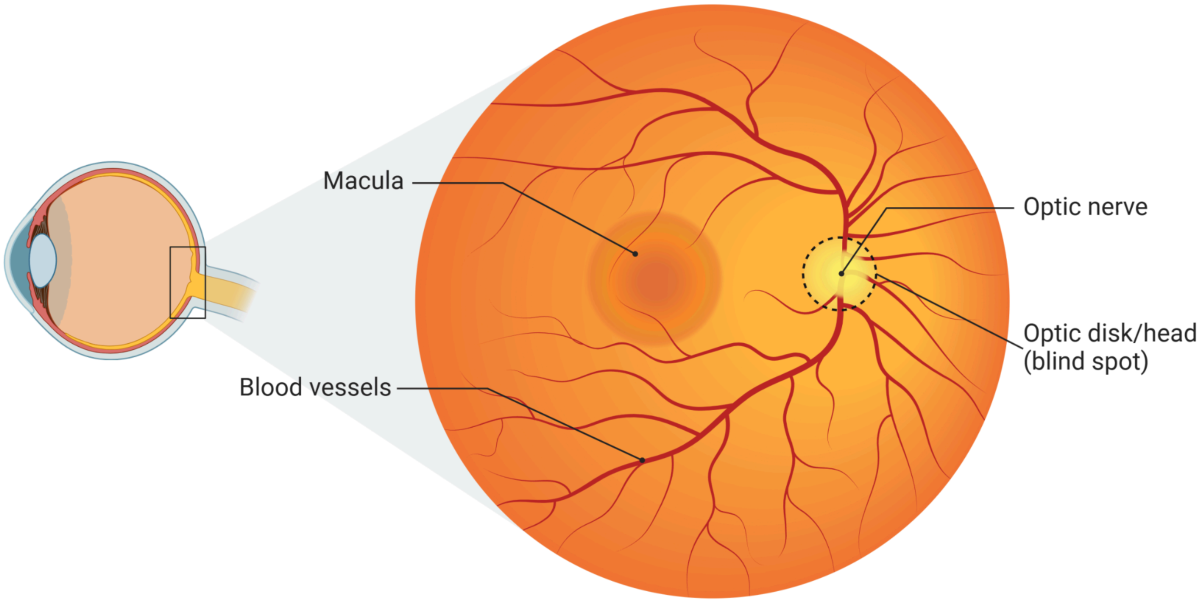

Figure 1-2. *Fundus of the Human Eye. The fundus of the eye is the interior surface that is opposite the lens and includes the retina, the optic disk (also known as the optic head or blind spot), the macula (with the fovea – spot rich in cone photoreceptors), and the blood vessels. This comprehensive Medical examination of the eye's interior enables the evaluation of a range of ocular and systemic conditions. The fovea within the macula is responsible for central vision, while the optic disk represents the point of exit of the optic nerve from the retina, thus creating a natural blind spot. The retina is supplied with essential nutrients by a network of blood vessels that traverse its surface. Created with BioRender.com (2024).*

Retina

The fundus of the eye (Figure 1-2), primarily its central and posterior parts, is covered by the retina - a light-sensitive tissue essential for converting visual input into neural signals (Masland, 2012a; Hoon et al., 2014). The retina consists of multiple neuronal layers, including photoreceptors (rods and cones), bipolar cells, horizontal cells, amacrine cells, and ganglion cells (Figure 1-3) (Hejtmancik et al., 2017). The vertebrate retina is "inverted," meaning photoreceptors are not directly exposed to light but are covered by other tissue layers. The innermost layer, the nerve fiber layer, contains the axons of retinal ganglion cells (RGCs), which converge at the optic disk to form the optic nerve. Below this is the ganglion cell layer with RGC cell bodies, followed by the inner plexiform layer, where RGC dendrites form synapses with bipolar and amacrine cells. The inner nuclear layer houses the cell bodies of bipolar, horizontal, amacrine, and Müller glial cells. Photoreceptors form synapses in the outer plexiform layer, while their cell bodies reside in the outer nuclear layer. The outer segments of photoreceptors, where phototransduction occurs (Palczewska et al., 2014), are embedded in the pigment epithelium, which absorbs excess light and facilitates pigment recycling. The retina receives nutrients and oxygen from the choroid, a vascular layer beneath Bruch's membrane.

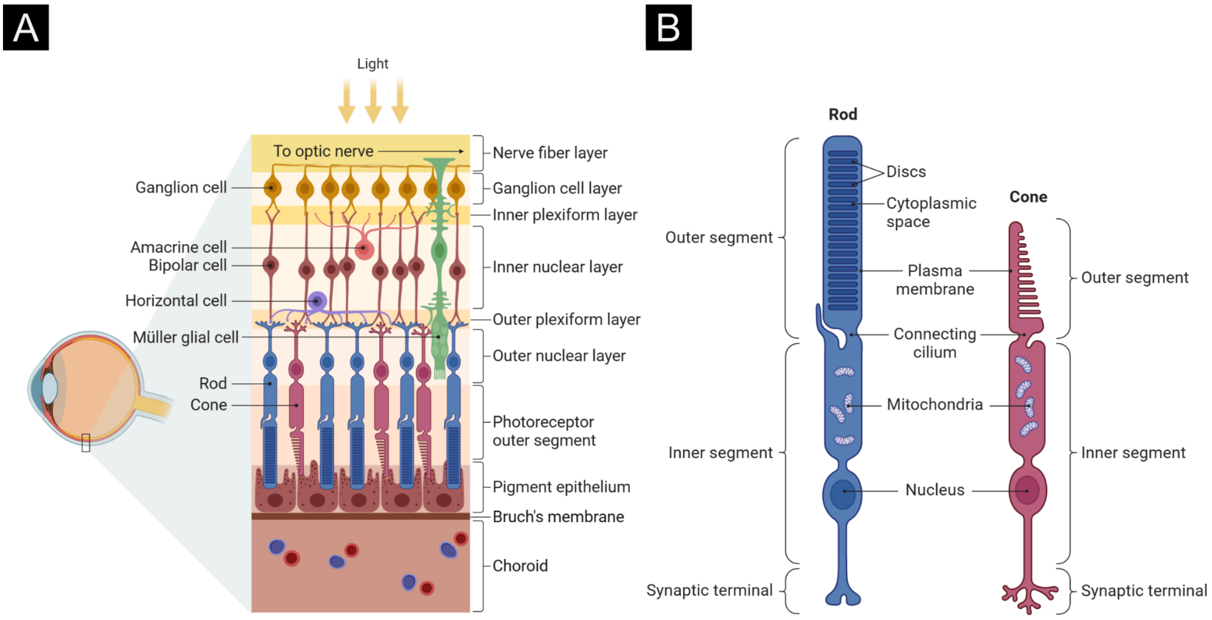

Figure 1-3. *Structure of the human retina (**A**) and morphology of photoreceptors (**B**). The left panel depicts the layered organization of the retina, emphasizing the various retinal cells that comprise it, including ganglion cells, amacrine cells, bipolar cells, horizontal cells, Müller glial cells, rods, and cones. Light passes through these layers to reach the photoreceptors. Müller glial cells, which span the entire thickness of the retina, provide structural and metabolic support to retinal neurons, maintain the blood-retinal barrier, and facilitate the regeneration of photoreceptors. The right panel illustrates the detailed morphology of rods and cones, the two types of photoreceptors, emphasizing their structural differences and specialized functions in vision. Adapted from "Structure of the Retina" and "Morphology of Photoreceptors" templates, by BioRender.com (2024).*

Photoreceptors (Hussey et al., 2022) have outer and inner segments and synaptic terminals (Figure 1-3B). The inner segment contains organelles, while synaptic terminals connect with bipolar cells (Euler et al., 2014). Rods, responsible for low-light vision, have outer segments with rhodopsin contained in stacked discs that capture light. Cones, responsible for color vision, contain photopsins (S-, M-, and L-opsins) that respond to different wavelengths of light (Figure 1-4), enabling trichromatic color vision in bright conditions (Hussey et al., 2022). Cones are concentrated in the macula, especially in the fovea, which provides sharp central vision, whereas the optic disk, lacking photoreceptors, forms the blind spot (Figure 1-5).

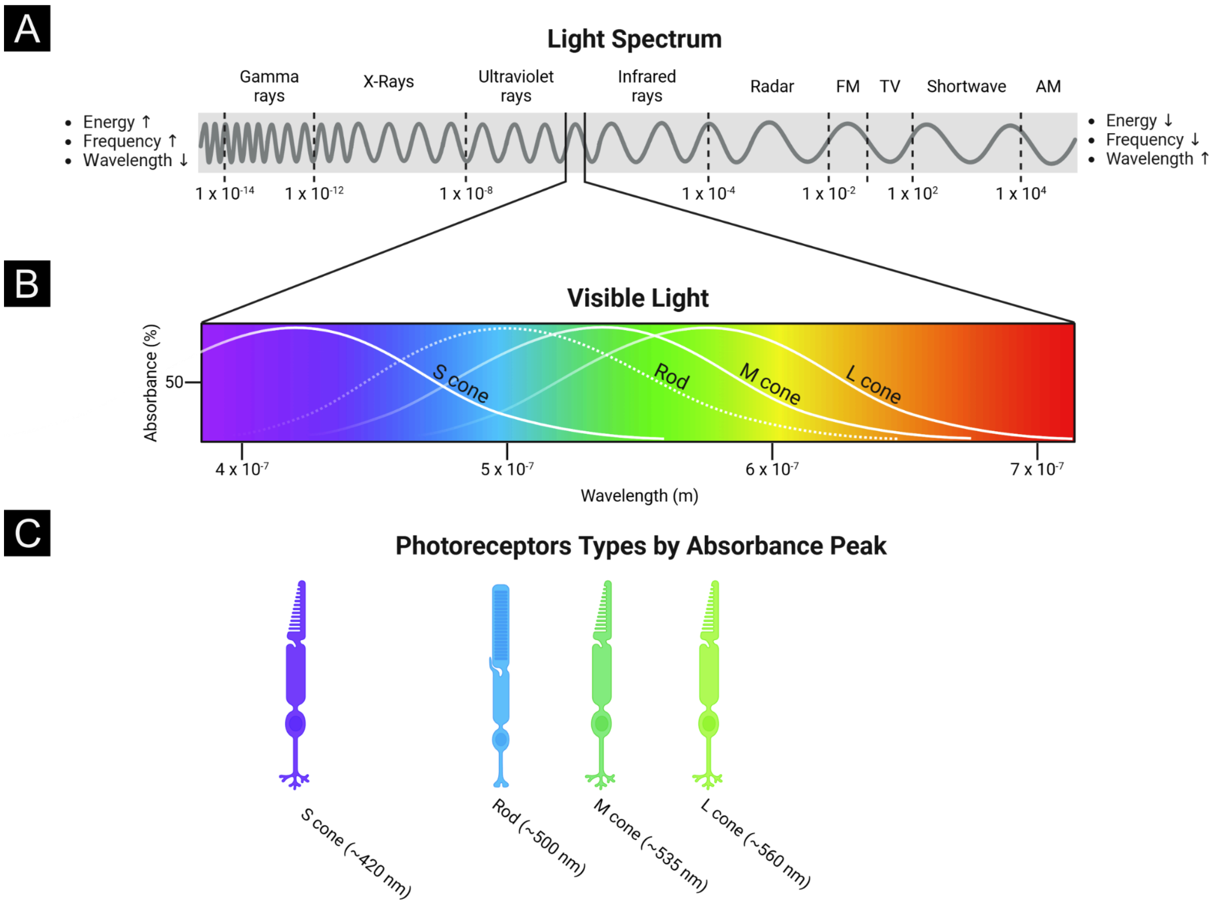

Figure 1-4. *Photoreceptor sensitivity across the electromagnetic spectrum. (**A**) The electromagnetic spectrum, highlighting the relationship between energy, frequency, and wavelength across different regions, from gamma rays to AM radio waves. (**B**) A focused view of the visible light spectrum, showing the absorbance spectra of the different photoreceptor types in the human eye. The S cone ("blue"), rod ("seeing in the dark"), M cone ("green"), and L cone ("red") photoreceptors are depicted, each with its specific absorbance peak within the visible light range. (**C**) Visual representation of photoreceptor types based on their peak absorbance wavelengths: S cones (~420 nm), Rods (~500 nm), M cones (~535 nm), and L cones (~560 nm) (Bowmaker and Dartnall, 1980). Created with BioRender.com (2024).*

Neural signals from photoreceptors are transmitted through synaptic connections in the retina. In the outer plexiform layer, photoreceptors connect with bipolar and horizontal cells; bipolar cells relay signals to RGCs in the inner plexiform layer, while horizontal cells modulate signals to enhance contrast (Kamermans and Spekreijse, 1999). Amacrine cells process signals within the inner retina, influencing RGC outputs (Masland, 2012b). RGC axons form the optic nerve, transmitting visual information to the brain. Müller glial cells provide structural and functional support, maintaining the retinal environment (Reichenbach et al., 1993). This intricate retinal architecture ensures efficient capture and transmission of visual information for further processing in the brain.

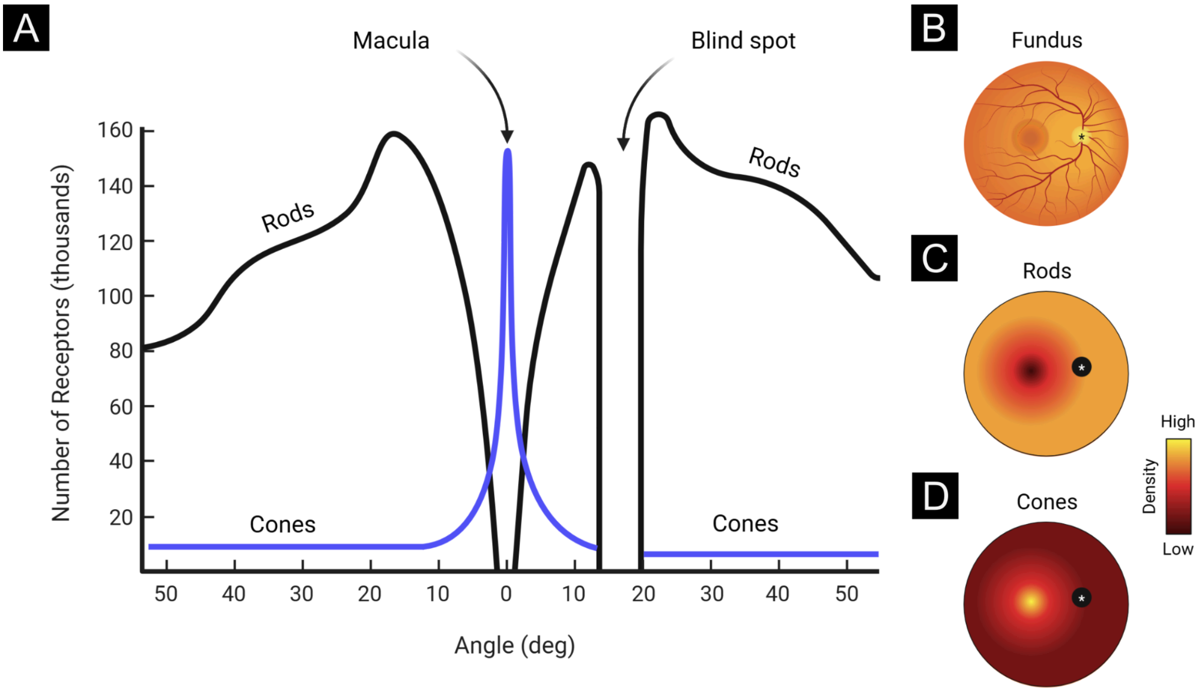

Figure 1-5. *Distribution of photoreceptors in the human retina. (**A**) The graph shows the distribution of rods and cones across the retina as a function of the angle from the fovea. Rods, responsible for scotopic (low-light) vision, are densely populated in the peripheral regions but are absent in the fovea, resulting in the characteristic dip at 0° (the foveal region). Cones, essential for photopic (daylight and color) vision, are concentrated in the fovea (centered around 0°) with a sharp peak, particularly in the macula region. The blind spot, located at around 15° temporal to the fovea, corresponds to the area where the optic nerve exits the eye, containing no photoreceptors. (**B**) A fundus image illustrating the general anatomy of the retina, with the macula and optic disc (blind spot) clearly visible. Asterisk (*) indicates a blind spot. (**C**) A heat map indicating the density of rod cells, showing high density in the peripheral retina. (**D**) A heat map showing the density of cone cells, with a peak at the fovea and a gradual decrease toward the periphery. Created with BioRender.com (2024).*

Pre-Processing of Information

"On" and "Off" Bipolar Cells

In darkness, photoreceptors release glutamate, affecting bipolar cells differently. Bipolar "on" cells, with metabotropic receptors (mGluR6), hyperpolarize in darkness and depolarize in light, while "off" cells, with ionotropic receptors (AMPA/kainate), depolarize in darkness. Rods connect 15-30 to one bipolar "on" cell, enhancing low-light sensitivity but reducing acuity. Cones typically connect in a 1:1 ratio with bipolar "on" and "off" cells, particularly in the central macula, supporting high visual acuity in bright conditions.

Horizontal Cells

Horizontal cells modulate interactions between photoreceptors and bipolar cells, enhancing contrast through lateral inhibition (Boije et al., 2016; Yan et al., 2020). These cells receive input from multiple photoreceptors and release gamma-aminobutyric acid (GABA) to inhibit neighbors, reducing glutamate output. This creates center-surround receptive fields in bipolar cells, highlighting edges and contrast by emphasizing light intensity differences.

Ganglion Cells

Ganglion cells receive bipolar cell input and transmit visual information via the optic nerve. Bipolar "on" cells depolarize in light, exciting RGCs, while "off" cells depolarize in darkness. RGCs have center-surround receptive fields, enhancing contrast detection. "On-center" RGCs respond to light increases, while "off-center" RGCs respond to decreases. In the fovea, small receptive fields allow high acuity, while larger fields in the periphery enhance sensitivity to motion and low light. The retina’s 100 million rods, 5 million cones, and 1 million RGCs highlight significant convergence (Nolte, 2012). RGC axons form the optic nerve, linking the retina to brain centers like the LGN, SC, and visual cortex.

Amacrine Cells

Amacrine cells refine bipolar and RGC connections, shaping temporal aspects of visual signals (Kolb, 1997). Located in the inner plexiform layer, these cells use diverse neurotransmitters to modulate RGC responses, either inhibiting with GABA or glycine or enhancing with excitatory signals. They specialize in processing transient visual changes, such as motion or light intensity shifts, enabling the retina to adapt to dynamic stimuli.

Output of Pre-Processed Information from the Eyeball via the Optic Nerve

The optic nerve, composed of RGC axons, transmits retinal signals to brain centers. At the optic chiasm, some axons cross hemispheres, ensuring visual field input is processed contralaterally. Most signals reach the LGN, which refines and relays them to V1. Additional projections include the SC (eye movement coordination), pretectal area (pupillary reflex; Carpenter and Pierson, 1973), and suprachiasmatic nucleus (circadian regulation; Hastings et al., 2018). This pathway is vital for visual processing and related functions.

Common Dysfunctions of the Eye

The eye is susceptible to various dysfunctions affecting photoreceptors, retinal layers, and the optic nerve. Disorders of photoreceptors include retinitis pigmentosa (RP), a genetic condition causing progressive degeneration of rods and cones, leading to night blindness and peripheral vision loss (Hartong et al., 2006), and cone-rod dystrophies, which impair color vision and central acuity (Hamel, 2007). The retina is also affected by age-related macular degeneration (AMD), characterized by degeneration of the macula, resulting in central vision loss (Friedman et al., 2004). Dysfunctional signaling within the retina can occur in conditions such as diabetic retinopathy, where damage to retinal blood vessels disrupts the inner retinal layers (Cheung et al., 2010). Glaucoma is a leading cause of optic nerve damage, often due to increased intraocular pressure, resulting in progressive loss of peripheral vision and eventual blindness (Weinreb et al., 2014). Additionally, optic neuritis, an inflammatory condition of the optic nerve, can cause sudden vision loss and is often associated with demyelinating diseases like multiple sclerosis (Petzold et al., 2010).

Information Pathways

Visual information flows along the optic nerve in multiple parallel pathways to subcortical and cortical structures (Figure 1-6). This section focuses on the key pathways, their destinations, and how the information they carry is processed and integrated. At the retinal level, different types of RGCs - including intrinsically photosensitive RGCs (ipRGCs), small bistratified RGCs (K cells), midget RGCs (P cells), and parasol RGCs (M cells) - transmit specific aspects of the visual scene, such as color, motion, and spatial detail. These pathways project to subcortical structures like the LGN, SC, suprachiasmatic nucleus (SCN), and olivary pretectal nucleus (OPN), which mediate functions such as visual integration, reflexive eye movements, pupillary reflexes, and circadian rhythm regulation.

At the cortical level, visual information is processed hierarchically in areas such as V1, V2, V3, V4, V5/MT, and higher regions like the inferior temporal cortex (ITC), superior parietal lobule (SPL), and inferior parietal lobule (IPL). These areas handle complex visual tasks, including motion perception, object recognition, and spatial awareness. The organization of parvocellular, magnocellular, and koniocellular pathways - established by specialized RGC types - ensures efficient transmission of visual information from the retina, which serves as the gateway to advanced processing at subcortical and cortical levels. Additionally, ipRGCs uniquely support non-image-forming processes, such as circadian rhythm regulation, highlighting the retina's pivotal role in initiating visual information processing.

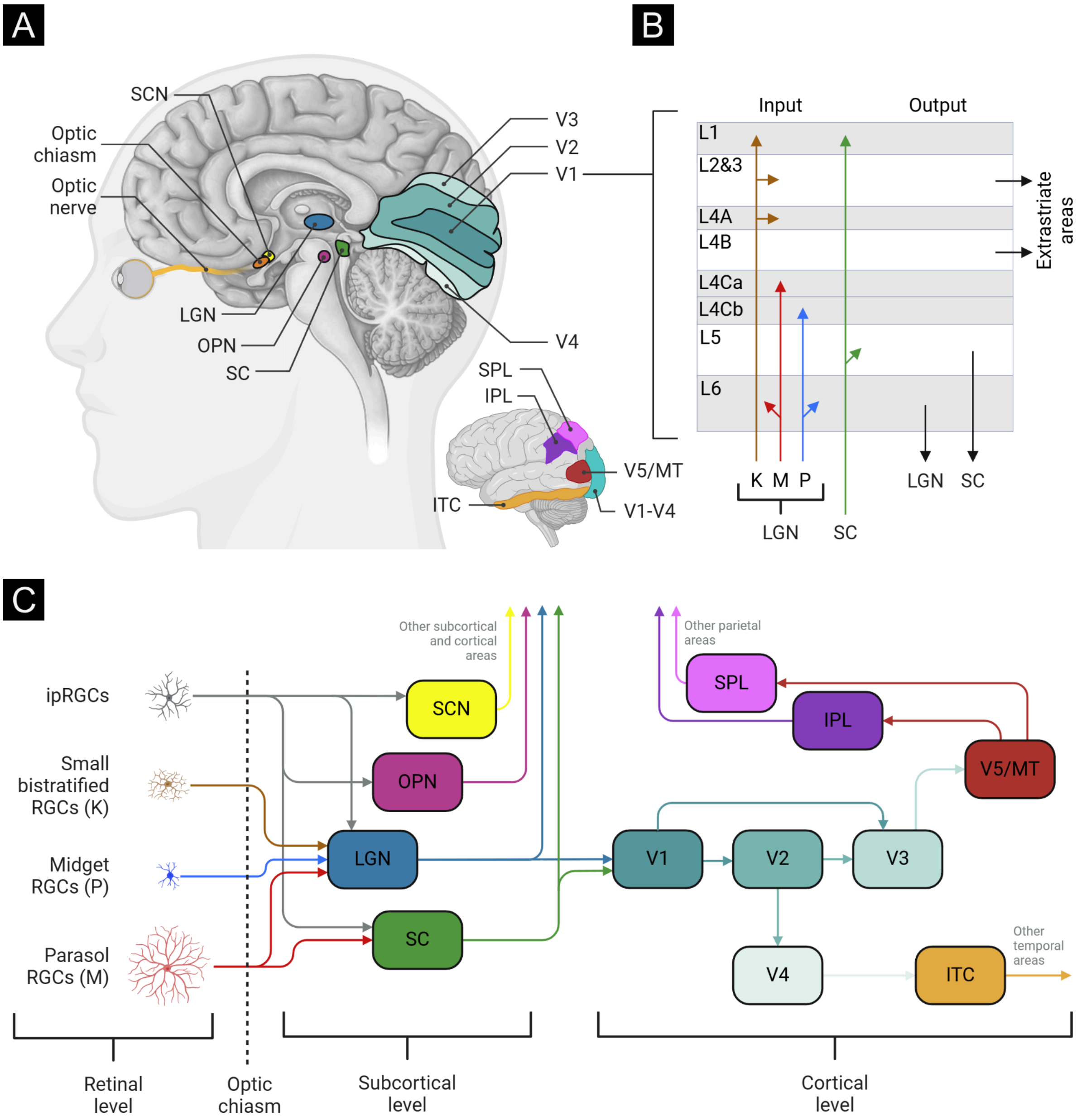

Figure 1-6. *(**A**) Overview of basic structures in the human visual system: The diagram highlights key anatomical structures involved in the processing of visual information, including the optic nerve, optic chiasm, suprachiasmatic nucleus (SCN), lateral geniculate nucleus (LGN), superior colliculus (SC), olivary pretectal nucleus (OPN), and the primary visual cortex (V1), as well as associated extrastriate areas (V2, V3, V4, V5; e.g. Winawer and Witthoft, 2015), the inferior temporal cortex (ITC), inferior parietal lobule (IPL), and superior parietal lobule (SPL). (**B**) Layers and streams of information in the primary visual cortex (V1): This diagram illustrates the laminar organization of V1, indicating the specific layers (L1-L6) where different streams of visual information (K, M, P pathways) are processed. It shows the inputs from the LGN and SC to specific layers in V1 and the outputs from these layers to extrastriate areas, and back to the LGN and SC. (**C**) Streams of visual information and connections across retinal, subcortical, and cortical levels: This diagram represents the flow of visual information from retinal ganglion cells (RGCs) - including intrinsically photosensitive RGCs (ipRGCs), small bistratified RGCs (K, koniocellular pathway), midget RGCs (P, parvocellular pathway), and parasol RGCs (M, magnocellular pathway) - through the optic chiasm to various subcortical structures (SCN, OPN, LGN, SC). The information is subsequently relayed to cortical areas (V1, V2, V3, V4, V5/MT), and further extends to regions such as ITC, IPL,*

and SPL, illustrating the complex processing required for the analysis of visual features, spatial orientation, and attention mechanisms. The diagram does not include feedback connections and minor bi-directional connections to other locations. The diagram considers only the most important structures and connections in the human visual system based on Felleman and Van Essen (1991). Created with BioRender.com (2024).

Parvocellular Pathway

The parvocellular pathway (P pathway) originates in midget RGCs concentrated in the fovea, specializing in high spatial resolution and processing fine details, particularly in red-green color vision (Lee et al., 2010; Masri et al., 2020). It is crucial for static or slowly moving objects, with a slow, sustained response, connecting to the parvocellular layers (3-6) of the LGN and projecting to the ventral stream, which handles object recognition and color processing (Javitt, 2015). Dysfunctions in this pathway, as seen in glaucoma, can impair fine detail perception and color discrimination, especially red-green differentiation (Masri et al., 2020; Yücel et al., 2003).

Magnocellular Pathway

The magnocellular pathway (M pathway) originates in parasol RGCs and is specialized in motion detection, luminance contrast, and high temporal resolution (Lee et al., 2010; Masri et al., 2020). It has a fast, transient response, lower spatial resolution, and connects to the magnocellular layers (1-2) of the LGN, projecting to the dorsal stream, which processes motion, spatial orientation, and depth (Javitt, 2015). Dysfunction in this pathway, as seen in dyslexia or neurodegenerative diseases, affects motion detection and contrast sensitivity, complicating tasks like object tracking and navigation (Masri et al., 2020; Yücel et al., 2003).

Koniocellular Pathway

The koniocellular pathway (K pathway) originates in small bistratified RGCs and processes blue-yellow color contrasts, complementing the P pathway in color vision (Hendry and Reid, 2000). It has lower spatial resolution and connects to interlaminar koniocellular layers of the LGN, contributing to both dorsal and ventral streams (Yücel et al., 2003). Dysfunction in this pathway impairs blue-yellow color discrimination, reducing overall color perception richness (Li et al., 2022).

Intrinsically Photosensitive Retinal Ganglion Cells

Intrinsically photosensitive retinal ganglion cells (ipRGCs), expressing melanopsin, regulate non-image-forming visual functions like circadian rhythms and the pupillary reflex (Mure et al., 2019). They project to the SCN, OPN, and LGN, influencing brightness perception, light-induced behaviors, and potentially prefrontal cortex functions related to emotional regulation (Lazzerini Ospri et al., 2024).

Subcortical Visual Structures

The subcortical part of the visual system includes key structures such as the LGN in the thalamus, the SC in the midbrain, the suprachiasmatic nucleus (SCN) in the hypothalamus, and the olivary pretectal nucleus (OPN) in the pretectal area, plays a crucial role in relaying, modulating, and integrating visual information before it reaches the cortical areas. These subcortical structures are not merely passive relays; rather, they actively shape visual perception through processes such as attention modulation, multisensory integration, and the coordination of motor responses. Subsequently, visual information is transmitted to the cortical level, where it undergoes further refinement and integration, culminating in the rich and detailed visual experiences that we perceive.

Lateral Geniculate Nucleus

The LGN, located in the thalamus, serves as a critical relay for transmitting visual information from the retina to V1 (Weyand, 2016). Its six layers are divided into magnocellular (motion and coarse outlines, layers 1-2), parvocellular (color and fine details, layers 3-6), and koniocellular (color contrast and multisensory integration, interlaminar regions). Beyond relaying information, the LGN actively refines it through feedback from V1, allowing the cortex to modulate visual signals based on attention and task demands. Additionally, the LGN connects to the SC and pulvinar, integrating visual inputs with motor responses and higher-order processes, supporting coherent perception and adaptive behavior.

Superior Colliculus

The SC, located in the midbrain, coordinates eye movements and visual attention by integrating sensory inputs from the retina via the retinotectal pathway for rapid detection and localization of stimuli (King, 2004; Liu et al., 2022). It receives additional input from the LGN and V1, facilitating complex visual processing and attentional shifts. The SC also integrates auditory and somatosensory information, supporting multimodal orienting responses. Its connections with the pulvinar, frontal eye fields (FEF), and posterior parietal cortex (PPC) enhance sensory integration, attention control, and saccadic planning. Subcortically, the SC works with the brainstem, basal ganglia, and cerebellum to execute precise eye and head movements, enabling efficient adaptation to dynamic environments.

Suprachiasmatic Nucleus

The SCN, located in the hypothalamus, serves as the body’s central circadian clock, regulating daily rhythms such as sleep-wake cycles, hormone release, body temperature, and feeding (Patton and Hastings, 2018). It maintains 24-hour cycles through a network of tightly coupled neurons and receives retinal input via ipRGCs through the retinohypothalamic tract. The SCN regulates melatonin secretion via the pineal gland and modulates sleep, feeding, and temperature through connections with other hypothalamic nuclei. It also influences autonomic functions like blood pressure and metabolism, aligning physiological processes with circadian rhythms.

Olivary Pretectal Nucleus

The OPN mediates the pupillary light reflex, regulating pupil size based on light intensity to protect the retina and optimize visual acuity (Gamlin et al., 1995). It receives input from ipRGCs via the retino-pretectal pathway and signals the Edinger-Westphal nuclei to control the sphincter pupillae muscles. The OPN also integrates visual and autonomic functions, contributing to circadian and systemic responses to light.

Dysfunctions of the Subcortical Structures

Dysfunctions in subcortical visual structures, such as the LGN and SC, can significantly impair visual processing. Damage to the LGN, a critical relay in the visual pathway, often results in homonymous visual field defects, where corresponding areas of the visual field in both eyes are affected (Horton and Hoyt, 1991). Lesions in the SC, integral for initiating eye movements, can disrupt saccadic eye movements, leading to difficulties in visual attention and orienting responses (Wurtz et al., 1982). Additionally, traumatic brain injuries can induce visual deficits through complement-dependent microglial phagocytosis of synapses within the dLGN, highlighting the role of immune responses in visual system pathology (Borucki et al., 2024).

Visual Cortical Areas

The cortical visual system extends from V1, which receives input from subcortical structures like the LGN, to higher areas such as V2, V3, V4, and V5/MT (Felleman and Van Essen, 1991). These regions process increasingly complex visual attributes, including orientation, motion, color, and shape. Hierarchical and parallel pathways integrate and refine visual input, enabling recognition, depth perception, and motion tracking. These processes underpin higher-order functions such as object recognition, spatial awareness, and visual attention, which are essential for interacting with the environment.

Primary Visual Cortex

The primary visual cortex (V1), or striate cortex, is located in the occipital lobe, primarily within the calcarine fissure (Grill-Spector and Malach, 2004; Tootell et al., 1998; Tong, 2003). It is crucial for initial cortical visual processing and has a high neuronal density (~200,000 per mm^2) compared to ~80,000 in other brain areas (Rockel et al., 1980). V1 is retinotopically organized and detects edges, orientations, spatial frequencies, and depth cues. Feedback from higher areas like V2, V3, and V4

(Felleman and Van Essen, 1991) refines processing based on attention and context. V1 also contains specialized cells for initial color and motion detection, making it a foundation for visual interpretation.

Secondary Visual Cortex

The secondary visual cortex (V2), or prestriate cortex, lies adjacent to V1 (Tong, 2003) and connects it to higher areas (V3, V4, V5/MT). V2 features specialized zones - thick stripes (motion/depth), thin stripes (color), and interstripes (form/orientation) - revealed by cytochrome oxidase staining. These zones integrate visual data for contour integration, depth perception, and figure-ground segregation. Extensive connections with subcortical structures like the Pulvinar and higher cortical areas allow V2 to modulate visual information based on context, attention, and cognitive factors.

Tertiary Visual Cortex

The tertiary cortex (V3), located in the occipital lobe, acts as an intermediary between earlier areas (V1, V2) and higher regions (V4, V5/MT) (Tong, 2003). It has dorsal (V3d) and ventral (V3v) subdivisions. V3d processes motion and spatial information ("where?/how?" stream), while V3v contributes to object recognition and form perception ("what?/who?" stream). V3 refines inputs from V1 and V2 for coherent perception of motion and spatial relationships, supporting dynamic visual interpretation.

V4 Area

The V4 area, part of the ventral stream, is critical for object recognition and color perception (Tong, 2003; Arcaro et al., 2009; Winawer and Witthoft, 2015). Its neurons are finely tuned to the color spectrum, enabling color constancy despite lighting changes. V4 also specializes in form and shape recognition, with neurons responsive to features like curvature and edges. Connections with V2 and the ITC integrate and refine visual data, supporting advanced visual tasks, visual memory, and attentional modulation to enhance relevant stimuli processing.

Middle Temporal Area

The Middle Temporal Area (MT/V5), located in the dorsal stream, specializes in motion processing (Tong, 2003; Kolster et al., 2010). It processes the direction and speed of moving objects, aiding in motion tracking and spatial navigation. MT/V5 refines inputs from V2 and V3 to support depth perception through motion parallax and integrates motion with form for recognizing dynamic objects. Connections with IPL and SPL regions facilitate motor planning and spatial orientation, enhancing real-time interaction in dynamic environments.

Dysfunctions of the Cortical Structures

Dysfunctions in cortical structures involved in visual processing can result in significant visual and perceptual impairments. Damage to the V1 can cause cortical blindness, where individuals lose conscious visual perception despite intact eyes and optic nerves (Aldrich et al., 1987). Lesions in the ventral stream, particularly the inferior temporal cortex, lead to visual agnosia, characterized by difficulties in recognizing objects or faces. Conversely, damage to the dorsal stream, including areas such as the posterior parietal cortex, results in deficits in spatial awareness and motion perception, impairing tasks like reaching for objects or navigating space (Karnath et al., 2001).

Visual Information Processing

The human visual system relies on a complex interplay of intracellular and extracellular (field) mechanisms to transmit, process, and integrate visual information (Buzsáki et al., 2012). These mechanisms include hyperpolarization, depolarization of neuronal membranes, and the generation of action potentials. Moreover, the electrical field fluctuations generated by ionic movements across neuronal membranes play a crucial role in modulating neuronal communication, contributing to the emergence of evoked potentials, neuronal oscillations, and multisensory integration.

Neural Activity

Hyperpolarization, Depolarization, and Action Potentials

When an action potential reaches the presynaptic terminal, it opens voltage-dependent calcium channels, triggering the exocytosis of neurotransmitter-filled vesicles into the synaptic cleft. The neurotransmitter binds to specific receptors on the postsynaptic membrane, causing ion channels to open or close, resulting in an influx or efflux of ions such as sodium, potassium, calcium, or chloride. This generates a postsynaptic potential (PSP), which can be excitatory (EPSP) if it depolarizes the membrane or inhibitory (IPSP) if it hyperpolarizes it. If the cumulative depolarization from multiple PSPs at the axon hillock surpasses a threshold, an action potential is initiated, propagating along the axon to the synaptic terminals, where the cycle repeats (Hodgkin and Huxley, 1939). Ionic currents and their spatial-temporal changes underpin nervous system information processing, with action potentials acting as key communication signals. While intercellular communication can also occur without action potentials (e.g., between photoreceptors and bipolar cells) or via electrical synapses (e.g., between rods and cones), these mechanisms are beyond the scope of this discussion.

Ionic-Based Electric Field Fluctuations

The movement of ions across neuronal membranes generates extracellular electric field fluctuations that play a crucial role in neural communication and coordination. These fluctuations, arising from collective ionic currents during synaptic transmission and action potential propagation, contribute to the local field potential (LFP) - a measure of the summed electrical activity of neuronal populations in a region (Buzsáki et al., 2012; Einevoll et al., 2013; Herreras, 2016). The LFP is influenced by factors such as synaptic inputs, intrinsic neuronal properties like membrane conductance and capacitance, and the surrounding neural architecture through which the electric field propagates. These fluctuations create a dynamic background that affects the excitability of individual neurons and their likelihood of firing action potentials. A key feature of extracellular electric field fluctuations is their ability to modulate the membrane potential of nearby neurons (Jefferys, 1995; Anastassiou et al., 2011). At a local scale, this phenomenon, known as ephaptic coupling, occurs when changes in the membrane potential of one neuron directly influence adjacent neurons. On a broader scale, field effects emerge when the geometry of a neuronal population generates a strong electric field that modulates the excitability of that population or neighboring regions (Jefferys, 1995). Such effects are particularly pronounced in densely packed neural structures like the hippocampus (Chiang et al., 2019) and cortex (Anastassiou et al., 2011), where they enhance neuronal synchronization. Additionally, field effects can be modulated by externally applied currents (Anastassiou et al., 2011; Chiang et al., 2019), forming the foundation for electrical neuromodulation of brain activity - the central focus of this thesis.

Evoked Potentials

Evoked potentials (EPs) are extracellular voltage changes generated in response to specific stimuli, such as visual inputs, or through artificial stimulation. Measured using electroencephalography (EEG) or LFP techniques, EPs reflect the summation of synchronous PSPs across large populations of neurons, offering insights into the timing, strength, and spatial distribution of neural responses (Luck, 2014). In visual processing, these responses originate from the activation of RGCs and propagate through the visual pathway, involving the LGN, V1, and higher cortical areas. Cortical pyramidal cells contribute significantly to EEG and EP signals due to their perpendicular alignment to the cortical surface.

EP generation begins with excitatory synaptic activation, where positive ions flow into postsynaptic neurons, creating localized negative extracellular voltages that form dipoles (Figure 1-7). The alignment and summation of these dipoles across populations of cortical neurons generate macroscopic electric fields detectable as EPs (Luck, 2014). The orientation of the equivalent current dipole determines the recorded EEG or magnetoencephalographic (MEG) signal, with enhanced signal strength facilitated by synchronized neuronal activity, often supported by ephaptic coupling and field effects (Senkowski and Engel, 2024). This synchronization is particularly important in visual processing, as it reflects the progression of visual information through neural networks, from initial sensory input to higher-order cortical integration.

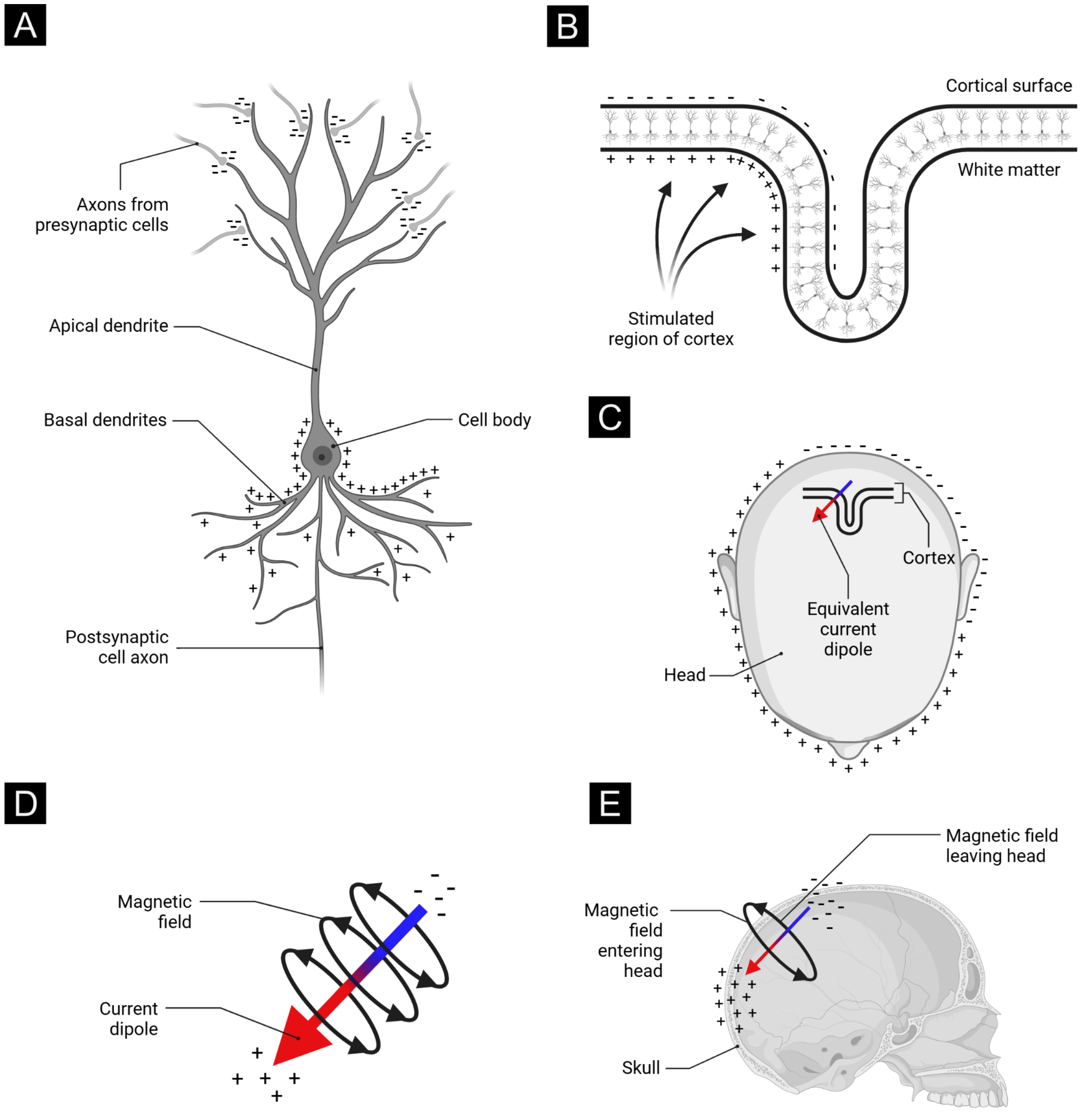

Figure 1-7. *Principles of electroencephalogram (EEG) and evoked potentials (EPs) generation, as well as magnetoencephalogram (MEG) and evoked fields (EFs). (**A**) Schematic of a pyramidal neuron during neurotransmission. An excitatory neurotransmitter is released from presynaptic terminals at the apical dendrite, leading to an influx of positive ions into the postsynaptic neuron. This influx creates a net negative extracellular voltage (denoted by "-" symbols) near the apical dendrite and establishes a small dipole, with current flowing from the apical dendrite through the neuron to the cell body and basal dendrites, where a net positive voltage (denoted by "+" symbols) is generated. The polarity of this dipole would reverse if an inhibitory neurotransmitter were*

*involved or if the neurotransmission occurred at the cell body or basal dendrites rather than the apical dendrite. (**B**) A cortical sheet containing many pyramidal cells illustrates how dipoles from individual neurons can summate when a region is active resulting in a larger, coherent dipole. (**C**) The summated dipoles from these neurons can be approximated by a single equivalent current dipole, represented as an arrow (vector), with the arrowhead indicating the positive end. The orientation and position of this dipole determine the distribution of positive and negative voltages recorded at the scalp, as captured by EEG. **(D)** A current dipole generates a surrounding magnetic field, shown here spiraling around the dipole. **(E)** A dipole beneath the skull generates an electromagnetic field that can be recorded by both EEG and MEG. EEG captures voltage differences between pairs of electrodes on the scalp, which leads to reduced spatial specificity due to the skull's conductive properties and the aggregation of signals from two electrodes per channel. MEG uses single sensors to detect magnetic fields, providing more localized and precise signals since magnetic fields pass through the skull with minimal distortion. MEG is more sensitive to tangential dipoles, while EEG is more sensitive to radial dipoles, making the two methods complementary in detecting neural activity. However, EEG is more portable and cost-effective. Created with BioRender.com (2024) based on Figure 2.2 from Luck (2014).*

Visual evoked potentials (VEPs), a subtype of EPs, are specifically tied to visual cortex activity. Early VEP components like N1 (N75) and P1 (P100) emerge from the initial processing in V1 within the first 100 ms of stimulus onset, influenced by stimulus attributes such as contrast and luminance (Jeffreys and Axford, 1972; Di Russo et al., 2002). Later components, such as N2 (N135) and P2, involve higher-order visual areas like V2 and V3, reflecting the integration of visual features and the construction of perceptual representations (Schmolesky et al., 1998). VEPs provide a temporal map of cortical processing, revealing how visual information is sequentially processed and integrated.

VEPs are extracted from EEG data by averaging responses across multiple presentations of a stimulus, canceling out noise while preserving consistent brain responses (Figure 1-8). This approach isolates key VEP components, such as N75, P100, and N135, which offer insights into the spatial and temporal dynamics of visual perception.

In addition to sensory-evoked potentials, electrically evoked potentials (EEPs) are induced through electrical stimulation, directly activating neural circuits. For instance, applying current to the retina can elicit action potentials in ganglion cells, bypassing sensory input to probe the visual system's excitability and connectivity (Foik et al., 2015; Sehic et al., 2016). EEPs, measurable through EEG or MEG, provide valuable insights into the functional integrity of visual pathways, offering a complementary perspective to sensory-evoked responses. These techniques are explored in detail within this dissertation to examine the dynamics of natural and artificial visual processing.

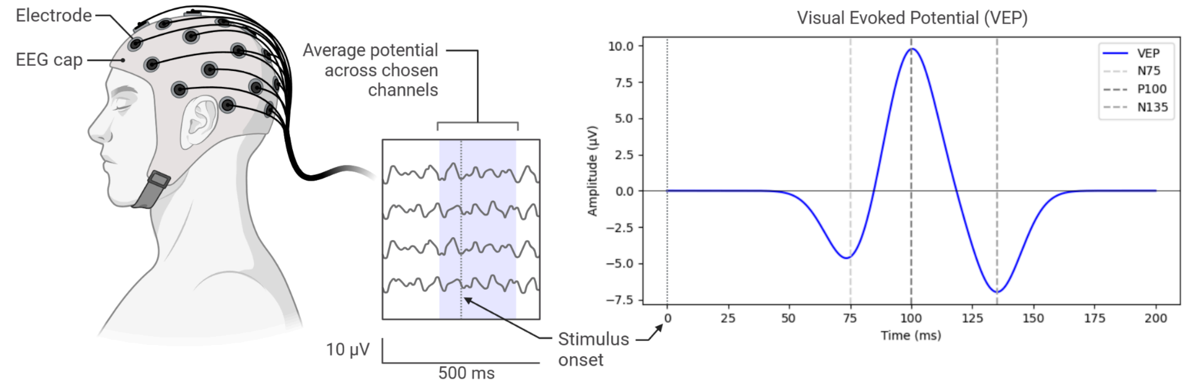

Figure 1-8. *Illustration of the process of recording and analyzing visual evoked potentials (VEPs) using electroencephalography (EEG). The figure shows an EEG cap with electrodes positioned on the scalp, recording the electrical activity generated by the brain in response to a visual stimulus. The raw EEG signals from multiple channels are averaged to obtain the VEP, which reflects the brain's response to the stimulus. The VEP waveform typically includes distinct components such as N75, P100, and N135, which correspond to different stages of visual information processing in the visual cortex. The timing and amplitude of these components provide critical insights into the integrity and function of the visual pathways. Content to the left of the VEP created with BioRender.com (2024).*

Neuronal Oscillations

Another level of complexity of information integration in the nervous system are neuronal oscillations. Neuronal oscillations, rhythmic patterns of neuronal activity at various frequencies, are fundamental to brain function, particularly in coordinating the processing and integration of sensory information, including visual inputs (Başar et al., 2001; Tallon-Baundry, 2003). In the visual system, these oscillations span several frequency bands, each contributing uniquely to different aspects of visual processing and perception.

Gamma oscillations (30-100 Hz) are critical for the local processing of visual features such as edges, orientation, and movement. These high-frequency oscillations facilitate the binding of different visual attributes - like color, shape, and motion - into a coherent percept, ensuring that various elements of the visual scene are integrated seamlessly. Gamma waves are also closely linked to visual attention, enabling the brain to focus on specific aspects of the visual input by synchronizing neuronal populations involved in processing these features (Tallon-Baudry, 2009).

Beta oscillations (12-30 Hz) play a significant role in active, conscious visual perception and the maintenance of attention. These oscillations are involved in the prediction of upcoming visual stimuli based on previous experience, helping to anticipate and prepare for what is seen next. Beta waves contribute to the continuity and stability of visual perception, particularly when processing familiar or expected visual information (Wróbel, 2000).

Alpha oscillations (7.5-12 Hz) are primarily associated with the suppression of irrelevant visual information, which enhances the brain's ability to focus on specific stimuli. By gating sensory input, alpha waves play a crucial role in visual attention, allowing for the selective processing of relevant information while filtering out distractions. This selective attention is essential for navigating complex visual environments (Clayton et al., 2018).

Theta oscillations (4-7.5 Hz) are linked to the encoding of visual memory and the integration of sensory information with previous experiences. These oscillations are particularly important in processing complex visual scenes and spatial navigation, as they help the brain to relate current visual input to stored memories, thereby aiding in the recognition and interpretation of the visual environment (Herweg et al., 2020).

Delta oscillations (0.1-4 Hz), while typically associated with sleep, also play a role in the visual system, particularly in the consolidation of visual memory and the offline processing of visual information during rest. Delta waves may facilitate the long-term storage of visual experiences and the integration of these experiences into a coherent memory framework, which can be accessed and utilized during waking hours (Harmony, 2013).

Through these oscillations, the visual system orchestrates the processing of sensory information across different temporal and spatial scales, ensuring that the brain can effectively interpret and respond to the visual world. Each frequency band contributes to a specific aspect of visual processing, from immediate feature detection to the integration of visual experiences into long-term memory, highlighting the complexity and adaptability of the visual system.

Modulation of Visual Information Processing

Overview of Neuromodulation Techniques

Classically, the term “neuromodulation” refers to an effect in which a neurotransmitter does not lead to strong depolarization and generation of action potentials, but to subthreshold changes in cell polarity, and thus modifies the neuron's responses to stimulation from other sources (increases/decreases the likelihood of spike generation; Longstaff, 2002). The term can also be used more generally to refer to the process of influencing the activity of the nervous system with external or internal stimuli to modify, regulate or modulate neuronal functions. In this context, neuromodulation encompasses a range of techniques designed to alter neuronal activity through targeted stimuli delivered to specific regions of the nervous system (Krames et al., 2009; Schalk et al., 2024). This broad field includes pharmacological, magnetic, electrical, light-based, and sound-based methods, each utilizing distinct approaches to modulate neuronal excitability and synaptic transmission. Pharmacological neuromodulation involves the administration of drugs to influence neurotransmitter activity by targeting specific receptors or pathways, offering precise control over chemical synaptic processes. Magnetic neuromodulation, such as transcranial magnetic stimulation (TMS), employs magnetic fields to induce electrical currents in the brain, modulating neural activity non-invasively. Electrical neuromodulation encompasses various techniques that apply electrical currents directly to neural tissues to alter their function, either invasively through implanted devices or non-invasively via surface electrodes. Light-based neuromodulation, including optogenetics, leverages light-sensitive proteins to control neuronal activity with high spatial and temporal precision, usually in genetically modified cells. Sound-based neuromodulation, such as ultrasound or auditory stimulation, uses sound waves to modulate neural circuits, sometimes reaching deeper brain regions inaccessible by other non-invasive methods. One of the other popular forms of neuromodulation is neurofeedback, which involves training individuals to self-regulate their brain activity by providing real-time feedback on neuronal signals (Marzbani et al., 2016).

Within the context of this dissertation, the focus is on neuromodulation techniques that utilize electrical currents to influence neural activity, particularly within the human visual system. Electrical stimulation (ES) has a long history, with the earliest documented use, in the context of visual system, dating back to 1755, when Charles LeRoy applied an electrical discharge to the eye surface of a cataract patient. The patient reported experiencing strong flashes of light, or phosphenes, marking the first recorded instance of ES generating visual sensations (Sehic et al., 2016). This exploration of electrical stimulation methods accelerated further in the 19th century with the invention of the electric pile by Volta, which laid the groundwork for understanding the therapeutic potential of direct current (DC) in neurology (Paulus, 2011). Alessandro Volta conducted experiments where he applied direct current to his own eyes using metal rods connected to a 50-volt circuit. He reported experiencing visual sensations akin to “a cloud of light” (Kaidheim, 1977). Later, in 1873, Henri Dor demonstrated the therapeutic potential of ES for various visual disorders, such as glaucoma, retinochoroiditis, and optic atrophy (Dor, 1873, as cited in Sehic et al., 2016). By 1929, Otfrid Foerster observed neural responses in the visual cortex when ES was applied to the eye (Foerster, 1929, as cited in Sehic et al., 2016). Furthermore, Rohracher (1935, as cited in Schwiedrzik, 2009) demonstrated that alternating current (AC) stimulation applied with various electrode configurations on the head could reliably induce peripheral phosphenes, marking an early success in visual system stimulation. This progress culminated in 1974, when suprathreshold ES was shown to elicit visual perceptions by stimulating the visual system (Dobelle and Mladejovsky, 1974). More recent studies, such as those by Chow et al. (2004), identified that subthreshold ES of the retina improved visual performance in patients with inactive subretinal chips, likely due to neuroprotective effects mediated by neurotrophic factors. Additionally, Santarnecchi et al. (2015), discuss the potential of transcranial electrical stimulation (tES) to modulate brain activity, emphasizing its application in enhancing cognitive abilities, which could extend to improving visual processing by targeting brain regions involved in vision. These findings sparked significant research interest into the effects of ES through animal studies and clinical trials, particularly for treating visual impairments in the following years.

Today, neuromodulation methods related to stimulation of the visual system and/or visual functions in cortical areas can be divided in terms of the form of applied current and location of stimulation electrodes. Among the most popular forms of current stimulation, we can mention direct current stimulation (DCS), alternating current stimulation (ACS), random noise stimulation (RNS) and pulsed current stimulation (PCS). On the other hand, in the context of electrode localization, we can mention transcranial, periorbital, transorbital, transpalpebral, transcorneal, suprachoroidal, epiretinal, subretinal and optic nerve current stimulation (Figure 1-9C). It is still possible to stimulate directly the surface of the cortex or its deep structures (Bosking et al., 2017), but we will focus here primarily on the head and areas around the eyes .The following sections will delve deeper into these techniques, exploring their mechanisms, applications, and the nuances of their therapeutic effects on the nervous system. We will begin by discussing the location of the electrodes and making a distinction between invasive and non-invasive stimulation based on them, which will help in discussing the forms of stimulation and their most common paradigms.

Location of Electrodes: Between Invasiveness and Non-Invasiveness

Electrical stimulation methods can be effectively discussed on two levels: first, based on the location of the stimulation electrodes, and second, based on the form of the applied current. The most common approach is transcranial stimulation, where electrodes are placed on the surface of the head (Antal et al., 2017, 2022) (Figure 1-9A). However, when focusing on stimulating the early stages of the visual system, more specific electrode placements are used (Sehic et al., 2016) (Figure 1-9C).

For example, electrodes placed directly on the cornea are referred to as transcorneal stimulation, while placement on the eyelids is known as transpalpebral stimulation. Electrode positioning on the sclera is called suprachoroidal stimulation, and on the retina, it is termed epiretinal stimulation. When placed beneath the retina, it is described as subretinal stimulation. Electrodes located between the eyelids and the eyebrow arch correspond to transorbital stimulation. Finally, for a placement that bridges the gap between transorbital and transcranial approaches, we propose referring to it as periorbital stimulation.

The term periorbital is more precise than transorbital for describing electrode placement above the eyebrow arch and on the cheeks below the eyes. Unlike transorbital, which has been used in studies such as Gall et al. (2016), periorbital better reflects the fact that the electrical stimulation is applied around the orbit rather than strictly through it. This distinction is crucial for clarity in describing stimulation setups targeting ocular structures. The induced electric field influences the eye, potentially eliciting retinal-based phosphenes, whose informational representation is transmitted via the visual pathway to the visual cortex. Adopting the term periorbital ensures accurate anatomical and functional descriptions in studies focused on the visual system.

This dissertation focuses on non-invasive current neuromodulation techniques, which hold significant potential in neuroscience and clinical applications. These methods modulate the function, physiology, and anatomy of the nervous system by altering its organic electric field without breaching the skin barrier or causing significant discomfort to the subject (Bestmann et al., 2017; Antal et al., 2017). All currently available non-invasive techniques are transcutaneous, relying on electrodes placed on the skin's surface to deliver the stimulation.

Form of Current

In addition to the location of the stimulation electrodes, the most crucial aspect of the stimulation paradigm is the choice of the form of applied current. DCS modulates neuronal excitability through sustained, low-intensity electric fields (Figure 1-9B, upper left; Figure 1-10). ACS engages neural oscillations by synchronizing electrical activity across networks (Figure 1-9B, upper right; Figure 1-11; Figure 1-12). RNS leverages stochastic resonance to enhance signal processing and communication between neurons (Figure 1-9B, lower left; Figure 1-13). PCS applies discrete pulses to selectively activate or inhibit specific neural pathways (Figure 1-9B, lower right; Figure 1-14). These forms will be further elaborated below in the context of their applications within the visual system.

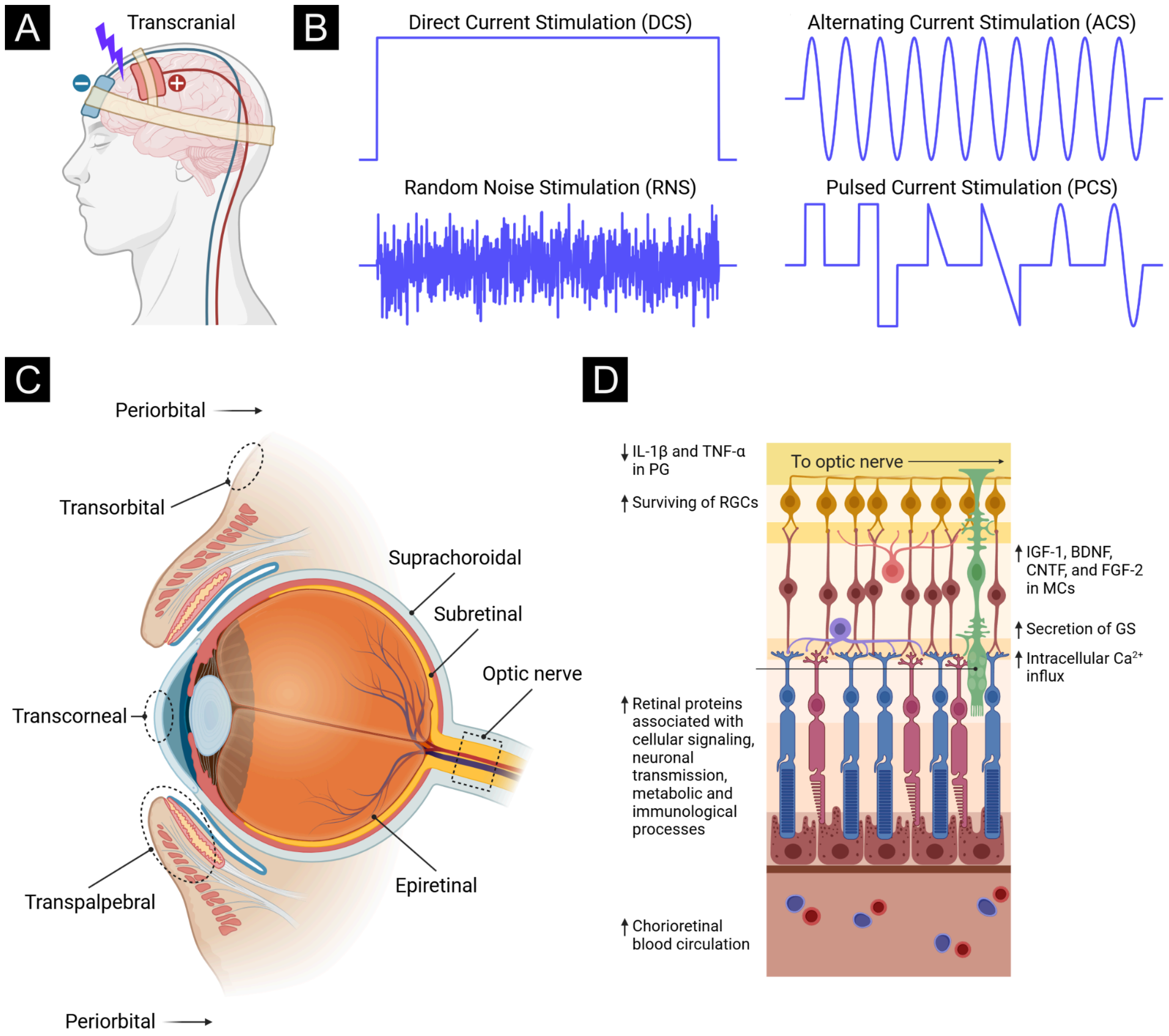

Figure 1-9. *Non-invasive electrical stimulation techniques. (**A**) Schematic representation of non-invasive electrical stimulation applied to the scalp, targeting underlying neural circuits through external electrodes to modulate brain activity for transcranial location of stimulation electrodes. (**B**) Waveforms associated with different non-invasive electrical stimulation methods. Direct current stimulation (DCS) involves applying a constant low-intensity direct current to modify neuronal excitability, either enhancing or inhibiting neural activity depending on the current's polarity. Alternating current stimulation (ACS) uses an alternating sinusoidal current to entrain neural oscillations at specific frequencies, potentially enhancing cognitive functions or sensory processing. Random noise stimulation (RNS) applies a random noise current to induce stochastic resonance, enhancing neural responsiveness and plasticity. Pulsed current stimulation (PCS) delivers a pulsed current intermittently to influence neural circuits, with effects depending on the frequency and pattern of the stimulation pulses. PCS can use a variety of waveforms, including squared, sawtooth and sinusoidal shapes, and can be applied in both monophasic and biphasic forms. (**C**) Various locations of stimulation electrodes. Periorbital location refers to the location somewhere between transorbital and transcranial, for example, the area above the eyebrows and on the cheeks. However, the boundaries between different locations are fluid. (**D**) Low-scale effects of current stimulation, whose electric field influence is focused on the eyeball, may involve neuroprotective mechanisms at the retinal level. These mechanisms include the upregulation of various neurotrophic factors, such as brain-derived neurotrophic factor (BDNF), ciliary nerve trophic factor (CNTF), fibroblast growth factor (FGF), and insulin-like growth factor 1 (IGF-1). Additionally, Müller cells (MCs), primary microglia (PG), and retinal ganglion cells (RGCs) may play a crucial role in mediating these effects. Processes like the regulation of glutamine*

synthetase (GS) and the involvement of tumor necrosis factor-α (TNF-α) further emphasize the cellular and molecular pathways potentially underlying the neuroprotective influence of ophthalmic current stimulation. Panels (A), (C), and (D) created with BioRender.com (2024). Panels (C) and (D) based on Figures 1 and 2 from Sehic et al. (2016), respectively.

Direct Current Stimulation

Overview of the Current Form and Basic Mechanisms of Action

DCS involves applying a mild direct current to the brain through the scalp via electrodes, typically comprising one anode and one cathode (Figure 1-9A and Figure 1-9B, upper left). The electrodes are generally large, ranging from 10 to 35 cm², allowing the current to reach broad brain regions. DCS employs a low-intensity current, typically between 0.5 and 2 mA, administered for durations spanning several to tens of minutes. The current flows in a constant direction - from the anode to the cathode - polarizing neuronal membranes beneath the electrodes (Lefaucheur, 2012). Anodal stimulation usually depolarizes the neuronal soma, increasing its likelihood of firing action potentials, while cathodal stimulation hyperpolarizes the soma, reducing the likelihood of neuronal firing. This modulation depends on the spatial organization of neurons relative to the induced electric field (IEF); neurons closer to the anode tend to hyperpolarize, while those nearer the cathode depolarize. As illustrated in Figure 1-10, anodal stimulation generates an inward current near the soma, leading to depolarization while simultaneously hyperpolarizing the apical dendrites. Conversely, cathodal stimulation produces an outward current, causing somatic hyperpolarization and apical dendritic depolarization. Although these changes in membrane potential do not typically elicit action potentials at standard stimulation intensities, they modulate neuronal excitability, altering the likelihood of action potential generation in response to subsequent synaptic inputs.

Beyond these immediate effects, DCS can induce sustained impacts on neuronal excitability and synaptic plasticity. Studies have shown that DCS can lead to long-lasting changes in excitability, as evidenced by TMS-induced motor responses that persist for minutes to over 24 hours, depending on the stimulation's duration and intensity (Herrera-Melendez et al., 2020). These prolonged effects are thought to involve mechanisms resembling long-term potentiation (LTP) and long-term depression (LTD) at glutamatergic synapses, central to synaptic plasticity and learning. NMDA receptor-mediated calcium influx plays a pivotal role in these processes, as pharmacological studies demonstrated that NMDA receptor antagonists blocked both the excitatory and inhibitory effects of DCS (Nitsche et al., 2003a), whereas NMDA receptor agonists prolonged excitatory effects (Nitsche et al., 2004). Furthermore, magnetic resonance spectroscopy studies have revealed that DCS can decrease GABA concentrations (Kim et al., 2014), thereby shifting the balance between excitatory and inhibitory neural activity.

Effects on Information Processing in the Visual System

DCS has been extensively studied for its effects on the visual system, demonstrating its ability to modulate cortical excitability and influence visual processing in a variety of ways. The earliest documented instance of DCS of the visual system dates back to 1755, when French physician Charles Le Roy applied direct current to a blind patient (due to cataract), resulting in the perception of light flashes, known as phosphenes. In the context of modern times, anodal and cathodal tDCS applied to the visual cortex alter phosphene thresholds induced by TMS, with anodal stimulation lowering thresholds and cathodal stimulation raising them, suggesting reversible and transient modulation of visual cortex activity (Antal et al., 2003). Over the occipital cortex, tDCS modulates VEPs in a polarity-specific manner, increasing or decreasing the amplitude of the N70 component depending on the type of stimulation applied, particularly for low-contrast stimuli (Antal et al., 2004). The method also induces prolonged changes in neuronal excitability and synaptic efficacy, highlighting its potential as a non-invasive tool for exploring visual psychophysics (Antal et al., 2006). Gender-specific effects have been reported, with anodal tDCS increasing cortical excitability more significantly in women than men, potentially influenced by gonadal hormones (Chaieb et al., 2008). Anodal tDCS reduces surround suppression within V1, indicative of its role in modulating intracortical inhibition, while cathodal stimulation shows no such effect (Spiegel et al., 2012). Further studies reveal polarity-specific effects of tDCS on magnocellular and parvocellular pathways, as well as frequency- and contrast-dependent modulation of visual thresholds and evoked potentials (Costa et al., 2015). Notably, 20 minutes of anodal tDCS applied to the visual cortex can improve visual acuity by approximately 15%, particularly in individuals with lower baseline acuity, and is associated with changes in visually evoked potentials and enhanced contrast sensitivity at high spatial frequencies (Reinhart et al., 2016). Additionally, electrical stimulation of the visual cortex evokes phosphenes, providing insights into cortical function and laying the groundwork for visual prosthetics, though achieving functional prostheses will require the creation of spatial-temporal activity patterns for complex visual perception (Bosking et al., 2017).

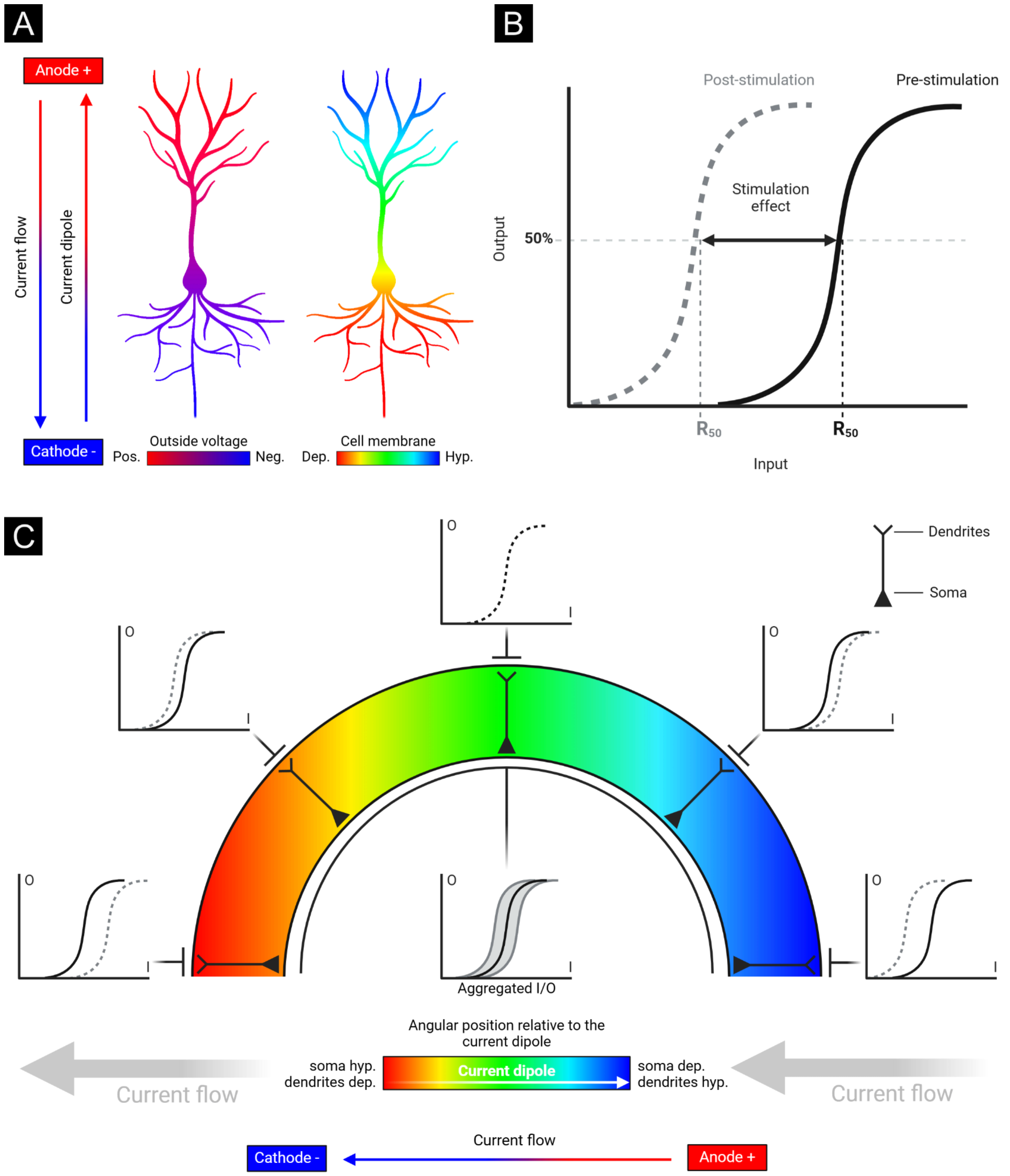

Figure 1-10. *Effects of the induced electric field (IEF) during direct current stimulation (DCS) on pyramidal neurons and their input-output (I/O) functions, depending on the angle of the electric dipole vector and external voltage effects. (**A**) Schematic representation of a pyramidal neuron illustrating the effects of direct current flow and external voltage on neuronal polarization. Under anodic DCS electrode (positive current flow from anode to cathode), the outside of the cell membrane close to the anode becomes positively charged, causing a differential effect on different parts of the neuron. Extracellulary positive voltage near the anode leads to hyperpolarization in dendrites due to an outward shift of ions, while the cell soma experiences depolarization as ions shift inward. This differential polarization depends on the orientation of the neuron relative to the electric field, with the soma being more prone to depolarization and the dendrites to hyperpolarization with top-down and cell-parallel anodic stimulation. (**B**) Graph illustrating the model I/O function of a neuron before and after stimulation. Anodic DCS*

*leads to a shift in the I/O curve due to the depolarization of the soma, which lowers the threshold for action potential generation. This results in increased neuronal excitability, reducing the amount of input required to achieve the same level of output as before stimulation. The dotted line indicates the I/O function post-stimulation, showing a leftward shift, which represents a decrease in activation threshold. (**C**) A circular diagram illustrating the relationship between various angles of the neuron's apical-axonal axis relative to the current dipole vector, along with the corresponding input/output (I/O) functions for each angle. In regions where the neuron's orientation aligns with the electric field such that the current flows toward the anode, somatic depolarization occurs due to the external voltage effects, reducing the activation threshold and increasing excitability. Conversely, when the neuron is oriented with its apical dendrites facing the cathode, where the current flows outward from the soma, somatic hyperpolarization occurs. This configuration typically requires a stronger input to overcome the inhibitory effect and generate an action potential. The aggregate I/O function at the center reflects the overall neuronal response in a spatially varying electric field. Anodic DCS decreases the activation thresholds of neurons primarily through somatic depolarization induced by the external voltage effects, thereby enhancing their excitability despite potential dendritic hyperpolarization. This effect is most pronounced when the neuron's orientation is such that the soma is depolarized. The differential effects on dendrites and soma, influenced by both internal polarization and external voltage shifts, highlight the complex interplay between neuronal orientation, electric field direction, and resulting neuronal excitability. Created with BioRender.com (2024) based on de Berker et al. (2013) and Lee et al. (2021b).*

Application in Neurorehabilitation

tDCS is extensively used in neurological rehabilitation to enhance brain recovery after conditions such as stroke, head trauma, or inflammatory diseases like multiple sclerosis (Lefaucheur et al., 2017). Given its efficacy in promoting neural recovery, it has also been tested in the treatment of visual disorders. In amblyopia, anodal tDCS was shown to increase VEP amplitude (Ding et al., 2016) and to transiently improve contrast sensitivity (Spiegel et al., 2013).

The studies by Plow and colleagues (2011; 2012a; 2012b) provide compelling evidence for the efficacy of combining occipital cortical tDCS with vision restoration therapy (VRT) in enhancing visual rehabilitation outcomes in patients with hemianopia. Plow et al. (2011) demonstrated that this combined approach was both feasible and safe. Compared to VRT with sham (placebo) stimulation, therapy with tDCS resulted in greater improvements in visual field expansion, enhanced visual cortical reorganization seen in fMRI, and improved activities of daily living.

In a clinical trial, Plow et al. (2012a) confirmed these findings, showing that the combination of tDCS and VRT significantly outperformed VRT with sham in terms of visual field expansion and activities of daily living, although subjective perceptions of improvement were unexpectedly higher in the sham group. A subsequent randomized controlled trial by Plow et al. (2012b) revealed that tDCS combined with VRT accelerated improvements in stimulus detection early in the training process, with more substantial visual field shifts manifesting after three months, indicating a task-specific enhancement of visual recovery. This trial also found that tDCS did not significantly improve contrast sensitivity or reading performance, underscoring the selective impact of tDCS on different aspects of visual function. Nevertheless, the results indicated that patients receiving combined treatment with tDCS exhibited accelerated recovery and a greater shift in the visual field border.

Together, these studies suggest that tDCS can effectively augment VRT, potentially offering a more robust therapeutic strategy for visual rehabilitation in hemianopia. In addition, the study by Olma et al. (2013) demonstrated that serial anodal tDCS applied over the visual cortex in subjects after occipital stroke led to significant long-term improvements in motion perception in the unaffected visual hemifield. These effects, observed after five consecutive days of stimulation, were sustained at 14- and 28-day follow-up assessments, suggesting that tDCS can induce neuroplastic changes in the visual cortex. The findings highlight the potential of tDCS for promoting long-term visual function recovery in patients with cortical lesions.

Moreover, the study by Kim et al. (2016) investigated the effects of tDCS combined with traditional occupational therapy on visual perception and ADL performance in stroke patients. Although there was no significant difference between the sham and tDCS groups, the experimental group achieved higher scores. Previous studies by Kraft et al. (2010) and Peters et al. (2013) suggest that tDCS may enhance perceptual learning, offering potential benefits for neurorehabilitation of visual functions.

In summary, these studies demonstrate that tDCS, particularly when combined with visual rehabilitation therapies such as VRT, can significantly improve visual field expansion, visual perception, and daily living activities in patients with conditions such as hemianopia and amblyopia.

Alternating Current Stimulation

Overview of the Current Form and Basic Mechanisms of Action

The ACS involves applying alternating electrical current to the tissue of interest (Figure 1-9B, upper right). This current periodically changes direction at specific frequencies, ranging from as low as 0.1 Hz to as high as 100 Hz, with stimulation durations lasting from several minutes to tens of minutes (Wischnewski et al., 2023). The typical transcranial ACS (tACS) setup, which is the most common, uses electrodes placed on the scalp, similar to those used in tDCS.

tACS delivers low-intensity currents, generating electric fields in the brain that typically range from 0.1 to 1 mV/mm (or 0.1 to 1 V/m) for commonly used intensities that avoid discomfort during stimulation (Alekseichuk et al., 2022). This field strength is sufficient to bias the timing of neuronal action potentials, influencing the likelihood of neural firing without directly inducing action potentials. However, the electric field intensity diminishes as it penetrates deeper cortical structures, making the effects of tACS most pronounced in superficial cortical areas.

Empirical studies suggest that a minimum effective field strength of approximately 0.3 to 0.4 mV/mm is required to achieve an 80-95% probability of modulating neuronal activity in the targeted regions (Figure 1-11A). When this threshold is met, tACS influences brain activity through three primary mechanisms (Figure 1-11B) (Alekseichuk et al., 2022; Wischnewski et al., 2023):

1. Neural spike-timing modulation and local entrainment (Figure 1-11B, upper panel). tACS can bias the timing of neural spikes, promoting synchronization of neuronal activity with the AC frequency (Herrmann et al., 2016). This occurs through rhythmic polarization and depolarization of neurons, aligning their firing patterns to the applied AC frequency during stimulation, referred to as "online effects”. Entrainment is most effective when the stimulation frequency matches the natural "eigenfrequency" of the targeted brain oscillations, such as the individual alpha frequency (~10 Hz) observed in EEG recordings. This frequency-matching phenomenon, illustrated by the "Arnold Tongue”, ensures that neurons synchronize optimally with the external oscillations (Figure 1-11C-E) (Salchow et al., 2016; Sabel et al., 2020a).

2. Induction of synaptic plasticity (Figure 1-11B, central panel). tACS can induce changes that persist beyond the stimulation period, known as "offline" or "after-effects”. For instance, Zaehle et al. (2010) demonstrated that alpha-frequency tACS increased the amplitude of alpha oscillations recorded after stimulation. Sustained neural entrainment over 10 to 30 minutes is thought to be necessary for inducing synaptic plasticity (Strüber et al., 2015), allowing tACS to influence longer-lasting changes in neural connectivity and function.

3. Modulation of long-range connectivity (Figure 1-11B, lower panel). By applying tACS over multiple brain regions, oscillatory activity between these areas can be synchronized. Depending on whether the regions are synchronized to the same or different AC phases, tACS can either enhance or disrupt inter-regional communication (Bola et al., 2014; Helfrich et al., 2014; Weinrich et al., 2017; Schwab et al., 2019). This modulation of connectivity can align time windows for neuronal depolarization and action potential firing, facilitating information flow within local networks and across large-scale brain networks.

The effects of ACS are influenced by various factors, including electrode placement, stimulation waveform, intensity, and the brain's concurrent activity state. These parameters collectively shape ACS's ability to modulate cognition and behavior in a frequency-specific manner, making it a versatile tool for both research and clinical applications targeting brain function.

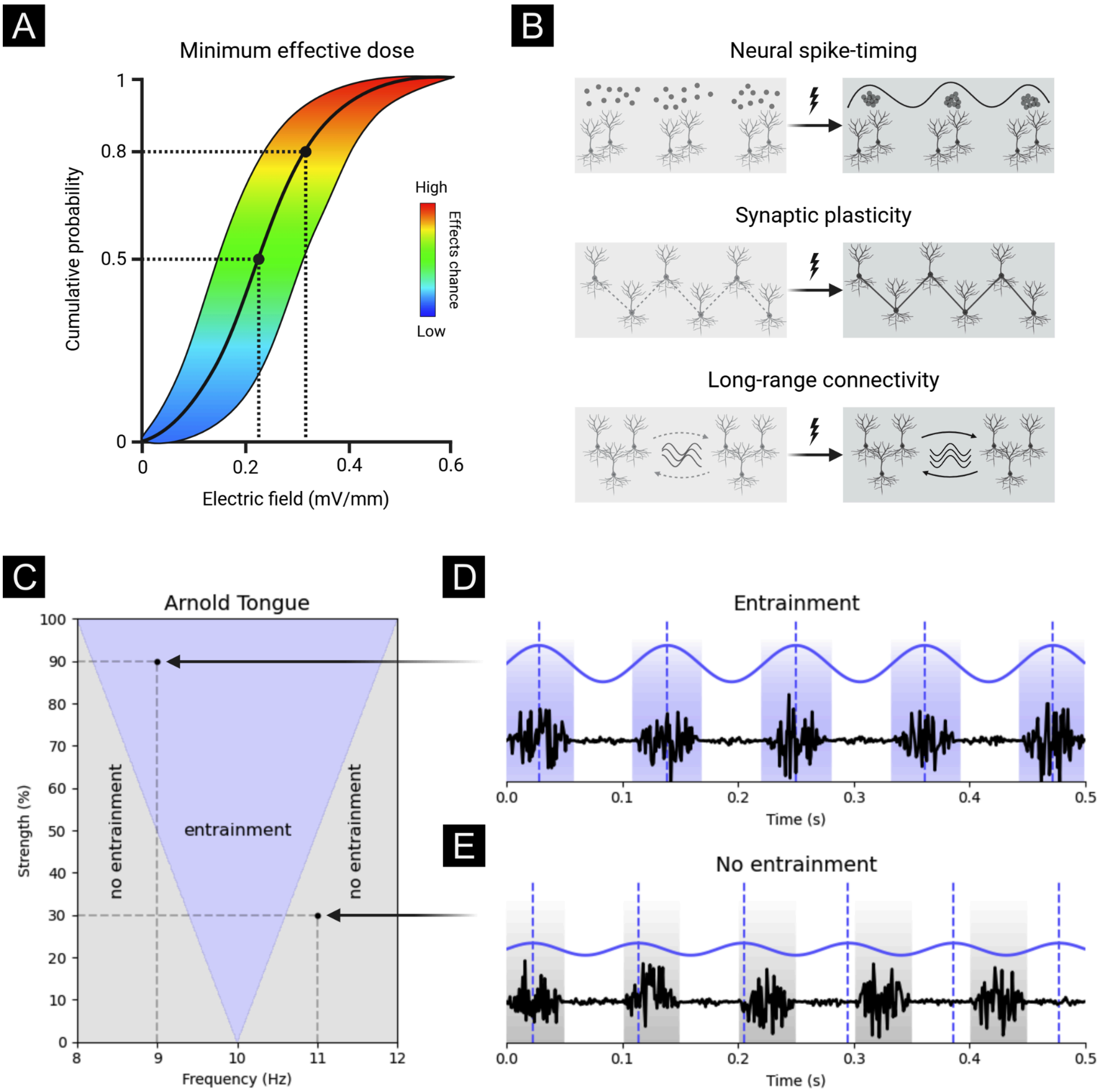

Figure 1-11. *Effects of alternating current stimulation (ACS) on neural mechanisms and brain function. (**A**) Dose-response curve illustrating the relationship between electric field strength (mV/mm) and the cumulative probability of achieving the minimum effective dose to modulate brain activity. The gradient area (blue to red) represents the probability of achieving the desired neural effect and includes a 99% confidence interval. Meta-analyses suggest that an electric field strength of approximately 0.3 mV/mm yields an 80% probability of modulating brain activity, while 0.4 mV/mm corresponds to a 95% probability. The unit mV/mm is equivalent to V/m (e.g., 0.5 V/m equals 0.5 mV/mm). Adapted from Alekseichuk et al. (2022). (B) Schematic representations of ACS effects when sufficient electric field strength is achieved: (1) modulation of spike timing leading to biased spiking and local neural entrainment during stimulation; (2) enhancement of synaptic plasticity, particularly via NMDA receptor pathways, with effects extending beyond stimulation; and (3) modulation of long-range connectivity through synchronization of brain regions, either in-phase or out-of-phase, to strengthen or weaken inter-regional connectivity. These mechanisms highlight ACS's potential for targeted cognitive and functional improvements. Adapted from Wishnewski et al. (2023). (C) Graphical representation of the Arnold Tongue, illustrating regions of frequency and amplitude where neural oscillations achieve entrainment. The x-axis represents the stimulation frequency (8–12 Hz), while the y-axis depicts the stimulation amplitude as a percentage. The central blue region shows the entrainment zone, where the driven oscillator, with an*

eigenfrequency of 10 Hz, synchronizes its phase and frequency to the external driving force. Outside this region, the oscillator fails to achieve synchronization. (D) Entrainment dynamics at 9 Hz driving frequency. The driven oscillator (eigenfrequency 10 Hz) successfully synchronizes to the external 9 Hz stimulation (blue signal), with peaks and troughs aligning (dashed lines), demonstrating neural entrainment within the Arnold Tongue region. (E) Failed entrainment dynamics at 11 Hz driving frequency. The external driving force is too weak and mismatched in frequency to shift the oscillator's eigenfrequency, resulting in no synchronization. Neural oscillations (black signal) remain independent of the external stimulation (blue signal), demonstrating the limits of neural entrainment. C-E subplots adapted from Sabel et al. (2020a). Created with BioRender.com (2024).

Effects on Information Processing in the Visual System

The effects of ACS on the visual system have been explored for decades, beginning with Rohracher's (1935, as cited in Schwiedrzik, 2009) early demonstration that ACS applied with various electrode configurations reliably induced peripheral phosphenes, marking a foundational success in visual system stimulation. Subsequent studies have expanded on this, with Kanai et al. (2008) showing that transcranial alternating current stimulation (tACS) over the occipital cortex interacts with ongoing cortical rhythms in a frequency-specific manner to induce phosphenes, with the most effective stimulation frequency influenced by ambient lighting and oscillatory activity. Schutter and Hortensius (2010) further highlighted the importance of volume conduction effects, reporting more intense phosphenes during frontalis-vertex tACS compared to occiput-vertex configurations, suggesting a retinal contribution to cortical stimulation effects. Naycheva et al. (2012) demonstrated that electrically evoked phosphene thresholds are significantly higher in patients with retinal diseases compared to healthy individuals, with the lowest thresholds observed at 20 Hz, underscoring the method's utility for assessing retinal function clinically. However, Brignani et al. (2013) raised concerns about tACS reliability in modulating brain oscillations, finding impaired task performance at specific frequencies (6 Hz and 10 Hz) over the occipito-parietal area but no evidence of retinotopically organized effects. Antal and Paulus (2013) provided an overview of tACS mechanisms, emphasizing its ability to synchronize or desynchronize cortical rhythms, induce neuroplasticity with long-term use, and impact functions ranging from motor performance to oncological treatments. Laakso and Hirata (2013) used computational modeling to confirm that tACS-induced phosphenes originate in the retina due to the eye's sensitivity to electrical stimulation, even with distant electrode placements. Schutter (2016) highlighted challenges in disentangling central and peripheral contributions to brain function and cognition during tACS-induced retinal phosphenes. Finally, Sabel et al. (2020a) reviewed tACS as a promising tool for modulating visual information processing and inducing brain plasticity, particularly when applied transorbitally or directly over the visual cortex.

Application in Neurorehabilitation

tACS has been used in neurorehabilitation efforts targeting the visual pathway for over 25 years (Abd Hamid et al., 2015; Sabel et al., 2020a). This technique demonstrates potential across various stages of the visual system, from the retina to the visual cortex, and is increasingly recognized for its ability to modulate visual perception, restore vision, and enhance neuroplasticity. Studies show that applying tACS at specific frequencies, such as alpha (8-12 Hz) or gamma (30-100 Hz), enhances visual perception by inducing phosphenes, modulating contrast sensitivity, and improving performance in tasks related to motion detection and object recognition (Kanai et al., 2008; Antal et al., 2008). These effects are attributed to the reinforcement of neural circuits within the visual system, highlighting ACS as a potent mechanism for enhancing visual processing in both healthy individuals and those with visual impairments. The induction of lasting after-effects beyond the stimulation period is particularly significant for vision restoration, with evidence suggesting improvements in visual acuity and visual field performance (Sabel et al., 2020a).

A case study showed that repetitive transorbital ACS (rtACS) applied to a patient with optic nerve atrophy significantly improved super-threshold visual field detection and perimetric thresholds, suggesting enhanced neural synchronization and transmission along the central visual pathway (Gall et al., 2010). Similarly, a clinical trial found that rtACS significantly increased defective visual field size and vision-related quality of life in patients with optic neuropathy, with improvements in the National Eye Institute Visual Function Questionnaire "general vision" subscale and static and kinetic perimetry compared to sham stimulation (Gall et al., 2011). Another study investigating brain functional connectivity in individuals with partial optic nerve damage revealed that rtACS enhanced short- and long-range alpha coherence, which correlated with improved detection abilities and processing speed, underscoring the role of brain connectivity in vision restoration (Bola et al., 2014). A randomized controlled trial further demonstrated that rtACS improved super-threshold visual field detection by 24% in partially blind patients with optic neuropathy, along with enhancements in near-threshold visual fields, reaction times, and static perimetry, suggesting increased neural coherence and brain plasticity (Gall et al., 2016). However, it is important to note that this study technically used PCS rather than ACS, as it employed bursts of biphasic square pulses with an unknown number and length per burst at frequencies of 8-25 Hz during 25-minute sessions.

In recent research, however, Enayati et al. (2024) explored the optimal parameters of transcorneal ACS in a mouse model of RP, showing that rectangular and ramp waveforms significantly improved photoreceptor survival and retinal function. These findings suggest promising applications for ACS in preserving vision in both human and mouse models of degenerative retinal diseases. By promoting synaptic plasticity and potentially reorganizing functional connectivity within the visual cortex, ACS offers a non-invasive and effective therapeutic intervention for neurorehabilitation programs aimed at vision restoration. Future advancements, including individualized protocols and computational modeling, are likely to further enhance its therapeutic potential, paving the way for more targeted and efficient interventions.

Random Noise Stimulation

Overview of the Current Form and Basic Mechanisms of Action

The third major non-invasive neuromodulation approach involving electrical current is RNS, which applies a random or "noisy" current (Figure 1-9B, lower left). Technically, RNS uses similar contacts and generally low-intensity current like the other techniques, but it stands out because its current fluctuates continuously in a random Gaussian noise pattern containing frequencies from 0.1 Hz to 640 Hz (Antal and Herrmann, 2016). Mechanisms underlying the effects of RNS are not fully understood, but several hypotheses have been proposed. In-vitro studies indicated that, on the cellular level, RNS affects the sodium (Na+) channels in neurons, potentially altering their activation and inactivation dynamics (Remedios et al., 2019) and inducing subtle changes in the neuronal membrane potentials. On a population level, RNS may operate through mechanisms like stochastic resonance (Moss et al., 2004; Pavan et al., 2019). Stochastic resonance (SR) is a nonlinear phenomenon where random noise added to a system can actually improve the detection of weak signals or enhance the information content of a signal, such as neural activity (Figure 1-12). This counterintuitive effect occurs because an optimal level of noise can help a subthreshold stimulus reach a detection threshold. In the context of RNS, the random noise stimulus, overlaid on natural subthreshold neural oscillations, can enhance the detection of weak signals by neurons, thereby improving sensory processing and perception. Moreover, the randomness of the noise can enhance neural communication and plasticity by preventing the neurons from becoming desensitized to repetitive stimulation patterns (Antal and Herrmann, 2016; Fertonani and Miniussi, 2017), thus promoting more robust neural responses across different frequencies. Notably, reversing electrode polarities in RNS does not reverse effects on cortical excitability (Antal and Herrmann, 2016), which confirms that the effects are due to the dynamic of random fluctuations of electric fields, not their direction.

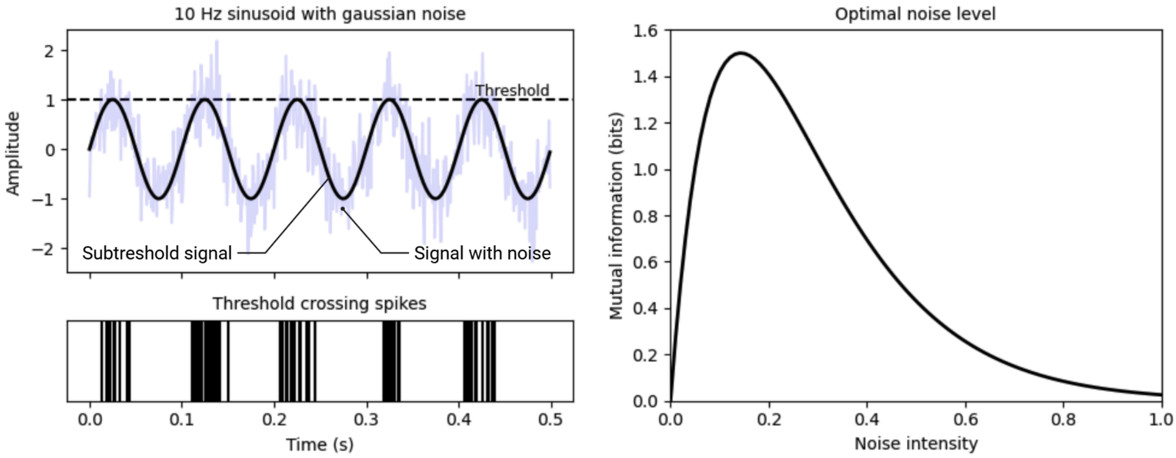

Figure 1-12. *Stochastic resonance in neural signal processing. The left panel illustrates a 10 Hz sinusoidal signal with added Gaussian noise. The original subthreshold signal (black line) does not cross the threshold for spike generation. However, with the introduction of noise (blue line), the combined signal surpasses the threshold, leading to threshold-crossing spikes generation (bottom plot), which are represented as discrete events over time. The right panel shows the relationship between noise intensity and mutual information (measured in bits). An optimal noise level maximizes information transfer, highlighting the beneficial effects of moderate noise in enhancing neural signal detection / spike generation. Beyond this optimal point, increasing noise intensity leads to a decline in mutual information, indicating a detrimental impact on neural information processing and integration. Based on Figure 1 from Moss et al., 2004, with arbitrary values not based on experimental data.*

Effects on Information Processing in the Visual System

Building on the unique mechanisms of action described earlier, transcranial RNS (tRNS) has demonstrated significant potential for modulating the visual system and enhancing various aspects of visual perception and processing. Through its stochastic resonance effects and ability to influence cortical excitability, tRNS can improve neural communication, enhance detection of weak stimuli, and promote plasticity in visual cortical networks. These properties make it a promising tool for advancing our understanding of visual system function and exploring therapeutic applications.

Herpich et al. (2015) demonstrated that high-frequency tRNS significantly enhances perceptual learning in global motion direction discrimination tasks compared to anodal tDCS, sham, and no-stimulation conditions in healthy adults. Similarly, van der Groen and Wenderoth (2016) showed that tRNS improves the detectability of weak visual stimuli through stochastic resonance, which optimizes performance in visual detection tasks. Van Koningsbruggen et al. (2016) further highlighted that tRNS applied over the visual cortex enhances value-driven attentional capture by potentiating plasticity in reward-associated visual learning tasks.

Comprehensive reviews, such as that by van der Groen et al. (2022), underscore the broader benefits of tRNS in enhancing perception, learning, and long-term plasticity. Potok et al. (2023) extended this work by demonstrating that tRNS applied to the V1 and retina significantly improves visual contrast sensitivity, enhancing the detection of weak stimuli through the modulation of retino-cortical pathways.

Application in Neurorehabilitation

Clinically, tRNS has shown considerable promise in improving visual functions for conditions such as amblyopia, hemianopia, myopia, and retinal disorders. For amblyopia, a condition characterized by reduced visual acuity due to abnormal visual development, tRNS applied over the visual cortex has resulted in significant improvements in both visual acuity and contrast sensitivity (Camilleri et al., 2016). Donkor et al. (2021) demonstrated that five daily sessions of tRNS significantly enhanced contrast sensitivity and uncrowded visual acuity in adults with amblyopia, though long-term improvements were less consistent. Notably, studies have shown that combining tRNS with perceptual training can enhance these effects (Campana et al., 2014, 2016).

tRNS has also been effective in rehabilitating patients with hemianopia, where vision is lost in half of the visual field due to cortical or optic pathway damage. When applied over the occipital cortex, tRNS facilitated visual field recovery (Fertonani et al., 2011). The improvement was believed to occur through the enhancement of residual visual processing capabilities, where tRNS amplified sub-threshold neural activity, thereby improving visual detection and perception in the impaired field. Herpich et al. (2019) further demonstrated that tRNS could boost visual learning in patients with chronic cortical blindness, leading to recovery of motion processing in the blind field within just ten days of training - a timeframe insufficient for significant improvement with training alone.

The potential of tRNS in managing myopia has also been explored. Early studies suggest that tRNS could modulate visual processing and potentially slow myopia progression by altering neural activity related to the accommodation reflex (Camilleri et al., 2014, 2016). In studies involving myopic patients, the combination of tRNS with contrast-detection tasks led to improvements in contrast sensitivity and visual acuity, further supporting the role of tRNS as a beneficial adjunct to behavioral training (Camilleri et al., 2014, 2016).

Moreover, Itzcovich et al. (2017) demonstrated that stochastic resonance, using optimal levels of dynamic Gaussian noise, significantly improves the detection of sub-threshold visual information in individuals with retinal disorders and impaired vision. This finding underscores the potential of tRNS and related approaches to enhance visual performance even in severely impaired populations by modulating neural responses to weak stimuli.

Pulsed Current Stimulation

Overview of the Current Form and Basic Mechanisms of Action

Among the lesser-known non-invasive stimulation paradigms, PCS stands out as particularly relevant to this work, being the fourth and final technique discussed in the context of applied current forms (Fitzgerald, 2014; Jaberzadeh et al., 2014; Malekahmad et al., 2024). PCS involves the application of short electrical pulses - delivered individually, in bursts, or continuously over periods ranging from several minutes to tens of minutes - most commonly via electrodes placed on the skin during transcranial stimulation or on the cornea during transcorneal stimulation (Figure 1-9B, lower right). The pulses vary widely in duration, amplitude, and frequency, typically lasting from a few milliseconds to several hundred milliseconds, with frequencies ranging from 1 Hz to several kHz. Additional parameters, such as the inter-pulse interval (IPI), the number of pulses per session, and pulse shape (e.g., monophasic, biphasic, sinusoidal, square, or sawtooth), further characterize this technique. PCS is distinguished by its intermittent nature, featuring alternating periods of stimulation and rest.

The basic mechanisms and effects of PCS share similarities with those of other electrical stimulation methods (Figure 1-13A). The outcomes depend not only on stimulation strength, duration, and intervals but also on timing relative to neural events or external stimuli. While PCS is often described as a continuous stimulation method in the literature (e.g., Malekahmad et al., 2024), even single monophasic or biphasic pulses can be delivered as part of a signal with a defined IPI over a specified period. PCS is also frequently referred to by alternative names, such as repetitive ACS (e.g., Gall et al., 2016) or transcorneal electrical stimulation (TES), which most often involves applying pulses of a specific type, duration and frequency over a set period, typically through corneal electrodes (Agadagba et al., 2023).

Importantly, the effects of PCS vary depending on the electrode placement, the region stimulated, and its relation to other nervous system events. PCS can, for instance, induce processes associated with spike-timing-dependent plasticity (STDP, Dan and Poo, 2006) (Figure 1-13B). Moreover, considering the effects observed in TMS, it is conceivable that PCS could also be employed in paired associative stimulation (PAS) (Classen et al., 2004), visual masking (de Graaf et al., 2014), or paired pulse stimulation (PPS) (Höffken et al., 2008), offering promising avenues for further exploration.

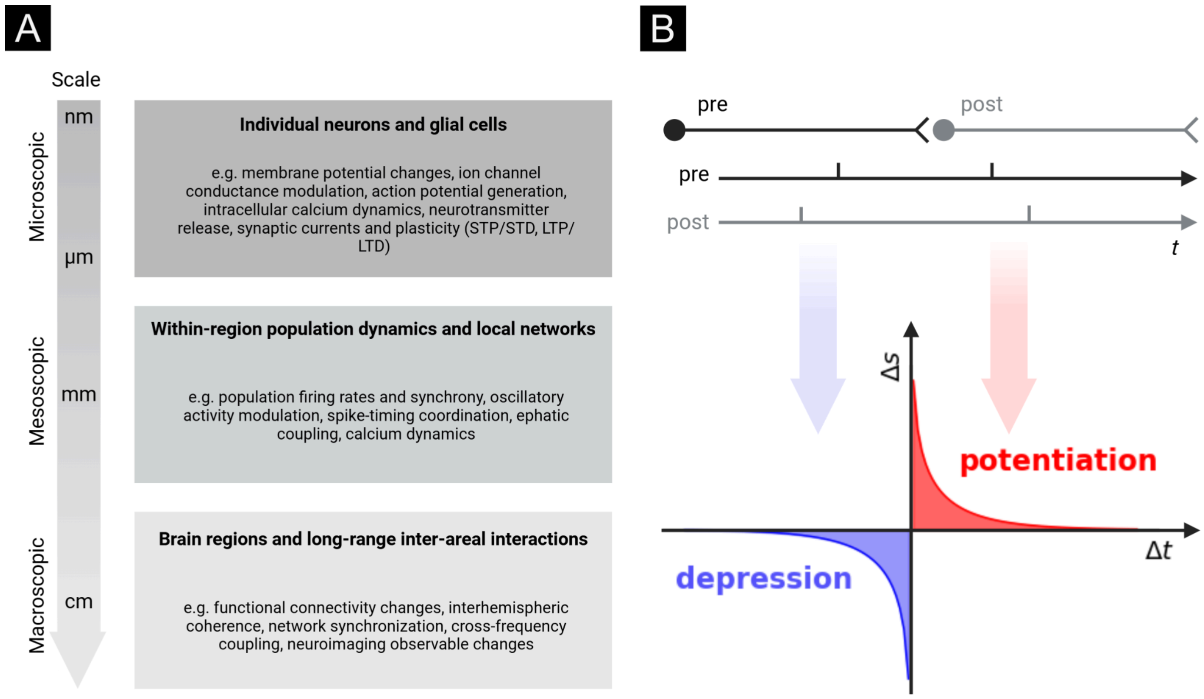

__Figure 1-13__. Multiscale effects of pulsed current stimulation (PCS) on neural activity. (__A__) Hierarchical effects and mechanisms of PCS at different neural organization levels: microscopic, mesoscopic, and macroscopic. Based on Bestmann and Walsh (2017). (__B__) Synaptic plasticity mechanisms dependent on spike-timing and their application to PCS. The upper diagram schematically illustrates the firing timelines of two connected neurons (t). Postsynaptic neuron (gray lines) can fire before or after the presynaptic neuron (black lines), which can lead to depression or potentiation between these cells. On the vertical axis (Δs) of the bottom plot changes in synaptic strength are shown, while the horizontal axis (Δt) represents the timing difference between pre-synaptic and post-synaptic spikes. When a pre-synaptic neuron fires shortly before a post-synaptic neuron (positive Δt), this often results in potentiation of the synapse, as indicated by the red curve. Conversely, when pre-synaptic neuron fires shortly after the post-synaptic neuron (negative Δt), depression occurs, represented by the blue curve. Based on Figure 2A from Zaehle et al. (2010) and Figure 1 from Dan and Poo (2006).

Effects on Information Processing in the Visual System

PCS has been shown to significantly influence information processing in the visual system, with effects observed at both the retinal and cortical levels. Sehic et al. (2016) reviewed the mechanisms underlying the effects of PCS, particularly when applied transcorneally, and highlighted its neuroprotective potential (Figure 1-9D). PCS enhances the production of neurotrophic factors such as BDNF, CNTF, IGF-1, and FGF-2, which support the survival of retinal ganglion cells (RGCs) and photoreceptors. It also promotes chorioretinal blood circulation, reduces inflammation by inhibiting cytokines like IL-1β and TNF-α, and activates L-type voltage-dependent calcium channels, leading to intracellular calcium influx. These pathways upregulate anti-apoptotic proteins (e.g., Bcl-2) while downregulating pro-apoptotic proteins (e.g., Bax), contributing to improved cell survival.

Additionally, PCS influences retinal proteins involved in neuronal signaling, metabolism, and immune processes, further enhancing retinal function and neuroprotection.

Several studies have investigated the effects of PCS on retinal function and vascular responses. Cohen (2009) demonstrated that prolonged pulse train stimulation can depress light-evoked responses in RGCs and lead to transient recovery delays, highlighting potential challenges in overstimulation. Conversely, Freitag et al. (2019) showed that PCS significantly enhances retinal vessel reaction to flickering light, suggesting benefits for addressing ocular microcirculation dysfunction. Su et al. (2022) reported that sinusoidal PCS at an optimal frequency of 20 Hz induces greater responsiveness in retinal neurons compared to rectangular waveforms, while Ye and Chan (2023) found that aperiodic PCS evoked higher spike rates and improved temporal precision in cortical responses, particularly at high frequencies like 20 Hz. These findings emphasize the importance of parameter optimization for retinal neuromodulation.

PCS also exerts notable effects on visual cortical responses. Ma et al. (2014) demonstrated that higher current intensities and longer pulse widths during transcorneal PCS increased cortical activation areas and hemodynamic changes, particularly in regions representing peripheral vision. Similarly, John et al. (2013) found that anodal suprachoroidal stimulation with variable pulse parameters elicited faster cortical responses and influenced activation thresholds through adjustments to interphase gap and pulse duration. Sun et al. (2018) compared transcorneal PCS with visual stimulation, showing that PCS elicited faster responses, with primary activation observed in the secondary visual cortex at higher stimulation intensities.

The broader potential of PCS in neurorehabilitation has also been highlighted. Jaberzadeh et al. (2014) demonstrated that anodal transcranial PCS enhances neuronal excitability through tonic and phasic mechanisms, suggesting its applicability in visual system rehabilitation. These findings, coupled with evidence of vascular, retinal, and cortical effects, position PCS as a versatile tool for restoring and optimizing visual system function. By carefully fine-tuning parameters such as pulse shape, frequency, and duration, PCS can be tailored to address specific clinical needs, including retinal prosthesis support and the treatment of neurodegenerative visual disorders.

Application in Neurorehabilitation

PCS has demonstrated significant potential in the rehabilitation of the visual system, particularly when used with transcorneal electrode placement. This technique has been effective in improving visual function, preserving neural connections, and slowing the progression of vision loss across a range of visual pathologies and conditions. However, the inconsistent terminology in the literature remains problematic. While PCS applied via the cornea is frequently referred to as transcorneal electrical stimulation, this term is often used inconsistently, encompassing protocols with varied electrode placements such as transorbital or transpalpebral stimulation. This lack of standardization complicates direct comparisons and interpretations of therapeutic outcomes. For instance, studies by Fedorov et al. (2011), Gall et al. (2010, 2011, 2016), and Sabel et al. (2011), which refer to their protocols as "transorbital ACS," actually employ PCS with differing localizations (mostly periorbital, see Figure 1-9C) and parameters. Despite these inconsistencies, the therapeutic potential of PCS remains clear and promising.

In addition to the clearly very interesting and clinically promising studies by Fedorov, Gall and Sabel, for "around the eye" PCS also Morimoto et al. (2006) reported significant improvements in residual retinal function, as measured by pupillary constrictions and phosphene thresholds, in patients with retinal degeneration such as RP and cone-rod dystrophy. Fujikado et al. (2006) demonstrated enhanced visual acuity in patients with nonarteritic ischemic optic neuropathy and traumatic optic neuropathy (TON), highlighting its therapeutic potential for these conditions. Schatz et al. (2011) found improvements in visual acuity and scotopic b-wave amplitudes in patients with RP, with better outcomes observed in specific functional parameters. Stett et al. (2023) showed that stimulation dose-dependently slows the progression of visual field area loss in RP, significantly reducing the annual decline rates in treated eyes.

Furthermore, Kurimoto et al. (2010) observed increased chorioretinal blood flow at the macula and midway between the optic disc and macula in healthy subjects, suggesting benefits for ocular perfusion. Oono et al. (2011) demonstrated improvements in visual function in eyes with branch retinal artery occlusion, particularly in long-standing cases. Xie et al. (2011) showed that stimulation predictably activates the visual cortex and produces phosphenes, with perceived locations aligning with stimulated retinal regions. Later, Xie et al. (2012) demonstrated that stimulation preserves the retinotopic map in individuals with retinal degeneration, maintaining the connection between the retina and primary visual cortex.

In rare conditions, Ozeki et al. (2013) reported sustained improvements in best-corrected visual acuity six months after treatment in a patient with Best vitelliform macular dystrophy. Naycheva et al. (2012) evaluated electrically evoked phosphene thresholds in healthy individuals and patients with retinal diseases, finding higher thresholds in pathological cases, with the lowest thresholds observed at 20 Hz across groups. Naycheva et al. (2013) also reported improvements in high-intensity flash sensitivity in patients with retinal artery occlusion.

Among these studies, transcorneal electrode placement was used in the research by Morimoto et al. (2006), Fujikado et al. (2006), Kurimoto et al. (2010), Xie et al. (2011, 2012), Oono et al. (2011), and Ozeki et al. (2013). Schatz et al. (2011) and Stett et al. (2023) used a transpalpebral or combined transpalpebral and transcorneal approach, while Naycheva et al. (2012, 2013) employed transorbital stimulation. These variations in techniques underscore the lack of standardization and consistency in the naming conventions of stimulation protocols, which complicates direct comparisons and interpretations of therapeutic outcomes.

Research Directions for Current Stimulation in the Visual System

Forms of current stimulation such as DCS, ACS, and RNS have been extensively studied regarding their mechanisms and neurorehabilitation potential. PCS has also been investigated, though primarily in the context of continuous stimulation rather than single pulses. To our knowledge, the response of the visual system to single current pulses remains unexplored. Key aspects, such as the threshold for phosphene detection under varying single-pulse parameters, behavioral and electrophysiological response characteristics to phosphenes, and comparisons with responses to light stimuli, have not been addressed. Furthermore, the potential of single current pulses to modulate the processing of visual information from other stimuli has yet to be tested.

Furthermore, although many studies have simulated the induced electric field for various electrode placements, a comprehensive analysis for single current pulses applied in a periorbital configuration - where the current vector alternates between electrodes above and below the eyes - is lacking. This configuration is particularly relevant for focusing the induced electric field at the initial stages of the visual pathway, such as the eyeballs. However, it is equally important to understand how the induced electric field behaves in the optic nerve and other brain regions. A comparison with configurations where the reference electrode is placed on the occiput, rather than below the eyes, could provide critical insights into how these variations affect the distribution and impact of the electric field on the visual system and beyond.

Considering these gaps, we propose that a valuable direction for future research would be to study PCS in the form of single pulses. Such research should aim to: (1) characterize the response of the visual system to single pulses, (2) assess their potential to modulate visual processing, and (3) evaluate their neurorehabilitation potential. Integrating exhaustive computer simulations of the induced electric field into this experimental framework would provide a solid computational basis. This approach could enhance our understanding of observed effects, improve the safety of participants and patients during stimulation, and contribute to advancing the field of neurorehabilitation.

Finally, we strongly emphasize the need to establish a standardized nomenclature for stimulation protocols, which should be based on two primary factors: (1) the location of the electrodes, represented by a lowercase letter, and (2) the form of the applied current, represented by capital letters. Additional details regarding specific parameters or unique aspects of a given protocol should be described using full phrases rather than being incorporated into the abbreviation. This approach would enhance clarity, facilitate comparisons across studies, and minimize confusion in the literature. For instance, in our study, if electrodes are placed over the eyebrows and on the cheeks, the localization is referred to as periorbital (see Figure 1-9C). When pulses are used, the stimulation is classified as PCS. Therefore, this setup can be described as periorbital PCS (pPCS). However, if we wanted to refer to this stimulation more generally, without specifying the form of the current, we could simplify it to pCS.

Aims of the Dissertation

The primary objective of this dissertation is to investigate PCS in the form of single pulses as a novel approach to neuromodulation. This research aims to characterize the visual system's response to single pulses, assess their potential to modulate visual processing, and evaluate their neurorehabilitation potential. By employing a periorbital localization of electrodes, the study focuses on achieving specificity of the induced electric field, targeting the eyeballs to elicit retinal phosphenes. Additionally, exhaustive computational simulations of the induced electric field are integrated to provide a solid framework for understanding the mechanisms of single-pulse PCS, ensuring safety and precision during stimulation. This approach addresses critical gaps in the field and contributes to advancing neurorehabilitation through innovative, targeted stimulation paradigms. Thus, this work is structured around the following key objectives:

1. Development of the stimulation setup for inducing an electric field in the visual system

    a. Conceptualization and evaluation of electrode locations and stimulation parameters

       The setup focuses on periorbital PCS (pPCS), with electrodes placed on the skin above and below the eyes, to achieve high specificity in targeting the eyeballs and optic nerve. Proposed electrode placements, stimulation parameters, and current forms will be optimized to maximize efficacy and minimize invasiveness.

    b. Modeling and simulation of induced electric field

       Computational models will be used to simulate the characteristics of the induced electric field, considering periorbital electrode configurations, stimulation signals, and parameters. These simulations will guide the optimization of the stimulation setup and evaluate the impact of pPCS on the visual pathway and surrounding neural regions, ensuring both efficacy and safety.

2. Experimental validation of the developed setup for modulating information processing in the visual system

    a. Dynamics of visual system responses to single-pulse periorbital current

       The response of the visual system to single sinusoidal pPCS pulses will be compared to LED flash stimuli. Behavioral data (e.g., reaction times to phosphenes or light stimuli) and electrophysiological recordings (EEPs and VEPs) will be analyzed to assess the dynamics of stimulation effects.

    b. Effects of pre-stimulus single-pulse pPCS on visual information processing

The influence of pPCS on visual information processing will be examined by delivering single pulses immediately before visual stimuli. EEG-recorded VEPs will measure differences in neural responses between conditions with and without stimulation, shedding light on pPCS's modulatory effects on neural processing.

Materials and Methods

Codebase

The codebase supporting this dissertation is available at https://github.com/piotrdzwiniel/nencki_phd. The repository includes scripts for calculations, figure generation, data preprocessing, data analysis, statistical inference, and results visualization, where applicable. The repository also contains some of the more relevant files related in one way or another to the research carried out as part of the dissertation, such as configuration files of the IEF. The repository does not contain raw and processed data due to limitations on the size of files that can be stored on GitHub.

Conceptualizing the Evolution of Neuromodulation Technique

The evaluation of pPCS, delivered as single current pulses, serves as the core focus of this dissertation. The following sections explore the location and type of stimulation electrodes, the characteristics of the stimulation signal, and the methodology for simulating the induced electric field. The objective is to propose and assess a novel approach to neuromodulating the visual system.

Location of the Electrodes

To maximize the specificity of the IEF in targeting the onset of the visual pathway, we aim to position the electrodes as close to the eyeballs as possible. However, unlike previous approaches that positioned stimulation electrodes around the eyes with a reference electrode on the occipital region of the head (e.g., Lee et al., 2021a) or on the arm (e.g., Gall et al., 2016), our method will restrict the placement of electrodes to the area around the eyes alone. Specifically, we will use a pair of electrodes for each eye with one placed directly above the eyebrow and the other on the cheek below the eye about the same distance from the eye. The line connecting the two electrodes will pass through the pupil of the stimulated eye. The upper electrode will serve as the anode (+), while the lower electrode will serve as the cathode (-). In total, four electrodes will be placed on the face, two for each eye, as illustrated in Figure 2-1A. This also ensures that when oscillating currents are applied, whether as single biphasic pulses, short segments of ACS, or RNS (Figure 2-1B), the IEF vector shifts between the electrodes while remaining consistently perpendicular to the anterior-posterior axis of the eye.

Type of the Electrodes

We decided to use relatively small, self-adhesive semi-rectangular electrodes, measuring 15 x 20 mm with rounded corners, commonly used for EMG recording (Spes Medica, Italy), to which clip-on cables are attached. These electrodes are small enough to ensure high IEF specificity, and their rounded corners should minimize edge effects. The relatively strong adhesive allows them to remain securely attached to the face for extended periods. Additionally, they are highly cost-effective compared to electrodes with integrated cables. They are more affordable than disposable electrodes and more hygienic than reusable ring or rubber electrodes embedded in saline-soaked sponges, which require cleaning after each use. Proposed approach shortens the preparation time for stimulation, reduces costs, and confines the impact of the IEF to the initial stages of the visual pathway. The distribution of the electric field induced with such electrodes' configuration was tested in a computer model explained in the following paragraphs.

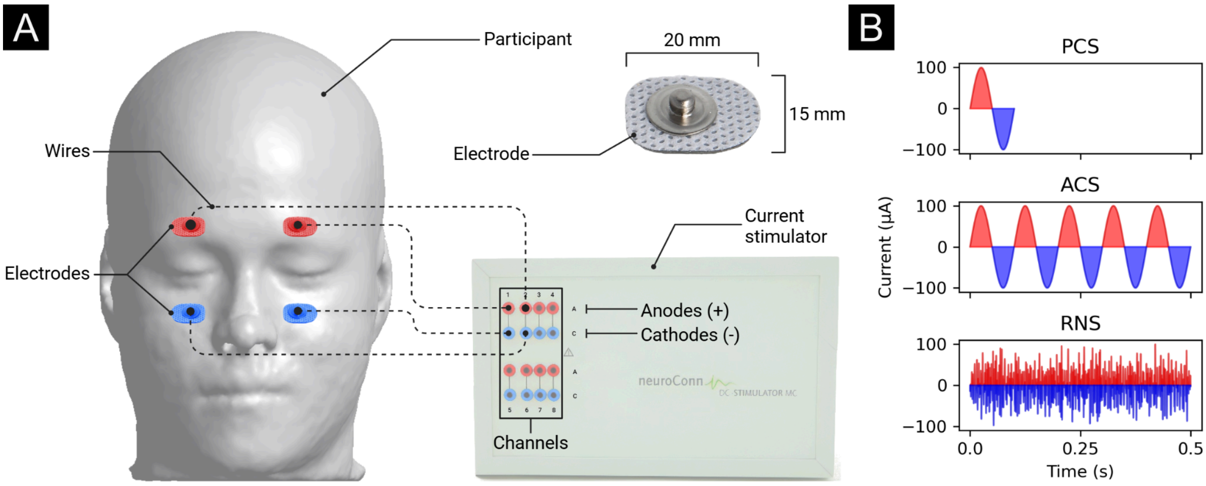

Figure 2-1. *Electrode placement and signal types for the proposed neuromodulation technique. (**A**) Electrode placement for the new neuromodulation technique concept, showing the arrangement of electrodes around the eyes. In this configuration, electrodes are positioned in pairs for each eye, with the upper electrodes (red) functioning as anodes (+) and the lower electrodes (blue) serving as cathodes (-). The electrodes used are rectangular, measuring 15 x 20 mm, with rounded corners. These self-adhesive electrodes are typically used for recording EMG signals but are also suitable for current stimulation due to their secure adhesion to the skin. This setup focuses the induced electric field (IEF) on the eyeball and optic nerve (in theory), ensuring specificity of stimulation while minimizing invasiveness. The dashed lines represent the connections between the electrodes and the stimulation device. (**B**) Examples of signals applied during the stimulation, including pulsed current stimulation (PCS), alternating current stimulation (ACS), and random noise stimulation (RNS). The top plot shows a single current pulse (PCS) where red indicates current flowing from the anode to the cathode, and blue indicates the reverse flow. The PCS presented is a single 100 µA biphasic sine pulse of 100 ms, or a single 10 Hz sine period – such impulses were used in described experiments.*

Properties of the Stimulating Current

Any current paradigm, PCS, ACS, RNS, or DCS with different characteristics, can be used in the periorbital stimulation. The key feature of our approach lies in the use of very brief stimulations, on the order of milliseconds, either on their own or directly preceding another sensory stimulus. Thus, in the computer simulation and in experimental studies we employed single biphasic sinusoidal pulses. The exact amplitude and duration of impulses will be described below, in the detailed methodology of each experiment. Below we present general considerations about current density and total charge - two key factors directly impacted by amplitude and duration of impulses.

Current density refers to the amount of electrical current passing through a given surface area, typically under the electrode, and is a measure of how concentrated the current is. Total charge, on the other hand, represents the cumulative amount of electrical charge delivered over time to the tissue, reflecting the overall energy transferred during the stimulation. Both are critical for ensuring the safety and effectiveness of current-based stimulation. As demonstrated by McCreery et al. (1990, cited in Nitsche et al., 2003b), current densities below 25 mA/cm² do not cause brain tissue damage, even with high-frequency ACS applied over several hours. On the other hand, in the context of total charge, brain tissue damage has been observed at a minimum threshold of 216 C/cm² below the stimulation electrodes (Yuen et al., 1981, cited in Nitsche et al., 2003b). Notably, these thresholds are not at all reached in stimulation paradigms. During typical tDCS using 1 mA current and 35 cm² rectangular electrodes, the current density is just 0.02857 mA/cm², and maximum total charge of 0.022 C/cm² (Nitsche et al., 2003b). However, during electrical stimulation, current distribution at the electrode-tissue (skin) interface is not uniform, with high concentration of current density at the electrode edge (Minhas et al., 2011) which may induce a risk of focused damage. There are also subjective sensory experiences to consider. Even with these lower tDCS parameters, users can experience discomfort during stimulation, such as pinching, burning, or even pain under the electrodes. It may be advisable to prepare the subject's skin by applying lidocaine cream to locally anesthetize the area under the stimulation electrodes. However, even with local anesthesia, pulsed or alternating current stimulation can also cause facial muscle spasms, which may cause discomfort despite the absence of pain. This discomfort is often linked to high impedance, which can result from poor contact between the electrodes and the skin surface, or may be an effect of the above mentioned edge effects.

The current density and total charge parameters should be in advance estimated, and here we present it for an example single sinusoidal biphasic current pulse, with a peak-to-peak amplitude of 100 µA and a total duration of 100 ms for both phases (i.e., one period of a 10 Hz sine wave), applied using 15 x 20 mm self-adhesive electrodes - one of the pulses we use in our research. Current density can be calculated using the formula:

$$J = \frac{I}{A}$$

where I is the current in milliamperes (mA) and A is the electrode area in square centimeters (cm²). To calculate the current density (J), we must use the peak amplitude of the pulse (I_{peak}), rather than the peak-to-peak amplitude. For symmetric biphasic pulses, the peak amplitude is half of the peak-to-peak value. The calculation for the total charge density of a single sinusoidal biphasic pulse can be determined based on the formula:

$$Q_{area} = \frac{I_{RMS} \times t_{half-phase}}{A}$$

where, Q_{area} stands for the total charge per unit area, which can be expressed in microcoulombs per square centimeter (μC/cm^2). I_{RMS} refers to the root mean square (RMS) current, which accounts for the effective value of the current during a sinusoidal waveform. For sinusoidal waves, I_{RMS} is calculated as the peak current amplitude divided by the square root of 2. Next parameter, $t_{half\text{-}phase}$ represents the time duration for one phase of the sinusoidal current, which is half of the total pulse duration. Finally, the A is the area over which the current is applied, typically measured in square centimeters (cm^2). For a single sinusoidal biphasic pulse with a peak-to-peak amplitude of 100 μA and a total duration of 100 ms, the RMS current is calculated as approximately 35.36 μA. Using this value, the total charge delivered during one phase of the pulse (lasting 50 ms) is determined to be 1.77 μC. When distributed over an electrode area of 3 cm², the total charge per unit area is approximately 0.59 μC/cm², with a corresponding current density of approximately 0.016 mA/cm². The exact calculations were included in the code repository. Notably, such a pulse produces a current density of about half the current density compared to a typical tDCS session with 1 mA current and 35 cm^2 electrode's surface (0.029 mA/cm²). The total charge for a standard tDCS session, such as the one described by Nitsche et al. (2003b), was reported to be 0.022 C/cm^2. The authors did not specify the duration of a typical stimulation session, however it can be estimated as a quotient of an accumulated and momentary current density (0.022 C/cm^2 ÷ 0.000029 A/cm^2), which equals 758.62 seconds. Almost five times less electrical charge would be delivered to the tissue for the same duration of the stimulation session with 100 ms 100 uA pulses applied via 3 cm^2 electrode (0.00448 C/cm² vs. 0.022 C/cm²). The relationships between electrode size, current intensity, and current density were calculated for the following parameter ranges for sinusoidal biphasic current pulses:

- Pulse current density (mA/cm²) for current amplitudes ranging from 0.0 to 0.5 mA and electrode areas from 0 to 5 cm².
- Pulse total charge (μC) for current amplitudes ranging from 0.0 to 0.5 mA and pulse durations from 0.0 to 0.5 seconds.
- Pulse total charge per unit area (μC/cm²) for charges ranging from 0 to 50 μC, electrode areas from 0 to 5 cm², and number of pulses (n) ranging from 0 to 1000.

The results are presented in Figure 3-1. Safety and non-invasiveness should increase further with the increase of the IPIs while maintaining the stimulation time, and by combining the application of single pulses with sensory stimuli.

Computer Simulations of the Induced Electric Field

Simulation Framework

In order to characterize the IEF for selected periorbital stimulation parameters, we performed computer simulations of IEF using the SimNIBS 4.0.1 software (Thielscher et al., 2015). SimNIBS is an advanced, open-source software package designed for simulating electric fields in the human brain during non-invasive brain stimulation techniques such as TMS and tES. SimNIBS translates the input parameters of tissue conductivity, stimulation settings, and structural head models into electric field distributions through a series of computational steps. The software uses head models from MRI scans (individual or templates) to create a highly accurate structural representation of the brain, including key tissues such as the scalp, skull, cerebrospinal fluid (CSF), gray matter (GM), and white matter (WM). Once the structural model and tissue conductivity profiles are established, SimNIBS applies the user-defined stimulation parameters, such as electrode placement and current intensity. Using finite element methods (FEMs), the software then solves the Maxwell equations to calculate the resulting electric field distribution within the brain. This process allows for precise predictions of the electric field's magnitude and direction across different brain regions, providing valuable insights into the potential effects of the stimulation.

In our IEF simulations, we focused primarily on the distribution of the electric field during electrical stimulation, assuming the size and location of the stimulation electrodes as described earlier in the dissertation - specifically, four 15 x 20 mm electrodes positioned above and below the eyes. The electrode placement was selected to ensure proximity to the eyeballs while avoiding possible interference with the Fp1 and Fp2 electrodes during simultaneous EEG recordings (Figure 2-2). Our primary interest was in determining the extent to which the IEF would affect the eyeballs, optic nerve, and the CNS. We hypothesized that the greatest impact would occur in the eyeballs, with a lesser effect on the optic nerve, and the least influence on the rest of the CNS. The simulations were conducted for a specific moment during an example current stimulation, focusing on the first amplitude peak of a single sinusoidal biphasic current pulse with a peak-to-peak amplitude of 100 µA and a duration of 100 ms. At this specific moment during the application of a single current pulse, the electrodes above the eyes carried a current of +50 µA, while the electrodes below the eyes carried a current of -50 µA.

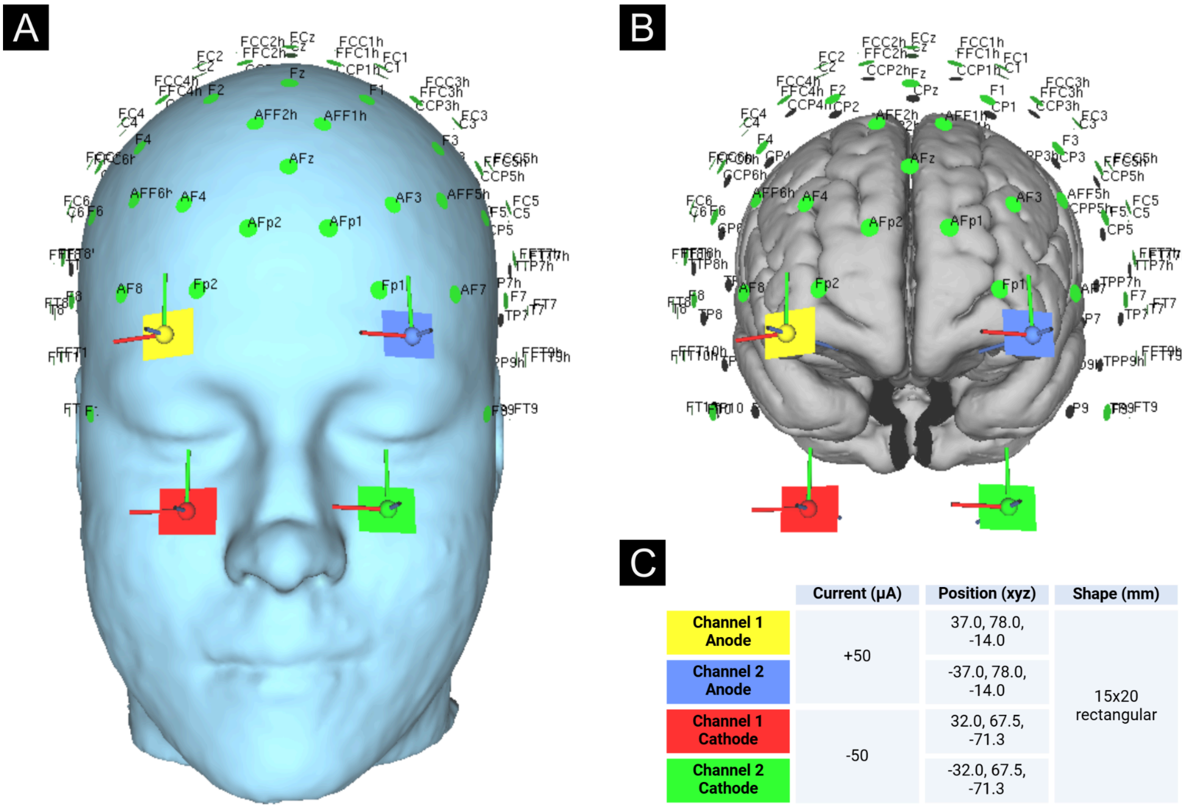

	Current (µA)	Position (xyz)	Shape (mm)
🟨 Channel 1 Anode	+50	37.0, 78.0, -14.0	15x20 rectangular
🟦 Channel 2 Anode		-37.0, 78.0, -14.0	
🟥 Channel 1 Cathode	-50	32.0, 67.5, -71.3	
🟩 Channel 2 Cathode		-32.0, 67.5, -71.3	

Figure 2-2. *Electrode configuration for periorbital current stimulation. (**A**) Anterior view showing the placement of four 15 x 20 mm rectangular electrodes positioned above and below the eyes for the stimulation setup. The blue (Channel 1 anode) and yellow (Channel 2 anode) electrodes are positioned above the eyes, while the red (Channel 1 cathode) and green (Channel 2 cathode) electrodes are placed below the eyes. EEG electrode locations (e.g., Fp1, Fp2) are marked for reference to ensure non-interference during potential simultaneous EEG recordings. (**B**) Superior view illustrating the positioning of electrodes relative to the brain structure. (**C**) Table summarizing the electrode configurations, including current values, electrode positions (in y, z, and x coordinates), and electrode shape details.*

Structural Data

In our study, the widely available ICBM Average Brain (ICBM152) dataset, expressed in MNI space (MNI152), was used as a head volume in which to simulate the IEF. This dataset, which is a standardized, averaged T1 structural image of 152 healthy subjects, provides a robust reference model for conducting simulations in healthy individuals (McConnell Brain Imaging Centre, 2024). This structured data is available in SimNIBS 4.0.1 software, both in a raw form and after segmentation to different tissue types (e.g., gray and white matter, cerebrospinal fluid, skull, scalp, and eyeballs). Standard segmentation as offered by the MNI152 head model is based on the *charm* tool (Puonti et al., 2020). Segmented, volumetric data (in NIfTI format) was translated into a mesh, (*.msh) files which was a final format used for performing computer simulations of the IEF. The conversion was done using the *nii2msh* tool, developed by the SimNIBS team and included in the software package.

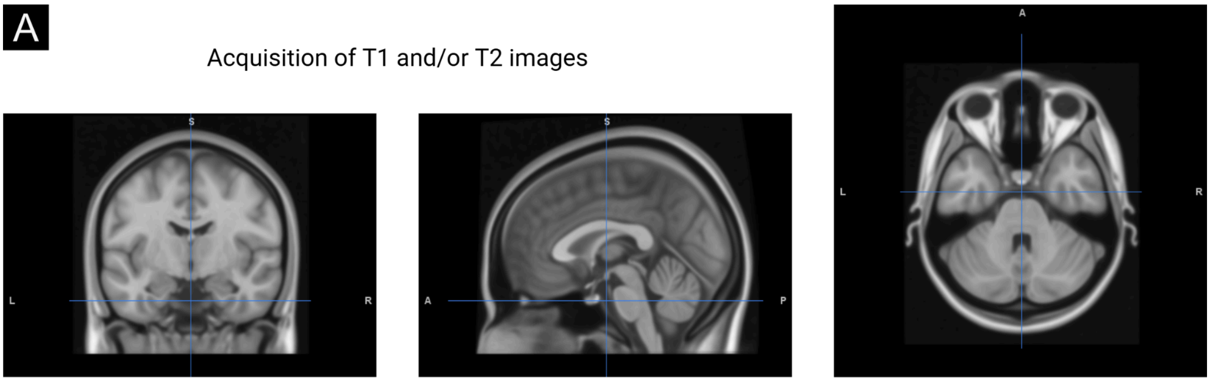
A

Acquisition of T1 and/or T2 images

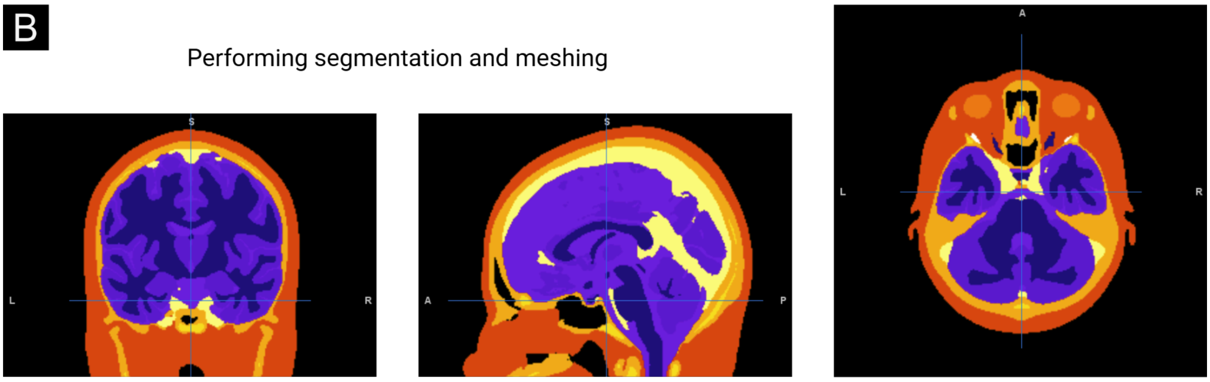
B

Performing segmentation and meshing

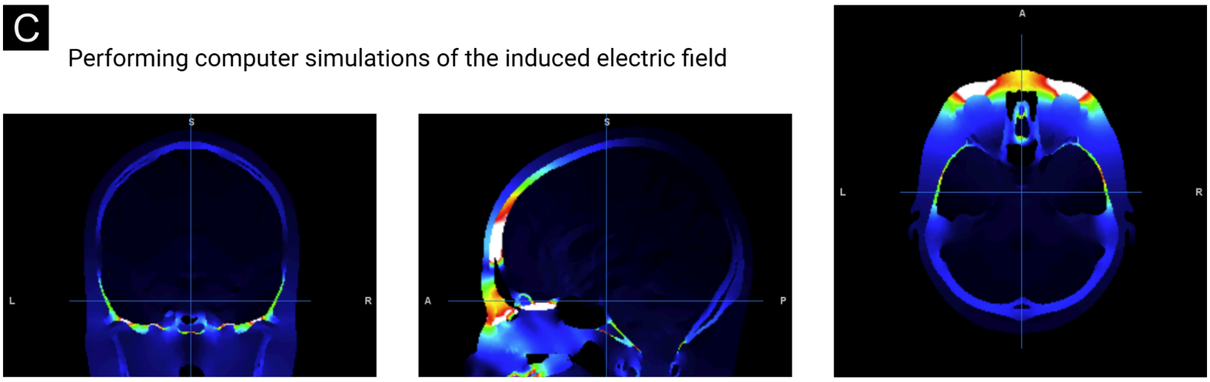
C

Performing computer simulations of the induced electric field

Figure 2-3. *General pipeline for induced electric field (IEF) simulations using MRI data. (**A**) T1 and/or T2-weighted MRI images, which serve as the basis for creating structural models of the head. T1w images are essential for brain segmentation, while T2w images can enhance skull and cerebrospinal fluid (CSF) segmentation. T1w images are typically acquired at low readout bandwidths to maximize signal signal-to-noise ratio (SNR). This, however, may displace spongy bone and fat due to chemical shift artifacts, complicating segmentation. To address this, T1w images should be acquired with fat suppression techniques like selective water excitation. Conversely, T2w images, acquired at high readout bandwidths, offer cleaner contrast between CSF and compact bone, making them preferable for skull segmentation. For detailed sequence parameters refer to Nielsen et al., 2018. (**B**) Segmentation and meshing of MRI data. Anatomical structures such as gray matter (GM), white matter (WM), skull, and CSF are segmented, and the resulting data is converted into a computational mesh. This mesh provides the geometric basis for finite element method (FEM) simulations. Segmentation of*

*NIfTI volumetric data was performed using the SimNIBS tool charm, while meshing the data was accomplished using the nii2msh tool. Simulation results can then be converted back into NIfTI format using the msh2nii tool, also part of the SimNIBS suite. For more detailed information on the segmentation and meshing pipeline, please refer to Puonti et al. (2020). (**C**) FEM-based simulation of the IEF. Using the meshed head model, FEM is applied to calculate the distribution of the electric field across different tissues during non-invasive brain stimulation, providing insights into how current flows through the head for given stimulation parameters. The simulations are performed using the SimNIBS software (Thielscher et al., 2015).*

Selection of Tissue Conductivity Values

The tissue conductivity values selected for computer simulations of the IEF (see Table 2-1) were different from those set by default in SimNIBS. The detailed critique of these default values is included in the appropriate Discussion subsection. The Swiss ITIS Foundation's database was chosen as a reliable, continuously updated source which specializes in providing various human tissue parameters, including conductivity for different frequency ranges (Hasgall et al., 2022). More specifically, we used conductivity values for the lower frequency range (up to 1 MHz) which are typically used for electrical brain stimulations (Swiss ITIS Foundation, 2024). It is important to clarify how the conductivity values for the scalp and eyeballs were determined. In SimNIBS, the "Scalp" parameter represents the conductivity for all tissues from the skin surface to the bone, with a default value set at 0.465 S/m. However, this default setting does not differentiate between the various layers, such as skin, fat, connective tissue, and muscle outside the skull. To address this, we calculated an averaged conductivity value for these tissues based on ITIS data, resulting in 0.1915 S/m - approximately half the default value used in SimNIBS. In addition, SimNIBS does not distinguish between the individual components of the eye, which are represented by the sum parameter ”Eye balls”. Therefore, we have averaged the electrical conductivity of the individual eye components to obtain a value of 0.9323 S/m for the eyeballs parameter. This is almost double the default value in SimNIBS software, which is 0.5 S/m. Conductivity values were taken for various parts of the eye, including aqueous humor, choroid, ciliary body, cornea, iris, lens, retina, sclera, and vitreous humor. Since vitreous humor constitutes approximately 80% of the eye’s volume (Azhdam et al., 2020), we used a weighted average to calculate the overall conductivity of the eyeball. We assigned a weight of 0.8 to the vitreous humor and 0.2 to the average conductivity of the remaining parts of the eye, ensuring a more accurate representation of the eyeball's overall conductivity. The following formula was applied:

$$\sigma_{eyeballs} = \frac{\left(W_{vitreous\ humor} \times \sigma_{vitreous\ humor}\right) + \left(W_{other} \times \sigma_{other}\right)}{2}$$

where $\sigma_{eyeballs}$ represents the conductivity of the eyeball, $W_{vitreous\ humor}$ is the weight of the vitreous humor, $\sigma_{vitreous\ humor}$ is its conductivity, W_{other} is the weight of the other components of the eye, and σ_{other} represents their average conductivity. This calculation resulted in:

$$\sigma_{eyeballs} = \frac{(0.8 \times 2.16\ S/m) + (0.2 \times 0.6835\ S/m)}{2} = 0.9323\ S/m$$

After verifying the default conductivity parameters in SimNIBS and selecting alternatives as described above, we moved on to declare the characteristics of the stimulation electrodes, their location and the parameters of the applied electric current.

***Table 2-1**. Conductivity values for various tissues. The second column contains conductivity values for low frequencies up to 1 MHz, while the third column lists the default conductivity values in the SimNIBS software, which are not specifically limited to low frequency ranges.*

Tissue	**Conductivity (S/m)**	
	Swiss ITIS Foundation	**SimNIBS**
Brain (white matter)	0.348	0.126 (*White Matter*)**
Brain (gray matter)	0.419	0.275 (*Gray Matter*)**
Brain (cerebrospinal fluid)	1.880	1.654 (*CSF*)**
Skull (cancellous)	0.100	0.025 (*Spongy Bone*)**
Skull (cortical)	0.006	0.008 (*Compact Bone*)**
Skull	0.018	0.010 (*Bone*)**
Muscles	0.461	0.160 (*Muscle*)**
Blood	0.662	0.600
Fat	0.078	
Connective tissue	0.079	
Skin	0.148	
Scalp	0.191*	0.465
Eye (cornea)	0.620	
Eye (sclera)	0.620	
Eye (iris)	0.461	
Eye (choroid)	0.662	
Eye (vitreous humor)	2.160	
Eye (lens)	0.345	
Eye (ciliary body)	0.461	
Eye (aqueous humor)	1.880	
Eye (retina)	0.419	
Eye	0.932*	0.500 (*Eye balls*)**

S/m - siemens per meter. * - these values were calculated on the basis of other values (see text for more details). ** - the parameter names of these values in SimNIBS differ from those in the first column of the table (the names are given in parentheses after the value where the name differs).

Other Settings and Simulations Execution

The electrode placement and stimulation parameters used in the simulations were previously described and are shown in Figure 2-2. Conductivities for most tissues were provided in the previous section. For both the electrode material and the conductive gel layer beneath the electrodes, a conductivity of 1 S/m was assumed. In the simulations, the focus was primarily on the magnitudes of the electric field (V/m) and current density (A/m²), but we also looked at the voltage distribution at the skin surface for different timestamps of a single sinusoidal biphasic current pulse. Detailed information on the implementation and technical aspects of the IEF simulations based on FEMs can be found in publications by the SimNIBS software developers. For further insights into the physical assumptions and programming details, please refer to works by Windhoff et al. (2013) and Thielscher et al. (2015).

Processing and Analysis of Simulation Results

The simulation process produced a *.msh (mesh) file containing multiple layers that represent both tissue types and simulation outcomes. From these results, we extracted key data, including magnitude of the IEF (V/m) and magnitude of the current density (A/m²) for the gray matter, white matter, and eyeballs using scripts written in Python. The *.msh file was then converted to a *.nii.gz (volumetric) files using the *msh2nii* tool developed by the SimNIBS team. This conversion transformed the meshes into volumetric data, enabling further processing, analysis, and quantification. Mango software (Research Imaging Institute, 2024), a tool used for visualizing, processing and analyzing neuroimaging data, was employed to create region of interest (ROI) masks on the structural MNI152 data, representing the eyeballs, optic nerves, and the rest of the brain (Figure 2-4). After loading the *.nii.gz file with the simulation results into Mango, the ROI masks were applied, and volumetric statistics were calculated for the eyeballs, optic nerves, and the rest of the brain. ROI-based volumetric data processing, analysis, and visualization were also performed using scripts written in the Python programming language. When discussing the results, we will present and discuss both surface and volumetric results. In the context of the analyses, we examined how IEF is affected by the shape, size and location of stimulating electrodes.

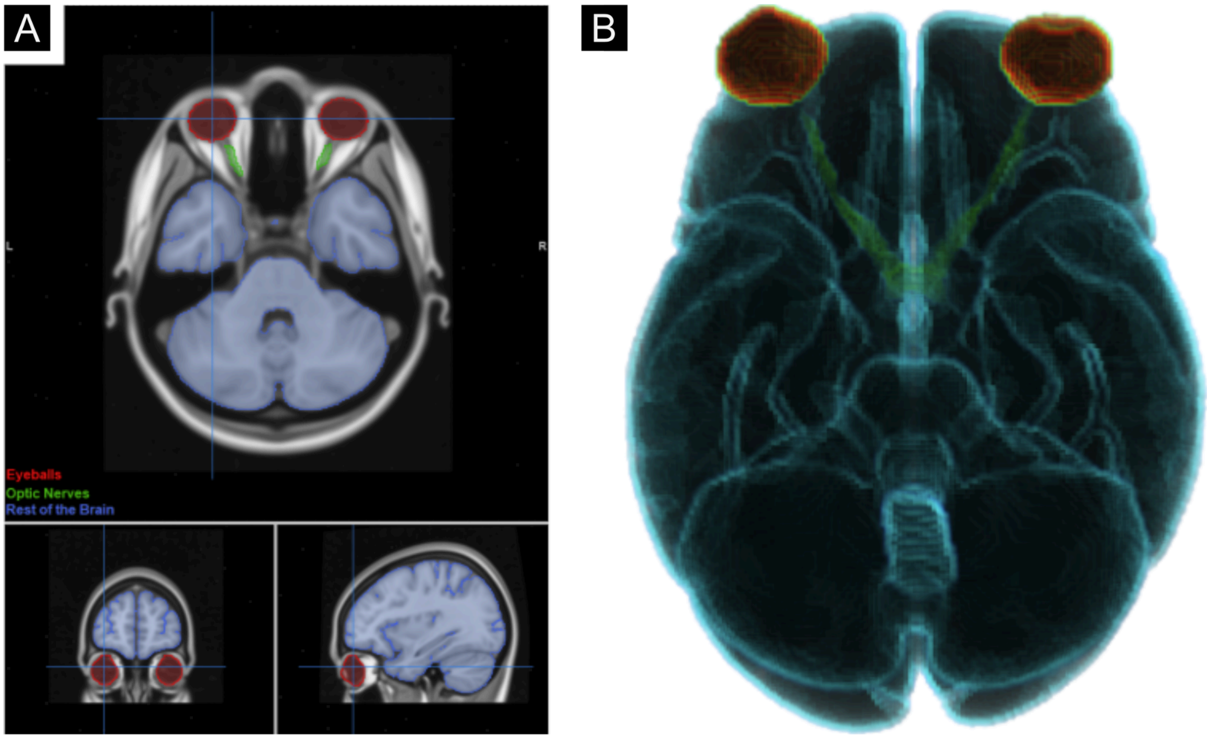

Figure 2-4. *Visualization of regions of interest (ROIs) in the MNI152 template space. (**A**) The structural MRI image in the MNI152 template space with overlaid ROIs representing different anatomical structures. The ROIs highlight the eyeballs in red, the optic nerves in green, and the rest of the brain's white and gray matter in blue. The three orthogonal views (axial, sagittal, and coronal) provide a comprehensive visualization of these regions. (**B**) A 3D surface rendering of the same ROIs, showing the eyeballs and optic nerves prominently on the ventral view of the brain, providing spatial context and anatomical relationships in a surface model. The renders were realized using the mayavi library in Python. These ROIs were then used in analyses of the characteristics of the induced electric field (IEF) in each of the three specified areas.*

Experimental Studies

Overview

As part of this dissertation, we describe two experimental studies in which we verified non-invasive periorbital pulsed current pulse stimulation (pPCS) in a form of single pulses.

1) In the first study, we administered single sinusoidal biphasic current pulses of varying amplitudes and durations, as well as LED light flashes, each administered separately. Participants responded to each stimulus type independently by pressing designated keys on a computer keyboard, and the EEG signal was recorded throughout the experiment.

2) In the second study, single sinusoidal biphasic current pulses were administered prior to the presentation of a visual stimulus in a form of checkerboard pattern reversal (CPR) to modulate the

processing of information related to that stimulus. In this study, participants did not provide behavioral responses; instead, we focused solely on analyzing the EEG signal.

Both studies utilized a largely similar hardware configuration, participant preparation methods, EEG recording parameters, stimulation protocols, and data processing and analysis techniques, with only subtle differences between them. Efforts were made to minimize redundancy in describing the methodology for each study wherever possible.

Ethical Approval

The experiments conducted with human subjects described in the dissertation complied with the principles of the Declaration of Helsinki and were approved by the Ethics Committee of the University of Warsaw (application number: 27/2017) and the Bioethics Committee at the Nicolaus Copernicus University in Torun, Collegium Medicum in Bydgoszcz (application number: KB 926/2018).

Recruitment and Preparation of Participants

Participants for each study were recruited via an online questionnaire, which provided general information about the study and was designed to select individuals who met the specified criteria. Exclusion criteria included being under 20 or over 40 years of age, having visual field impairments, psychiatric or neurological disorders, a history of epileptic seizures, head injuries with loss of consciousness, dependence on psychoactive substances, implanted electronic devices, pregnancy, or cancer. Additionally, participants were instructed to refrain from consuming caffeine for six hours and psychoactive substances for 24 hours before the session.

Upon arrival at the laboratory, before the experiment, participants were informed about the study's purpose, exact course of the experiment, and provided with an informed consent form. They were also advised that they could withdraw at any time without providing a reason. Participants sat in front of the procedural computer screen, where different tasks or stimuli were presented depending on the study they were involved in. In the first study, participants responded to LED flashes and to phosphenes they might experience during pPCS. In the second study, subjects observed CPRs displayed on the screen, but did not provide behavioral responses. The EEG signal was recorded, pPCS was applied, and visual stimuli were presented in each of the three studies.

The skin was cleansed using 70% ethanol and further prepared with NuPrep peeling gel (Weaver and Company), with special attention to the areas where the stimulation (and EEG) electrodes are placed on the spots with high density of sebaceous glands. Next, an EEG cap was fitted, with the number of active electrodes varying depending on the specific experiment. Contact between the electrodes and the scalp was maintained using SuperVisc conductive gel (Brain Vision Solutions). Finally, the stimulation self-adhesive electrodes were attached to the designated areas on the face. The entire preparation process took approximately one hour. Participants were then given at least five to ten minutes to adjust their vision in a darkened room before the procedure began. We are talking here about the first phase of dark adaptation, the predominantly cone phase (Longstaff, 2002).

Hardware Configuration

A hardware configuration was employed that allowed for the simultaneous administration of current stimulation, visual stimulation, and EEG signal recording (Figure 2-5). This setup was used across all experiments, with minor hardware and software modifications specific to each experiment.

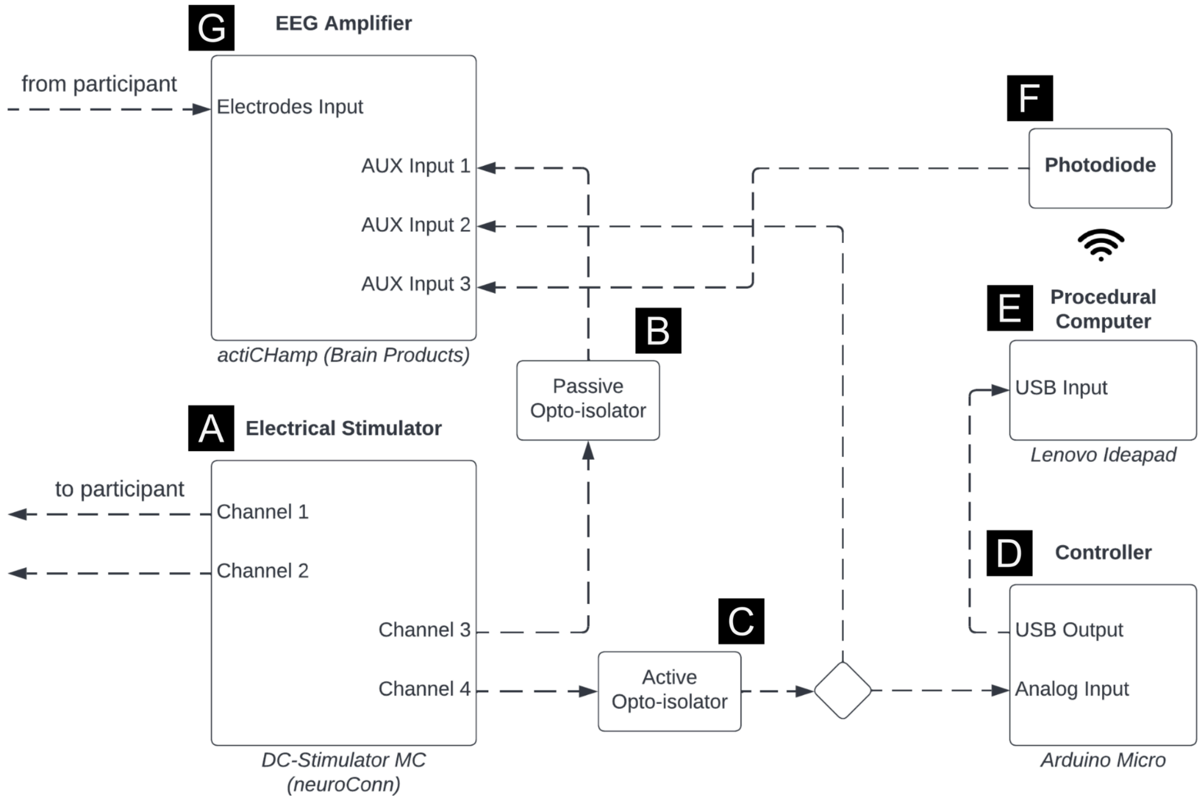

Figure 2-5. *Diagram and description of the hardware configuration used in the experiments. The DC-Stimulator MC (neuroConn, GmbH) (**A**) was responsible for delivering current stimulation to the participants via channels 1 and 2, which administered the stimulation through four self-adhesive electrodes positioned around the eyes. Channel 3 transmitted the stimulation signal to the EEG amplifier (**G**) for event marking during EEG processing, while channel 4 sent TTL-like pulses to the Arduino module (**D**). Opto-isolators (**B**, **C**) ensured electrical isolation between the stimulator, EEG amplifier, and Arduino module, protecting the participants and equipment from electrical interference. The Arduino module converted the TTL-like signals into virtual keystrokes, transmitted to the procedural computer (**E**), which controlled the progression of the experimental procedure and triggered the visual stimuli. In the first study, these stimuli were flashes from an LED lamp mounted on the top edge of the*

*procedural computer screen (not shown on the diagram to preserve its readability), while in the second and third studies, they were reversals of a checkerboard pattern on the computer screen. A photodiode (**F**) was attached to the procedural computer screen to detect checkerboard pattern reversals (CPRs) and send the signal to the EEG amplifier for precise event marking.*

Current Stimulator

A DC-Stimulator MC (neuroConn, GmbH), running a customized stimulation program, was responsible for delivering current stimulation to the participants. It also transmitted information about the applied stimulation to the EEG amplifier and indirectly controlled the visual stimulation and overall course of the experimental procedure. Custom stimulation programs were prepared in Python, saved in *.mat format, and then converted to *.bfs format using a dedicated proprietary tool provided by neuroConn before being loaded into the stimulator. The sampling frequency of the stimulator, for both analog-digital and digital-analog conversion, was 16 kHz. The stimulator was equipped with four channels, each featuring two unipolar outputs (Figure 2-5A). The first two channels were used to administer current stimulation via four self-adhesive 15 x 20 mm semi-rectangular EMG electrodes (Spes Medica Spa), with one pair allocated to each eye. For each pair, one electrode was positioned on the cheek below the eye (cathode) and the other on the forehead above the eyebrow (anode). The accepted skin-to-electrode impedance threshold was 50 kΩ. The third channel transmitted the stimulation signal to the EEG amplifier, which was later used during EEG data processing for event extraction. The fourth channel sent a TTL-like signal, which, when processed through an Arduino module, advanced the experimental procedure on the procedural computer and triggered the visual stimuli. In the first study, these stimuli were flashes from an LED lamp, while in the second study, they involved checkerboard stimulus reversals CPRs (on a computer screen). Signals from the third and fourth channels passed through optoisolators before reaching the target devices.

Opto-isolators (Optocouplers)

For safety reasons, the connection of the current stimulator to the EEG amplifier and the Arduino module was realized via opto-isolators. An opto-isolator (or optocouplers) operates by using a LED to transmit received electrical signals as light impulses to a photodetector, effectively allowing electrical isolation between its input and output while enabling signal transmission in electronic circuits. The passive opto-isolator was placed between the current stimulator and the EEG amplifier to decouple the systems physically, thus protecting the participants and the recording equipment from electrical interference or overvoltage (Figure 2-5B). This isolation also prevented the EEG amplifier from being saturated by the stimulation signal. Active optoisolators, powered by an external 9V battery, were used to transmit TTL-like control signals to other components, such as the Arduino module, also allowing the stimulator to be physically isolated from the rest of the devices included in the hardware configuration (Figure 2-5C).

Arduino Module

The Arduino Micro module was programmed to process TTL-like pulses from the stimulator and convert them into emulated keystrokes on a virtual keyboard (Figure 2-5D) and send them via USB to the procedural computer, where they controlled the progression of the experimental protocol and initiated visual stimuli. In the first experiment, a signal from the Arduino module controlled the experimental procedure on the procedural computer and triggered flashes of light in the LED lamp. In the second experiment, the Arduino module controlled the procedure by reversing the checkerboard pattern displayed on the procedural computer screen, which served as the light stimulus in these studies. The module played a crucial role in synchronizing electrical stimulation with visual stimuli, ensuring that both types of stimulation occurred in a precisely timed sequence, and the procedure proceeds accordingly in time.

Procedural Computer

The procedural computer used in the study was a customized Lenovo Ideapad 700 laptop running Windows 10, equipped with an Intel i7-6700HQ 2.6 GHz CPU, 16 GB of DDR4 RAM, a GeForce GTX 950M GPU, and a 256 GB SSD. The laptop had a maximum screen resolution of 1080p, with a screen size of 340x190 mm and a refresh rate of 60 Hz. The extent of the field of view (FOV) engaged during the experimental procedures by the screen was calculated using the following formula:

$$\theta = 2 \times arctan\left(\frac{y}{2x}\right) \times \frac{180}{\pi}$$

where θ is the FOV in degrees, y is the dimension of the screen (width or height) under consideration, and x is the distance from the participant to the screen. The *arctan* function calculates the angle in radians, while the factor $180 / \pi$ converts this angle from radians to degrees. Given that the participants' distance from the screen was set to 80 cm in each study, the FOV of the procedural computer screen encompassed approximately 24.0 by 13.5 degrees.

In each study, the Arduino module transmitted signals that directed the computer’s behavior through custom Java programs run on this computer. These programs were responsible for displaying the experimental procedure on the screen, capturing participants' responses, and presenting the visual stimuli (Figure 2-5E). As a reminder, the control of the procedural computer operated as follows: the TTL-like pulse generated by the stimulator → passed through an active optoisolator → was transmitted to the analog input of the Arduino module → where the software translated the input current into an emulation of pressing a specific button on a virtual keyboard → which was sent to the procedural computer via a USB cable → and a program written in Java on that computer responded accordingly to these virtual button presses → allowing the experimental procedure to progress. As a result, the stimulator was the stimulating-coordinating unit, and its signals determined the course of the entire experiment.

Synchronization of Visual Stimuli

In the first study, a four-diode LED lamp mounted directly above the screen of the procedural computer was used to deliver the flash stimulus. The LED lamp was triggered by a TTL-like signal from the current stimulator via the Arduino module and the same TTL signal was sent to the EEG amplifier. In the second study, a photodiode was attached to the computer screen to detect the exact moments of each checker-board pattern reversal (Figure 2-5F). The photodiode then sent this information to the EEG amplifier. Recorded TTL and photodiode signals were used off-line to precisely segment the EEG data into epochs, aligned with the onset of the visual stimuli.

EEG Amplifier

EEG data were recorded using the actiCHamp EEG amplifier (Figure 2-5G), actiCAP EEG caps, Ag/AgCl active electrodes, and Recorder software (all from Brain Products, GmbH). The EEG amplifier captured bioelectrical signals from the participants' heads through 64 active electrodes in the first study, and 128 in the second study, with the ground electrode placed at Fpz and the reference electrode at FCz. This setup produced raw EEG data containing 63 or 127 channels of bioelectric activity from the brain (reference electrode was automatically excluded). Additionally, the system recorded three auxiliary signals: two from the current stimulator and one from the photodiode, all of which were used for marking events in the EEG signals. These signals were crucial for accurately aligning the EEG data with the experimental stimuli, allowing for the precise extraction of evoked responses. The sampling frequency for all channels was set to 1000 Hz. Hardware and software filters included a low-pass filter at 280 Hz, with an accepted skin-to-electrode impedance threshold of 10 kΩ.

Data Acquisition, Processing, Analysis and Visualization

In the first study, behavioral data and EEG data were collected, while in the second study only EEG data were collected. Data were processed, analyzed, and visualized primarily using the Python programming language and various libraries, including Pandas, NumPy, SciPy, Matplotlib, Seaborn, MNE (Gramfort et al., 2013; Jas et al., 2018), and more. We also made some use of MS Excel to store and process the selected data and JASP (JASP Team, 2024) to analyze it and make statistical inferences about it.

Study 1: Dynamics of Visual System Responses to Single-Pulse Periorbital Current and LED Stimulation

Aims of the Study

The primary objective of the first study was to establish a profile of the human nervous system's EEG response to periorbital electrical impulses (electrically evoked potential, EEPs), and to compare these with the visual evoked potentials (VEPs) elicited by LED flash stimulation. A secondary goal was to determine the thresholds for phosphene perception and the response times during single-pulse stimulation. Phosphenes are subjective light sensations experienced during electrical (or magnetic) stimulation, caused by activation of cells of the visual pathway and as such they offer a way to behaviorally estimate the parameters of effective electrical (or magnetic) stimulation.

Participants and their Preparation for the Experiment

The study included 20 healthy volunteers (10 females and 10 males) with an age of 24.9 ± 1.68 years (mean ± SEM) on the day of the experiment (23.8 ± 1.80 for females; 25.9 ± 1.56 for males). Two of the female participants were left-handed. Two of the male participants had myopia, including one uncorrected. Three of the female participants had myopia, including one uncorrected. In this study, there was no split into groups - all participants were participating in the same experimental procedure.

Participants were prepared for the experiment as described above, except that a small amount of Emla 5% cream (Aspen Germany, GmbH), containing lidocaine and prilocaine (25 mg/g + 25 mg/g), was applied to the skin at the stimulation electrode sites. A drop of less than half a centimeter in diameter, with an approximate volume of 0.065 cm^3, was placed on each spot. This was done to gently anesthetize the skin under the stimulation electrodes during the experiment, isolating participants from potential cutaneous sensory experiences that might occur during stimulation. This was crucial to ensure that participants' behavioral responses were based on the phosphene experience induced by the current pulse, rather than any accompanying skin sensation, which could lead to type I errors in responses (i.e. falsely reporting a phosphene experience due to skin sensations).

Additionally, during this study, we demonstrated the phosphene sensation to participants while checking impedance under the stimulation electrodes, ensuring they understood what to expect before beginning the main experimental task.

Experimental Procedure

The experimental procedure is detailed and described in Figure 2-6. After preparing the participant for the study and demonstrating the impression of phosphene, the experimental procedure was started. First, the participant was presented with five boards with information on what the experiment is about and how it will be conducted. The entire experiment was divided into six parts (*procedure* blocks). Each part consisted of 15 segments consisting of 10 trials dedicated to one of 10 experimental conditions, i.e. visual stimulation or current stimulation in the form of a current pulse of one of nine combinations of duration (10, 50, 100 ms) and amplitude (100, 200, 300 µA, peak-to-peak). The stimulation conditions within each segment were delivered with pseudorandom order, the same for all participants. In total, each experimental condition was repeated 15 times within a single experimental block, and 90 within the whole experiment. The blocks were separated by 3-minute periods during which the participant could rest with eyes closed and mentally recuperate before the next block. During these *rest* periods we also recorded the EEG signal.

A single trial of the experimental procedure (Figure 2-6D) was dedicated to a single experimental condition and lasted between 4 and 4.5 seconds. It consisted of three main parts: the “fixation”, which lasted 1 s; the “cue” part, which lasted 1-1.5 s, during which the participant received a hint about what kind of stimulation to expect – visual or electrical. When the cue was an LED symbol, the stimulation was a LED flash. The lightning symbol announced the application of a current pulse. The cue symbols were surrounded by an orange square. The transition of the square color from orange to green indicated the start of the stimulation part. This period lasted 2 s, during which the participant was subjected to a visual or electrical stimulus according to pseudorandom order. Stimulation always started at 1 s timestamp of this part and lasted 100 ms for the visual stimulation and for 10, 50 or 100 ms for current stimulation. The participant's task was to press the left arrow key on the keyboard when the LED flashed, or the right arrow key when the participant experienced a phosphenic sensation. The participant was allowed to give answers throughout the expectation part, after the stimulus onset. In total, a single block lasted an average of 638.9 ± 1.0 seconds, or approximately 10 minutes and 39 seconds. Including breaks between blocks, the entire experiment ideally took less than an hour and a half.

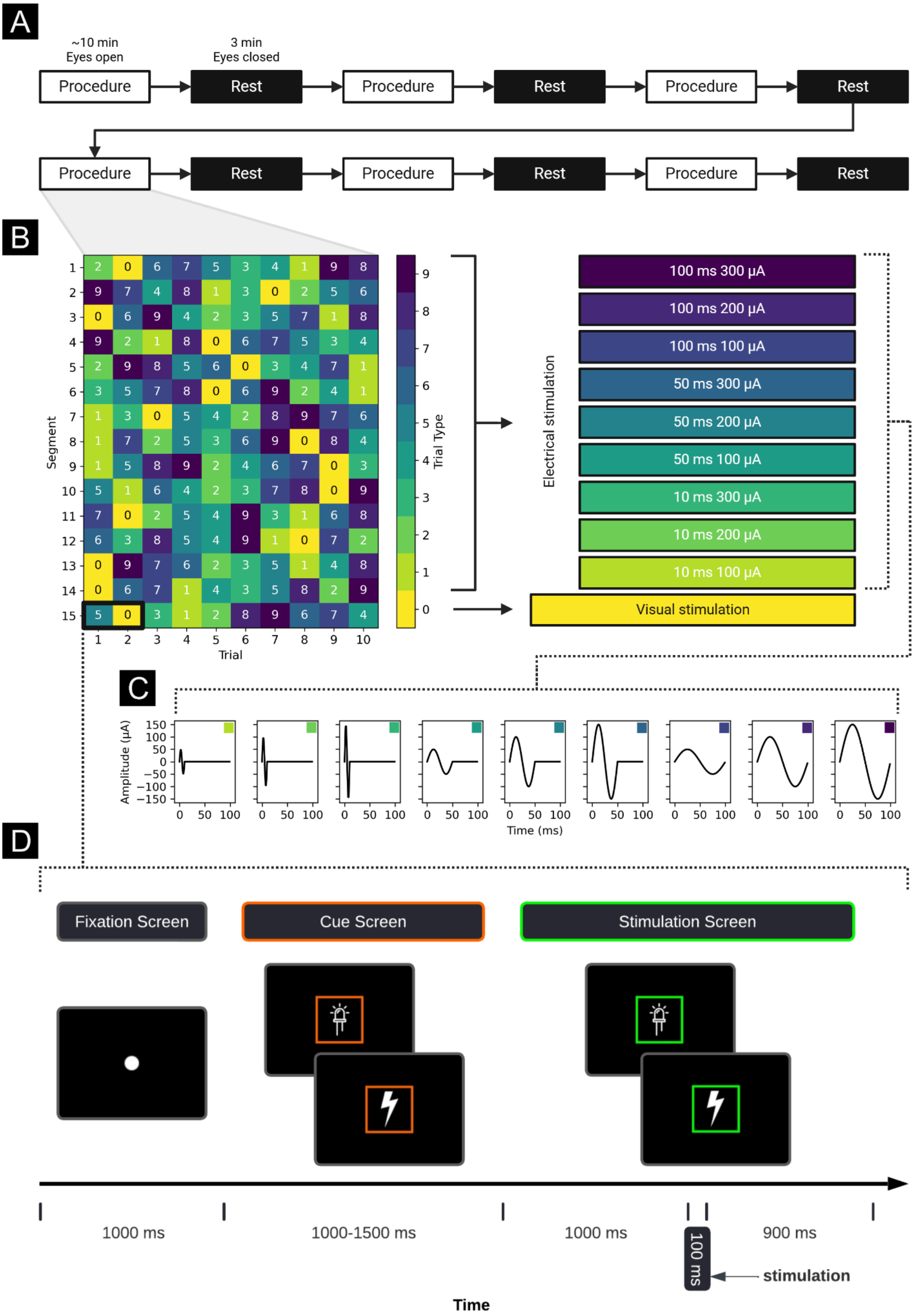

Segment	1	2	3	4	5	6	7	8	9	10
1	2	0	6	7	5	3	4	1	9	8
2	9	7	4	8	1	3	0	2	5	6
3	0	6	9	4	2	3	5	7	1	8
4	9	2	1	8	0	6	7	5	3	4
5	2	9	8	5	6	0	3	4	7	1
6	3	5	7	8	0	6	9	2	4	1
7	1	3	0	5	4	2	8	9	7	6
8	1	7	2	5	3	6	9	0	8	4
9	1	5	8	9	2	4	6	7	0	3
10	5	1	6	4	2	3	7	8	0	9
11	7	0	2	5	4	9	3	1	6	8
12	6	3	8	5	4	9	1	0	7	2
13	0	9	7	6	2	3	5	1	4	8
14	0	6	7	1	4	3	5	8	2	9
15	5	0	3	1	2	8	9	6	7	4

Figure 2-6. *Schematic representation of the experimental procedure in the first study. (**A**) The experimental procedure was divided into six blocks of about 10 minutes each, each followed by 3 minutes of rest with eyes closed and simultaneous recording of the EEG signal. (**B**) Each block consisted of 15 segments, and each*

*segment included 10 trials with shuffled experimental conditions: visual stimulation using an LED flash (type 0) or application of a current pulse of one of nine combinations of length and amplitude (types 1-9) (**C**). (**D**) Each individual trial, consisted of three parts: 1) a 1000 ms period of fixation on a white fixation point displayed in the center of the screen; 2) a 1000 and 1500 ms cue period informing the subject what type of stimulation to expect, i.e. an LED flash or application of a current pulse; cue icons (LED or a lightning) were surrounded by an orange square; 3) a color change from orange to green indicated the start of the stimulation period which lasted 2000 ms; the stimulus would start at 1000 ms and last 100 ms in case of visual stimulation and 10, 50 or 100 ms in case of current stimulation. The participant was asked to give keyboard responses to perceiving an LED flash (left arrow) or experiencing phosphenes during current stimulation (right arrow).*

Data Processing

Behavioral Data

Behavioral data were collected using a procedural computer that ran the previously mentioned Java program. This program recorded information about the progress of the procedure in real-time, writing it to text files. The recorded data included the time, index, type, and part of the current trial, as well as any responses given by the participant, including the time and type of those responses. The example of such data is shown in Figure 2-7. During analysis, the behavioral responses were classified as "valid" if the participant pressed the correct button between 1.1 and 2 s within the stimulation period; "invalid" the answer came before 1.1 s timestamp or if the wrong key was pressed; any other situation was considered as "no response".

The participant's response time was calculated using the following formula:

$$T_R - T_S - 1000 = T_{response}$$

where T_R represents the Unix time in milliseconds corresponding to the participant's provided response, and T_S represents the Unix time in milliseconds corresponding to the beginning of the "expectation" phase of the trial. To calculate the participant's true response time to the stimulus, the formula subtracts T_S from T_R and then deducts an additional 1000 ms. The adjustment accounts for the fact that stimulation began 1000 ms after the expectation phase screen appeared.

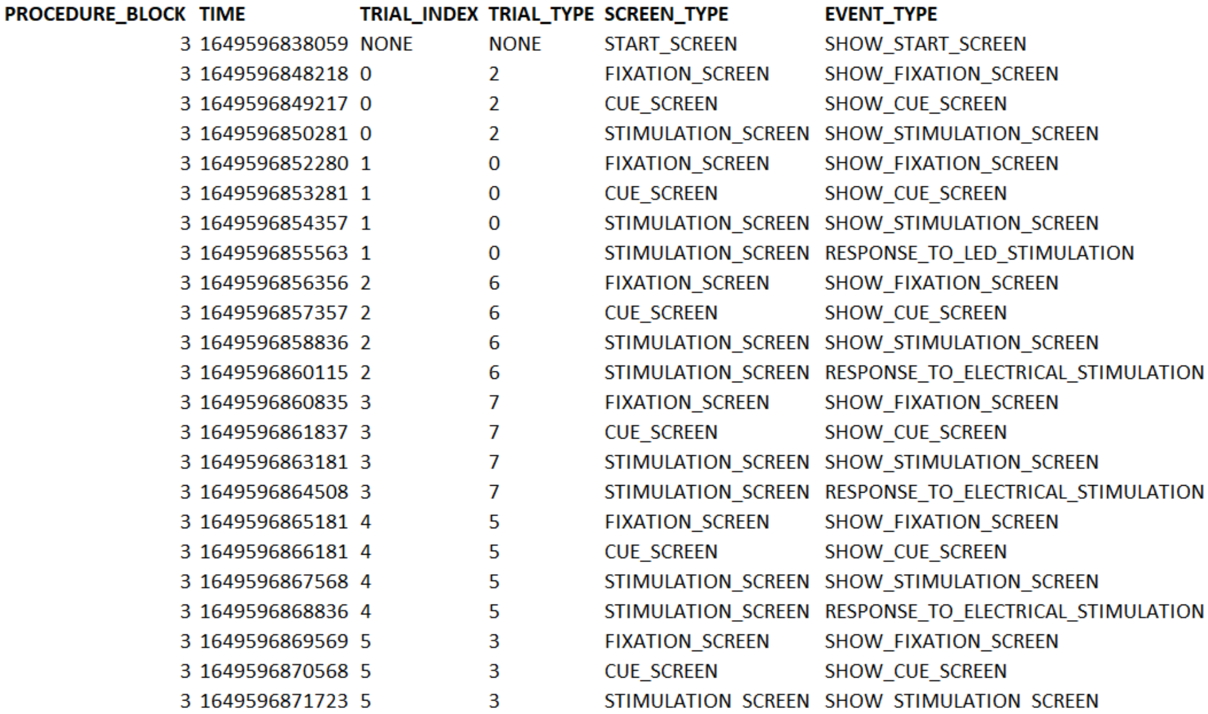

PROCEDURE_BLOCK	TIME	TRIAL_INDEX	TRIAL_TYPE	SCREEN_TYPE	EVENT_TYPE
3	1649596838059	NONE	NONE	START_SCREEN	SHOW_START_SCREEN
3	1649596848218	0	2	FIXATION_SCREEN	SHOW_FIXATION_SCREEN
3	1649596849217	0	2	CUE_SCREEN	SHOW_CUE_SCREEN
3	1649596850281	0	2	STIMULATION_SCREEN	SHOW_STIMULATION_SCREEN
3	1649596852280	1	0	FIXATION_SCREEN	SHOW_FIXATION_SCREEN
3	1649596853281	1	0	CUE_SCREEN	SHOW_CUE_SCREEN
3	1649596854357	1	0	STIMULATION_SCREEN	SHOW_STIMULATION_SCREEN
3	1649596855563	1	0	STIMULATION_SCREEN	RESPONSE_TO_LED_STIMULATION
3	1649596856356	2	6	FIXATION_SCREEN	SHOW_FIXATION_SCREEN
3	1649596857357	2	6	CUE_SCREEN	SHOW_CUE_SCREEN
3	1649596858836	2	6	STIMULATION_SCREEN	SHOW_STIMULATION_SCREEN
3	1649596860115	2	6	STIMULATION_SCREEN	RESPONSE_TO_ELECTRICAL_STIMULATION
3	1649596860835	3	7	FIXATION_SCREEN	SHOW_FIXATION_SCREEN
3	1649596861837	3	7	CUE_SCREEN	SHOW_CUE_SCREEN
3	1649596863181	3	7	STIMULATION_SCREEN	SHOW_STIMULATION_SCREEN
3	1649596864508	3	7	STIMULATION_SCREEN	RESPONSE_TO_ELECTRICAL_STIMULATION
3	1649596865181	4	5	FIXATION_SCREEN	SHOW_FIXATION_SCREEN
3	1649596866181	4	5	CUE_SCREEN	SHOW_CUE_SCREEN
3	1649596867568	4	5	STIMULATION_SCREEN	SHOW_STIMULATION_SCREEN
3	1649596868836	4	5	STIMULATION_SCREEN	RESPONSE_TO_ELECTRICAL_STIMULATION
3	1649596869569	5	3	FIXATION_SCREEN	SHOW_FIXATION_SCREEN
3	1649596870568	5	3	CUE_SCREEN	SHOW_CUE_SCREEN
3	1649596871723	5	3	STIMULATION SCREEN	SHOW STIMULATION SCREEN

Figure 2-7*. Snippet of behavioral data recorded by the procedural computer during the experiment. The data includes the current procedure block number, trial index, trial type, displayed screen type, and event type, along with the corresponding timestamp in milliseconds (UNIX time). The indexing of block numbers started from zero, meaning that block No. 3 in the presented data corresponds to the fourth block of the experimental procedure. Notably, the order of trial types aligns with that shown in Figure 2-6. Additionally, for the 10-ms pulses (trial types 2 and 3), the participant did not respond, which may suggest that the pulses did not generate a perception of phosphenes or that they were too weak for the participant to detect.*

EEG Data

EEG preprocessing and analyses were performed with custom written Python scripts using the packages described in the section Data Acquisition, Processing, Analysis and Visualization. The processing was primarily aimed at cleaning the signal, filtering it to the frequencies of interest, segmenting it into epochs and grouping them and averaging relative to the experimental conditions for each participant. Additionally, because the EEG signal was recorded between blocks of the experimental procedure during the “rest” period, frequency distributions for these segments of the experiment were also computed.

Filtering

In this study, a bandpass filter was applied to retain frequencies between 1 and 40 Hz, effectively eliminating low-frequency drift and high-frequency noise that could obscure relevant brain activity. This was achieved using a fourth-order Butterworth biquadratic (second-order sections) infinite impulse response (IIR) band-pass filter. Additionally, a zero-phase notch filter was used to remove 50

Hz power line noise and its harmonics. The notch filter was configured to eliminate frequencies at 50, 100, 150 Hz, and so on, up to 500 Hz. This dual-filtering process ensured that the EEG data remained focused on the frequency range most relevant for analyzing brain activity while minimizing interference from external electrical sources.

Channel Interpolation

Channel interpolation in EEG is a widely used technique to replace "bad" channels - those affected by excessive noise or artifacts - with estimated values derived from neighboring channels (Cohen, 2014). To identify channels for interpolation, we performed a thorough visual inspection of the signal, separately for the data from *procedure* and *rest* blocks. The recorded EEG was of good quality. An average of 0.13 ± 0.04 channels per dataset required interpolation in the *procedure* blocks. Only TP9, TP10, and T7 channels were excluded, and this occurred in just 10 datasets. For the data from *rest* periods, an average of 0.18 ± 0.05 channels per dataset required interpolation. In total, 13 datasets required interpolation, with TP9, TP10, T7 and T8 channels affected by excessive noise.

Re-Referencing

After completing the filtering and interpolation processes, the EEG data underwent re-referencing. The average reference (i.e. the average activity across all channels) was used, which reduces common-mode noise and minimizes the influence of the physical reference that could affect all channels equally. This step ensures that the data reflects only the brain's electrical activity, minimizing any potential confounding effects from external sources.

Independent Component Analysis

ICA is a form of blind source separation that assumes observed signals are linear mixtures of statistically independent source signals. This technique allows for the decomposition of EEG into independent components (ICs), which include both accurate representations of neural activity and repetitive artifacts such as ocular movements, muscular interference, environmental noise, and heartbeats. The ICA can extract as many components as there are input EEG channels which, in the case of multichannel data, is computationally expensive. A more optimal approach is to reduce the number of components based on the amount of variance they explain. Thus, Principal Component Analysis (PCA) was used to identify a smaller number of components that capture a high ($\geq$ 99.9999%) percentage of the variance. Therefore, in this study, we used the FastICA algorithm, set to find 20 components which was enough to detect artefacts of eye blinks, eye movements and also components representing current pulse stimulation artifacts. The components were identified by a typical shape, time of incidence and strong frontal location. On average 3.49 ± 0.08 components were excluded per dataset extracted for the *procedure* blocks. For the *rest* blocks, the average exclusion was

1.46 ± 0.10 components. The difference is mainly due to the need for additional exclusion of components representing pPCS artefacts in procedural blocks.

Signal Segmentation (Epoching)

After applying ICA, a high-pass filter with a cutoff of 1.0 Hz was reapplied to remove any residual low-frequency drift that may have been introduced during ICA processing. Such drift, if left uncorrected, could persist into the segmented epochs and might not be fully addressed by baseline correction. Next, we performed segmentation, a critical step for the analysis of evoked potentials. The EEG signal from *procedure* blocks was divided into equal segments, referred to as epochs, starting -500 ms before, and lasting to +1000 ms relative to the onset of stimulation events. Following segmentation, the epochs were averaged to improve the signal-to-noise ratio, effectively isolating the signal of interest associated with the experimental events (see Figure 1-9). Baseline correction was applied to EP sweeps based on the mean from the whole pre-stimulus period to reset the amplitude of the evoked potential, ensuring a consistent starting point from the onset of the event. Lastly, a visual inspection of the epochs was conducted to exclude those containing artifacts not removed during earlier preprocessing steps. On average, only 5.0 ± 1.2 epochs were excluded per dataset (0.56%).

Data Analysis

Phosphene Detection Threshold and Response Times to Stimuli

The analysis of behavioral data focused on participants' responses to the applied stimuli. Specifically, we assessed the percentages of valid, none, and invalid responses for each stimulus type: a 100 ms LED flash and current pulses with varying durations (10, 50, 100 ms) and amplitudes (100, 200, 300 μA). For pPCS, the analysis centered on participants' responses to the phosphene experience, enabling the determination of a phosphene detection threshold based on the characteristics of the current pulse. Additionally, we examined response times to both the perceived LED flashes and the experienced phosphenes.

In order to verify the existence and characteristics of response trends for different parameters of pPCS, we utilized linear regression modeling to fit a trend line to the data and calculate the coefficient of determination (R^2) in the context of behavioral and electrophysiological data, including valid response rate, valid response time, and averaged EEG potentials. The R^2 value represents the proportion of variance in the dependent variable explained by the regression model and is a key metric for evaluating the quality of the fit. An R^2 value close to 1 indicates that the model explains most of the variance in the data, suggesting a strong linear relationship, whereas a value close to 0 implies that the model explains little of the variance, indicating a weak or non-linear pattern.

To identify the parameters of the pPCS that corresponded to a 50% participant behavioral and electrophysiological response a Naka-Rushton function was fit to the collected data (Naka and Rushton 1966), In this approach, the total stimulus (*stim*) is calculated based on pPCS parameters - specifically, amplitude (*A*) and duration (*d*) - to determine the total charge per pulse (*Q(d,A)*), which serves as the input to the Naka-Rushton function. The function is expressed as:

$$f(d,A) = r_{max} + r_{base}\left(\frac{Q(d,A)^{n}}{Q(d,A)^{n}+\sigma_{Q}^{n}}\right)$$

where r_{max} is the maximum response, n defines steepness of the response curve, σ is the stimulus intensity producing a half-maximal response, and r_{base} represents the baseline response.

In this study, the *response* refers to either the behavioral or electrophysiological response of participants, depending on the type of experimental data to which the model is fitted. Additionally, parameters other than the stimulus input (*stim*), which are related to the participant’s response to the eliciting stimulus, are estimated using *curve_fit* function from the *scipy.optimize* package (full implementation of the approach can be found in the repository). This estimation is performed by fitting the input *stim* data and the corresponding experimental response data to the Naka-Rushton model.

As part of the results presented in this dissertation, we extended the standard Naka-Rushton framework into a multi-factor model incorporating total charge, pulse amplitude, and saturated duration to better capture the complex dynamics of pCS responses. Additionally, for the electrophysiological data, we applied a normalized scale using the maximum response to LED stimulation as a reference, enabling standardized comparisons across conditions.

Finally, to examine the potential effects of stimulation type on responses and response times, we conducted an analysis of variance (ANOVA). One participant was excluded from further behavioral and electrophysiological data analysis due to providing invalid responses in 89.9% of all trials, with an average response time of 436.5 ms before the stimulus.

Electrical and Visual Evoked Potentials

After preprocessing the EEG signal, we calculated evoked potentials for each experimental condition. The visualization of averaged evoked potentials was performed for a cluster of eight occipital electrodes: PO7, PO3, POz, PO4, PO8, O1, Oz, and O2. This cluster was selected to capture the activity from the primary visual cortex and surrounding regions, which are critical for processing visual and phosphene-related stimuli. To gain insights into the late components of the evoked potentials, we conducted statistical comparisons focusing on the 150-300 ms time window after stimulus onset. This window was chosen as it is less susceptible to artifacts from current stimulation and reflects higher-order visual processing, such as those associated with the P2 component. These analyses allowed us to compare the neuronal responses elicited by electrical and visual stimulation under controlled experimental conditions unaffected by pPCS-related artifacts.

Frequency Spectrum of Resting-State EEG Data

During the experimental procedure, rest blocks were interspersed between procedural blocks, allowing for periods of rest during which participants kept their eyes closed while EEG signals were recorded. To investigate potential changes in the EEG signal across these rest blocks, a series of resting-state frequency analyses was conducted. Fast Fourier Transform (FFT) was employed to calculate frequency distributions, enabling the identification of power within specific frequency bands. Linear regression modeling was used to examine trends in power changes across consecutive rest blocks, with a primary focus on the alpha band (8-12 Hz). Additionally, power spectral density (PSD) analyses were performed to generate topographic maps of selected frequency bands, providing a visual representation of power distribution across the scalp. These complementary approaches allowed for a comprehensive analysis of both temporal and spatial dynamics of EEG activity during the resting-state periods. The detailed implementations, particularly for more complex functions and calculations such as FFT and PSD, along with the functions and packages used, can be found in the repository.

Study 2: Effects of Pre-Stimulus Single-Pulse Periorbital Current Stimulation on Visual Information Processing

Aims of the Study

The primary aim of the second study was to examine how the electric stimulation would influence the processing of the following visual stimuli. In this study, visual stimuli were presented on the monitor screen as checkerboard pattern reversals, with the current pulse applied immediately before each pattern reversal. The pulses tested include both short, low-intensity pulses with a low probability of inducing phosphenes, and longer, higher-intensity pulses with a greater likelihood of triggering retinal action potentials and consequent phosphene sensations. The analysis focused primarily on EEG data recorded during the experiment, with particular attention to visual evoked potentials.

Participants and their Preparation for the Experiment

The study included 32 healthy volunteers (16 females and 16 males) with a mean age of 25.9 ± 0.7 years on the day of the experiment (25.7 ± 1.0 for females; 26.0 ± 0.8 for males). Sixteenth of the participants had corrected myopia (including 9 women). Handedness was not verified in this study. The participants were randomly divided into two groups: an experimental group that received electrical stimulation (EXP) and a placebo group without such stimuli (SHAM). The division was conducted to ensure a balanced number of participants of each sex in each group, with 8 women and 8 men in each group. Both groups were informed that they were receiving current stimulation. The mean age of the placebo group was 26.7 ± 1.0 years (women 27.0 ± 1.6, men 26.3 ± 1.1), while that of the experimental group was 25.1 ± 0.9 years (women 24.5 ± 1.2, men 25.7 ± 1.3). Participants were prepared for the study as described in the section common to all experiments.

Experimental Procedure

The experimental procedure, illustrated in Figure 2-8, involved displaying reversals of two checkerboard patterns with alternating black and white fields. Depending on the experimental group and phase of the procedure, pPCS in the form of pulses with specific characteristics was applied immediately before each checkerboard reversal.

Visual Stimulus

The checkerboard pattern covered the entire screen, spanning approximately 24.0 by 13.5 degrees, with each checker measuring 0.4° in size. A white fixation dot with a diameter of 0.3° was displayed at the center of the screen. The Michelson contrast (Michelson, 1927) between the light and dark fields was 70.3%, calculated using the following formula:

$$C_M = \left(\frac{L_{max} - L_{min}}{L_{max} + L_{min}}\right) \times 100$$

This formula calculates the Michelson contrast (C_M) by taking the difference between the maximum (L_{max}) and minimum (L_{min}) luminance values, dividing it by their sum, and then scaling the result by a factor of 100. Luminance measurements were performed with a Konica Minolta LS-100 photometer in a darkened room, with values expressed in cd/m^2. The recorded luminance values for the dark and light fields were 17.5 and 100.4 cd/m^2, respectively, while the luminance of the white fixation point was 207.5 cd/m^2.

Procedure Scheme

All participants underwent an experimental procedure comprising 6 experimental blocks (Figure 2-8A). The first and last blocks were the *prologue* and *epilogue* blocks, respectively. In these blocks, participants, regardless of their experimental group, were presented with visual stimuli in the form of CPRs displayed on the screen without preceding current stimulation. Each block contained 120 CPR repetitions, with an inter-stimulus interval (ISI) of 2.25 ± 0.25 seconds. Consequently, each of these blocks lasted approximately 5 minutes.

Procedure blocks were positioned between the *prologue* and *epilogue* blocks, in the middle of the experimental procedure. Each of these blocks consisted of 30 segments, each containing 9 trials dedicated to one of the 9 experimental conditions (Figure 2-8B). Considering the number of segments and trials in each block, there were 270 trials, resulting in 30 repetitions of each experimental condition. The experimental block on average lasted 10 minutes and 3 seconds (9:00 – 11:15), considering that the trial duration ranged from 2 to 2.5 seconds. In total, across the four *procedure* blocks, each experimental condition was repeated 120 times. The order of conditions within each segment was not randomized, it remained consistent across segments. In these blocks, for conditions indexed 1 through 8, CPRs were preceded by pPCS in the form of single, sinusoidal biphasic pulses with specific combinations of duration (12.5, 25, 50, and 100 ms) and amplitude (100, 200 µA) (Figure 2-8C). "Directly preceded" indicates that the current pulse concluded precisely at the onset of the CPR (Figure 2-9A). The experimental condition indexed as 0, in contrast, involved CPRs without preceding pCS, thus serving as independent visual stimuli identical to those in the *prologue* and *epilogue* blocks. The key distinction between the experimental and placebo groups was that in the placebo group, all trials were of 0 type, meaning that no current pulse was applied prior to the CPR.

There were 3 minute *rest* periods between the experimental blocks (*prologue*, *procedure*, and *epilogue*), which provided participants with a break from the monotonous experimental procedure and offered experimenters an opportunity to check and adjust the hardware configuration. No EEG data was recorded during *rest.* The total duration of the whole experimental procedure was approximately 65 minutes.

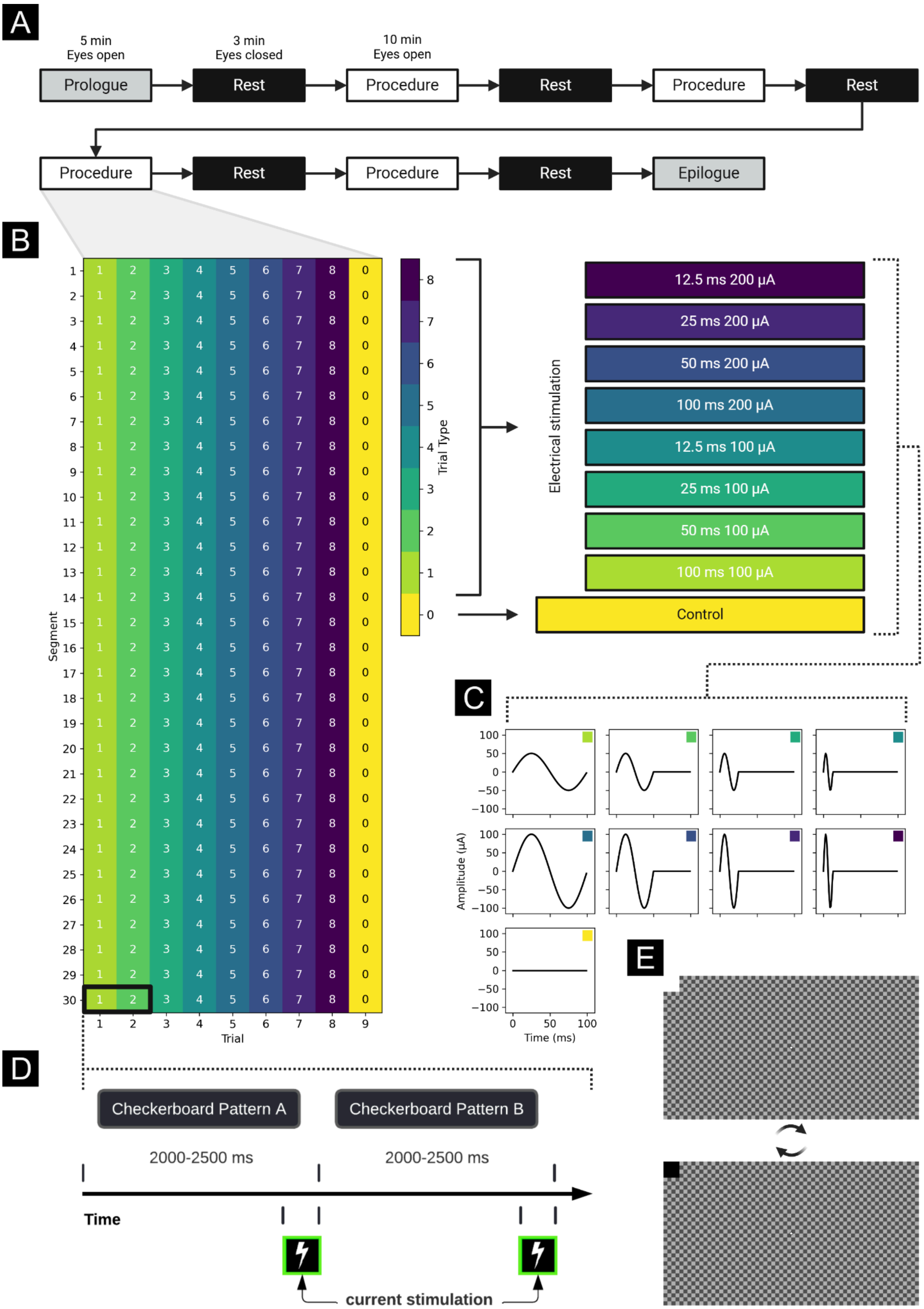

Segment	1	2	3	4	5	6	7	8	9
1	1	2	3	4	5	6	7	8	0
2	1	2	3	4	5	6	7	8	0
3	1	2	3	4	5	6	7	8	0
4	1	2	3	4	5	6	7	8	0
5	1	2	3	4	5	6	7	8	0
6	1	2	3	4	5	6	7	8	0
7	1	2	3	4	5	6	7	8	0
8	1	2	3	4	5	6	7	8	0
9	1	2	3	4	5	6	7	8	0
10	1	2	3	4	5	6	7	8	0
11	1	2	3	4	5	6	7	8	0
12	1	2	3	4	5	6	7	8	0
13	1	2	3	4	5	6	7	8	0
14	1	2	3	4	5	6	7	8	0
15	1	2	3	4	5	6	7	8	0
16	1	2	3	4	5	6	7	8	0
17	1	2	3	4	5	6	7	8	0
18	1	2	3	4	5	6	7	8	0
19	1	2	3	4	5	6	7	8	0
20	1	2	3	4	5	6	7	8	0
21	1	2	3	4	5	6	7	8	0
22	1	2	3	4	5	6	7	8	0
23	1	2	3	4	5	6	7	8	0
24	1	2	3	4	5	6	7	8	0
25	1	2	3	4	5	6	7	8	0
26	1	2	3	4	5	6	7	8	0
27	1	2	3	4	5	6	7	8	0
28	1	2	3	4	5	6	7	8	0
29	1	2	3	4	5	6	7	8	0
30	1	2	3	4	5	6	7	8	0

Figure 2-8. *Schematic representation of the experimental procedure in the second study. (**A**) The experimental procedure included four block types: "Prologue/Epilogue", "Rest", and "Procedure". The procedure began and concluded with the "Prologue" and "Epilogue" blocks, each lasting approximately 5 minutes. During these blocks, participants observed checkerboard pattern reversals (CPRs) without preceding current stimulation, regardless of*

*their experimental group. Each block contained 120 CPRs. The "Rest" blocks, of which there were five, served as breaks for participant relaxation and for checking experimental equipment. These 3-minute blocks required participants to keep their eyes closed, with no EEG recording conducted. If necessary, adjustments were made to the stimulation and recording electrodes, and experimental equipment was recalibrated during these breaks. Finally, the procedure included four "Procedure" blocks, each lasting about 10 minutes. In these blocks, CPRs were presented following a current pulse with specific parameters, varying by trial type and the participant's assignment to either the experimental or placebo group. (**B**) Each "Procedure" block consisted of 30 segments made up of 9 trials of one of 9 types. Types 1-8 included the application of a current pulse of a combination of specified duration (12.5, 25, 50, 100 ms) and amplitude (100, 200 μA) immediately before CPR (**C**). Type 0, on the other hand, "Control," considered CPR without preceding current stimulation. (**D**) Each trial, displaying one of the two checkerboard patterns, lasted 2.25 ± 0.25 seconds. At the end of each pattern display, a current pulse was applied, depending on the trial type. This pulse application was immediately followed by a reversal of the checkerboard pattern on the screen (**E**), initiating the next trial. In each "Procedure" block, there were 30 repetitions of each trial type, resulting in a total of 120 repetitions per experimental condition across the four experimental blocks.*

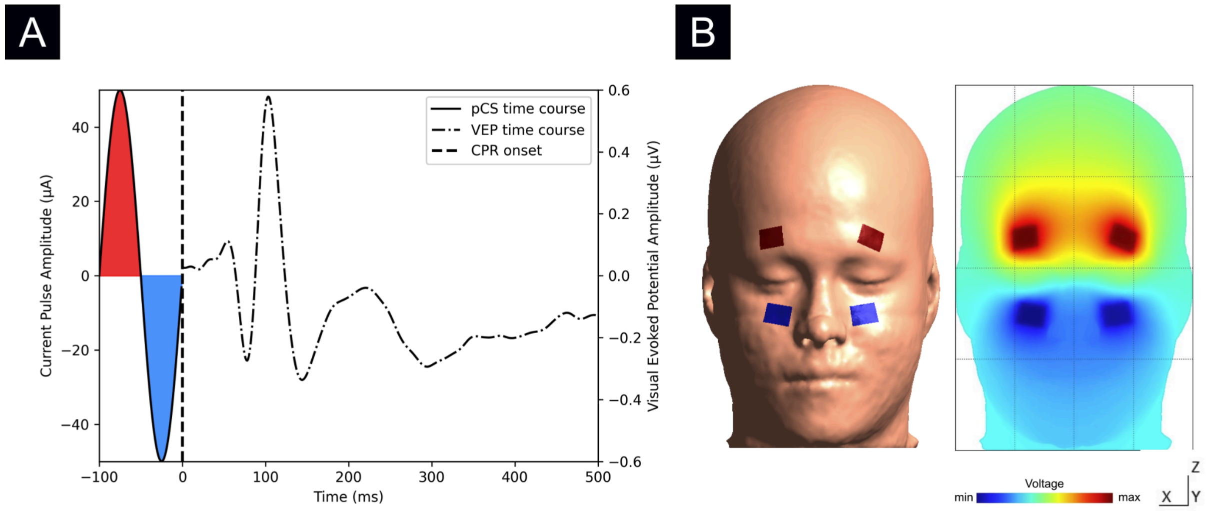

***Figure 2-9.** Visualization of current pulse application and corresponding visual evoked potential (VEP) with electrode placement and induced electric field (IEF) (**A**) Visualization of a periorbital current stimulation (pCS) in a form of 100 ms pulse with an amplitude of 100 μA preceding visual stimulation in the form of a checkerboard pattern reversal (CPR). This CPR serves as the source of neuronal activity, reflected in the occipital EEG signal as a VEP. The VEP is characterized by three peaks occurring at approximately 75 ms (N75), 100 ms (P100), and 135 ms (N135), respectively. The colored shading beneath the curve of the current pulse indicates the direction of current flow between the stimulation electrodes: red signifies current flow from the upper to lower electrodes, while blue indicates flow from the lower to upper electrodes. The Y-axis scale for the current pulse waveform is represented from the perspective of the upper electrodes. (**B**) Visualization of the stimulation electrode locations (left image) and a simulation of the IEF on the participant's skin surface at the first peak amplitude of the current pulse (right image).*

Data Processing

Overview

In the second study, only the EEG signal was available, which required processing through the same steps as in the first study: selecting and interpolating “bad” channels, filtering and re-referencing the signal, performing ICA, and finally segmenting the signal.

Channel Interpolation

Upon visual inspection, an average of 0.34 ± 0.07 channels per dataset were interpolated in the experimental group, compared to 0.51 ± 0.10 channels in the placebo group. Among the most frequently excluded channels were Fp1, Fp2, AF7, AF8, Tp9, Tp10.

Filtering and Re-Referencing

The EEG signal underwent preprocessing using a 4th-order Butterworth biquadratic (second-order sections) infinite impulse response (IIR) band-pass filter, covering a frequency range of 0.1-40 Hz. Additionally, a zero-phase finite impulse response (FIR) notch filter, with a length of 6.6 seconds, was employed to eliminate grid artifact frequencies and their harmonics (ranging from 50 Hz to 500 Hz in 50 Hz increments). The selection of these filter types was driven by the need to minimize edge artifacts associated with concurrent pPCS-induced EEG disturbances. Following the filtering process, the signal was re-referenced to the average of all channels.

Independent Component Analysis

The performance of ICA followed the same method and component exclusion criteria as outlined in study one, with an average of 1.21 ± 0.05 components excluded per participant.

Signal Segmentation (Epoching)

Data segmentation, or epoching, of the EEG signal was performed using the moments of CPRs as the onset points (zero points) of the epochs. Each epoch spanned a temporal range from -875 ms to +1125 ms relative to the onset. As a result, each epoch consisted of 2001 samples, corresponding to the same number of milliseconds, considering the EEG signal's sampling rate.

Based on visual inspection, 27.1 ± 3.7 epochs per dataset (where ± represents the standard error of the mean) were identified and excluded from further processing due to excessive noise, abrupt changes in signal amplitude, or the presence of artifacts such as electrode drift, electrical interference, and all other signal disturbances not addressed during ICA analysis. The average number of bad epochs identified during the *prologue* and *epilogue* phases was 17.9 ± 2.8 for the experimental group and 9.16 ± 1.4 for the sham condition. During the main *procedure*, the average number of epochs identified was 43.8 ± 5.4 for the experimental group and 37.7 ± 5.1 for the sham condition.

Finally, baseline correction was applied to the epochs, with the baseline defined as the interval from -875 ms to -200 ms preceding the visual stimulus. Subsequently, the intra-subject epoched data were normalized across all channels and conditions and represented as Z-score values. Normalizing EEG data to z-scores before analyzing e.g. P1N1 and P1N2 VEP components ensures comparability across participants and sessions by removing individual baseline differences and accounting for variability in amplitude distributions. Values in z-space were represented with the unit μV.

Data Analysis

Effects of Current Stimulation on Visual Evoked Potentials

After segmenting the EEG data and grouping them according to the experimental conditions, VEPs were calculated for the occipital cluster of seven electrodes: O1, O9, OI1h, Oz, OI2h, O10, and O2. The peak amplitudes were extracted from the main VEP components - N75 (N1), P100 (P1), and N145 (N2) (see Figure 1-9). Next, P1N1 and P1N2 peak-to-peak amplitudes were calculated as a main measure of VEP magnitude.

P1N1 and P1N2 amplitudes were compared between the consecutive blocks of experimental procedure and between experimental and sham groups. In particular, *procedure* blocks were compared to *prologue* to estimate direct stimulation effects and *epilogue* block was compared to *prologue* to capture any potential changes persisting after the stimulation. Additionally, we investigated the progression of the stimulation effect across and within each of the four *procedure* blocks, and within the *epilogue* block. The global stimulation effect was examined by pooling data from all conditions involving current pulse application prior to CPR. The potential role of current pulse characteristics was evaluated by separately analysing each trial type.

Results

Induced Electric Field During Periorbital Current Stimulation

Stimulation Current Parameters

The estimated relationship between electrode size, current intensity, and current density, are illustrated in Figure 3-1. The calculations indicated that the use of the proposed small (3 cm^2), self adhesive electrodes, would ensure reduction in the total charge delivered during sinusoidal biphasic current pulse stimulation, with well preserved effective current density. The density of 0.016 mA/cm², obtained for the example pulse of 100 μA and 100 ms was nearly half the value obtained with protocols typically used in tDCS i.e. 1 mA amplitude and 35 cm² rubber/sponge electrodes soaked in saline solution.

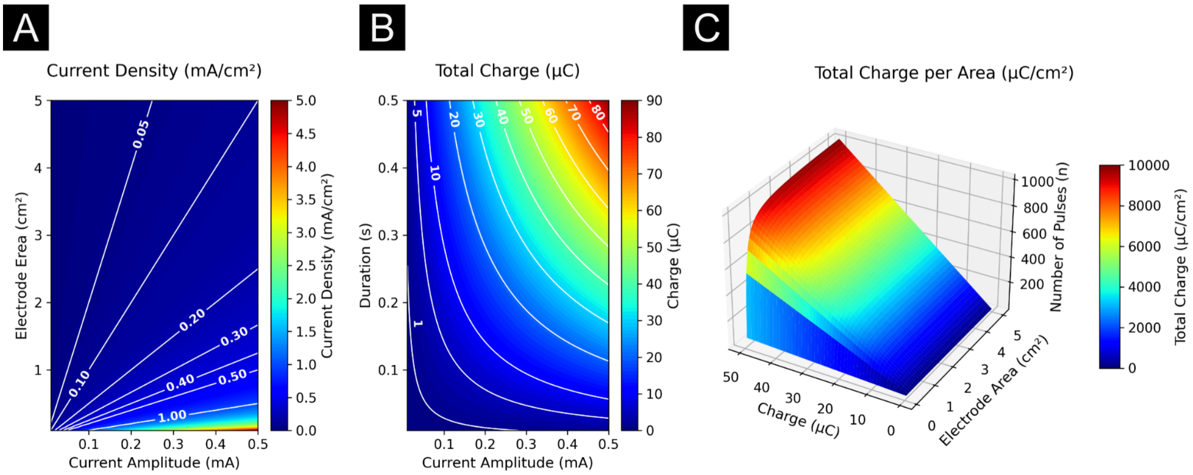

__Figure 3-1.__ Relation between electrode size, current amplitude and overall stimulation intensity for stimulation using sinusoidal biphasic current pulses. Panel (__A__) shows the pulse current density (mA/cm²) distribution below the stimulation electrode as a function of current peak amplitude (mA) and electrode area (cm²) for a sine biphasic pulse. Panel (__B__) illustrates the pulse total charge (μC) based on the peak-to-peak amplitude (mA) of the sine biphasic pulse and pulse duration (s), where the duration refers to the length of the entire pulse (both phases). Panel (__C__) represents the cumulative charge (μC/cm²) delivered during stimulation as a function of pulse total charge, pulse number (n) and electrode area (cm²).

Temporal Dynamics of Applied Current

In the pPCS setup we developed, involving two electrodes placed above the eyes and two electrodes below, it is crucial to understand the temporal dynamics of the applied current based on its characteristics. Consider a single sinusoidal current pulse with a 100 ms duration and a peak-to-peak amplitude of 100 µA, as discussed earlier. Stimulation is administered through bipolar channels with outputs for two stimulation electrodes, labeled A and B, positioned above and below each of the participant's eyes, respectively. Assuming electrode A serves as the positive pole, and an alternating current with a frequency of 10 Hz and a maximum amplitude of 50 µA is applied for 100 milliseconds, we generate a 100 ms pulse with a peak-to-peak amplitude of 100 µA. The values at electrodes A and B can then be determined for the consecutive time points with an interval of 0, 0.01 second.

It is important to note that the electric field is induced throughout the entire duration of the pulse, with the greatest change in the IEF occurring between the peaks of the pulse, where the difference in current intensity is maximal. This is also when the most significant change in the potential of nerve cells affected by the field takes place in the eyes. To calculate these values over time, the characteristics of the bipolar channel and alternating current stimulation must be considered. For this setup, we assume that one electrode acts as the cathode (negatively charged) and the other as the anode (positively charged). Conventional current flows from the anode (positive) to the cathode (negative), while electrons flow in the opposite direction, from the cathode to the anode - direction of current flow is key in determining the voltage sign at each electrode. The formula for an AC sine wave allows to calculate instantaneous current at any given time:

$$I(t) = I_{max} sin(2\pi f t)$$

where $I(t)$ is the instantaneous current at time t, I_{max} is the maximum amplitude of the current (50 µA in an example case), f is the frequency of the AC (10 Hz), and t is the time (e.g. 100 ms). If electrode A is the positive pole (anode) and electrode B is the negative pole (cathode), the current at electrode A (I_A) will be equal to the current I, while the current at electrode B (I_B) will be the negative of I. Thus, the current values for each electrode at each time point can be calculated. For instance, at $t = 0.01\ s$:

$$I(0.01) = 50 sin(2\pi \times 10 \times 0.01) \approx 29.39\ \mu A$$

Therefore, at 0.01 s (10 ms), the current at electrode A will be 29.39 µA, and at electrode B, it will be -29.39 µA. The values for the considered example pulse are presented in Figure 3-2A. These results offer insight into the time-dependent changes in current application and their influence on the surrounding tissue, providing a detailed context for the IEF dynamics discussed in the dissertation.

A

Time (s)	I(t) (µA)	Electrode A	Electrode B
0.000	0.00	0.00	0.00
0.005	15.45	15.45	-15.45
0.010	29.39	29.39	-29.39
0.015	40.45	40.45	-40.45
0.020	47.55	47.55	-47.55
0.025	50.00	50.00	-50.00
0.030	47.55	47.55	-47.55
0.035	40.45	40.45	-40.45
0.040	29.39	29.39	-29.39
0.045	15.45	15.45	-15.45
0.050	0.00	0.00	0.00
0.055	-15.45	-15.45	15.45
0.060	-29.39	-29.39	29.39
0.065	-40.45	-40.45	40.45
0.070	-47.55	-47.55	47.55
0.075	-50.00	-50.00	50.00
0.080	-47.55	-47.55	47.55
0.085	-40.45	-40.45	40.45
0.090	-29.39	-29.39	29.39
0.095	-15.45	-15.45	15.45
0.100	0.00	0.00	0.00

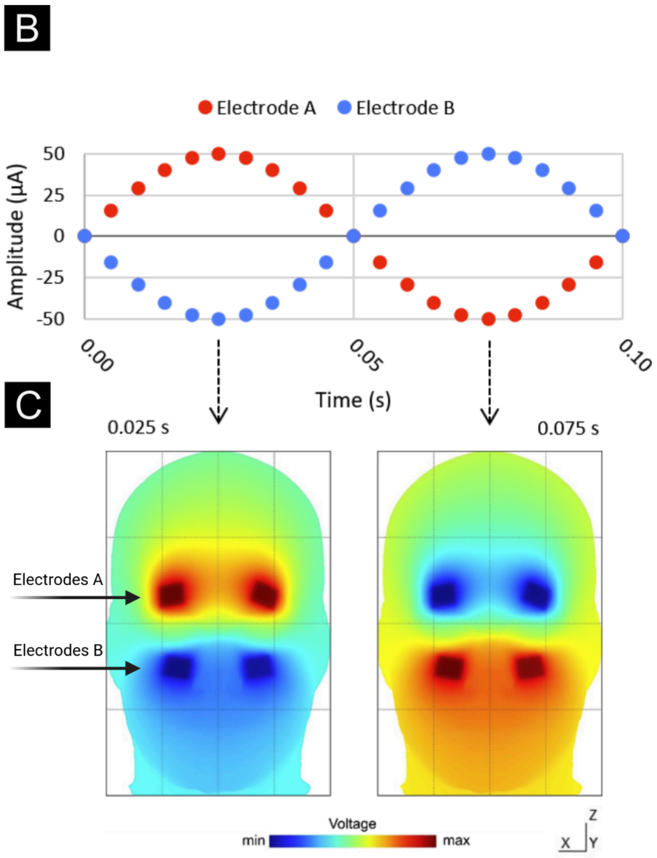

Figure 3-2. *The temporal dynamics of the applied current during a 100 ms pulse with amplitudes ranging from -50 µA to +50 µA, commonly referred to in the dissertation as a 100 µA pulse. (**A**) On the left, the table shows calculated values for electrodes A (above the eyes) and B (below the eyes) at specified time intervals, demonstrating changes in current magnitude over time. (**B**) The upper right panel presents a visualization of the current waveforms for each electrode, highlighting the periodic nature of current fluctuations during stimulation. (**C**) The lower right panel depicts spatiotemporal patterns of induced electrical voltage at the skin surface at 25 ms and 75 ms during the pulse, based on computer simulations.*

Two key points should be highlighted at this stage. First, the largest potential difference within the stimulated tissue occurs between the peaks of the applied current pulse - specifically, at timestamps of 25 ms and 75 ms for a 100 ms pulse. During this 50 ms window, the most significant changes in the IEF take place in the affected tissues, representing the period when this form of stimulation has the greatest impact.

Second, during this interval, the IEF polarity reverses by 180 degrees. Simulations of a sinusoidal pulse with zero onset show an inversion of the electric field vector, resulting in a reversal of the field's sign and a shift in surface voltage beneath the electrodes (Figure 3-2C). Initially, the current flows from the upper electrodes to the lower electrodes for 50 ms, then reverses direction for the next 50 ms (Figure 3-3A). The current magnitude peaks in two successive phases, with the vector direction reversing by 180 degrees in the second phase (Figure 3-3B). On the other hand, the vector orientation is constantly nearly perpendicular to the anterior-posterior axis of the eyeball (Figure 3-4B). As the field vector is aligned with the current flow between the upper and lower electrode, its trajectory is arched rather than a strictly linear one. Additionally, the vector's angle varies based on the measurement location within other locations in the nervous system.

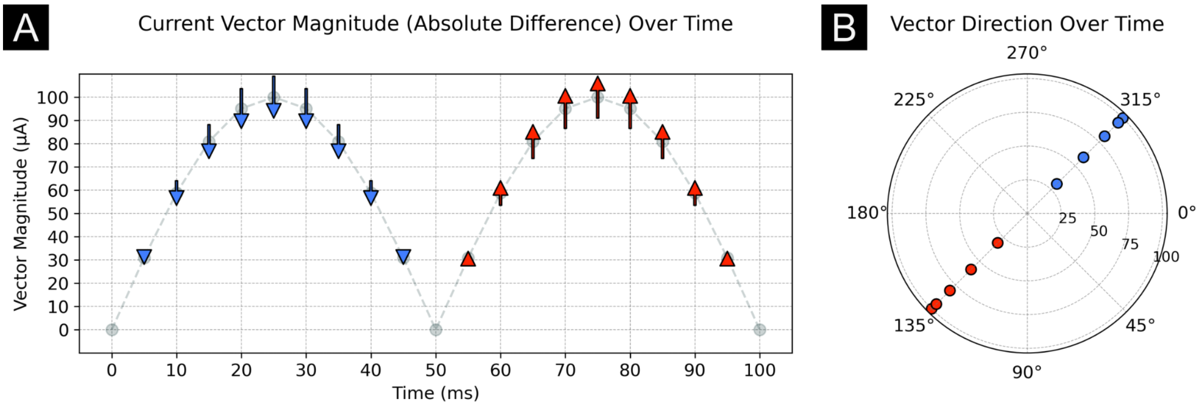

Figure 3-3. *The magnitude and direction of the current vector during the application of a single sinusoidal current pulse of 100 ms duration with a peak-to-peak amplitude of 100 µA. (**A**) The first subplot illustrates the changes in vector magnitude over time, showing two distinct phases of rise and fall. The arrows indicate the direction of current flow, where the direction corresponds to the movement of current from the upper to the lower electrodes (from the anode to the cathode), flowing across the stimulated tissue region. This represents the evolving direction of the current vector during the pulse application. The length of the arrow denotes the vector's magnitude - longer arrows correspond to greater magnitudes, while the absence of an arrow indicates a moment of zero magnitude. (**B**) The second subplot shows the direction of the vector over time using a polar plot. The axes represent angular directions, with 0° indicating the initial vector orientation. The plot demonstrates a 180-degree reversal of the vector direction during the second phase of the applied pulse, emphasizing changes in the current's flow direction relative to the electrode arrangement. The degree values were determined by applying the arctan2 function to the current values of electrode B and electrode A and converting the result from radians to degrees.*

It is important to note that the temporal dynamics of the IEF described here with a single sinusoidal current pulse also apply to ACS. In this context, ACS can be viewed as a continuous series of sinusoidal pulses with zero IPI, resulting in multiple cycles of rising and falling amplitudes, accompanied by a reversal of the electric field vector throughout the stimulation period.

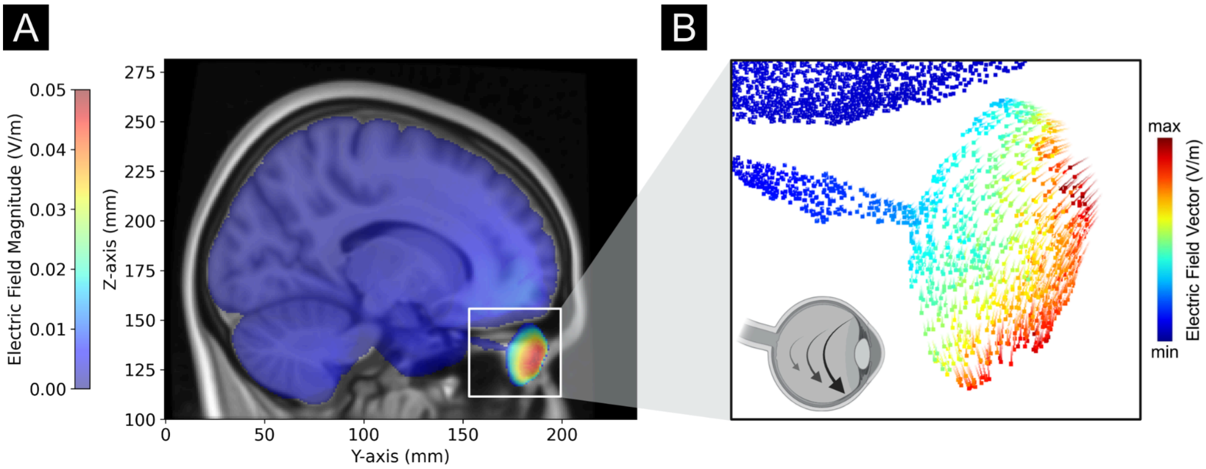

Figure 3-4. *Magnitude and vector of the induced electric field (IEF) during the application of a single sinusoidal current pulse delivered through electrodes placed above and below the eyes at the first amplitude peak (25 ms). (**A**) The average electric field magnitudes for a head slices containing the eyeball are shown, overlaid on the corresponding structural data slice (volumetric data; MNI152). To use the sagittal slice, we identified its location by determining the central X-dimension of the dataset and selecting the index 75 along this axis. The MNI coordinate of the sagittal slice was 15, -126, -172. (**B**) The electric field vector at this amplitude peak is depicted using comet symbols, where the head and tail illustrate the direction of the field, while the color indicates the field strength (surface data). The head points in the direction of the vector, and the tail represents the trailing end. A longer tail signifies a higher vector magnitude. At the 25 ms mark, the current flows from the upper electrodes to the lower electrodes, inducing an electric field in the eyeball with a vector that is nearly perpendicular to the anterior-posterior axis of the eye and directed downward. At the second amplitude peak, occurring at 75 ms during the 100-ms sinusoidal current pulse, the field vector would reverse by 180 degrees and is directed upward (not shown in the Figure).*

Key takeaways:

1. Significant changes in the IEF occur during pulse peaks at 25 ms, 75 ms, and between, possibly affecting tissue potential the most.
2. The IEF reverses direction by 180 degrees during each cycle of the sinusoidal pulse.
3. The IEF vector follows a slightly arched trajectory between the stimulating electrodes.

Spatial Dynamics of Applied Current

Shape of the Electrodes

One of the primary objectives of this dissertation was to perform IEF simulations to examine electrode locations, type, and applied current parameters for the proposed pPCS setup. Simulations were conducted for electrodes placed above and below the eyes, using a single sinusoidal current pulse with a duration of 100 ms and a peak-to-peak amplitude of 100 µA. Specifically, the focus was on the first amplitude maximum of this pulse, occurring at 25 ms.

The highest surface IEF values were observed on the facial skin directly beneath the electrodes, particularly at their edges, exceeding 1.5 V/m. This phenomenon arises from the concentration of current at the electrode edges, which creates a discontinuity in current distribution and leads to a higher density of electric field lines in the surrounding area.

Since there were reports indicating higher current density at the corners of square electrodes (Minhas et al 2011) we compared rectangular and ellipsoid electrodes in our simulations. The electrodes had dimensions 1.5 x 2.0 cm for rectangular and 1.692 x 2.257 cm for ellipsoid electrodes, ensuring a matched area (3 cm^2) and axis-length ratio (~0,75).

The results of IEF simulation indicated that the shape of the electrode did not strongly influence the occurrence of the edge effect. As shown in Figure 3-5, the maximum electric field magnitude (EFM) value for the ellipsoidal electrode was 1.7609 V/m^2, as compared to 1.7667 V/m for the rectangular electrode. However, the distribution of all values within the spatial window were not significantly different, as indicated by the Kolmogorov-Smirnov test for the full range (KS = 0.062, p-value = 0.238) (see Figure 3-7A). Within the normalized field range from 0.6 to 1.0, the ellipsoid electrodes exhibited a higher proportion of field values (2.65%) compared to the rectangular electrodes (1.31%) (see insert in Figure 3-5B), however, the Kolmogorov-Smirnov test indicated no significant difference between these distributions either (KS = 0.389, p-value = 0.332).

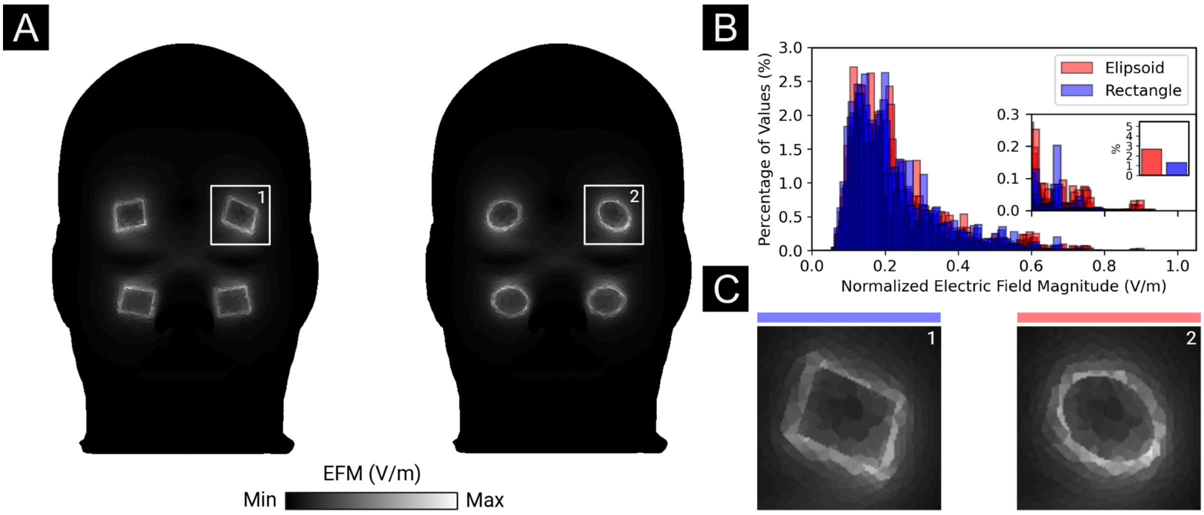

Figure 3-5. *Comparison of electric field distributions for rectangular and ellipsoidal electrodes with axis lengths adjusted to most closely match the rectangular electrode ensuring equal surface area (3 cm^2) and an identical axis-length ratio. (**A**) The maximum value on the normalized scale corresponds to the highest electric field*

*observed for the ellipsoidal electrode (1.7609 V/m), while the minimum value is 0 V/m. (**B**) Histogram of unique values of normalized electric field magnitudes comparing rectangular (blue) and ellipsoidal (red) electrodes, illustrating differences in value distributions, particularly in the upper magnitude range (inserts). The second-level inset illustrates the percentage distribution of values for both electrode types within the 0.6 to 1.0 range. (**C**) Spatial distribution of electric field with clearly visible concentration at the edges of the respective electrodes; note more bright pixels for ellipsoid electrode.*

The shape-related difference in intensity of edge effect were reported by (Minhas et. al 2011) for large electrode sizes (35 cm^{2}). Accordingly, we also performed simulations for different electrode surface areas, either in a range typical for small-sized, stick-on electrodes (which were employed in our experimental studies) or those used in transcranial current stimulation.

First, we modeled small-sized electrodes with non-balanced surface areas: a 1.5 × 2 cm rectangular electrode (3 cm^{2}) and a 1.5 x 2 cm ellipsoid electrode (235.62 mm^{2}). The ellipsoid electrodes exhibited a further increase in high-field values compared to the rectangular ones, particularly in the normalized range from 0.6 to 1.0. As shown in Figure 3-7B, the distributions for the full 0-1 range differed significantly, as confirmed by the Kolmogorov-Smirnov test (KS = 0.109, p-value = 0.003). For the 0.6-1.0 range, significant differences in the field distributions were also evident (KS = 0.638, p-value = 0.010), as illustrated in the inset of Figure 3-6B.

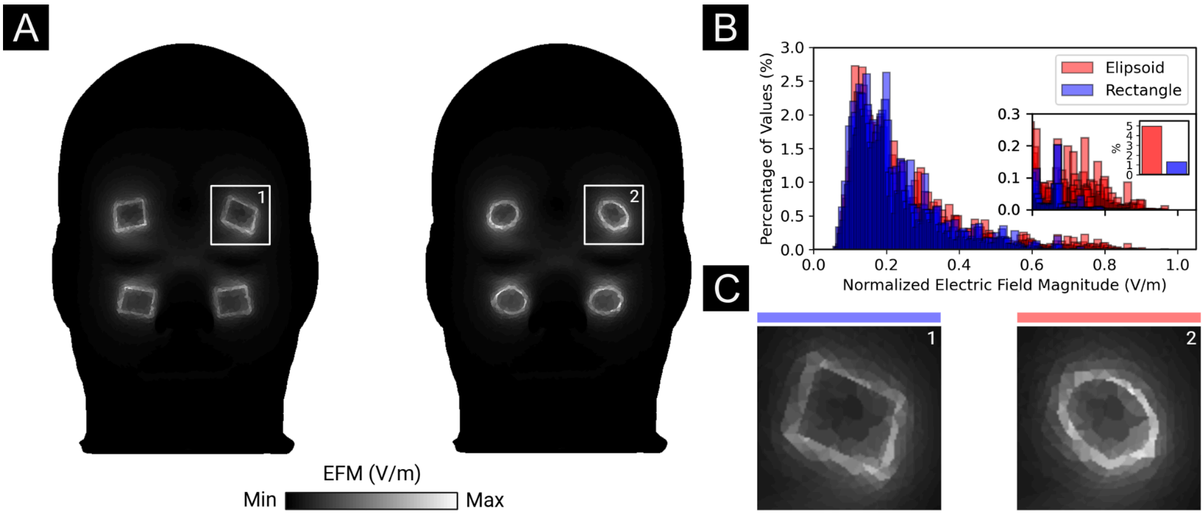

Figure 3-6. *Comparison of electric field distributions for rectangular and ellipsoidal electrodes with unequal surface area (rectangular, 3 cm^{2}; ellipsoid, 235.62 mm^{2}). Figure scheme as in 3-5: (**A**) Normalized electric field intensities beneath the electrode placements for rectangular (left) and ellipsoidal (right) electrodes; (**B**) Histogram of unique values of normalized electric field magnitudes comparing rectangular (blue) and ellipsoidal (red) electrodes, with the range above 0.6 expanded in the insert). The second-level inset illustrates the percentage distribution of values for both electrode types within the 0.6 to 1.0 range. (**C**) Spatial distribution of electric field with clearly visible concentration at the edges of the respective electrodes. There are even more high field values*

in ellipsoid electrodes than in case of equal surface electrodes (Figure 3-5 B). The minima and maxima in A and C are identical to those shown in Figure 3-5.

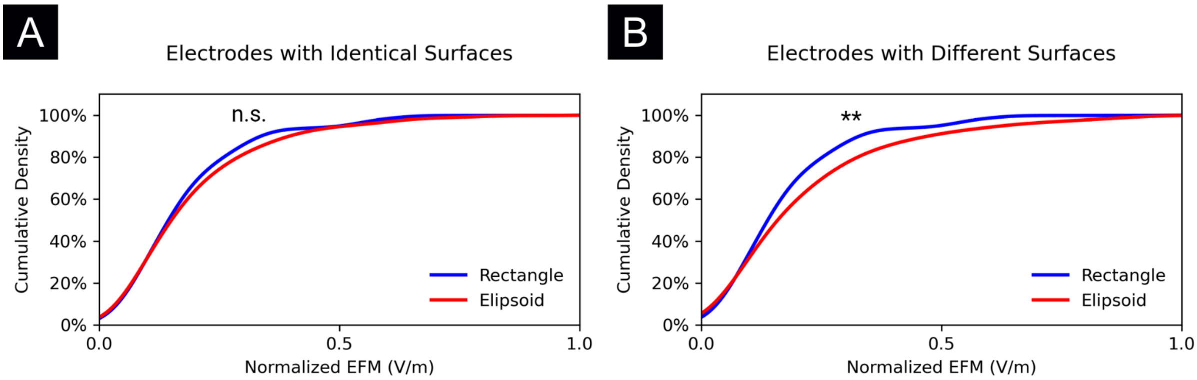

Figure 3-7. *Comparison of cumulative density distributions of normalized electric field magnitude (EFM, V/m) for ellipsoid and rectangular electrodes. (**A**) Distributions for electrodes with identical surface areas show no significant differences (n.s.) in the 0-1 range, as indicated by the Kolmogorov-Smirnov test. (**B**) Distributions for electrodes with different surface areas show significant differences (** - p-value < 0.01) in the 0-1 range, highlighting the effect of the electrode's surface on EFM distribution.*

The role of electrode size and shape was further examined by simulating the field distribution below larger electrodes, mimicking those placed in sponges soaked in saline solution - commonly used in transcranial current stimulation. To this end, we examined a 5 x 7 cm rectangular electrode with an area of 35 cm², placed in a 5 mm thick sponge cover, as well as an ellipsoidal electrode with axis lengths of 5.78 x 7.71 cm, corresponding to the area and aspect ratio of the rectangular electrode. These electrodes were positioned at the back of the head for convenience and, as part of the computer simulations, served as a cathode with a current level of -100 µA, while the two anodes, located above the eyes, were set at +50 µA each, as previously described. With these impulse parameters, the current density under the electrode is expected to be approximately 0.033 mA/cm² for a 3 cm² electrode and 0.006 mA/cm² for a 35 cm² electrode. However, computer simulation results reveal that the maximum current density magnitude is 0.031 mA/cm² for smaller electrodes, 0.0175 mA/cm² for larger ellipsoid electrodes, and 0.0115 mA/cm² for rectangular electrodes.

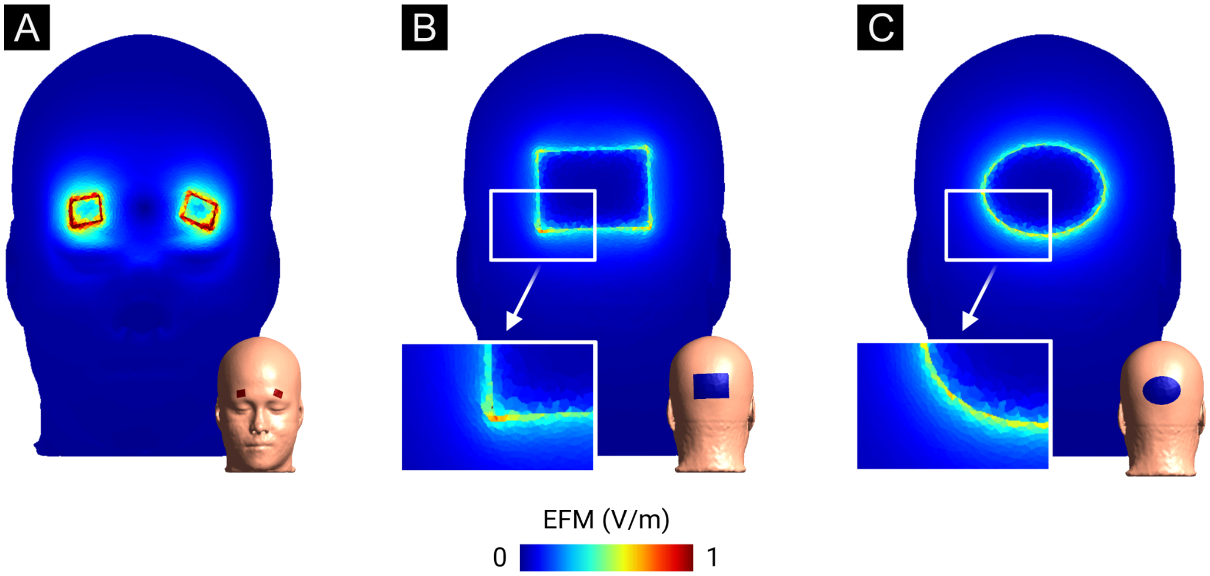

Figure 3-8. *Electric field magnitude (EFM) distribution for different electrode configurations. (**A**) Bipolar periorbital configuration showing EFM distribution concentrated near the edges of the small electrodes placed above the eyes. (**B**) Rectangular electrode placed at the occipital region, highlighting EFM accumulation at the corners, demonstrating the edge effect. The inset shows a magnified view of the concentrated field lines at the corners. (**C**) Ellipsoidal electrode placed at the occipital region with a more uniform EFM distribution along the perimeter. The inset illustrates a detailed view of the smoother field concentration along the curved edge.*

The results of the computer simulations for large electrodes are visualised in Figure 3-8. The maximum field values were 0.786 V/m and 0.755 V/m for the rectangular and ellipsoid electrodes, respectively - 2.25 and 2.33 times lower than those observed with smaller electrodes of corresponding shapes. Moreover, in the case of the rectangular electrode the highest field values indeed accumulated at the corners (Figure 3-8B). In contrast, for the ellipsoidal electrode, the field was more evenly distributed along the edges (Figure 3-8C). The difference in the normalized EFM distributions between large rectangular and ellipse electrodes was significant across the full 0-1 range (KS = 0.128, p-value < 0.001; Figure 3-9C). This effect was even more pronounced in the high-field range (0.5-1.0), where the Kolmogorov-Smirnov test confirmed statistically significant differences (KS = 0.393, p-value = 0.009) (see inset in Figure 3-9B). These findings, along with the shift in the cumulative density curve (Figure 3-9C), demonstrate that the elliptical electrodes consistently produced higher EFM values compared to rectangular electrodes with the same surface area.

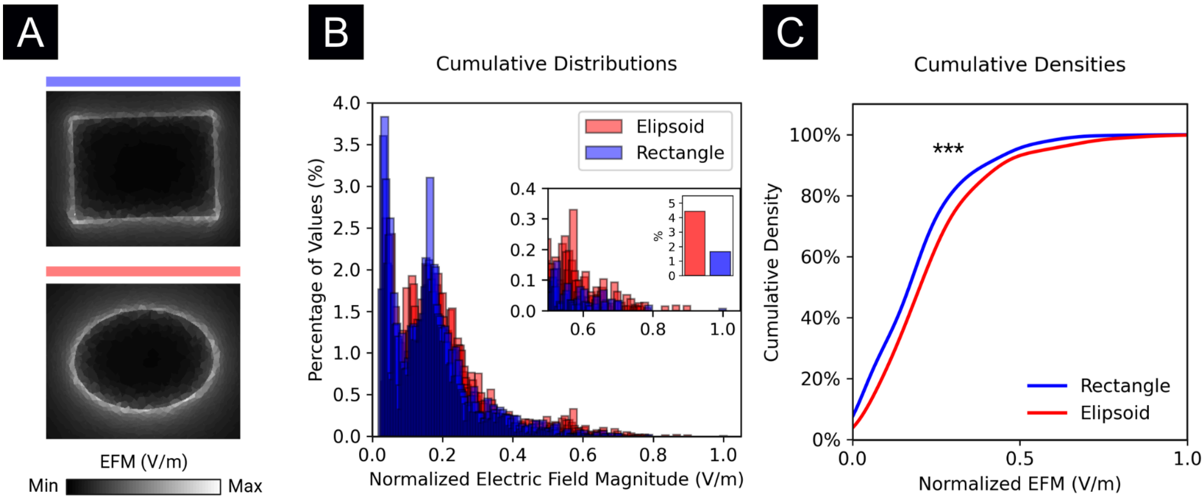

Figure 3-9. *Comparison of electric field magnitude (EFM) distributions and cumulative densities for ellipsoid and rectangular electrodes with identical surface areas. (**A**) Heatmaps of the EFM distributions demonstrate higher field intensities for the ellipsoid electrode compared to the rectangular electrode. (**B**) Histogram of normalized EFM values shows the overall distribution of field magnitudes, with an inset highlighting the differences in the high-field range (0.5-1.0), where ellipsoid electrodes exhibit higher values. (**C**) Cumulative density plot indicates a significant difference in the overall distribution between the two electrode shapes (*** - p-value < 0.001, KS = 0.13), with a notable divergence in the high-field range, as observed in the inset of panel B.*

Performed simulation indicated that the overall strength of the edge effect is related to the current density at the electrode, but it is also modified by the shape of the electrode. The phenomenon occurs in the 3 dimensional space in which the brink of an electrode forms an axis with field lines turning perpendicular to it. The most uniform distribution happens along straight lines, while the curves and angles further concentrate electric field lines, resulting in a localized increase in its intensity. Interestingly, the curved edge of an ellipse electrode seems to focus the field stronger than the straight verge of a square electrode and stronger than straight corners.

On the other hand, in the context of computer simulation results, the observed corner effects (or lack of them) may also stem from spatial representation of the field simulation results. In particular the resolution of mesh nodes might be not sufficient to detect the subtle differences in field distribution at the edge of a small electrode. This may explain the lack of corner effect detected in our simulation of small square electrodes.

In conclusion, the results of the computer simulations indicate that the edge effect varies between rectangular and ellipsoidal electrodes, both for small and larger electrode sizes, with these differences becoming more pronounced as the electrode size increases. Given the substantial nature of these variations, we believe that electrode shape should be a key consideration when determining the optimal stimulation setup. Nonetheless, we emphasize that the current density under the stimulation electrodes remains the most critical factor for ensuring participant safety and comfort during stimulation.

Key takeaways:

1. Highest IEF values were consistently observed at electrode edges due to current concentration.
2. Higher current density under the electrode seems to be the primary driver of stronger edge effects.
3. The current concentration at the edges is moderately modulated by the pattern of straight lines, angels and curvatures in an electrode shape.

Distribution of IEF as a Function of Location of the Electrodes

Our computer-based IEF simulations primarily focused on the periorbital placement of the stimulation electrodes, as detailed in the Materials and Methods section. However, we compared them with an alternative electrode configuration: two anodes positioned above the eyes, but with a single cathode located at the back of the head. We modified the cathode's type and size, using a rubber-carbon electrode placed within a sponge pouch soaked in a saline solution. The electrode's dimensions were adjusted to 5 x 7 cm. Both this type and size are commonly used in tDCS studies. This section presents and briefly discusses the results for each configuration, along with their comparisons.

It is important to note that surface field data derived from the mesh representation differs from volumetric data. While surface-based simulations provide insights into the distribution of electric fields across volume surfaces, accurate numerical values of the IEF within the brain are best obtained through voxel-based analyses after converting mesh to volumetric data. Thus, to gain deeper insights, the surface data (*.msh) were converted into volumetric form (*.nii.gz) for further analysis. Some discrepancy in field values is expected after conversions so the direct comparison of two types of the results is not possible.

We will present both surface and volumetric results, with numerical analyses primarily centered on the volumetric data. This applies to both electrode configurations compared in this dissertation: the bipolar periorbital configuration and the frontal-occipital configuration.

Bipolar Periorbital Configuration

In the pPCS setup we developed, we utilized a bipolar periorbital configuration for the stimulation electrodes, placing all electrodes in close proximity to the eyes. Specifically, two electrodes serve as anodes above the eyes, while two electrodes serve as cathodes below the eyes (Figure 3-10A). Notably, during the application of a sinusoidal current pulse or alternating current, the roles of the anodes and cathodes alternate depending on the phase of the stimulation.

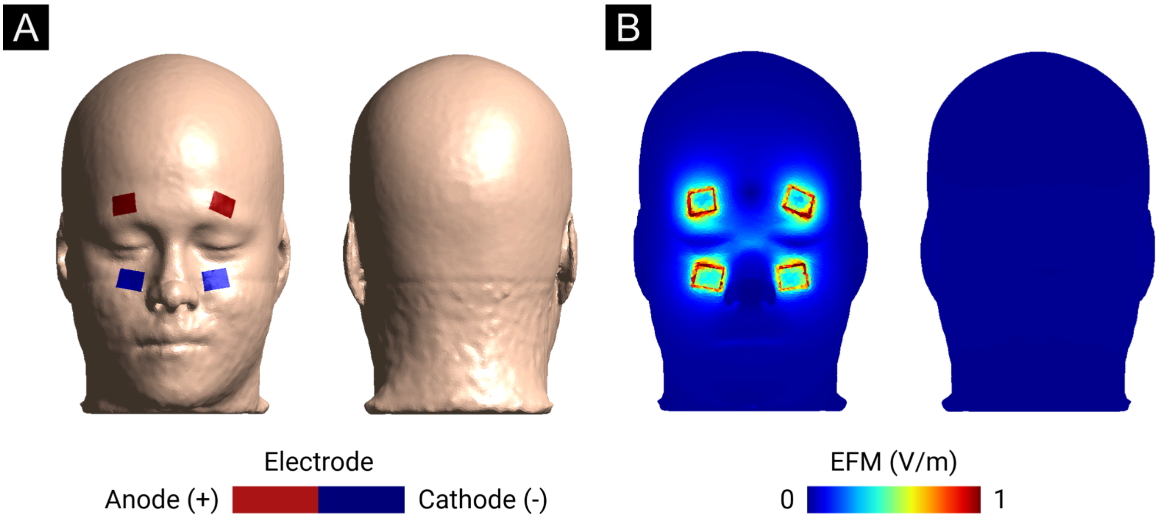

Figure 3-10. *Electrode placement and electric field distribution for the bipolar periorbital configuration. (**A**) Illustration of electrode positioning on the head for the bipolar periorbital setup, showing the anode (red) and cathode (blue) configurations from frontal and posterior views. (**B**) Electric field magnitude (EFM, V/m) distribution map resulting from stimulation with a 100 ms, 100 µA single sinusoidal current pulse, shown at the 25 ms time point corresponding to the first amplitude peak. The colormap ranges from 0 to 1 V/m, highlighting regions of varying electric field intensities across the surface of the head.*

IEF Measure in Surface Data

For the bipolar periorbital configuration, the magnitude of the electric field was highest on the facial skin beneath the stimulation electrodes, with edge values reaching up to 1.7667 V/m. The EFM within the head tissues was much lower and concentrated primarily in the frontal-middle part of the eyes (Figure 3-11). The value observed on the surface of the eyeballs was 0.0844 V/m; 0.0749 V/m in the white matter of the optic nerve and as low as 0.0225 V/m was noted in the gray matter in the anterior cortical region. This results aligns with our expectations for the distribution of the electric field induced with periorbital localization of the stimulation electrodes showing the greatest impact at the initial point of the visual pathway, with minimal influence on other regions of the nervous system.

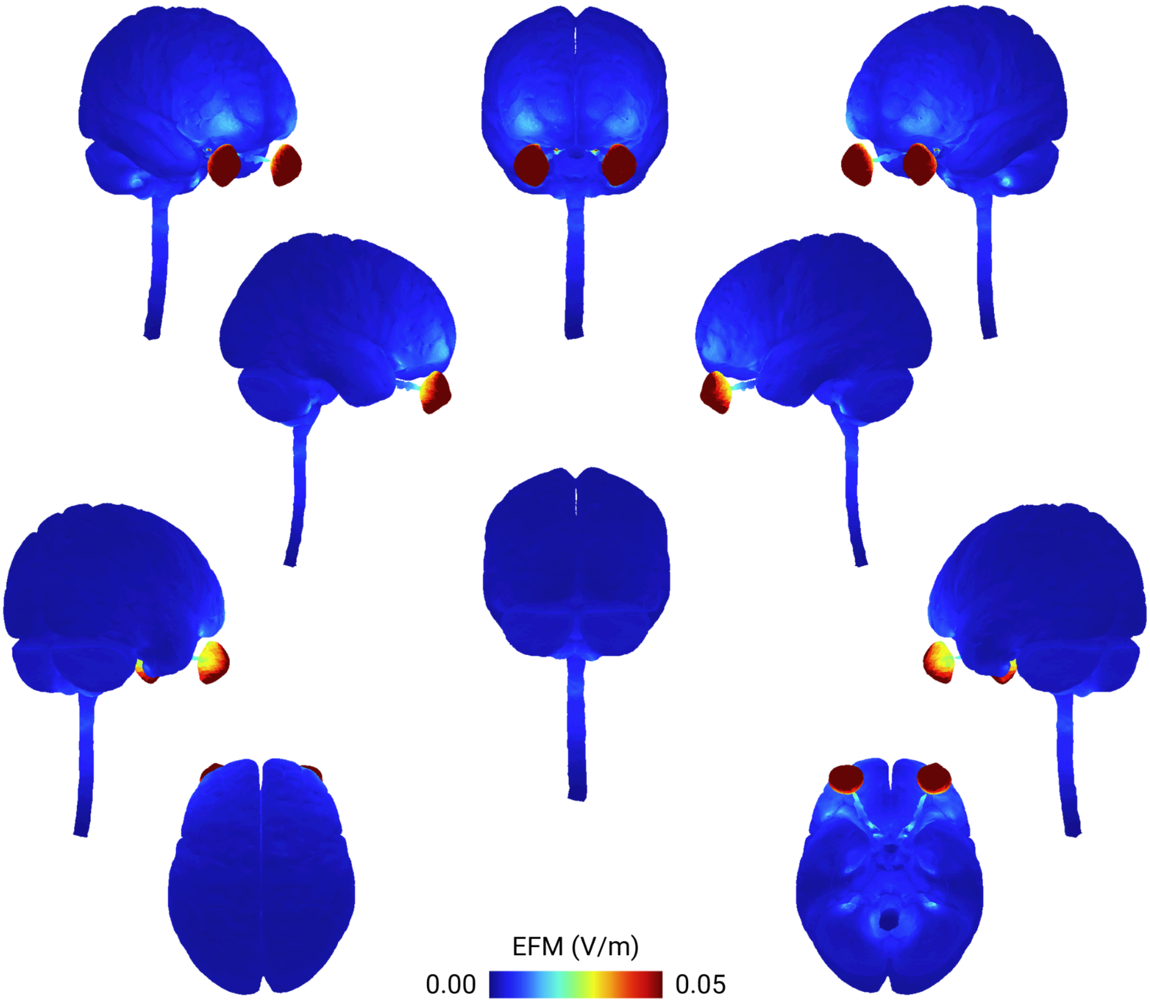

Figure 3-11. *Electric field magnitude (EFM, V/m) distribution across various brain views for bipolar periorbital stimulation (surface mesh representation). The figure shows multiple perspectives, including lateral, superior, and inferior views, illustrating the spatial distribution and intensity of the electric field. The colormap ranges from 0.00 to 0.05 V/m, indicating areas of low (blue) to high (red) field magnitudes.*

Electric Field Distribution Within Head Volumes

Four major volumes were identified for further analysis: the “Scalp”, “Eyeballs”, “Optic Nerve”, and the “Rest of the Brain”. The scalp encompasses the skin, fat, connective tissue, and muscles located outside the skull, as detailed in the Materials and Methods section. The other three volumes were extracted using the three ROIs shown in Figure 2-6. It is important to note that the rest of the brain includes gray and white matter (GM, and WM, respectively) but excludes the optic nerve, spinal cord, or CSF. Statistical description of the IEF values obtained in the extracted volumes is in Table 3-1 and illustrated in Figure 3-12.

Table 3-1. *Global and point statistics for the electric field magnitude (EFM, V/m) obtained from computer simulations of the electric field (IEF) induced by the bipolar periorbital configuration. The table presents the mean EFM, the sum of magnitudes for all voxels, the standard deviation (SD), count (number of voxels), and maximum (Max) and minimum (Min) voxel values for the scalp and three regions of interest (ROIs): Eyeballs, Optic Nerve, and Rest of the Brain (comprising gray matter (GM) and white matter (WM)).*

Volume	**Electric Field Magnitude [V/m]**					**Voxel Count**
	Mean	**Sum**	**SD**	**Max**	**Min**	
Scalp	0.0048	58,016.5	0.0255	1.1187	0.0000	12,220,000
Eyeballs	0.0489	857.8	0.0108	0.0779	0.0256	17,542
Optic Nerve	0.0102	16.6	0.0043	0.0375	0.0048	1,637
Rest of the Brain	0.0035	5,652.2	0.0018	0.0244	0.0052	1,638,915

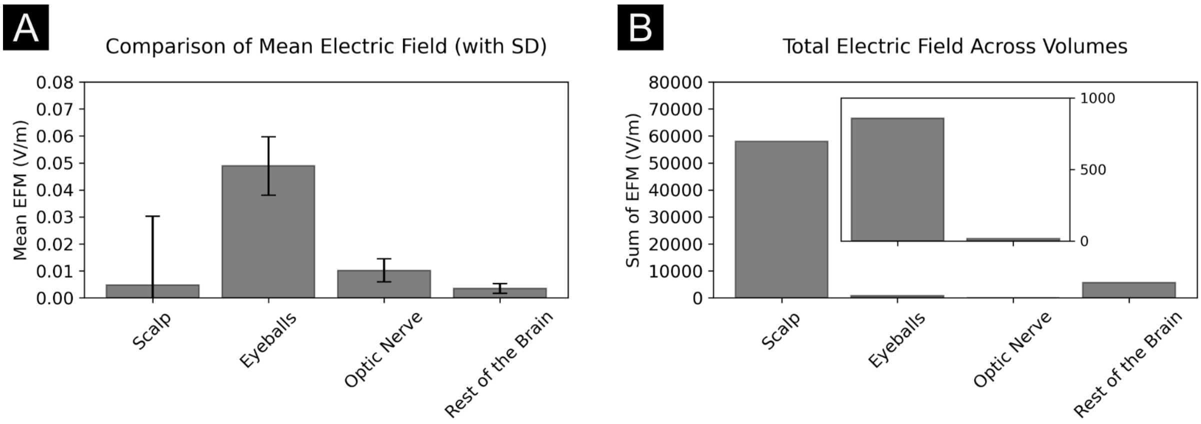

Figure 3-12. *Comparison of electric field magnitude (EFM, V/m) across different anatomical volumes for the bipolar periorbital configuration. Panel (**A**) displays the mean EFM with standard deviation (SD) error bars for each volume (for N see last the column of Table 3-1). Panel (**B**) illustrates the sum of the EFM for all the voxels from each volume. The inset provides an enlarged view of the smaller sums observed for the eyeballs and optic nerve.*

The volumetric data were consistent with the surface data, revealing that the highest EFM value was observed in the scalp volume at 1.1187 V/m, approximately 14 times higher than the maximum EFM in the eyeballs (0.0779 V/m). Nevertheless, the maximum EFM in the eyeballs was only 6.96% of the maximum observed in the scalp, highlighting a significant reduction in EFM. This aligns somewhat with the general assumption that approximately 80% of the electric field generated during transcranial stimulation is attenuated by intervening structures (Vöröslakos et al., 2018). In our study, attenuation was measured as 93% for electrodes near the eyeballs despite the fact that the eyes are an exposed part of the nervous system. Deeper structures exhibited even greater attenuation, with the maximum EFM in the optic nerve reaching only 0.0375 V/m - equivalent to 3.35% of the scalp maximum (97% attenuation). For the rest of the brain volume the maximum EFM was 0.0244 V/m, or 2.18% of the scalp maximum, indicating 98% attenuation. Notably, this attenuation pattern underscores how the distribution of the electric field varies across different facial and deeper structures. By closely examining the distribution of the EFM on the surface of the face, we observed that the EFM decreases sharply beyond the stimulation electrodes. Ultimately, despite the relatively large field attenuation, this electrode configuration appears to stimulate the eyeballs effectively thanks to the shunting effect of the IEF toward the eyeballs.

Specifically, in the context of neural tissues, we observed the highest mean EFM values in the eyeballs (0.0489 V/m). This value is nearly five times greater than the average EFM in the optic nerve (0.0102 V/m) and almost 14 times higher than the average EFM in the rest of the brain (0.0035 V/m). It is also ten times greater than the average EFM in the scalp (0.0048 V/m). This finding is notable for several reasons. First, the highest mean IEF is observed in the eyeballs, attributed to their high conductance. Second, the EFM value is still high in the optic nerve, located just behind the eyeball. Third, the effect of the IEF on the rest of the nervous system appears negligible compared to its impact on the eyeballs with this electrode configuration. Lastly, the low average EFM in the scalp is related to its large volume, and many voxels located mostly far from stimulating electrodes.

The EFM values align with our intended objective of concentrating the effects of pPCS specifically on the eyeballs. This is supported not only by the EFM data but also by the results of IEF simulations for current density magnitude (CDM, A/m^2) (Figure 3-13). Current density magnitude (magnJ) represents the strength of the current density in each voxel (or node), independent of its direction. While current density (J) is a vector quantity that includes both the magnitude and direction of the current flow in a voxel (or node), magnJ (|J|) is the scalar value obtained by normalizing J, providing the absolute magnitude of the current density without any directional information. Thus, to calculate the total current for the volumes of interest (in amperes), we used the following formula:

$$I_{total} = \sum_{i=1}^{N_{vox}} I_{vox} = \sum_{i=1}^{N_{vox}} \left(magnJ_i \times A_{vox} \right)$$

The formula calculates the total current (I_{total}) within a given volume by summing the contributions from all individual voxels. Each voxel's contribution is determined by multiplying the magnitude of the current density ($magnJ_i$), which represents the absolute amount of current per unit area, by the surface area of the voxel (A_{vox}). The total current is obtained by summing these individual contributions across all voxels (N_{vox}) in the volume. This method provides a measure of the total current flowing through the volume without incorporating directional information, focusing solely on the magnitude of the current density. Since the conversion from a mesh format to volumetric data (*.msh → *.nii.gz) involves scaling the current density magnitude based on voxel surface area, the total sum of the current density magnitude in the volumetric data remains equal to I_{total}, but requires changing the unit from A/m2 to µA.

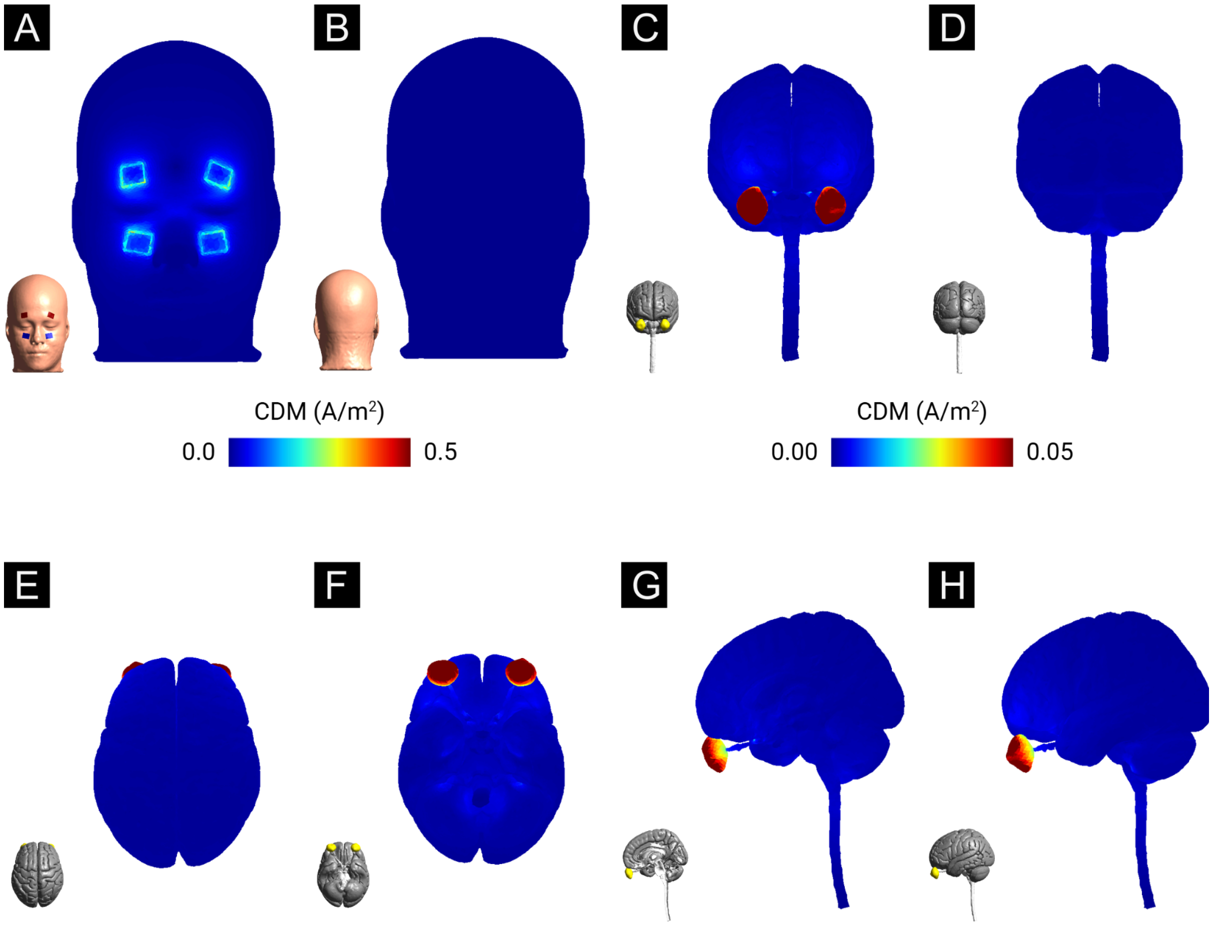

Figure 3-13. *Current density magnitude (CDM, A/m²) surface distribution for the bipolar periorbital configuration. (**A**) Anterior view of the head illustrating the placement of periorbital electrodes, with notable edge effects visible in the CDM distribution. (**B**) Posterior view of the head. (**C-H**) Various views, including anterior, posterior, superior, inferior, sagittal, and temporal perspectives, depicting the distribution of current density within the eyeballs, gray matter (GM), and white matter (WM). Note that a different scale is used for panels (A-B) compared to panels (C-H) to appropriately reflect variations in CDM.*

These findings further emphasize the potential to isolate the effects of the bipolar periorbital configuration on the eyeballs. For CDM, we observed the highest values beneath the electrodes, particularly along their edges, confirming the presence of an edge effect for current density as well. Interestingly, the maximum CDM on the skin was only three times higher than in the eyeballs, measuring 0.2182 A/m² for the scalp and 0.0726 A/m² for the eyeballs (see Table 3-2 and Figure

3-14). In the optic nerve, the maximum CDM was 0.0131 A/m², while in the rest of the brain it measured 0.0085 A/m². Notably, the average CDM in the eyeballs was 0.0456 A/m², the highest among all the regions examined. The second-highest average CDM was observed in the optic nerve at 0.0035 A/m², followed by the rest of the brain at 0.0013 A/m², and finally the scalp at 0.0009 A/m², which is nearly 51 times lower than that of the eyeballs. Given the relatively small number of voxels representing the eyeballs compared to the rest of the brain - a difference of nearly 100-fold - it is noteworthy that the total current in the eyeballs is only 2.7 times lower than that in the rest of the brain (799.5 vs. 2174.7 A/m^2). This reflects a significant distribution of current density focused on the eyeballs during stimulation relative to the rest of the nervous system.

Table 3-2. *Global and point statistics for the results of computer simulations of the induced current density (CDM, A/m^2) expressed in volumetric form for the bipolar periorbital configuration. The table presents the mean CDM (A/m^2), the standard deviation (SD, A/m^2), the total number of voxels (Count), and the maximum (Max, A/m^2) and minimum (Min, A/m^2) values for the scalp and three regions of interest (ROIs): Eyeballs, Optic Nerve, and Rest of the Brain (comprising gray matter (GM) and white matter (WM)). Additionally, the table includes I_{total} (μA), representing the total current flowing through each region, calculated by summing the contributions from all voxels within the region based on the voxel area and current density magnitude.*

Volume	**Current Density Magnitude [A/m^2]**					**Voxel Count**
	Mean	**SD**	**Max**	**Min**	**I_{total}**	
Scalp	0.0009	0.0050	0.2182	0.0000	11,313.0	12,220,000
Eyeballs	0.0456	0.0101	0.0726	0.0089	799.5	17,542
Optic Nerve	0.0035	0.0015	0.0131	0.0017	5.8	1,637
Rest of the Brain	0.0013	0.0007	0.0085	0.0000	2,174.7	1,638,915

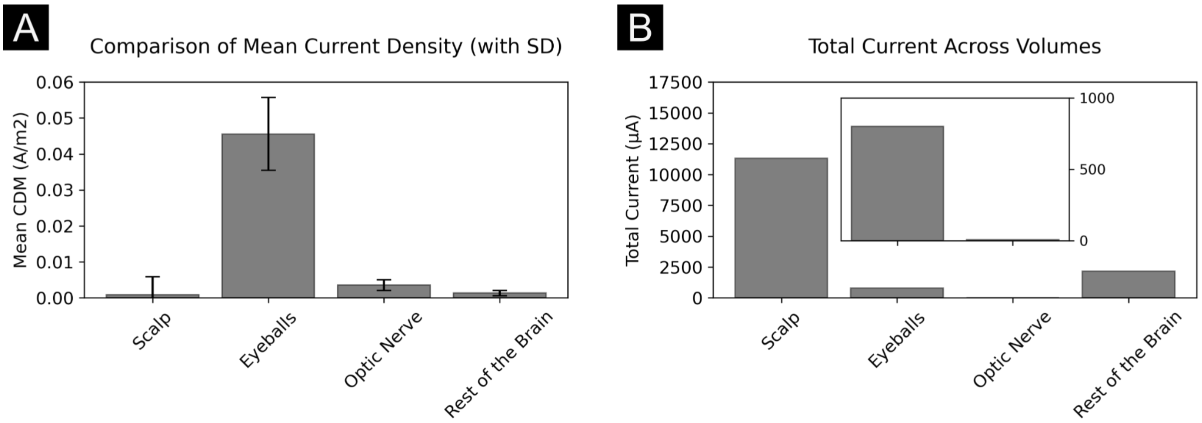

***Figure 3-14**. Comparison of current density magnitude (CDM) and total current across different anatomical volumes for the bipolar periorbital configuration. Panel (**A**) displays the mean CDM (A/m^2) with standard deviation (SD) error bars for each volume. Panel (**B**) illustrates the total current (I_{total}, µA) for each volume. The inset provides an enlarged view of the smaller total currents observed for the eyeballs and optic nerve.*

Bipolar Frontal-Occipital Configuration

The second configuration tested was the bipolar frontal-occipital configuration, which utilized two electrodes positioned above the eyes with a single large electrode placed on the occipital region at the location of the EEG Oz electrode (Figure 3-15). This electrode was a rectangular, 5 x 7 cm rubber-carbon electrode with an area of 35 cm^2, enclosed in a 5 mm thick sponge soaked in a saline solution with a conductivity of 1 S/m, typical for tDCS applications. The simulation was conducted for a single sinusoidal current pulse with a peak-to-peak amplitude of 100 µA and a duration of 100 ms, specifically analyzed at a 25 ms timestamp corresponding to the first amplitude peak. During this peak, the electrodes above the eyes served as anodes, while the occipital electrode functioned as the cathode. The current on the electrodes above the eyes was +50 µA each, while the current on the occipital electrode was -100 µA in total, maintaining current balance between the anodes and the cathode to ensure a net zero current amplitude.

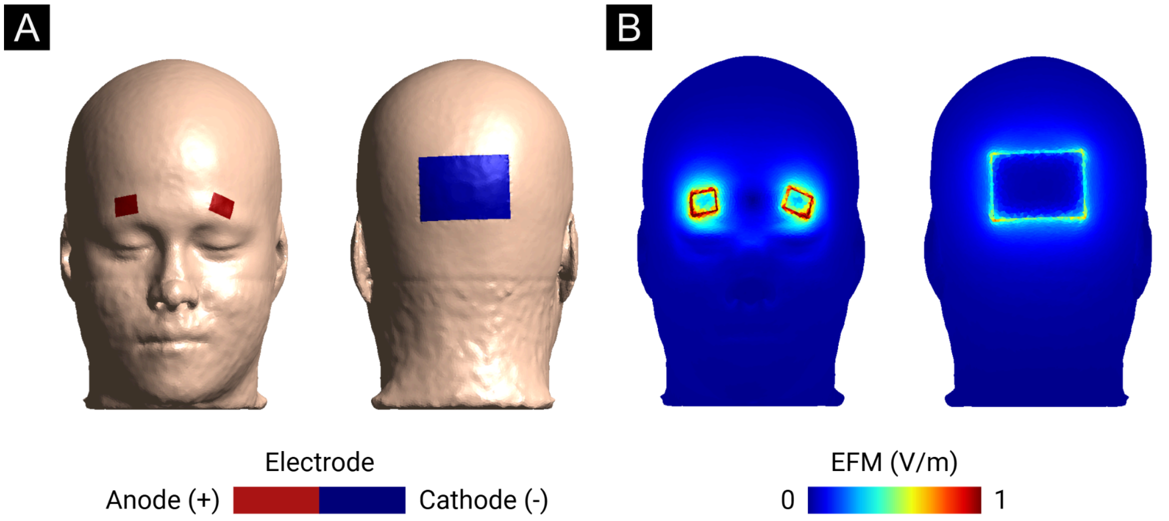

Figure 3-15. *Electrode placement and electric field distribution for the bipolar frontal-occipital configuration. (**A**) Illustration of electrode positioning on the head for the bipolar frontal-occipital setup, showing the anode (red) and cathode (blue) configurations from frontal and posterior views. (**B**) Electric field magnitude (EFM, V/m) distribution map resulting from stimulation with a 100 ms, 100 μA single sinusoidal current pulse, shown at the 25 ms time point corresponding to the first amplitude peak. The colormap ranges from 0 to 1 V/m, highlighting regions of varying electric field intensities across the surface of the head.*

From the surface simulation results (Figure 3-15B), it is evident that the EFM beneath the stimulation electrodes on the face is consistent with the values observed for the periorbital configuration (Figure 3-10B). For the occipital electrode located at the back of the head, the EFM is consistent with the results presented in Figure 3-8B, which examined the impact of electrode shape and size on IEF. Specifically, due to the larger surface area of the cathode, its current density (0.003 mA/cm^2) is much lower than that of the anodes (0.016 mA/cm^2).

With such electrodes pattern the maximum EFM on the scalp surface (1.6173 V/m) was observed beneath the frontal electrodes. This value was approximately 20 times higher than the maximum EFM observed on the surface of the eyeballs, which reached 0.0797 V/m, localized primarily in the upper regions of the eyes (Figure 3-16). Within white matter, the peak EFM was measured at 0.2389 V/m in the optic nerves, making it roughly 6.8 times lower than the scalp maximum but 3 times higher than the maximum EFM observed in the eyeballs. In contrast, the maximum EFM within gray matter was 0.0666 V/m, observed in both the anterior and occipital regions of the cortex. This value was approximately 24 times lower than the scalp maximum and slightly lower than the maximum EFM recorded in the eyeballs.

As seen in Figure 3-16 the bipolar frontal-occipital configuration is effective in targeting deeper structures relevant to vision: the optic nerve was significantly influenced, and both the frontal cortex and, to a greater extent, the occipital cortex demonstrate moderate levels of EFM. This distribution of the IEF indicates that, beyond the primary focus on the eyes and optic nerves, the stimulation extends to cortical regions associated with higher visual processing, albeit to a lesser degree. This nuanced distribution highlights the spatial specificity of the stimulation, targeting all key stages of the visual pathway, while emphasizing its potential for broader modulation of visual and associated cortical networks.

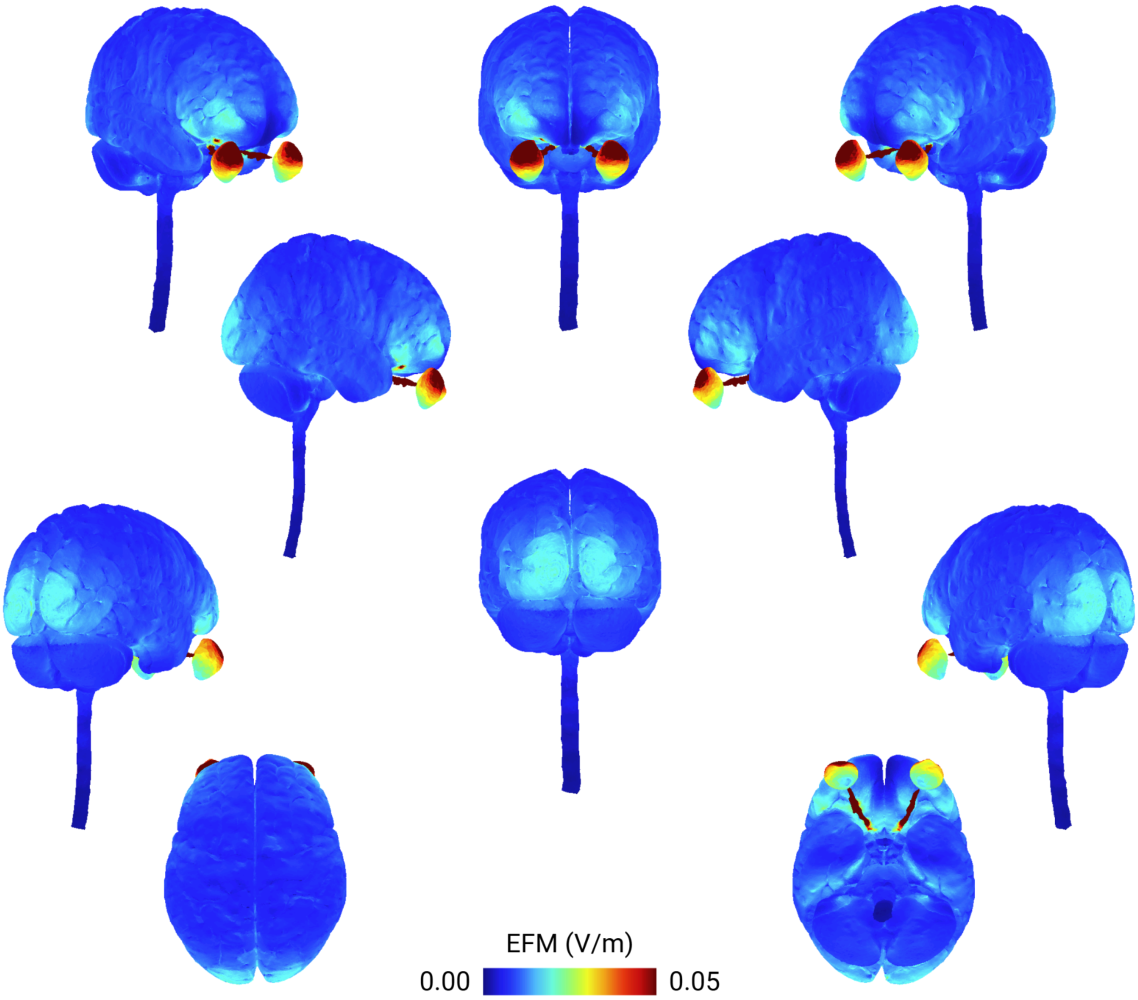

Figure 3-16. *Electric field magnitude (EFM, V/m) distribution in surface mesh representation across various brain views for bipolar frontal-occipital stimulation. The figure shows multiple perspectives, including lateral, superior, and inferior views, illustrating the spatial distribution and intensity of the electric field. The colormap ranges from 0.00 to 0.05 V/m, indicating areas of low (blue) to high (red) field magnitudes.*

The results presented in Table 3-3 summarize key volumetric statistics for the EFM under the bipolar frontal-occipital electrode configuration. Among the examined regions, the optic nerve exhibited the highest mean EFM value of 0.0407 V/m, with a total summed magnitude of 66.6 V/m across 1,637 voxels and a maximum voxel value of 0.1462 V/m. This result highlights the concentration of the electric field within deeper vision-related structures. The scalp, while having a lower mean EFM of 0.0062 V/m, displayed the largest summed EFM value at 75716.9 V/m due to its extensive coverage of 12,220,000 voxels, with a maximum voxel value of 1.0695 V/m. This indicates a significant but distributed field effect along the scalp surface, consistent with electrode placement.

The eyeballs showed a mean EFM of 0.0353 V/m, with a total sum of 619.2 V/m and a maximum voxel value of 0.0936 V/m distributed across 17,542 voxels, indicating a focused field impact in this area, primarily localized within the upper regions of the eyes. The rest of the brain, comprising gray ad white matter, demonstrated a mean EFM of 0.0096 V/m, a total summed magnitude of 15782.3 V/m, and a maximum voxel value of 0.0951 V/m across 1,638,915 voxels. This reflects a broader but less intense distribution compared to more localized regions such as the optic nerve and eyeballs.

Table 3-3. *Global and point statistics for the results of computer simulations of the induced electric field (IEF) expressed in volumetric form for the bipolar frontal-occipital configuration for the electric field magnitude (EFM, V/m). The table presents the mean EFM, the sum of magnitudes for all voxels, the standard deviation (SD), count (number of voxels), and maximum (Max) and minimum (Min) voxel values for the scalp and three regions of interest (ROIs): Eyeballs, Optic Nerve, and Rest of the Brain (comprising gray matter (GM) and white matter (WM)).*

Volume	**Electric Field Magnitude [V/m]**					**Voxel Count**
	Mean	**Sum**	**SD**	**Max**	**Min**	
Scalp	0.0062	75,716.9	0.0253	1.0695	0.0000	12,220,000
Eyeballs	0.0353	619.2	0.0100	0.0936	0.0161	17,542
Optic Nerve	0.0407	66.6	0.0285	0.1462	0.0068	1,637
Rest of the Brain	0.0096	15,782.3	0.0022	0.0951	0.0000	1,638,915

Figure 3-17A complements these findings by illustrating the mean EFM values with their associated standard deviations (SDs) across different regions. The optic nerve exhibited the highest mean EFM, followed by the eyeballs, while the scalp and the rest of the brain had comparatively lower mean values. Figure 3-17B displays the total summed EFM for each volume, with the scalp showing the largest cumulative value due to its large volumetric area. The inset provides a detailed view of the summed values for the eyeballs and optic nerve, emphasizing their localized but pronounced field effects. The EFM concentration was highest in regions with the lowest voxel counts. These results clearly demonstrate that the induced electric field (IEF) had the greatest impact on the optic nerve, followed by the eyeballs and cortical regions, particularly the occipital cortex. In comparison, the scalp showed a lower level of field intensity, indicating a more superficial and dispersed effect. This distribution emphasizes the field's concentration on critical structures along the visual pathway, while maintaining a moderate influence on the cortical surface and minimal impact on the outer scalp layer.

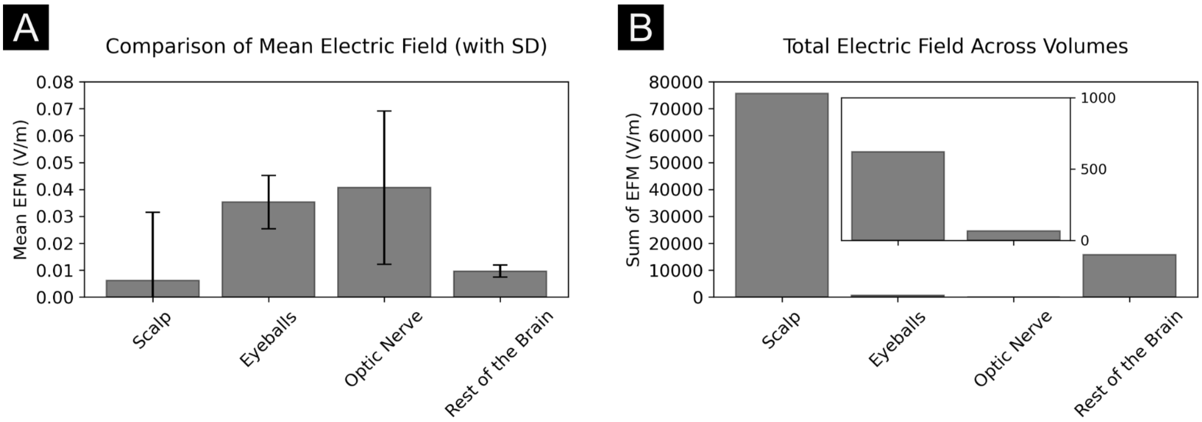

Figure 3-17. *Comparison of electric field magnitude (EFM, V/m) across different anatomical volumes for bipolar frontal-occipital configuration. Panel (**A**) displays the mean EFM with standard deviation (SD) error bars for each volume. Panel (**B**) illustrates the total sum of the EFM for each volume. The inset provides an enlarged view of the smaller sums observed for the eyeballs and optic nerve.*

Going further, let's look at the CDM for the bipolar frontal-occipital configuration. The surface distribution of CDM is illustrated in Figure 47. The anterior view of the head highlights strong edge effects and high CDM concentrations around the borders of the periorbital electrodes underneath, while the posterior view shows a less pronounced edge effect for the large occipital electrode embedded in a saline-soaked sponge due to the spread of the current density along bigger area. In the context of neural tissues, the highest CDM values were concentrated in the upper portions of the eyeballs, reflecting strong shunting effects from the upper periorbital electrodes. Additionally, relatively high CDM values were observed along the optic nerves, indicating significant penetration of the induced field into deeper visual structures along the visual pathway. In contrast, negligible CDM was observed in the remaining regions of the brain, underscoring the focused and localized nature of the stimulation effect on initial stages of the visual system. High surface current density was primarily localized near the electrodes and around the eyes, with minimal influence on adjacent brain regions.

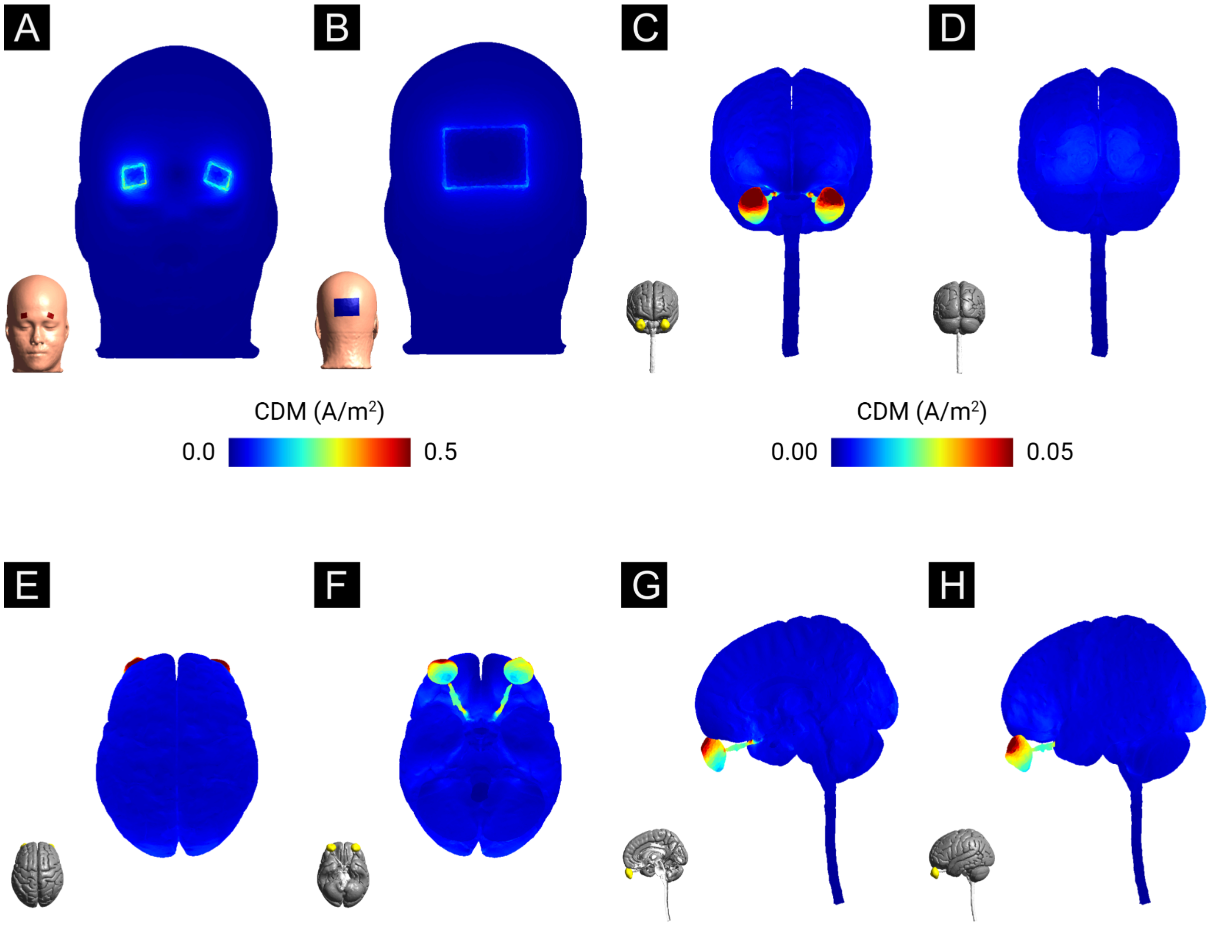

Figure 3-18. *Current density magnitude (CDM, A/m^2) surface distribution for the bipolar frontal-occipital configuration. (**A**) Anterior view of the head illustrating the placement of periorbital electrodes, with notable edge effects visible in the CDM distribution. (**B**) Posterior view of the head showing the much weaker edge effect of a large rubber-carbon electrode embedded in a sponge soaked in a salt solution. (**C-H**) Various views, including anterior, posterior, superior, inferior, sagittal, and temporal perspectives, depicting the distribution of current density within the eyeballs, gray matter (GM), and white matter (WM). Note that a different scale is used for panels (A-B) compared to panels (C-H) to appropriately reflect variations in CDM.*

Moving to the volumetric results (Table 3-4 and Figure 3-19), the scalp exhibited a lowest mean CDM of 0.0012 A/m^2, yet had the highest total current of 14,764.7 µA due to its extensive surface area (12,220,000 voxels). The maximum observed CDM on the scalp was 0.2086 A/m^2, primarily near the anterior electrode edges. The eyeballs demonstrated a highest mean CDM of 0.0329 A/m^2, with a total current of 577.1 µA distributed across 17,542 voxels, and a maximum value of 0.0688 A/m^2 concentrated in the upper regions. The optic nerve exhibited a second highest mean CDM of 0.0142 A/m^2, with a total current of 23.2 µA across 1,637 voxels, and a maximum of 0.0509 A/m^2, indicating effective targeting of deeper visual structures with the frontal-occipital configuration. The rest of the brain displayed a mean CDM of 0.0037 A/m^2, a total current of 6,063.0 µA, and a maximum value of 0.0331 A/m^2 over 1,638,915 voxels, indicating a broader but less intense distribution compared to the

EFM. This difference was particularly pronounced in the occipital cortex located directly beneath the occipital electrode.

Table 3-4. *Global and point statistics for the results of computer simulations of the induced current density (CDM, A/m^2) expressed in volumetric form for the bipolar frontal-occipital configuration. The table presents the mean CDM (A/m^2), the standard deviation (SD, A/m^2), the total number of voxels (Count), and the maximum (Max, A/m^2) and minimum (Min, A/m^2) values for the scalp and three regions of interest (ROIs): Eyeballs, Optic Nerve, and Rest of the Brain (comprising gray matter (GM) and white matter (WM)). Additionally, the table includes* I_{total} *(μA), representing the total current flowing through each region, calculated by summing the contributions from all voxels within the region based on the voxel area and current density magnitude.*

Volume	**Current Density Magnitude [A/m^2]**					**Voxel Count**
	Mean	**SD**	**Max**	**Min**	**I_{total}**	
Scalp	0.0012	0.0049	0.2086	0.0000	14,764.7	12,220,000
Eyeballs	0.0329	0.0093	0.0688	0.0150	577.1	17,542
Optic Nerve	0.0142	0.0099	0.0509	0.0024	23.2	1,637
Rest of the Brain	0.0037	0.0009	0.0331	0.0000	6,063.0	1,638,915

Lastly, the volumetric results are further contextualized in Figure 3-19. These findings indicate a distinct distribution of CDM across different anatomical regions, highlighting varying levels of exposure and concentration. The scalp, due to its extensive surface area, exhibited a broad distribution with relatively low intensity, emphasizing the influence of surface coverage on CDM summation (total current). The eyeballs, with their high mean CDM and concentrated maximums, particularly in the upper regions, reflect a more focused electric field impact, which could be highly relevant for precision-targeted interventions. The optic nerve showed significant CDM targeting, highlighting its susceptibility and the effectiveness of the frontal-occipital configuration in targeting this particular stage of the visual system. The rest of the brain displayed a broader yet less intense CDM distribution compared to the EFM, indicating a more diffuse effect and underscoring the strong influence of the anterior electrodes in close proximity to the eyeballs. It is worth noting that current density does not penetrate tissues as easily as the electric field, further emphasizing the targeted nature of the induced current.

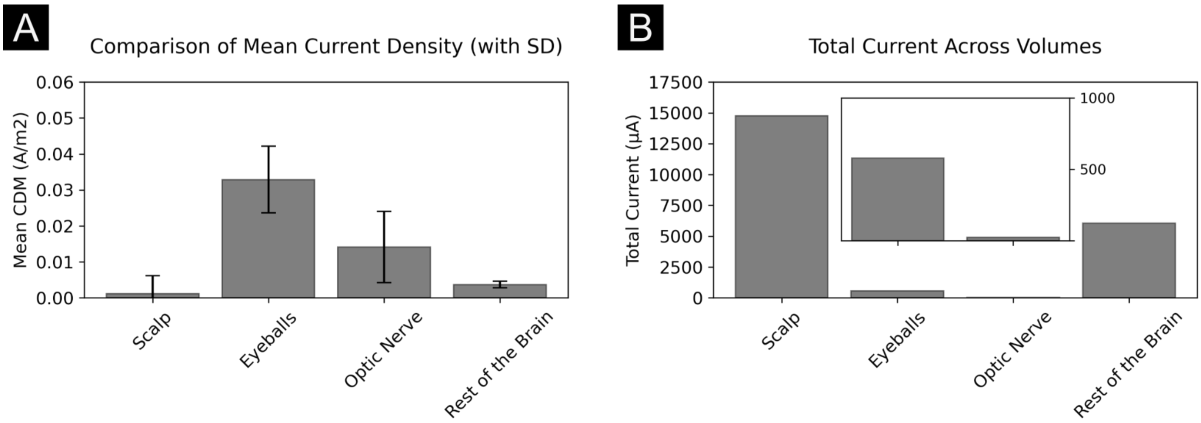

Figure 3-19. *Comparison of current density magnitude (CDM) and total current across different anatomical volumes for the bipolar frontal-occipital configuration. Panel (**A**) displays the mean CDM (A/m^2) with standard deviation (SD) error bars for each volume. Panel (**B**) illustrates the total current (I_{total}, µA) for each volume. The inset provides an enlarged view of the smaller total currents observed for the eyeballs and optic nerve.*

Comparison of Bipolar Periorbital and Frontal-Occipital Configurations

In this section, we compare the results of the bipolar periorbital and frontal-occipital electrode configurations, focusing on the surface and volumetric data for EFM and CDM. This comparison aims to illustrate the spatial distribution and intensity differences across key regions of interest, including the scalp, eyeballs, WM, and GM.

Table 3-5 presents the maximum EFM values for selected surfaces (meshes) across the compared configurations. The periorbital configuration demonstrated a maximum EFM of 1.7667 V/m on the scalp, which was higher than the 1.6173 V/m observed for the frontal-occipital configuration. This difference is likely due to the concentrated positioning of the periorbital electrodes, leading to increased localized intensity. Conversely, the frontal-occipital configuration exhibited higher maximum values in WM (0.2389 V/m) and GM (0.0666 V/m) compared to the periorbital setup, indicating a deeper penetration and distribution of the electric field. The eyeballs also exhibited a slightly higher maximum EFM for the periorbital configuration (0.0844 V/m) compared to 0.0797 V/m for the frontal-occipital setup, aligning with the primary targeting of the very beginning of the visual pathways by the former.

***Table 3-5.** Electric field magnitude (EFM, V/m) maxima for selected surfaces (meshes) for compared configurations.*

Configuration	**Surface**			
	Scalp	**Eyeballs**	**WM**	**GM**
Periorbital	1.7667	0.0844	0.0749	0.0225
Frontal-Occipital	1.6173	0.0797	0.2389	0.0666

Moving forward, Figure 3-20 provides a detailed visualization of the volumetric differences in EFM for the two configurations. Figure 3-20A illustrates the spatial distribution of the electric field, highlighting the concentrated impact of the periorbital electrodes on the eyeballs compared to the broader and deeper influence of the frontal-occipital electrodes on various stages of the visual pathway, including the eyeballs, optic nerves, and occipital cortex. The difference map in Figure 3-20B emphasizes the contrast in field intensity between the configurations, while the inset bar chart quantifies the mean differences in EFM across key anatomical regions for both setups, underscoring the greater impact of the periorbital configuration on the eyeballs and the more pronounced effect of the frontal-occipital configuration on the optic nerves and the rest of the brain.

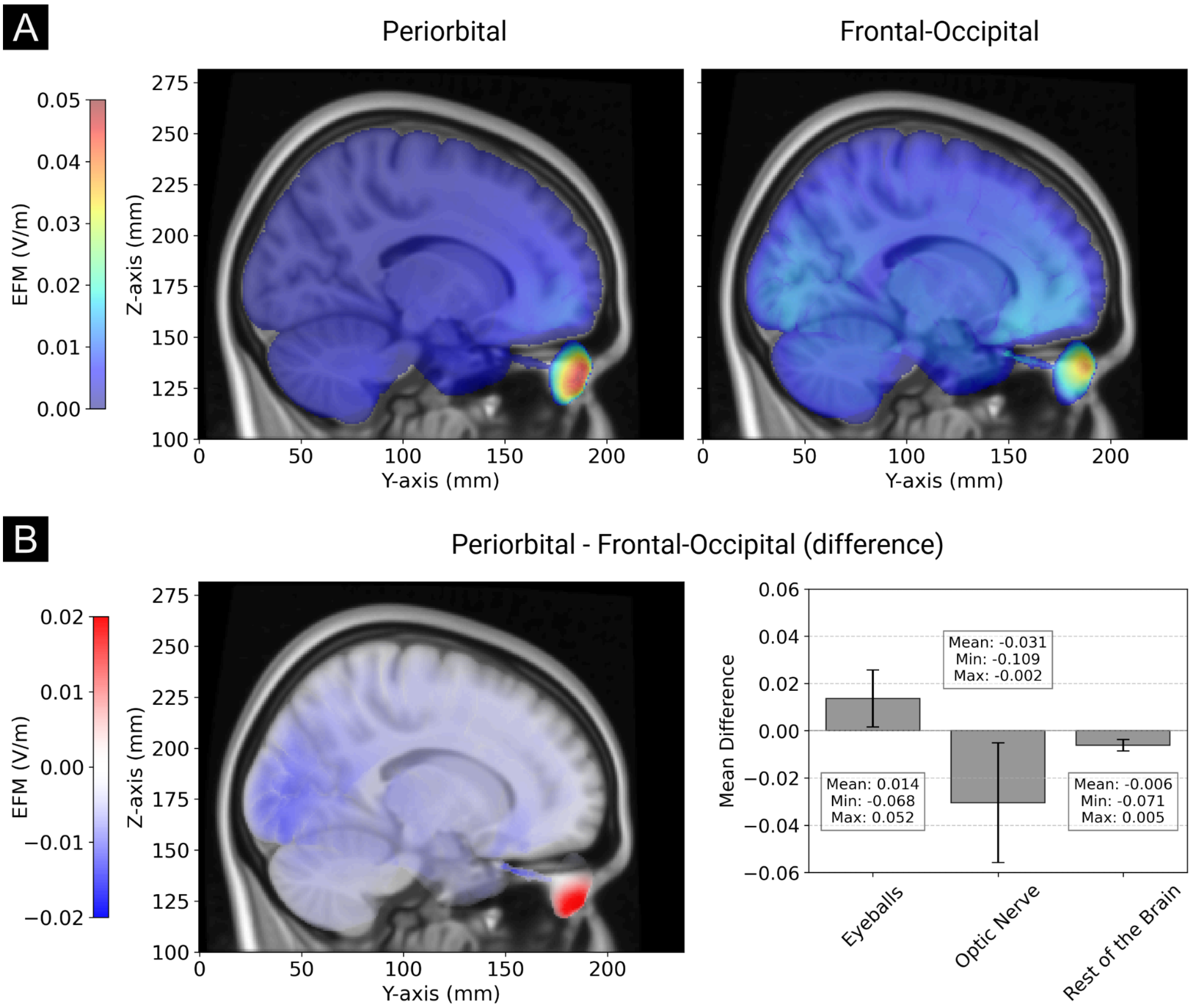

Figure 3-20. *Differences in electric field magnitude (EFM, V/m) for two stimulation electrode locations: periorbital and frontal-occipital. (**A**) Visualization of the electric field distribution for periorbital (left) and frontal-occipital (right) electrode configurations, highlighting spatial variations in field intensity across brain regions. The method of visualization is the same as that described in the description of Figure 3-16A. (**B**) Difference map illustrating the contrast in EFM between the two configurations (periorbital minus frontal-occipital). The inset bar chart quantifies mean differences in EFM for specific anatomical regions: eyeballs, optic nerve, and rest of the brain, with mean values, minima, maxima, and standard deviations indicated.*

Furthermore, Table 3-6 highlights the maximum CDM values for the selected surfaces. The periorbital configuration showed a maximum CDM of 0.3445 A/m² on the scalp, compared to 0.3154 A/m² for the frontal-occipital configuration, again reflecting the localized intensity near the periorbital electrodes, but as we recall, the highest values of current density for the latter configuration were also observed for the front electrodes. The eyeballs exhibited slightly higher maximum CDM values under the periorbital setup (0.0787 A/m²) compared to 0.0743 A/m² for the frontal-occipital configuration. In contrast, the frontal-occipital configuration demonstrated higher maximum CDM values in WM (0.0831 A/m²) and GM (0.0279 A/m²), consistent with its broader but deeper field distribution.

Table 3-6. *Current density magnitude (CDM, A/m^2) maxima for selected surfaces (meshes) for compared configurations.*

Configuration	**Surface**			
	Scalp	**Eyeballs**	**WM**	**GM**
Periorbital	0.3445	0.0787	0.0260	0.0094
Frontal-Occipital	0.3154	0.0743	0.0831	0.0279

In addition, Figure 3-21 presents the volumetric differences in CDM for the two configurations. Panel A visualizes the distribution of CDM, with the periorbital configuration showing concentrated effects for the eyes anterior-middle regions, while the frontal-occipital configuration exhibits a broader spread across eyes and optic nerves, but less intense in the rest of the brain as for the EFM. The difference map in Panel B illustrates the contrast between configurations, with the periorbital setup demonstrating once more a stronger impact on the eyeballs, while the frontal-occipital configuration displays a stronger impact on the optic nerves and a more diffuse influence across the rest of the brain. The inset bar chart quantifies the mean differences in CDM, highlighting the periorbital configuration's targeted focus compared to the broader distribution seen with the frontal-occipital setup and targeting deeper parts of the visual pathway.

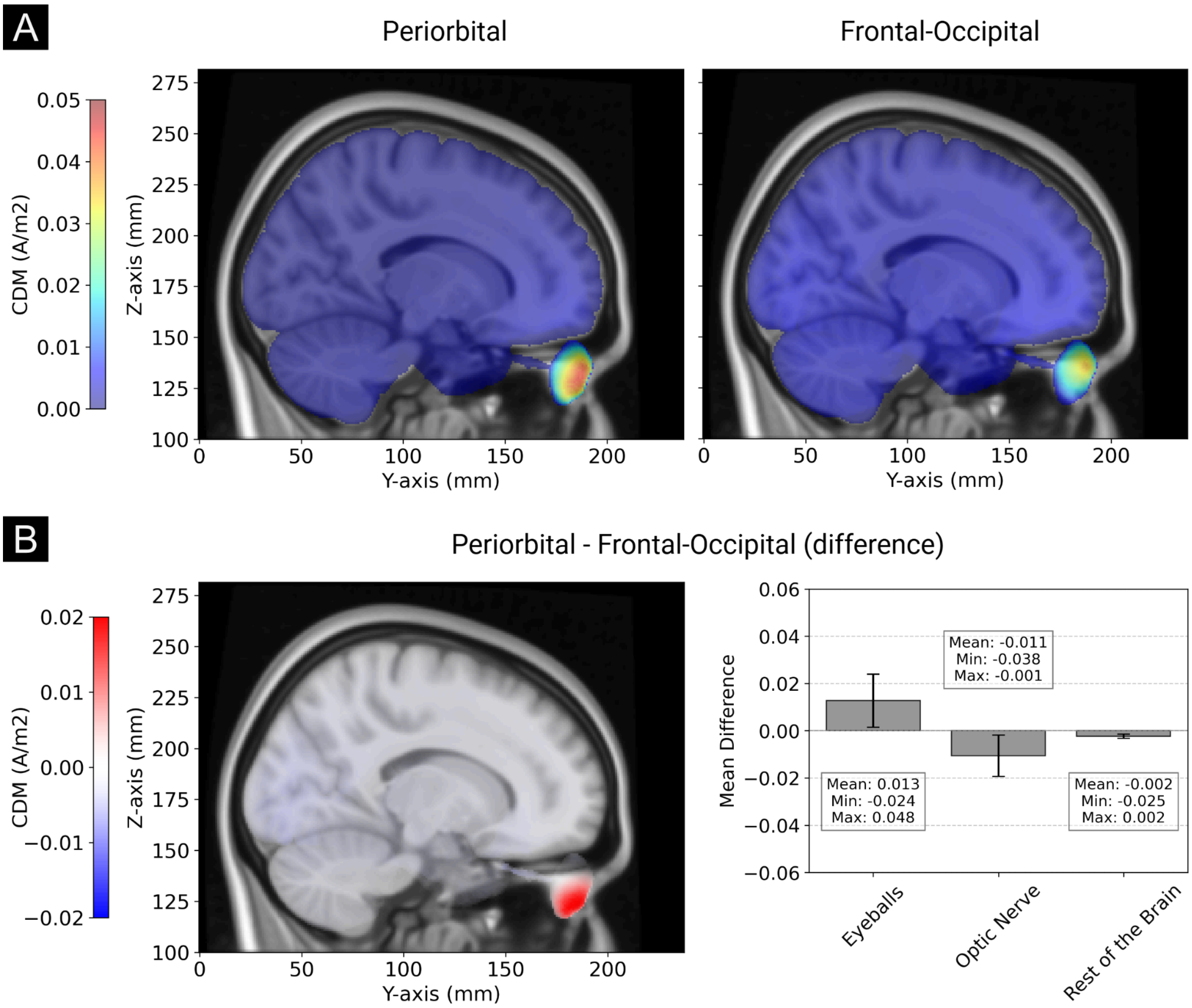

Figure 3-21. *Differences in current density magnitude (CDM, A/m^2) for two stimulation electrode locations: periorbital and frontal-occipital. (**A**) Visualization of the CDM distribution for periorbital (left) and frontal-occipital (right) electrode configurations, highlighting spatial variations in field intensity across brain regions. (**B**) Difference map illustrating the contrast in CDM between the two configurations (periorbital minus frontal-occipital). The inset bar chart quantifies mean differences in CDM for specific anatomical regions, including the eyeballs, optic nerve, and the rest of the brain, with mean values, minima, maxima, and standard deviations indicated. Created using the same methodology as Figure 3-20.*

Finally, the statistical analysis comparing the EFM distributions for two electrode configurations (periorbital and frontal-occipital) across three different ROIs - eyeballs, optic nerve, and the rest of the brain - revealed significant differences. For the eyeballs, the Kolmogorov-Smirnov (KS) test for comparison of the entire distribution functions of two datasets indicated a significant difference between the two configurations, with a KS statistic of 0.4775 and a p-value < 0.001, highlighting distinct distribution profiles. Similarly, the optic nerve ROI exhibited significant differences in EFM distributions, as evidenced by a KS statistic of 0.6005 and a p-value < 0.001, indicating a marked divergence in how the electric field affects this structure under each configuration. The rest of the brain also showed significant differences, with a KS statistic of 0.8987 and a p-value < 0.001, reflecting broader but substantial alterations in EFM distribution (Figure 3-22A).

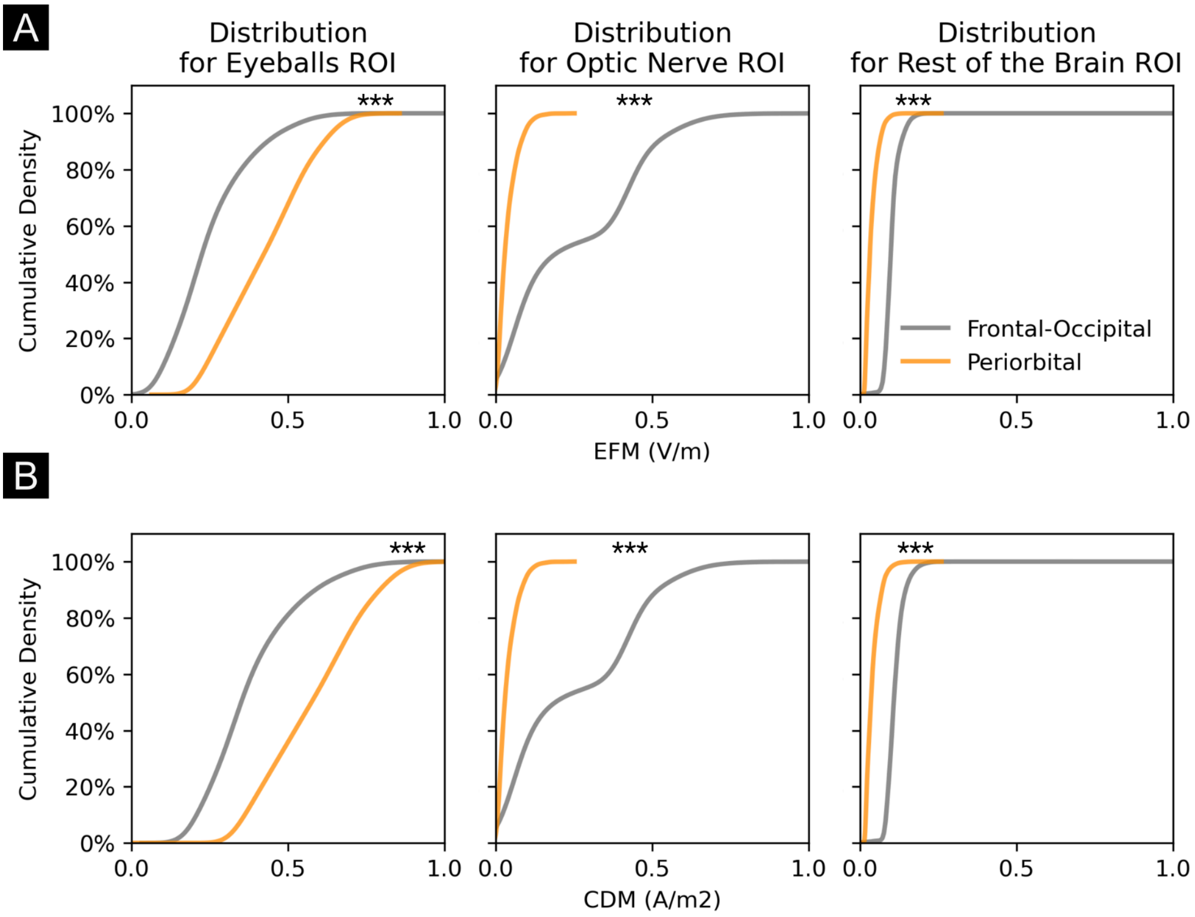

*Figure 3-22. Kernel density estimation (KDE) cumulative density plots illustrating the distribution of flattened volume values for different regions of interest (ROIs) across two electrode configurations: periorbital (orange) and frontal-occipital (gray). (A) The plots depict the normalized distributions of electric field magnitude (EFM) for the eyeballs, optic nerve, and rest of the brain. (B) Similarly, cumulative density plots for current density magnitude (CDM) show distinct distribution characteristics for each configuration, highlighting significant contrasts in current density targeting across the ROIs. All values are normalized for total minimum and maximum across both configurations, and statistical significance is denoted by Kolmogorov-Smirnov tests with ***p < 0.001 for all comparisons.*

Parallel analyses of CDM also showed significant differences across the same ROIs. For the eyeballs, the KS test statistic was 0.4776 (p-value < 0.001), confirming significant variation in CDM distributions between the configurations. The optic nerve presented a KS statistic of 0.6005 (p-value < 0.001), consistent with observed shifts in field targeting, while the rest of the brain showed a KS statistic of 0.8970 (p-value < 0.001), further demonstrating pronounced changes in current density spread across broader brain regions (Figure 3-22B). These results collectively underscore the substantial impact of electrode configuration on both electric field and current density distributions, emphasizing differential targeting and intensity effects within considered neural ROIs.

More specifically, based on the distributions and their statistical comparisons, the two configurations appear to differ across each of the three ROIs. For the periorbital configuration, the eyeballs exhibit higher values, while the optic nerve and the rest of the brain show lower values for both EFM and CDM.

Key takeaways:

1. Localized vs. broad effects: The periorbital configuration concentrated its impact on the anterior-middle regions of the eyeballs, while the frontal-occipital setup exhibited broader influence across the eyeballs, optic nerves, and occipital cortex.
2. The beginning of the visual pathway vs. the entire visual pathway: The periorbital configuration is well-suited for stimulating the beginning of the visual pathway, while the frontal-occipital configuration effectively stimulates the entire visual pathway, extending from the eyes to the occipital cortex.
3. EFM vs. CDM: In the periorbital configuration, the electric field and current are primarily localized similarly around the eyes. In contrast, with the frontal-occipital configuration, EFM is more diffuse, affecting the eyes, optic nerve, and occipital cortex, while CDM is primarily concentrated in the eyes and optic nerve.

Parameters of Current Stimulation Selected for Experimental Testing

We ultimately selected the periorbital electrode configuration for the experimental study, utilizing the electrodes, their placement, and the single current pulses discussed and tested in the computer simulations. This configuration was chosen due to its ability to maximize the induced electric field's effects on the eyeballs, which serve as the origin of the visual pathway. In the Study 1 we aimed to test the capability of pPCS in the form of single current pulses in activating retinal ganglion cells and inducing retinal phosphene generation and their perception. Current pulses ranged from 10 ms @100 μA to 100 ms @300 μA. Data analysis was focused on identifying the optimal parameters for phosphene generation. In the Study 2 Specifically, we aimed to explore how single pulses applied periorbitally could modulate the processing of subsequent visual stimuli, thereby assessing the visual information modulation potential of current stimulation in this form.

Responses to Single-Pulse Periorbital Current and LED Stimulation (Study 1)

Phosphene Detection Threshold

The choice of a stimulation intensity is defined to effectively evoke desired responses without leading to adverse effects. It is thus necessary to estimate the threshold of such effective stimulation. There is no clear and definitive information in the literature regarding what constitutes the phosphene detection threshold. It is most commonly defined based on behavioral responses of individuals subjected to stimulation (Naycheva et al., 2012) or on the electrophysiological responses of the visual cortex (Taylor et al., 2010). Therefore, in our study, we adopted the behavioral threshold at 5% of the valid response rate. For the electrophysiological response, we defined the threshold as 10% of the maximum response in the 150-300 ms window for the occipital cluster, where the maximum response corresponds to the one elicited by the visual (LED) stimulus.

The difference arises from the nature of the responses being measured. Behavioral responses, such as the valid response rate, are absolute and straightforward to interpret, as they directly reflect participants' observable actions, e.g., reporting phosphene perception. These responses inherently provide a clear threshold, such as 5% of trials, below which the stimulus can be considered undetectable.

In contrast, electrophysiological responses require the establishment of a reference point to determine the threshold. Unlike behavioral responses, EEG signals are measured in relative terms and are influenced by background noise and variability in cortical activity. To account for this, we defined the threshold as 10% of the maximum response observed in the 150-300 ms window for the occipital cluster, where the maximum corresponds to the response elicited by the LED stimulus. This approach allows us to standardize the threshold in the absence of an absolute measure, ensuring that the electrophysiological response is evaluated relative to a clear and biologically meaningful reference point.

In the behavioral part of our Study 1, the light stimulus was detected with very high accuracy and there was negligible proportion of invalid responses across all trial types indicating the participants' ability to maintain focus during the procedure, and respond appropriately (Figure 3-23 and Table 3-7). The detection of electrically evoked phosphenes depended on the duration and the amplitude of stimulating current. There were almost no valid responses for shortest (10 ms) impulses at lower amplitudes (with slightly better performance at 300 µA, however still not reaching the 5% threshold) and almost perfect performance was noted for longer 200 and 300 µA pulses.

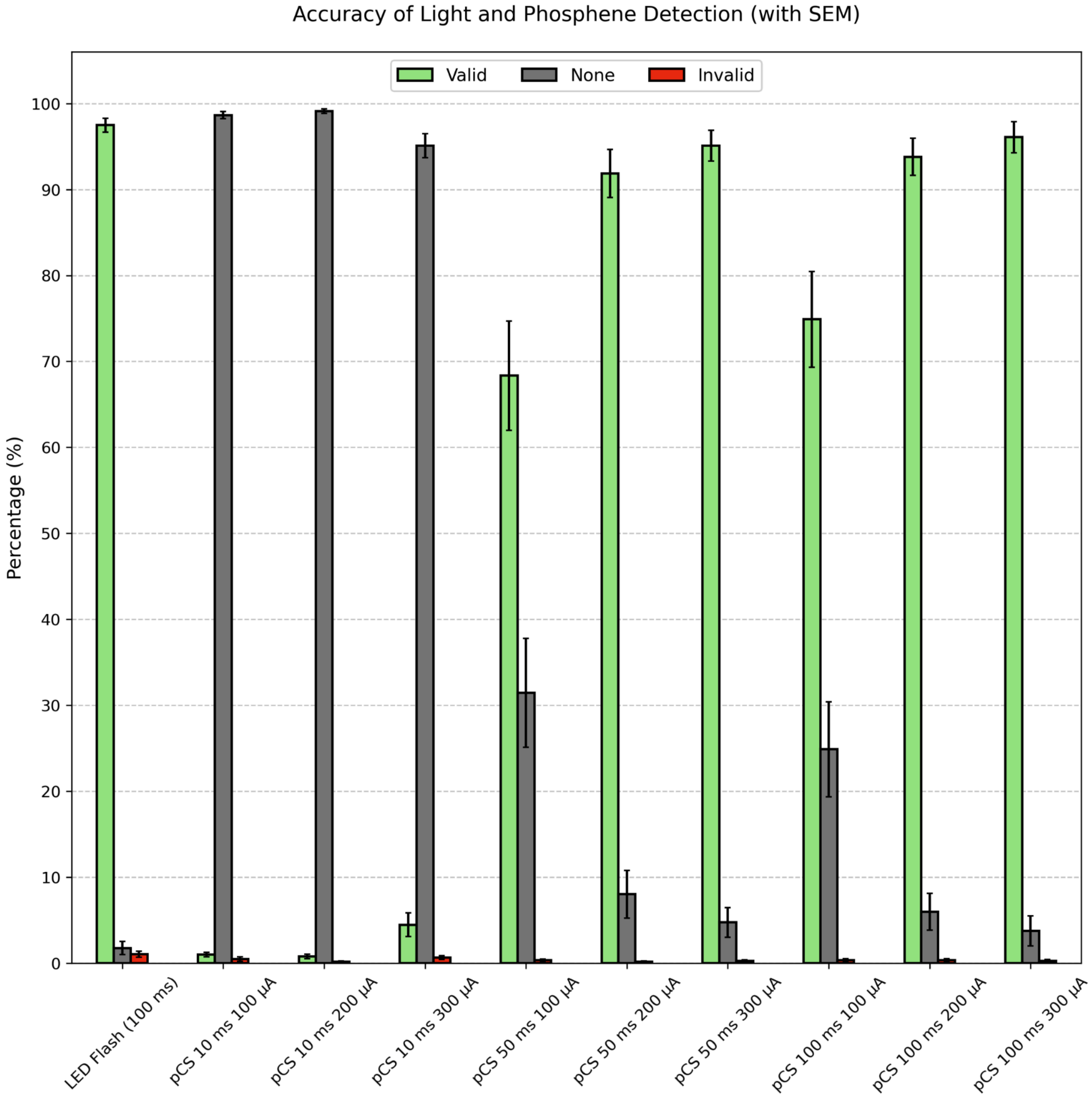

Figure 3-23. *Accuracy of stimulus detection. The percentages for valid, none, and invalid response types. Trial types include light stimulus -"LED Flash (100 ms)" and pCS impulses with differing durations (10, 50, 100 ms) and amplitudes (100, 200, 300 µA). Data presented as mean with SEM, for statistical description see Table 3-7.*

Table 3-7. *Descriptive statistics for the percentage of valid responses across different trial types.*

Statistic	**Trial Type**									
	LED	**10 ms**			**50 ms**			**100 ms**		
		100 µA	**200 µA**	**300 µA**	**100 µA**	**200 µA**	**300 µA**	**100 µA**	**200 µA**	**300 µA**
N	19	19	19	19	19	19	19	19	19	19
Median	98.9	1.1	0.0	2.2	71.1	96.7	98.9	81.1	97.8	98.9
Mean	97.5	1.0	0.8	4.4	68.3	91.9	95.1	74.9	93.8	96.1
SEM	0.8	0.3	0.3	1.4	6.4	2.8	1.8	5.6	2.2	1.8
SD	3.6	1.2	1.1	6.0	27.7	12.1	7.8	24.3	9.4	7.9
Minimum	87.8	0.0	0.0	0.0	2.2	57.8	75.6	18.9	68.9	72.2
Maximum	100.0	3.4	3.3	24.4	98.9	100.0	100.0	100.0	100.0	100.0

SEM - standard error of the mean; SD - standard deviation

To test statistical significance of the noted differences we conducted a one-way ANOVA for “Valid Response Rate” as dependent variable and “Trial Type” as fixed factor. The results of Welch's ANOVA indicate a statistically significant effect of trial type on the percentage of valid responses ($F(9, 70597) = 2152.22$, p-value < 0.001, $\eta^2 = 0.907$). The Welch's test was chosen due to a violation of the homogeneity of variances assumption, as confirmed by a significant Levene’s test. The post-hoc tests were performed with Tukey's correction to control for multiple comparisons with LED trials as a baseline versus pPCS types (Table 3-8). LED flash demonstrated a substantially higher rate of valid responses compared to shorter-duration pPCS (10 ms) across all current amplitudes. LED flash responses were also significantly better (but to a smaller extent) than 50 ms 100 µA and 100 ms 100 µA pPCS. However, comparisons between LED flash and the stronger pPCS pulses (50 ms and 100 ms with the 200 and 300 µA) did not reveal significant differences. In the context of comparisons between pulses, most of them were statistically significantly different. There were no statistically significant differences, however, between 50 ms 100 µA and 100 ms 100 µA stimuli, as well as between other pairs with the same amplitudes for these durations. This indicates that the 50 ms and 100 ms pulses generate similar valid response rates, despite slight numerical differences observed at first glance for valid response rates. Furthermore, no significant differences were found between 50 ms 200 µA and 300 µA stimuli or between 100 ms 200 µA and 300 µA stimuli. The trial types did not differ significantly neither from the LED flash, suggesting that pPCS with these specific parameters produced an effect similar to an external visual stimulus.

Table 3-8. *Post-hoc comparisons between trial types using Tukey's correction. The table presents pairwise differences in valid response rates, including the mean difference, t-value, Cohen's d (effect size), and adjusted p-value.*

Comparisons - Trial Types			**Mean Difference**	**t**	**Cohen's d**	**p-value$_{tukey}$**
LED versus:	10 ms	100 μA	96.49	22.37	7.26	< .001***
	10 ms	200 μA	96.73	22.42	7.27	< .001***
	10 ms	300 μA	93.04	21.57	7.00	< .001***
	50 ms	100 μA	29.15	6.76	2.19	< .001***
	50 ms	200 μA	5.61	1.30	0.42	0.952
	50 ms	300 μA	2.40	0.56	0.18	1.000
	100 ms	100 μA	22.59	5.24	1.70	< .001***
	100 ms	200 μA	3.68	0.85	0.28	0.998
	100 ms	300 μA	1.40	0.33	0.11	1.000

*** - p-value < 0.001

As a next analytical step the Naka-Rushton algorithm was used to fit the data and to fully characterize the non-linear, saturating nature of valid response rates in response to specific pulse characteristics.

First we implemented the standard single-factor Naka-Rushton function, (as described in the Materials and Methods section), with the total charge per pulse as the independent variable in the function. This parameter, calculated from the duration and amplitude of the current pulses, reflects the total stimulus intensity hypothesized to influence the valid response rate. The purpose of fitting the Naka-Rushton function to the valid response rate data was to establish a relationship between total charge per pulse and response probability, aiming to identify the current pulse parameters that would yield a 50% probability of a valid response. The results revealed a clear dependency between pulse amplitude and the required pulse duration to achieve specific response probabilities; however, we have reservations about these findings, which will be discussed shortly. For a 50% modeled response, the pulse duration was 43.70 ms at 100 µA, 22.31 ms at 200 µA, and 14.99 ms at 300 µA. When targeting a 90% modeled response, the required durations increased to 83.24 ms at 100 µA, 42.42 ms at 200 µA, and 28.54 ms at 300 µA. Additionally, for a 5% response threshold, the pulse durations were 29.48 ms at 100 µA, 14.98 ms at 200 µA, and 10.06 ms at 300 µA. It is important to note that these values represent averages calculated for amplitude ranges of ±5 µA around the specified amplitudes.

The function performed well in explaining the data, achieving a goodness-of-fit R^2 of 0.9797 and an average difference between predicted and actual valid response rates of 3.54% (see left panel in

Figure 2-25 and Table 3-9). However, the function was not entirely accurate. For instance, it predicted identical response rates for 50 ms 200 µA and 100 ms 100 µA pulses, despite the actual valid response rates differing significantly: 91.88% for the shorter pulse and 74.90% for the longer pulse. This discrepancy is likely due to both pulses having the same total charge per pulse (3.54 µC). Total charge alone failed to capture important dynamics in how stimulus parameters influence the activity of the visual system and in result the valid response rates to phosphenes. Specifically, this indicates the presence of additional physiologically or behaviorally relevant factors, such as the temporal profile of charge delivery and the amplitude of the stimulus. To address these shortcomings, the Naka-Rushton framework was expanded to incorporate three key factors: total charge, amplitude, and duration. Total charge ($Q(d, A)$) serves as the fundamental driver of response thresholds and saturation, with higher charges typically eliciting stronger responses until saturation occurs. Amplitude (A) is crucial, as higher amplitudes delivered over shorter durations may increase effectiveness by rapidly activating more responsive neural elements. Finally, duration (d) might diminish effectiveness when the same total charge is spread over a longer time, potentially due to neural adaptation or suboptimal recruitment dynamics. This extended framework could be mathematically expressed as a custom three-factor Naka-Rushton-like model, better equipped to capture the nuances of stimulus-response dynamics.

$$f(d, A) = r_{max} + r_{base}\left(\frac{Q(d,A)^n}{Q(d,A)^n+\sigma_Q^n}\right)\left(\frac{A^m}{A^m+\sigma_A^m}\right)\left(\frac{\delta^p}{\delta^p+d^p}\right)$$

The first component of the model, enclosed in the initial parentheses, mirrors the single-factor Naka-Rushton function that uses total charge per pulse as the primary factor. Next, an amplitude-specific module is introduced to account for the increased effectiveness of higher amplitudes at the same charge. The final module introduces a saturating function that decreases as the duration d increases. The parameter δ serves as a "reference duration," determining the point at which the duration factor significantly diminishes the pulse's effectiveness. For very short durations ($d < \delta$), this ratio remains close to 1, emphasizing the heightened efficacy of short, high-amplitude pulses. Conversely, for longer durations, the factor decreases, reflecting the idea that distributing the same total charge over a longer time period is less effective in eliciting a strong response. This captures a key principle of temporal dynamics in neural stimulation. While much of the source code developed for this thesis is available in the accompanying repository, the importance of the proposed three-factor Naka-Rushton function warrants its explicit presentation here, particularly with respect to the implementation details of the duration saturation function (Figure 3-24).

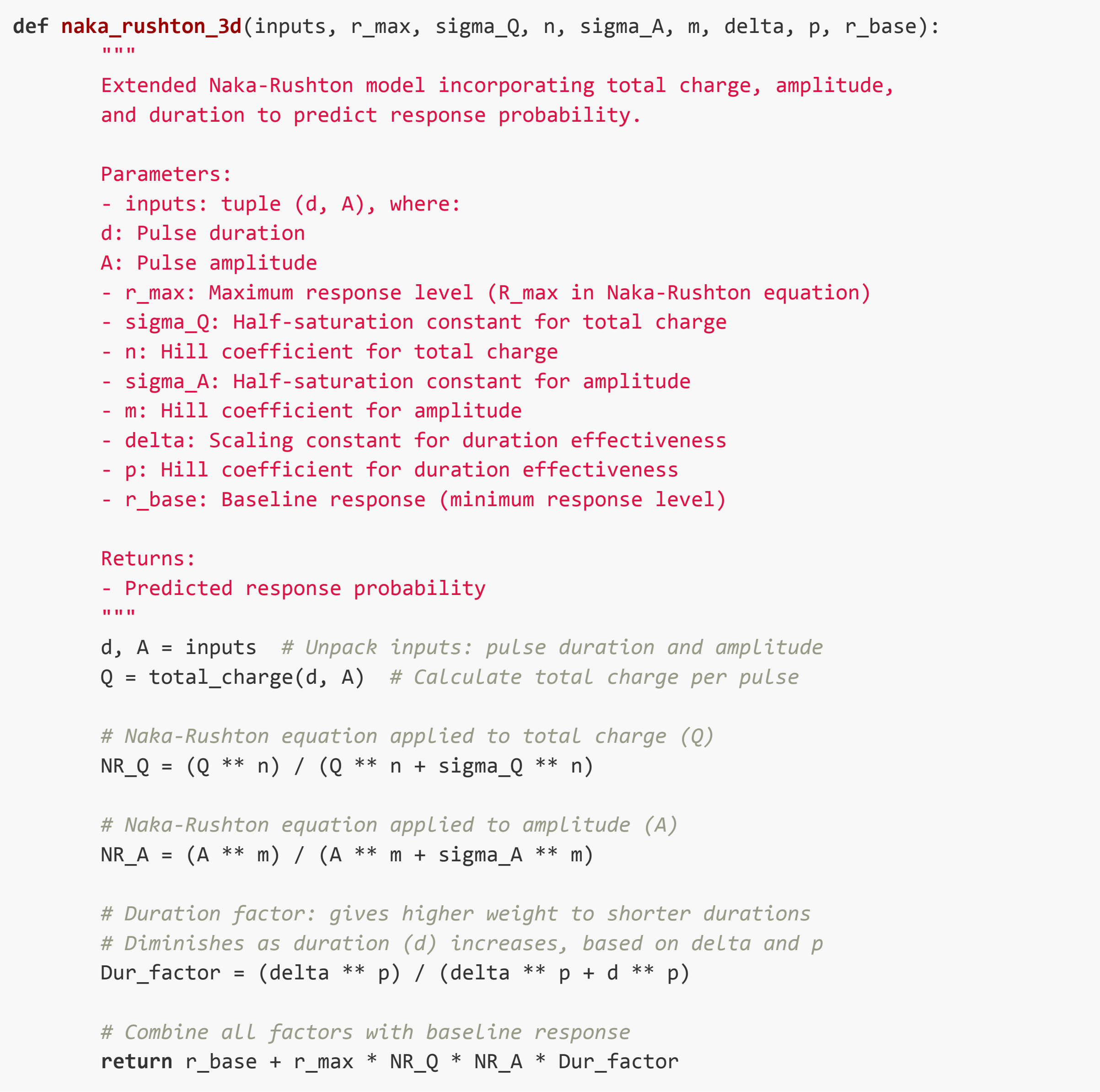

```python
def naka_rushton_3d(inputs, r_max, sigma_Q, n, sigma_A, m, delta, p, r_base):
        """
        Extended Naka-Rushton model incorporating total charge, amplitude,
        and duration to predict response probability.

        Parameters:
        - inputs: tuple (d, A), where:
        d: Pulse duration
        A: Pulse amplitude
        - r_max: Maximum response level (R_max in Naka-Rushton equation)
        - sigma_Q: Half-saturation constant for total charge
        - n: Hill coefficient for total charge
        - sigma_A: Half-saturation constant for amplitude
        - m: Hill coefficient for amplitude
        - delta: Scaling constant for duration effectiveness
        - p: Hill coefficient for duration effectiveness
        - r_base: Baseline response (minimum response level)

        Returns:
        - Predicted response probability
        """
        d, A = inputs  # Unpack inputs: pulse duration and amplitude
        Q = total_charge(d, A)  # Calculate total charge per pulse

        # Naka-Rushton equation applied to total charge (Q)
        NR_Q = (Q ** n) / (Q ** n + sigma_Q ** n)

        # Naka-Rushton equation applied to amplitude (A)
        NR_A = (A ** m) / (A ** m + sigma_A ** m)

        # Duration factor: gives higher weight to shorter durations
        # Diminishes as duration (d) increases, based on delta and p
        Dur_factor = (delta ** p) / (delta ** p + d ** p)

        # Combine all factors with baseline response
        return r_base + r_max * NR_Q * NR_A * Dur_factor
```

Figure 3-24. *Implementation of the extended three-factor Naka-Rushton function, modeling response probabilities as a function of total charge, amplitude, and duration. The model integrates separate Naka-Rushton equations for total charge and amplitude, with a duration-dependent scaling factor to account for the enhanced effectiveness of shorter pulses.*

The three-factor custom version of the Naka-Rushton function fitted the experimental data almost perfectly (right panel in Figure 3-25 and Table 3-9). It achieved a goodness-of-fit R^2 of 1.000 (intentionally reported to four decimal places) and an average difference between predicted and actual valid response rates of just 0.14%. Thus, with this three-factor model, we can better differentiate conditions that have the same total charge but differ in how that charge is delivered, hopefully providing more accurate predictions.

The comparison between the single-factor and three-factor refined Naka-Rushton models highlights notable differences in the predicted pulse durations required to achieve 50% and 90% response probabilities. For 50% responses, the three-factor model predicted shorter durations compared to the single-factor model: 13.60 ms for 300 µA (a reduction of 9.27%), 20.26 ms for 200 µA (a reduction of 9.19%), and 41.54 ms for 100 µA (a reduction of 4.94%). For 90% responses, the differences were more pronounced, with the three-factor model predicting 18.37 ms for 300 µA (a reduction of 35.63%) and 29.86 ms for 200 µA (a reduction of 29.63%). It is worth noting that the three-factor model did not provide a value for a 90% response at 100 µA, as the maximum modeled response for a 100 ms pulse at 100 µA was approximately 75%, making a 90% response unachievable within the modeled parameter range. For a 5% response threshold, the three-factor model predicted pulse durations of 10.15 ms for 300 µA, 15.25 ms for 200 µA, and 30.42 ms for 100 µA. Compared to the single-factor model, these represent percentage increases of 0.90% (300 µA), 1.80% (200 µA), and 3.19% (100 µA). This difference underscores the importance of incorporating multiple factors to refine predictive accuracy of the model and account for non-linear interactions between these parameters. However, it is important to note, that due to the low density of the data matrix (three pulse durations and three amplitude levels), this part of the calculations has a low level of reliability, and more data points are required to achieve robust and reliable results for the predictive power of the model.

The question remains how this model will perform in future experimental studies involving different pulse durations and amplitudes, as well as with other participants and under varying experimental conditions. The current implementation of the model (source code) is designed to work with data in percentage form. However, the model can be easily adapted to accommodate data in other formats. Additionally, as demonstrated later with the EEG data (Figure 3-31C), the data can be normalized to a percentage scale using an external reference maximum, such as the response to visual stimulation, when fitting the model to brain activity data from electrical stimulation.

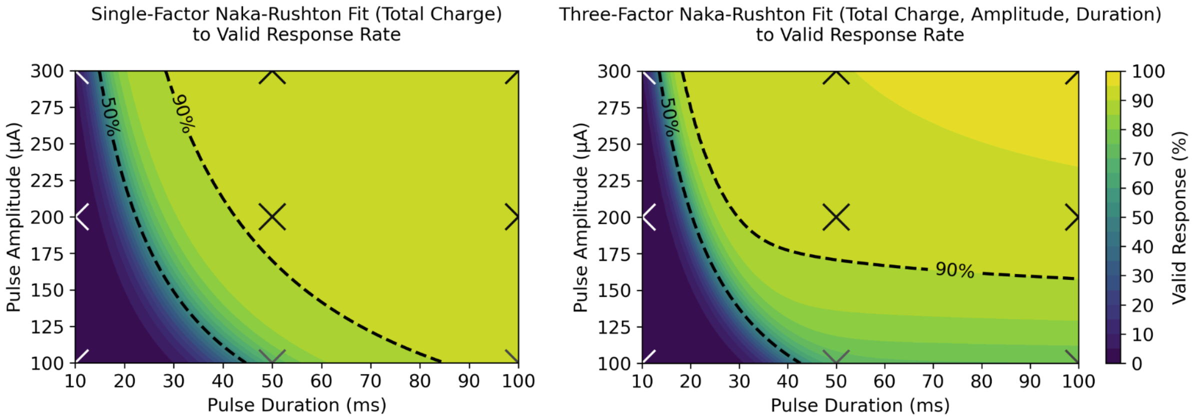

Figure 3-25. Comparison of single-factor and three-factor Naka-Rushton fits for predicting valid response rates. The panel on the left presents the single-factor Naka-Rushton fit, using total charge per pulse (a product of sinusoidal, biphasic pulse duration and amplitude) as the sole predictor of valid response rates for phosphene perception. The panel on the right showcases the extended three-factor Naka-Rushton fit, which incorporates total charge, amplitude, and duration as predictors. The contour maps illustrate the percentage of predicted valid responses, with color bars indicating the response rate levels. The contour map levels are spaced by 5% increments, resulting in 20 levels. Dashed black lines mark the 50% and 90% fitted valid response thresholds, highlighting the interplay between pulse duration and amplitude. Observed data points are overlaid for reference (X's).

***Table 3-9.** Comparison of predicted and actual valid response rates (%) for the single-factor and three-factor Naka-Rushton models. The single-factor model uses total charge per pulse as the sole predictor, while the three-factor model incorporates total charge, amplitude, and duration. Average absolute differences between the actual data and the fitted data highlight a clear distinction between the models, with the single-factor Naka-Rushton model showing a larger difference of 3.54 compared to the much smaller difference of 0.14 for the three-factor model. Notably, the bolding and underlining of selected values draw particular attention to the differences observed for the 100 ms 100 µA pulse, which has the same total charge as the 50 ms 200 µA pulse.*

Function Type	**Values**	**Trial Type**								
		10 ms			**50 ms**			**100 ms**		
		100 µA	**200 µA**	**300 µA**	**100 µA**	**200 µA**	**300 µA**	**100 µA**	**200 µA**	**300 µA**
Single-Factor	Predictions	0.56	0.74	4.96	68.12	90.31	90.43	90.31	90.43	90.43
	Actual	0.99	0.76	4.44	68.34	91.88	95.09	74.90	93.81	96.08
	Difference	-0.44	-0.02	0.52	-0.22	-1.56	-4.66	**<u>15.41</u>**	-3.38	-5.65
Three-Factor	Predictions	0.86	0.90	4.44	68.34	92.12	94.85	74.90	93.56	96.32
	Actual	0.99	0.76	4.44	68.34	91.88	95.09	74.90	93.81	96.08
	Difference	-0.14	0.14	0.00	0.00	0.25	-0.24	**<u>0.00</u>**	-0.25	0.24

Key takeaways:

1. Assuming a 5% valid response rate as the threshold for phosphene perception, modeled data suggests required pulse durations of 10.15 ms for 300 µA, 15.25 ms for 200 µA, and 30.42 ms for 100 µA.
2. Longer pulse durations demonstrated response saturation, particularly evident when comparing medium and long pulses.
3. Higher amplitudes consistently elicited strong responses, similar to those induced by light stimuli, highlighting their effectiveness.
4. The standard Naka-Rushton model provided reasonable predictions but failed to account for differences linked to the timing of charge delivery.
5. A custom three-factor model, integrating total charge, amplitude, and duration, significantly improved the accuracy of predictions, emphasizing the role of amplitude in shorter pulses.

Response Times to Stimuli

The next step involved examining the response times to light stimulus and electrically evoked phosphenes. Trials with non-effective 10 ms pulses at 100 µA and 200 µA were excluded from the analysis and only valid responses were estimated from other trial types. The valid response time values for the included trial types, along with the other basic descriptive statistics, are provided in Table 3-10 and plotted in Figure 3-27A,B. The shortest response time (338.22 ± 18.53 ms; mean ± SEM) was observed for the natural visual stimulus (100 ms LED flash), and the longest (521.10 ± 60.32 ms) for the least effective pCS (10 ms 300 µA).

Table 3-10. *Descriptive statistics for valid response times for each trial type.*

Statistic	**Trial Type**							
	LED	**10 ms**	**50 ms**			**100 ms**		
		300 µA	**100 µA**	**200 µA**	**300 µA**	**100 µA**	**200 µA**	**300 µA**
Median	343.09	544.00	425.74	373.19	343.55	426.53	382.81	368.69
Mean	338.22	521.10	444.99	386.59	369.03	453.44	396.26	382.28
SEM	18.53	60.32	16.78	16.02	15.84	18.10	16.02	15.65
SD	80.76	233.60	73.14	69.82	69.06	78.87	69.81	68.20

SEM - standard error of the mean; SD - standard deviation

We first conducted a one-way ANOVA to investigate the effect of the fixed factor “Trial Type” on the dependent variable “Valid Response Time”. Levene's test for equality of variance indicated a violation of the homogeneity of variance assumption. As a result, Welch's ANOVA, which corrects for unequal variances, was applied to ensure the robustness of the analysis. The results revealed a statistically significant effect of trial type on valid response time ($F(7, 58.864) = 4.9$, p-value < 0.001, $\eta^2 = 0.219$). The partial eta-squared indicates a medium effect size, suggesting that 21.9% of the variance in valid response time can be attributed to differences between trial types. The post-hoc pairwise comparisons were performed using Tukey’s correction for multiple testing to identify the specific trial types responsible for the observed effect. The statistically significant comparisons are summarized in Table 3-11.

Table 3-11. *Summary of post-hoc pairwise comparisons for valid response times across trial types.*

Comparisons - Trial Types		**Mean Difference**	**t**	**Cohen's d**	**p-value$_{tukey}$**
LED	10 ms 300 µA	-182.88	-5.23	-1.81	< .001***
	50 ms 100 µA	-106.77	-3.25	-1.06	0.03*
	100 ms 100 µA	-115.22	-3.51	-1.14	0.014*
10 ms 300 µA	50 ms 100 µA	76.11 ms	2.18	0.75	0.372
	50 ms 200 µA	134.51	3.85	1.33	0.004**
	50 ms 300 µA	152.07	4.35	1.50	< .001***
	100 ms 100 µA	67.66 ms	1.94	0.67	0.529
	100 ms 200 µA	124.84	3.57	1.23	0.011*
	100 ms 300 µA	138.82	3.97	1.37	0.003**

*** - p-value < 0.001, ** - p-value < 0.01, * - p-value < 0.05

The 10 ms 300 µA trials evoked responses significantly later than the LED stimulus and then other 300 µA and 200 µA trials. Also for both 100 µA stimuli (50 ms and 100 ms) response times were longer than for LED light and no different from 10 ms 300 µA (Table 3-11). This effect is comorbid with valid response rates as the detection of 100 µA stimuli was also lower than for light stimulus (Figure 3-23, Table 3-7, 3-8).

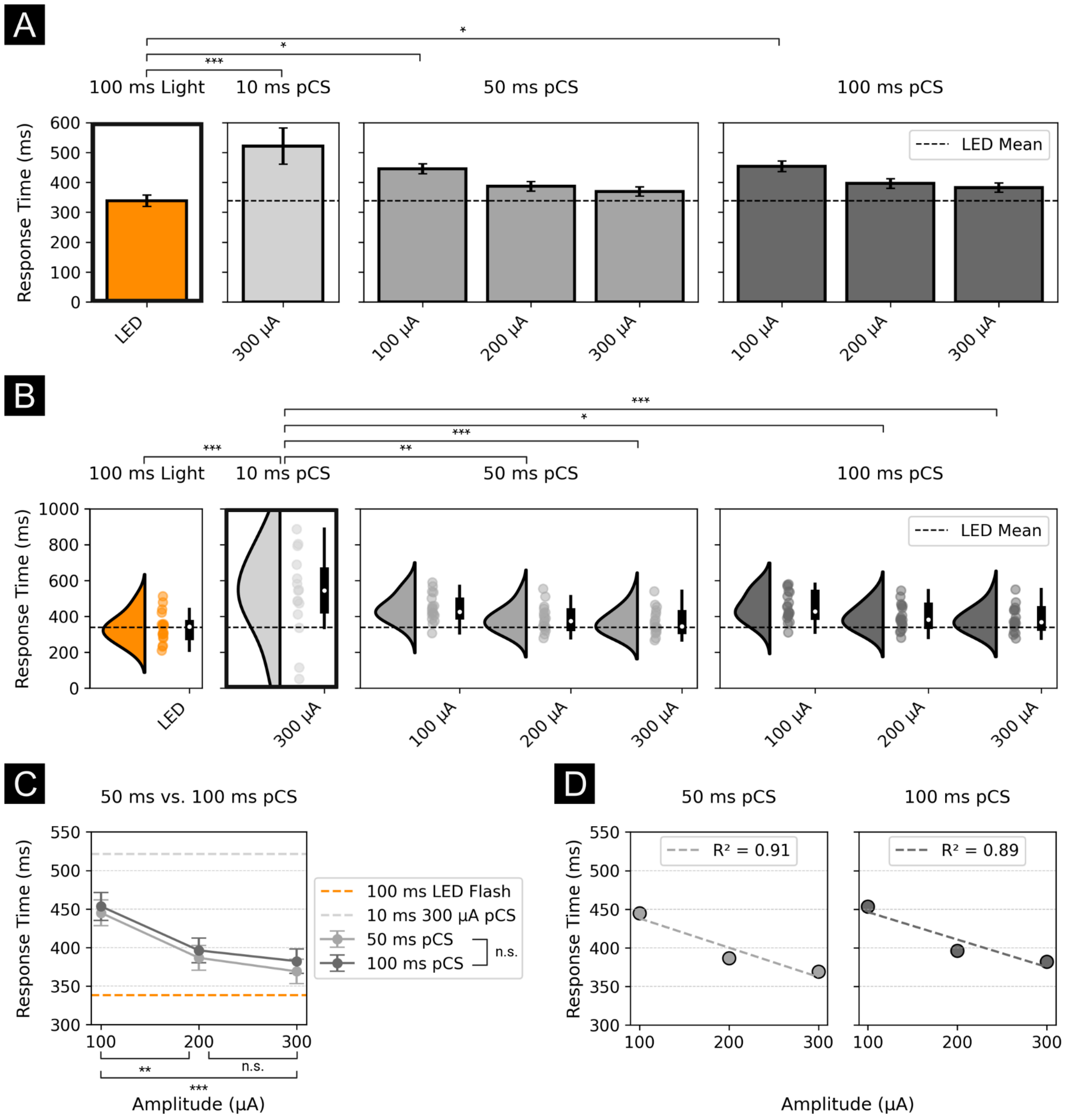

Figure 3-27. *Comprehensive analysis of valid response times across trial types and stimulation parameters. (**A**) Bar plots illustrate the mean valid response times with standard error of the mean (SEM). Statistical significance markers indicate the results of post-hoc tests comparing the 100 ms LED flash with other trial types. The dashed horizontal line in the periorbital current stimulation (pCS) graphs represents the mean valid response time for the 100 ms LED flash, serving as a reference. (**B**) Raincloud plots, comprising kernel density estimation, scatter plots, and box plots, visualize the distribution of values for each trial type. The white dots within the box plots represent the median values. Statistical significance markers indicate the results of post-hoc tests comparing pCS 10 ms 300 μA pulse with other trial types. Similarly, the black dashed line denotes the mean valid response time for the 100 ms LED flash for reference. (**C**) The line graph with SEM compares valid response times for pCS pulses of 50 ms and 100 ms, analyzed through a mixed ANOVA for pulse duration and amplitude. The statistical significance markers in the legend indicate no significant differences for the pulse duration factor (n.s.) and significant differences between subsequent amplitude levels (asterisks). Dashed lines represent the mean valid response times for the 100 ms LED flash (orange) and the 10 ms 300 μA pCS (light gray). (**D**) Scatter plots with fitted linear regression models display valid response times separately for 50 ms pulses (left) and 100 ms pulses*

*(right) across amplitudes of 100, 200, and 300 μA. Statistical significance markers: *** - p-value < 0.001, ** - p-value < 0.01, * - p-value < 0.05, n.s. - p-value >= 0.05.*

In addition, in order to test both the impact of pulse length, pulse amplitude, as well as the potential interaction between the two factors for 50 and 100 ms pulses, we performed a one-way ANOVA in a mixed scheme, where the dependent variable was "Valid Response Time," and the fixed factors were "Pulse Duration" and "Pulse Amplitude". For pulse length, the results were found to be statistically insignificant ($F(1, 108) = 0.608$, p-value 0.437, $\eta^2 = 0.005$) and there was no interaction of factors ($F(2, 108) = 0.012$, p-value = 0.989, $\eta^2 = 0.000$). However, for the amplitude factor, we noted statistical significance ($F(2, 108) = 11.126$, p-value < 0.001, $\eta^2 = 0.170$), attesting to the role of this factor in the observed valid response time results. The post-hoc tests (Tukey's) showed that there were significant differences in response times between the amplitude levels of 100 μA and 200 μA ($M_{diff} = 57.797$, $t = 3.520$, p-value = 0.002, $d = 0.807$) and 300 μA ($M_{diff} = 73.560$, $t = 4.480$, p-value < 0.001, $d = 1.028$). In contrast, there were no significant differences between the 200 and 300 μA levels ($M_{diff} = 15.753$, $t = 0.960$, p-value = 0.604, $d = 0.220$). The results for this comparison are presented in Figure 3-27C.

The linear regression models further confirm the observed trends for the pulse amplitude. For 50 ms pulses, valid response times decreased by 0.38 ms for every 1 μA increase in amplitude. This value is derived from the regression equation: response time = 476.16 - 0.38 × amplitude, where 476.16 represents the intercept (the estimated response time at 0 μA) and -0.38 is the slope (the rate of change in response time per unit increase in amplitude). The model explains 91% of the variance in response times ($R^2 = 0.91$). For 100 ms pulses, response times decrease by 0.36 ms per 1 μA increase in amplitude, with an intercept of 481.82 and a slope of -0.36. This model accounts for 89% of the variance in response times ($R^2 = 0.89$).

Key takeaways:

1. Fastest response to light flash: Participants responded the quickest to the LED flash, with a mean response time of 338.22 ± 18.53 ms.
2. Higher amplitudes of current pulses consistently lead to faster response times, with minimal differences between the pulse durations (within a considered range of 50 and 100 ms).
3. Very short current pulses were least effective in evoking detectable phosphenes. The 10 ms pulse hardly reached the detection threshold of 5% at 300 μA intensity. The low probability of detection was accompanied by the slow response time (521.10 ± 60.32 ms).

Electrical and Visual Evoked Potentials

The neural responses elicited by both visual (LED flash) and periorbital pulsed current stimulation (pPCS) in a form of single biphasic sinusoidal pulses were visualized as of evoked potentials for the occipital electrode cluster (PO7, PO3, POz, PO4, PO8, O1, Oz, O2) (Figure 3-28). This cluster was specifically chosen to capture activity from the primary visual cortex and surrounding regions, which are critical for processing visual stimuli and phosphene perception. For the 100 ms LED flash condition (Figure 3-28C), we observed clear, distinct P1 components around 100 ms post-stimulus and later positive activity in the 150-300 ms window. The P1 component is consistent with early visual cortical processing in response to light stimuli (Luck, 2014), while the later activity in the 150-300 ms range likely reflects higher-order processing, which is linked to perceptual integration and attentional allocation (Di Russo et al., 2002). The full-sensor topographical maps for the 150-300 ms window notably reveal an occipitoparietal source, reinforcing its association with the visual perceptual processing of the stimuli (see Figure 3-28C, bottom topographical map).

In the pPCS conditions, however, the interpretation of early evoked response in the time window from the stimulus onset to its end is less straightforward. Clear, positive P1-like wave (e-P1) was detectable in EEP, however its latency seemed to overlay with the end of current pulse for 50 and 100 ms trials. Only for the shortest, 10 ms pulses the first positive e-P1 peak appeared after the completion of stimulation - at around 26-30 ms. There was also a linear increase in e-P1 amplitude (Table 3-12) with rising current intensity (100, 200, 300 μA, respectively) for subsequent pPCS trial types suggests that residual artifacts from the current pulses remain in the signal, despite ICA and other preprocessing steps. This is further supported by the topographical maps for e-P1 for pPCS trial types, which reveal a frontal dipole configuration that is uncharacteristic of true occipital neural activity. These observations imply that the early responses in the stimulation window are strongly contaminated (if not dominated) by residual artifacts rather than genuine neural activity.

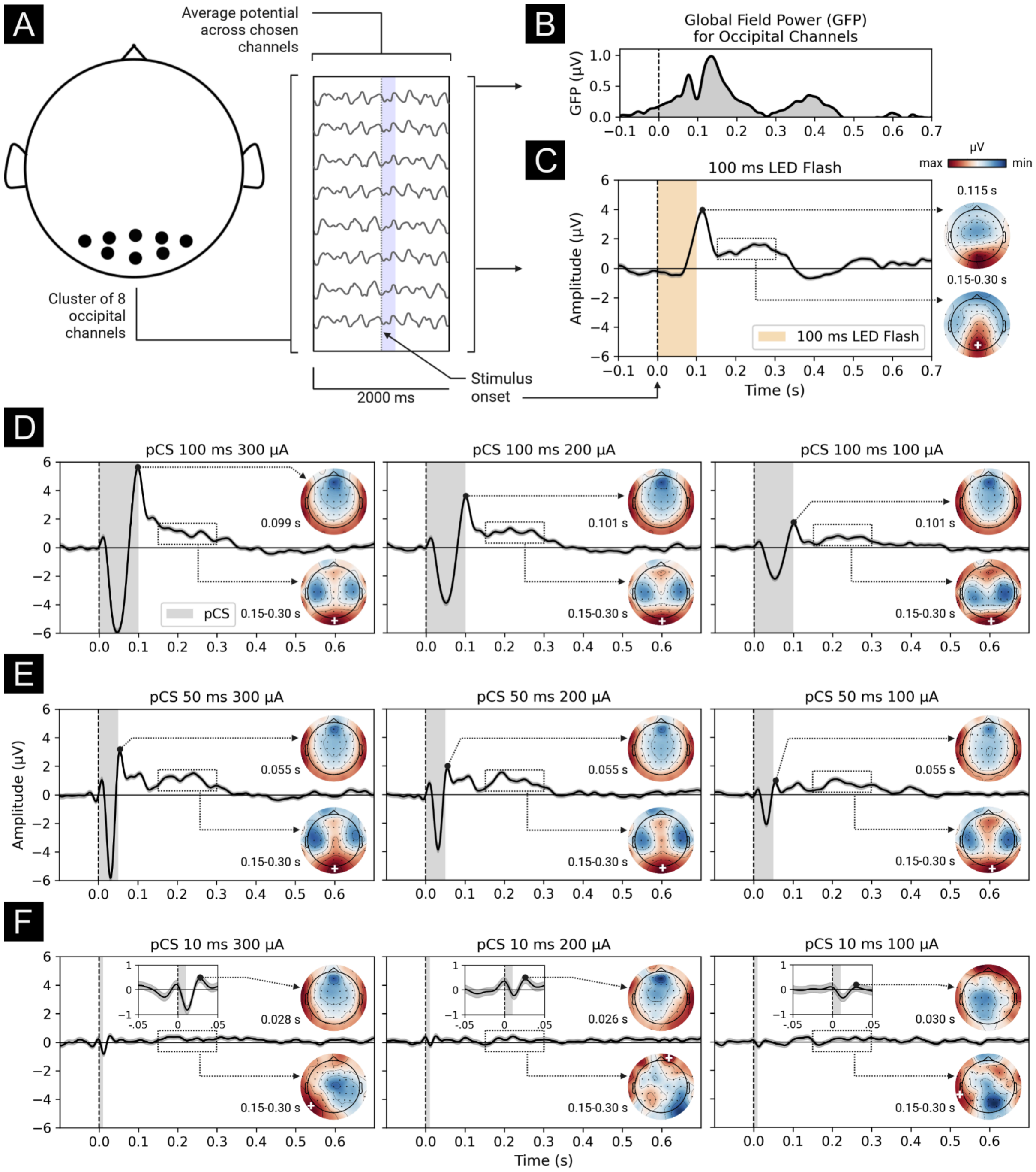

Figure 3-28. *Visualization of grand average visual evoked potentials (VEPs) and electrical evoked potentials (EEPs) across occipital electrodes for LED and periorbital current stimulation (pCS) conditions. (**A**) A cluster of 8 occipital electrodes (PO7, PO3, POz, PO4, PO8, O1, Oz, O2) was selected to illustrate the grand average VEPs and EEPs. (**B**) The global field power (GFP) for the occipital cluster is displayed for the 100 ms LED flash condition, showing the overall signal strength and variability across the selected electrodes. (**C**) The VEP for the 100 ms LED flash condition reveals a prominent P1 component approximately 100 ms after stimulus onset. The orange-shaded area indicates the duration of the visual stimulation. The right side of the panel shows two topographical maps: the upper map presents the voltage distribution at the peak amplitude of the VEP observed at 115 ms, while the lower map depicts the average voltage distribution between 150-300 ms. Both maps highlight occipital activation, with the "+" symbol marking the spatial location of the maximum voltage at the lower map. (**D-F**) The panels show VEPs and EEPs for different conditions of pCS: 100 ms (**D**), 50 ms (**E**), and 10 ms*

*(**F**) pulses with amplitudes of 100 µA, 200 µA, and 300 µA. Each subplot contains the averaged signal across the occipital cluster, with vertical dashed lines marking the stimulus onset. The topographical maps in each condition illustrate the spatial distribution of the response at specific time points, indicating occipital activation at the lower maps i.e. devoted to the 150-300 ms time window.*

Table 3-12. *Maximum and minimum values from topographical maps (topomaps) for first positive amplitude peak (P1 and e-P1) after first negative peak (N1), as shown in Figure 3-28. Trial types. Trial types: 0: 100 ms LED Flash, 1: 10 ms 100 µA, 2: 10 ms 200 µA, 3: 10 ms 300 µA, 4: 50 ms 100 µA, 5: 50 ms 200 µA, 6: 50 ms 300 µA, 7: 100 ms 100 µA, 8: 100 ms 200 µA, and 9: 100 ms 300 µA, respectively.*

P1/eP1 Amplitude [uV]	**Trial Type**									
	LED	**10 ms**			**50 ms**			**100 ms**		
		100 µA	**200 µA**	**300 µA**	**100 µA**	**200 µA**	**300 µA**	**100 µA**	**200 µA**	**300 µA**
Max	1.36	0.12	0.16	0.23	0.62	0.88	1.00	0.86	1.17	1.12
Min	-0.86	-0.14	-0.15	-0.18	-0.47	-0.70	-0.80	-0.70	-0.76	-0.77
Latency [ms]	115	30	26	28	55	55	55	101	101	99

Computational Simulations of Stimulation Artifact

To further investigate whether the waves observed in the stimulation window reflect genuine neural response or residual artifacts, we conducted a series of computational simulations. In these simulations, we injected sinusoidal pulses, both without and with added noise, into clean rest EEG data to evaluate the performance of ICA in artifact removal (Figure 3-29). When pulses without noise were injected, ICA successfully isolated them in a single component, and excluding this component restored the initial signal with high fidelity. However, when noise was added to the pulses before their injection, ICA struggled to clearly separate the pulses from the rest of the EEG signal. In such cases, ICA identified multiple components (e.g., two) containing pulse representations. These components closely resembled the evoked potentials recorded for pPCS conditions, particularly in the stimulation window. Although removing all such components resulted in a reasonably clean signal, it also led to a flattening of the "stimulation window," indicating some loss of information. These simulation results, combined with the preprocessing steps applied to the experimental data, suggest that during the preprocessing of procedure block signals, some components containing partial representations of pPCS artifacts may not have been fully removed. This residual artifact likely represents the main source of the amplitude observed in the stimulation window, which is further supported by the linear relationship of e-P1 amplitude and latency with current amplitude for subsequent values of 100, 200, and 300 µA.

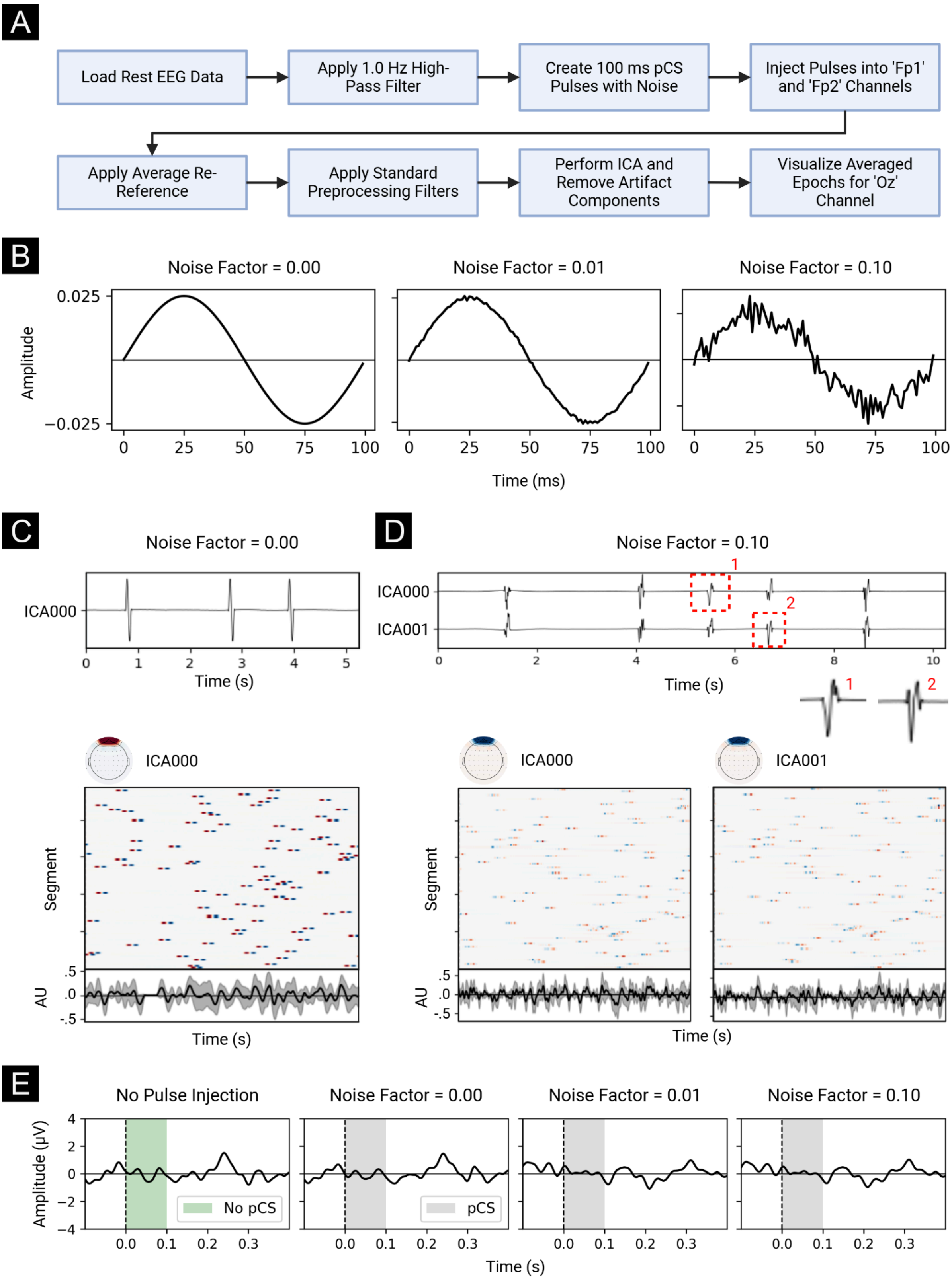

Figure 3-29. *Simulated evaluation of independent component analysis (ICA) performance in removing pulse artifacts from EEG signal. (**A**) Overview of preprocessing steps. Rest EEG data was loaded, and a 1.0 Hz high-pass filter was first applied to remove slow-drift activity before pulse injection. Sinusoidal current stimulation pulses were created and injected into the Fp1 and Fp2 channels with varying levels of added noise. Noise was generated as random values sampled from a Gaussian distribution with a mean of zero and a standard deviation*

*proportional to the pulse amplitude, scaled by a specified noise factor (Noise Factor = 0.00, 0.01, or 0.10). For example, a higher noise factor resulted in greater distortion of the sinusoidal pulses. After pulse injection, average re-referencing was applied to spread the artifacts across all channels. Standard preprocessing steps, identical to those used for the procedure blocks with real single-pulse periorbital current stimulation (pCS) artifacts, were then applied, including a 1.0 Hz high-pass filter, a 50 Hz notch filter, and a 40 Hz low-pass filter. These filters are critical for noise removal but can introduce edge artifacts, particularly when applied to high-amplitude pulse artifacts in EEG signals, especially if the sampling frequency of the signal is relatively low and if pulse artifacts are of high amplitude and short duration. Finally, ICA was performed to identify and exclude components representing pulse artifacts, and averaged epochs for the 'Oz' channel were visualized to evaluate the effectiveness of artifact removal. (**B**) Sinusoidal, biphasic, 100 ms pulses with varying noise levels. Pulse shapes were modified by adding random noise scaled by a noise factor as mentioned above. (**C**) Performance of ICA for signal with injected pulses without noise. When no noise was added, ICA successfully identified a single component that clearly represented the pulse artifact. This allowed for effective removal of the artifact from the signal by the exclusion of the component. (**D**) Performance of ICA for signal with injected pulses with noise (noise factor = 0.10). For higher noise levels, ICA identified at least two components that partially represented the pulse artifact. Segments marked with red squares (1 and 2) show temporal patterns that closely resemble the averaged evoked potentials observed for pCS conditions in Figure 3-28D-F. This resemblance suggests that the pulse artifact, when distributed across multiple independent components, becomes difficult to fully exclude, as some components containing artifact-related signals may also include genuine neural activity and thus are not removed. As a result, the residual pulse artifacts in these components, when averaged across epochs, contribute to the patterns observed in the evoked potentials for pCS conditions. This highlights the challenges in achieving precise artifact removal without compromising genuine neural signals. (**E**) The averaged evoked potentials for the 'Oz' electrode are shown for conditions with no pulse injection and for simulated pulses with Noise Factors of 0.00, 0.01, and 0.10. In the no-pulse condition, the signal remains clean and artifact-free. For noise factor = 0.00, ICA effectively removes the pulse artifact, restoring the original signal. However, as the noise factor increases, ICA struggles to fully isolate the artifact within a single component, instead requiring the exclusion of multiple components. This results in flattened or distorted responses within the stimulation window (0.0-0.1 s) and potential artifact residuals if not all components containing artifact representations are excluded. These findings indicate that higher noise levels hinder ICA's ability to accurately separate and remove pulse-related components, leading to either residual artifact contamination or loss of genuine neural activity. This limitation is particularly relevant to real-life scenarios involving pCS artifacts in EEG signals.*

Analysis of P2 Component

The simulation confirmed that the earliest EPP window is contaminated by the artifact of electric stimulus. Therefore, to focus on genuine neural activity, the analysis was shifted to later time windows that are less affected by artifacts. As evidenced in Figure 3-30C, the 150-300 ms time window reveals a clear positive potential following the LED flash. This activity, based on topographical maps, is strongly localized in the occipital region, with a maximum centered over the Oz electrode. The spatial distribution and timing of this activity suggest that it is associated with the late P2 component, which reflects higher-order visual information processing, including perceptual integration and attentional allocation (Luck, 2014; Di Russo et al., 2002).

Interestingly, this positive potential was not unique to the LED flash condition. It was also observed in pPCS conditions for electrical pulses lasting 50 ms and 100 ms, within full amplitude range (100, 200, and 300 µA, Figure 3-28C). The presence of this activity across these pPCS conditions suggests that similar neural mechanisms may be engaged during the perception of phosphenes induced by electrical stimulation. This positive potential is notably absent for 10 ms pulses, indicating that such short pulses may fail to evoke notable occipital activation at the level necessary to elicit phosphenes. Indeed, this pattern of positive activity in the 150-300 ms window paralleled behavioral results (valid response rate and valid response time). Conditions that elicit higher valid response rates and faster response times are precisely those that show pronounced positive potentials in this time window. This suggests that the observed activity in the occipital region during this period is closely tied to the processing of visual stimuli, whether in the form of an LED flash or phosphenes induced by electrical stimulation.

Given these findings, the 150-300 ms time window emerges as a critical period for inter-condition analysis. Additionally, the Oz electrode, where the topographical maximum of this potential is observed, provides a focal point for these comparisons (see Figure 3-28C, bottom topographical maps, and Table 3-13). Thus, for each participant, we selected the Oz electrode and calculated the average potential over the 150-300 ms window for each trial type (see results in Figure 3-30). Descriptive statistics, including means, are presented in Table 3-14.

Table 3-13. *Maximum and minimum values (µV) from topographical maps (topomaps) for the time window 150-300 ms, as shown in Figure 3-28C-F. These values represent data from the entire map, with the maxima marked by white crosses on the lower topomaps in Figure 3-28. Notably, the maxima consistently appeared near the Oz electrode's region.*

P2	**Trial Type**									
	LED	**10 ms**			**50 ms**			**100 ms**		
		100 µA	**200 µA**	**300 µA**	**100 µA**	**200 µA**	**300 µA**	**100 µA**	**200 µA**	**300 µA**
Max	1.36	0.12	0.16	0.23	0.62	0.88	1.00	0.86	1.17	1.12
Min	-0.86	-0.14	-0.15	-0.18	-0.47	-0.70	-0.80	-0.70	-0.76	-0.77

Table 3-14. *Descriptive statistics for the average potential (μV) over the 150-300 ms window for each trial type.*

Statistic	**Trial Type**									
	LED	**10 ms**			**50 ms**			**100 ms**		
		100 μA	**200 μA**	**300 μA**	**100 μA**	**200 μA**	**300 μA**	**100 μA**	**200 μA**	**300 μA**
Mean	1.269	-0.086	-0.044	0.070	0.561	0.849	0.976	0.691	1.078	1.022
SEM	0.279	0.063	0.076	0.095	0.163	0.171	0.211	0.132	0.221	0.237

SEM - standard error of the mean

The observed average values reflect the trends identified earlier in the behavioral data. Specifically, the highest average amplitude was recorded for the 100 ms LED flash (1.269 µV), while for the 10 ms pulse, the potential amplitude in this window was close to zero. Among the 50 and 100 ms pulses, the amplitude was lower than for LED, with a visible tendency to increase with the duration and amplitude of the current stimulus.

To statistically compare these averages and determine the presence of a stimulation-type effect, we conducted a one-way ANOVA. The dependent variable, "Average of P2", was defined above, while the fixed factor, "Trial Type", represented the type of stimulation (visual or pPCS). Since Levene's test indicated significant heterogeneity of variances (p-value < 0.001), Welch's correction was applied to ensure the robustness of the statistical comparisons. A one-way ANOVA showed a significant effect of stimulation type, $F(9, 72.369) = 12.654$, p-value < 0.001, $\eta^2 = 0.279$. Post-hoc comparison (Table 3-15) was first focused on the LED versus pPCS pairs which came out to be significant only for the shortest, 10 ms stimuli (Figure 3-30A). Responses to these short stimuli were also different from responses to most of the longer pulses (Figure 3-30B). On the other hand, the responses to 50 and 100 ms pulses of all current intensity were not significantly different from LED responses.

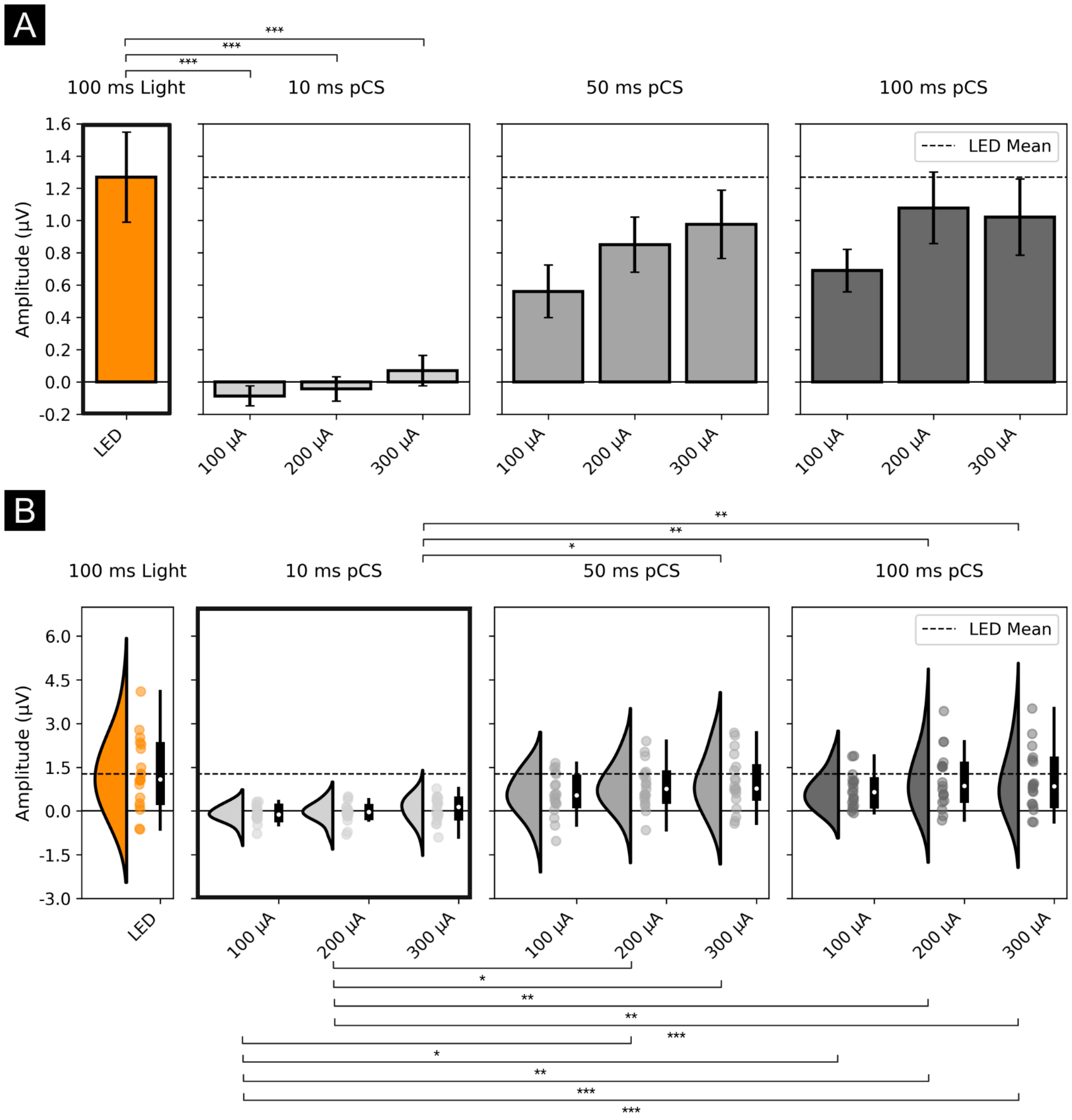

Figure 3-30. *Analysis of average potentials in the 150-300 ms time window for the occipital electrode Oz across trial types. (**A**) Bar plots illustrate the mean potential calculated over the 150-300 ms time window for the Oz occipital electrode for all participants considered in the analysis. Error bars represent standard error of the mean. Statistically significance markers indicate the results of post-hoc tests comparing the 100 ms LED flash with other trial types. The dashed horizontal line in the single-pulse periorbital current stimulation (pCS) subplots represents the mean potential for the 100 ms LED flash, serving as a reference. (**B**) Raincloud plots, comprising kernel density estimation, scatter plots, and box plots, visualize the distribution of values for each trial type. The white dots within the box plots represent the median values. Statistical significance markers indicate the results of post-hoc tests comparing 10 ms pulses with other pulse durations, excluding the LED flash, which was discussed in the previous plot. Similarly, the black dashed line denotes the mean valid response time for the 100 ms LED flash for reference.*

Table 3-15. *Summary of post-hoc pairwise comparisons for 150-300 ms time window averaged potentials across trial types.*

Comparisons - Trial Types		**Mean Difference**	**t**	**Cohen's d**	**p-value$_{tukey}$**
LED	10 ms 100 µA	1.355	5.364	1.740	< .001***
	10 ms 200 µA	1.312	5.195	1.685	< .001***
	10 ms 300 µA	1.198	4.745	1.539	< .001***
10 ms 100 µA	50 ms 200 µA	-0.936	-3.705	-1.202	0.01*
	100 ms 100 µA	-1.063	-4.207	-1.365	0.002**
	100 ms 200 µA	-1.165	-4.612	-1.496	< .001***
	100 ms 300 µA	-1.108	-4.387	-1.423	< .001***
10 ms 200 µA	50 ms 200 µA	-0.893	-3.536	-1.147	0.018*
	50 ms 300 µA	-1.020	-4.038	-1.310	0.003**
	100 ms 200 µA	-1.122	-4.442	-1.441	< .001***
	100 ms 300 µA	-1.065	-4.218	-1.368	0.002**
10 ms 300 µA	50 ms 300 µA	-0.906	-3.588	-1.164	0.015*
	100 ms 200 µA	-1.008	-3.992	-1.295	0.004**
	100 ms 300 µA	-0.952	-3.768	-1.222	0.008**

*** - p-value < 0.001, ** - p-value < 0.01, * - p-value < 0.05

Moreover, we conducted linear regression analyses to examine the relationships between pulse amplitude and the resulting averaged potentials for two, behaviorally effective pulse durations (50 and 100 ms). Similarly, for the 50 ms pPCS condition, the linear fit produced an intercept of 0.3805, a slope of 0.0021, and an R^2 of 0.9520. In the case of the 100 ms pPCS, the intercept was 0.5991 with a slope of 0.0017 and an R^2 of 0.6247. These regression parameters suggest slight but relatively stable increase of potential values with stronger stimulation currents (Figure 3-31A).

The results of the mixed ANOVA with "Average P2" as the dependent variable and "Pulse Duration" and "Pulse Amplitude" as fixed factors were based on a 2 x 3 comparison, where two durations (50, 100 ms) and three amplitudes (100, 200, 300 µA) were tested. The analysis revealed no statistically significant main effects or interactions. Specifically, the main effect of pulse duration was not significant ($F(1, 108) = 0.733$, p-value = 0.394, $\eta^2 = 0.006$), indicating that variations in pulse duration did not meaningfully influence the average P2 response. Similarly, the main effect of pulse amplitude failed to reach statistical significance ($F(2, 108) = 2.291$, p-value = 0.106), though the effect size ($\eta^2 = 0.040$) suggests an existence of a slight difference. Post-hoc comparisons for pulse amplitude did not reveal statistically significant differences between any of the levels. However, the effect sizes indicated a discernible trend: the comparison between 100 and 300 µA demonstrated a higher effect size (d = -0.445) compared to the 100 vs 200 µA comparison (d = -0.403). Meanwhile, the difference between 200 and 300 µA exhibited the lowest effect size (d = -0.042). Although these results were not statistically significant, the observed trend in effect sizes suggests that larger amplitude differences (e.g. 100 vs. 300 µA) may have a more noticeable, albeit non-significant, impact on the average P2 response (see Figure 3-31B).

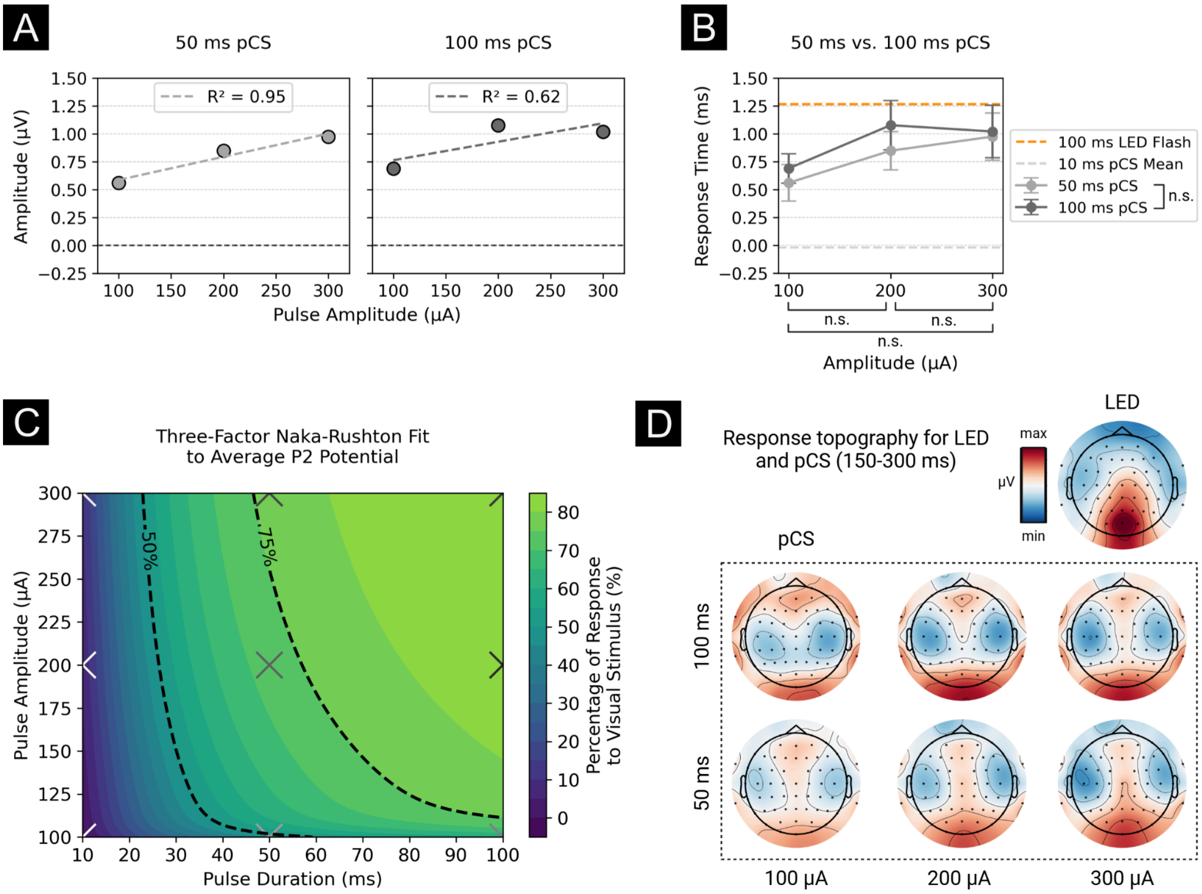

*Figure 3-31. Comprehensive analysis of the 150-300 ms time window: (**A**) Linear regression results for averaged amplitudes in the 150-300 ms time window across different single pulse amplitudes for 50 ms, and 100 ms periorbital current stimulation (pCS), with R² values indicating goodness of fit. (**B**) Comparison of averaged potentials in the 150-300 ms time window between 50 ms and 100 ms pCS, showing no significant differences (n.s.). There were also no significant differences for the amplitude factor (n.s.). (**C**) Three-factor Naka-Rushton model fit to normalized averages in the 150-300 ms time window, corresponding to the late P2 component for convenience. The model incorporates pulse amplitude, duration, and total charge, with R² = 0.9948 and an average absolute error of 2.22%. The "X" marks represent pCS data points used in the model. Note that the response color scale reaches only 85%. (**D**) Topographical maps of averaged potentials in the 150-300 ms time window for pCS (50 ms and 100 ms) and LED stimulation, demonstrating spatial distributions and highlighting stronger occipital activation for LED.*

Naka-Rushton Model for EEP P2 Wave

We further explored the parametric space by applying our custom three-factor Naka-Rushton model to characterize how total charge, amplitude, and saturated duration jointly influenced the average potentials. For this analysis, we normalized the EEP data by setting the LED potential as the maximum reference and the 10 ms 100 µA pPCS potential as the minimum reference creating 0-100% scale normalized scale. This approach allowed us to interpret the pPCS results in direct relation to the LED stimulation effect. The model demonstrated an excellent fit to the data, with a goodness-of-fit R^2 of 0.9948 and an average absolute difference between the actual and predicted values of only 2.22%. The modeling results, illustrated in Figure 3-31C, show how alterations in the stimulation parameters can modulate the resulting evoked potentials. Detailed data on the actual values, predicted values, and differences are provided in Table 3-16.

The results of the three-factor Naka-Rushton model for the 150-300 ms potential provided additional insights into the required pulse durations for specific modeled response levels at given pulse amplitudes. To achieve a modeled response of 50%, the required pulse durations were 51.32 ms for 100 µA, 26.36 ms for 200 µA, and 22.93 ms for 300 µA. For a modeled response of 10%, representing the arbitrary electrophysiological threshold potential, the required durations were shorter: 15.91 ms for 100 µA, 11.36 ms for 200 µA, and 10.13 ms for 300 µA.

Topography of EEP P2 Wave

Finally, to gain insight into the spatial distribution of the recorded responses, we revisited topographical maps for the 150-300 ms window under various stimulation conditions. These maps, presented in Figure 3-31D, facilitate visual comparisons of the potential distributions elicited in different trial types. The color scale is derived from the LED topographical map, ensuring consistent referencing of minima and maxima across conditions. Despite the inability to analyze early visual components due to the presence of current artifacts, this 150-300 ms window provides a confirmation that visual processing related to single-pulse pPCS is occurring. Moreover, topography of 150-300 ms wave offered a direct electrophysiological indication that information elicited by a current pulse applied within the eyeballs is being processed in a manner comparable to the processing of LED flash information. This finding is likely indicative of the site of generation of a phosphenic sensation, particularly for the 50 and 100 ms pulses. Detailed interpretations will be discussed in the relevant discussion section.

Table 3-16. *Predicted and actual normalized average potentials for the 150-300 ms time window for the three-factor Naka-Rushton model which incorporates total charge, amplitude and duration of the current pulse. Normalization is performed for the 10 ms 100 µA pulse potential as minimum and 100 ms LED flash potential as maximum.*

Values	**Trial Type**								
	10 ms 100 µA	**10 ms 200 µA**	**10 ms 300 µA**	**50 ms 100 µA**	**50 ms 200 µA**	**50 ms 300 µA**	**100 ms 100 µA**	**100 ms 200 µA**	**100 ms 300 µA**
Predictions	-0.78	5.94	9.61	45.97	72.24	76.42	58.82	82.34	84.20
Actual	0.00	3.10	11.51	47.75	69.00	78.38	57.34	85.90	81.77
Difference	-0.78	2.84	-1.91	-1.78	3.24	-1.95	1.48	-3.57	2.43

average absolute difference = 2.22; goodness of fit (R^2) = 0.9948

Key takeaways:

1. The current artifact induced in the EEG signal cannot be fully removed from the EEP waveform making it impossible to analyze early visual components.
2. Later component of the EEP waveform (150-300 ms post stimulus) reflects subsequent visual processing of visual and electrically induced activity.
3. The effective current pulses (50 and 100 ms) elicit activity in the occipital region within the 150-300 ms window, comparable to the activity induced by the 100 ms LED flash. The strongest activation occurs at the Oz electrode for both types of stimulation, emphasizing the focal nature of the occipital response.
4. Electrophysiological activity observed with visual and current stimulation reflects trends similar to those observed in the behavioral data, with lack or negligible response to 10 ms pulse and comparable differences between effective 50 and 100 ms conditions.
5. Naka-Rushton model for pulse characteristics: A custom Naka-Rushton curve, based on total charge, amplitude, and pulse duration saturation, effectively predicts the percentage of activity induced relative to LED stimulation. The model achieves an error margin of 2.22%, demonstrating its accuracy in modeling induced activity as a proportion of the maximum response observed for LED.

Changes in Resting-State Frequency Distribution Throughout the Experimental Procedure

Between the experimental blocks, there were 3-minute *rest* periods during which the participants relaxed with their eyes closed before proceeding to the next block. During these periods, we recorded the EEG signal to investigate if and how its characteristics, particularly over occipital areas, would change over time.

The analysis focused on the power of alpha band over the occipital electrodes cluster indicated a noticeable increase in alpha power between the first and last *rest* block (Figure 3-32A). To further investigate this trend, we applied linear regression modeling. The results indicated a positive slope (3.10), suggesting a gradual increase in alpha power over time. The intercept (2.32) represents the initial alpha power difference relative to the baseline, and the coefficient of determination ($R^2 = 0.82$) demonstrates a strong fit of the linear model, explaining over 82% of the variance in the data (Figure 3-32B). However, this observed trend did not reach statistical significance when evaluated using one-way ANOVA, possibly due to high resting-state alpha variability between participants (Table 3-17). The ANOVA results revealed no significant effect of the block factor on alpha power, F(5, 114) = 0.074, p-value = 0.0998, with a negligible effect size ($\eta^2 = 0.003$).

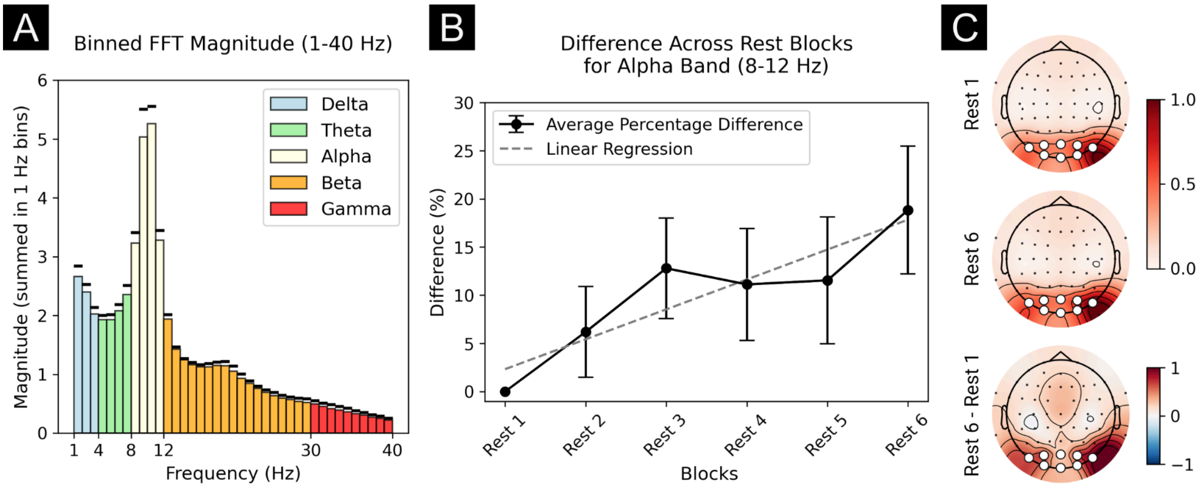

Figure 3-32. *Frequency results for the occipital cluster electrodes aggregated across all participants. (**A**) Frequency distribution of the occipital electrodes cluster signals' amplitude (absolute value of the complex FFT output, in μV) in the 1-40 Hz range, grouped into 1 Hz bins. The frequency ranges for delta (1-4 Hz), theta (4-8 Hz), alpha (8-12 Hz), beta (12-30 Hz), and gamma (30-40 Hz) are indicated. The main bar chart shows the distribution for the first rest block, with black horizontal dashes marking the peak values from the distribution of the last rest block. (**B**) Relative differences between consecutive rest blocks for the alpha range (8-12 Hz) expressed as percentage differences relative to the first rest block. Error bars represent the standard error of the mean. The grey dashed line shows the linear regression model fitted to the data. (**C**) Power spectral density*

topographic maps calculated using Welch's method for the alpha range (8-12 Hz) for the first and last rest blocks. The difference between the blocks is also presented at the bottom of the panel. The color scales are normalized separately: one set for the top and middle topomaps, and another for the bottom topomap. The occipital cluster electrodes are marked with a white circles. These were electrodes: PO7, PO3, POz, PO4, PO8, O1, Oz, and O2.

Table 3-17. *Descriptive statistics for alpha band (8-12 Hz) magnitudes across all participants, measured at the occipital electrodes cluster for all rest blocks. These were electrodes: PO7, PO3, POz, PO4, PO8, O1, Oz, and O2.*

Block	**Mean**	**SEM**	**STD**
Rest 1	16.807	2.884	12.896
Rest 2	17.911	3.037	13.583
Rest 3	18.051	2.599	11.622
Rest 4	18.441	3.023	13.518
Rest 5	18.137	2.727	12.196
Rest 6	19.201	2.859	12.786

SEM - standard error of the mean; STD - standard deviation

Key takeaways:

1. The alpha band activity was prominent in the EEG signal during the *rest* blocks, confirming the relaxed state of participants.

2. Alpha power showed a trend of increase across subsequent rest blocks, as supported by linear regression analysis. However, this trend was not statistically significant when tested with ANOVA.

3. Large interindividual differences in alpha power were observed across participants. These variations likely contributed to the lack of statistical significance in group-level analyses, highlighting the high variability in resting-state neural activity between individuals.

Effects of Pre-Stimulus Single-Pulse Periorbital Current Stimulation (Study 2)

The primary aim of the second study was to examine how the electric stimulation would influence the processing of the following visual stimuli. The analysis focused on VEP data from occipital electrodes cluster, for which peak-to-peak amplitudes of their main waves (P1N1 and P1N2, see Figure 1-9) were measured and compared between the initial *prologue* block, where the CPR visual stimuli occurred independently and the procedure blocks in which CPR was preceded by current stimulation. The effect of experimental manipulation was estimated by measuring, for each condition from *procedure* and *epilogue* blocks, the amplitude change from the *prologue* values (the resulting values are addressed in further text as relative amplitudes).

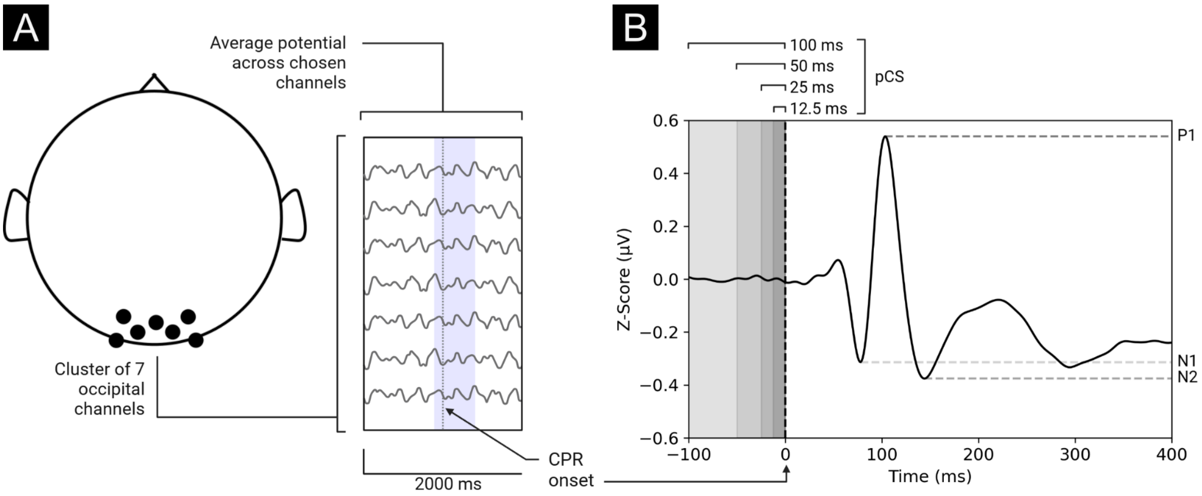

Figure 3-33. *Illustration of the visual evoked potential (VEP) analysis procedure for P1N1 and P1N2 relative amplitudes. (**A**) Diagram showing the cluster of 7 occipital electrodes used for VEP extraction. (**B**) Example VEP waveform grand-averaged across all participants and occipital cluster electrodes for the prologue block, with marked N1, P1, and N2 components. The vertical dashed line indicates the onset of the checkerboard pattern reversal (CPR). The shaded areas before the onset represent the time windows of periorbital current stimulation (pCS), applied in the form of single pulses with specific durations (12.5, 25, 50, and 100 ms).*

Global Stimulation Effect

First, we examined whether there was any cumulative effect of current stimulation. As can be seen on the Figure 3-34, and in Table 3-18 the relative peak-to-peak VEP amplitudes (both P1N1 and P1N2 components) were negative, indicating that VEPs recorded during *procedure* blocks (averaged for all current pulse parameters, excluding *control* no-current condition), were smaller than during the *prologue*. The Wilcoxon signed-rank test revealed that this effect was significant in the experimental (EXP) group, for both P1N1 and P1N2 components (P1N1: V = 1200.5, p-value < 0.001, r = -0.709; P1N2: V = 881.5, p-value < 0.001, r = -0.786, where *r* is Rank-Biserial Correlation). Conversely, for the placebo (SHAM) group, no significant differences were observed for either component (P1N1: V = 3393.0, p-value = 0.081, r = -0.178; P1N2: V = 3773.5, p-value = 0.400, r = -0.086).

Next we tested if this global effect was dependent on the characteristic of current pulse stimuli. To address this, we run a two-way ANOVA with a fixed factor for "Group", comprising two levels: EXP and SHAM. The second fixed factor, "Condition" included eight levels, i.e. conditions representing current pulse applications of specific durations (100 ms, 50 ms, 25 ms, and 12.5 ms) and amplitudes (100 µA and 200 µA), thereby excluding the control condition (see Figure 2-9). Table 3-18 presents the summary descriptive statistics for relative amplitudes (for both P1N1 and P1N2) for all trials from the EXP and SHAM groups.

Table 3-18. *Summary statistics for P1N1 and P1N2 relative amplitudes, pooled from all experimental conditions with current stimulation. Table includes median, mean, standard error of the mean (SEM), standard deviation (STD), minimum, and maximum values for the experimental (EXP) and placebo (SHAM) groups. Amplitude data represented as Z-Scored potential values.*

Descriptive Statistic	**P1N1 relative amplitude (change from *prologue*)**		**P1N2 relative amplitude (change from *prologue*)**	
	EXP	**SHAM**	**EXP**	**SHAM**
Median	-0.266	-0.014	-0.164	-0.032
Mean	-0.245	-0.023	-0.241	-0.013
SEM	0.031	0.012	0.024	0.015
STD	0.346	0.139	0.27	0.171
Minimum	-1.254	-0.339	-0.701	-0.418
Maximum	0.441	0.293	0.423	0.404

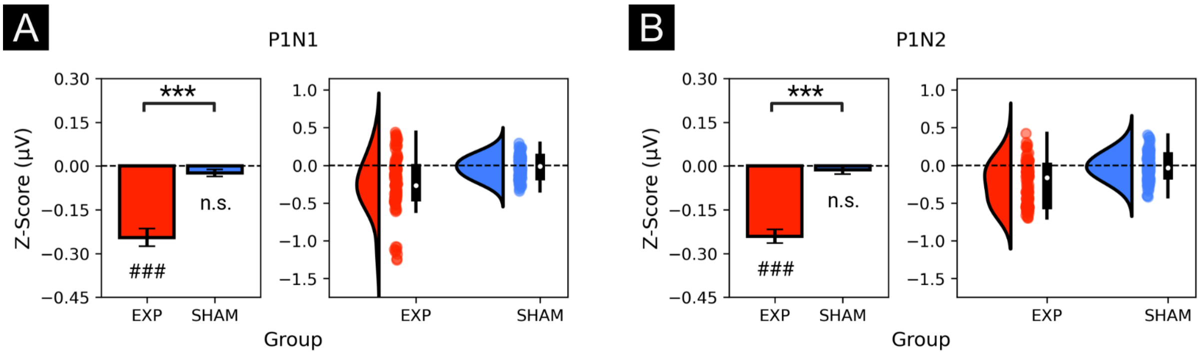

Figure 3-34. *Global effects of periorbital current stimulation (pCS) preceding the visual CPR stimulus on VEP amplitudes. (**A**) P1N1 relative (procedure minus prologue) peak-to-peak amplitude. (**B**) P1N2 relative peak-to-peak amplitude. Left panels in (A) and (B) present mean Z-scores values with standard error of the mean; right panels depict kernel density estimates of data with scatter plots and box plots. White dots in the box plots represent medians. Statistical significance is marked by* $^{\#\#\#}$ *for the relative VEP amplitude difference from zero (p-value < 0.001); and by *** (p-value < 0.001) for EXP versus SHAM comparison, highlighting the global effect of pCS compared to the placebo group.*

As indicated by the Shapiro-Wilk test, SHAM group data were normally distributed (P1N1, W = 0.985, p = 0.190; P1N2, W = 0.992, p-value = 0.680), while the EXP data deviated from normality (P1N1, W = 0.934, p-value < 0.001; P1N2, W = 0.946, p-value < 0.001). However, given the high Shapiro-Wilk statistics (close to 1), we conducted a closer, visual inspection of the distributions and we found out that the EXP P1N1 distribution contained few outliers that influenced skewness (g_1 = -0.611), while the P1N2 distribution appeared slightly bimodal without any outliers (g_1 = 0.059). Despite these findings, we proceeded with the ANOVA since it is known to be relatively robust when deviations from normality are not severe, as was the case in our data, and it allows to test for interaction effects.

The analysis confirmed a significant main effect of "Group" (i.e. the global difference between EXP and SHAM groups) on both the P1N1 and P1N2 relative amplitudes, with large effect sizes (Table 3-19). There was, however no significant main effect for "Condition" (representing pulse characteristics) and no significant "Group" * "Condition" interaction for both tested VEP components i.e. P1N1 and P1N2. The nonparametric Kruskal-Wallis test also confirmed significant "Group" effects (p-value < 0.001, η^2 = 0.172) and lack of "Condition" effects (p-value = 0.999, η^2 = 0.000).

Table 3-19. *Summary of two-way ANOVA results for the P1N1 and P1N2 relative amplitudes, including the sum of squares, degrees of freedom (df), mean square, F-statistic, p-values, and partial eta-squared (η^2) for the main effects (group and condition) and their interaction term (group * condition). Amplitude data represented as Z-Scored potential values.*

Relative Amplitude	**Cases**	**Sum of Squares**	**df**	**Mean Square**	**F**	**p-value**	**η^2**
P1N1	Group	3.139	1	3.139	42.973	< .001***	0.151
	Condition	0.027	7	0.004	0.052	1.000	0.001
	Group * Condition	0.066	7	0.009	0.128	0.996	0.003
	Residuals	17.530	240	0.073			
P1N2	Group	3.326	1	3.326	61.878	< .001***	0.204
	Condition	0.003	7	0.000	0.009	1.000	0.000
	Group * Condition	0.064	7	0.009	0.169	0.991	0.004
	Residuals	12.900	240	0.054			

*** - p-value < 0.001

The post-hoc analyses using Tukey's tests indicated that the EXP versus SHAM comparisons for practically all the individual pulse conditions reached statistical significance with medium to large Cohen's d values (see Table 3-20, and Figure 3-35 for details). Only for the shortest impulse (12.5 ms) applied with 200 µA, the P1N1 amplitude reduction was not significant (p = 0.084). There were no evident tendencies for VEP amplitude changes to follow the duration or strength of the current stimulation.

Table 3-20. *Mean differences (EXP minus SHAM) of relative VEP amplitudes, Cohen's d, t-values, and adjusted p-values from Tukey's post-hoc comparisons between the EXP and SHAM groups, listed for each pulse condition specified in the first column, for the P1N1 and P1N2 peak-to-peak relative amplitudes.*

Relative Amplitude	**Condition**	**Mean Difference: EXP - SHAM**	**Cohen's d**	**t**	**p-value$_{tukey}$**
P1N1	100 ms 100 μA	-0.208	-0.770	-2.179	0.030*
	50 ms 100 μA	-0.254	-0.941	-2.662	0.008**
	25 ms 100 μA	-0.235	-0.870	-2.461	0.015*
	12.5 ms 100 μA	-0.194	-0.717	-2.027	0.044*
	100 ms 200 μA	-0.209	-0.773	-2.186	0.030*
	50 ms 200 μA	-0.272	-1.008	-2.851	0.005**
	25 ms 200 μA	-0.233	-0.863	-2.440	0.015*
	12.5 ms 200 μA	-0.166	-0.614	-1.736	0.084
P1N2	100 ms 100 μA	-0.269	-1.159	-3.279	0.001**
	50 ms 100 μA	-0.172	-0.743	-2.103	0.037*
	25 ms 100 μA	-0.246	-1.062	-3.004	0.003**
	12.5 ms 100 μA	-0.205	-0.886	-2.507	0.013*
	100 ms 200 μA	-0.236	-1.020	-2.884	0.004**
	50 ms 200 μA	-0.264	-1.137	-3.217	0.001**
	25 ms 200 μA	-0.234	-1.008	-2.852	0.005**
	12.5 ms 200 μA	-0.197	-0.850	-2.403	0.017*

** - p-value < 0.01, * - p-value < 0.05

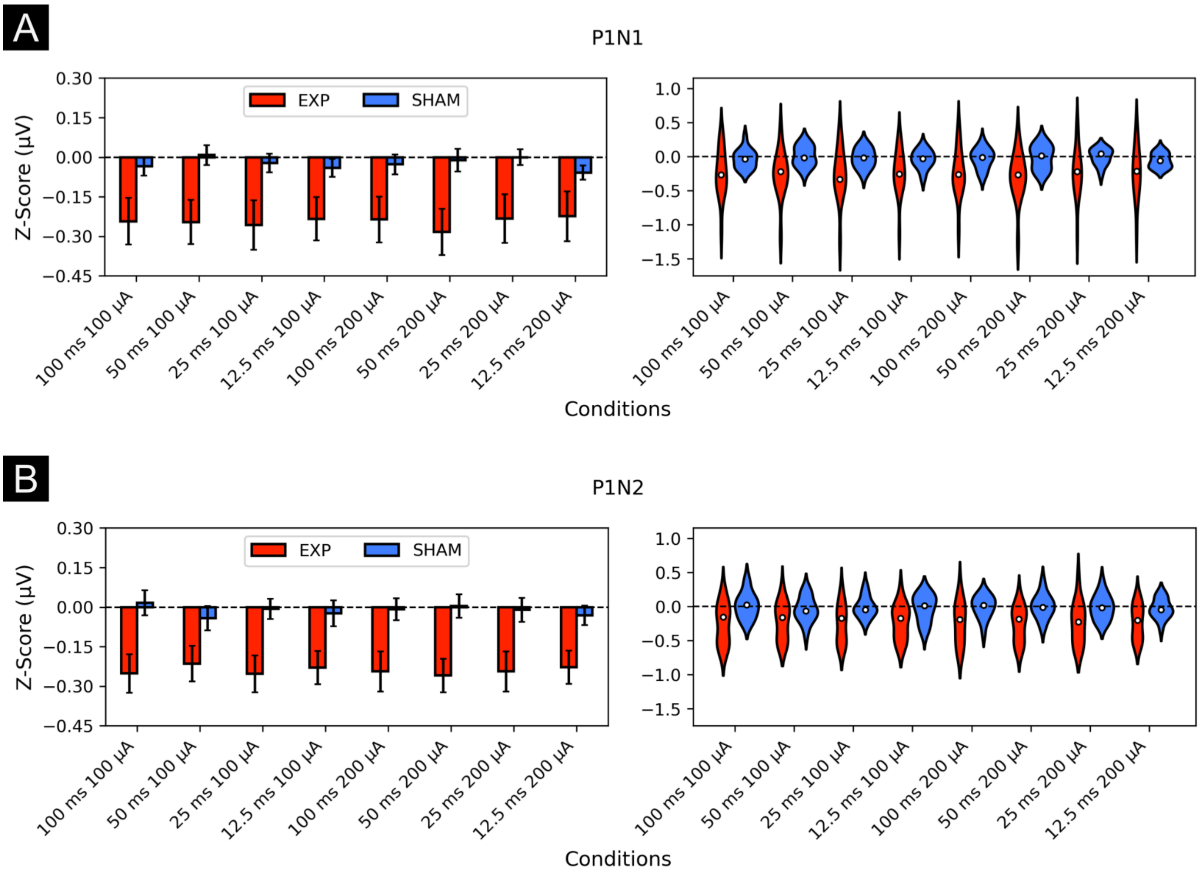

Figure 3-35. *Relative (procedure minus prologue) peak-to-peak VEP amplitudes for individual parameters (pulse durations and amplitudes) of periorbital current stimulation in experimental and placebo groups. (**A**) P1N1 relative peak-to-peak amplitude. (**B**) P1N2 relative peak-to-peak amplitude. Left panels in (A) and (B) present mean Z-scores values with standard error of the mean; right panels depict data distributions using violin plots with kernel density estimates for each condition. White dots within the individual violin plots indicate medians.*

Key takeaways:

1. Periorbital current pulse stimulation, preceding checkerboard reversal visual stimulus, elicited a significant, global reduction in VEP peak-to-peak P1N1 and P1N2 amplitudes (as compared to control, *prologue* values) not seen in the SHAM group.

2. There were no apparent amplitude differences attributable to specific pulse characteristics (duration or amplitude).

Short-Term Temporal Generalization of the Stimulation Effects

As can be seen in Figure 3-36, the reduction of VEP peak-to-peak amplitude was also observed for the *control* condition, i.e. CPR stimulus without preceding pPCS, that was present within each *procedure* block (see Figure 2-9 in methods). In the EXP group, mean relative VEP amplitudes were -0.250 for P1N1 and -0.235 for P1N2. Both were significantly different from zero, as indicated by the Wilcoxon signed-rank test (V = 18, p-value = 0.008, r = -0.735 for P1N1; V = 22, p-value = 0.016, r = -0.676 for P1N2). For the SHAM group no VEP reduction was detected (relative amplitudes were not different from zero, p-value = 0.782 for P1N1 and p-value = 1.000 for P1N2).

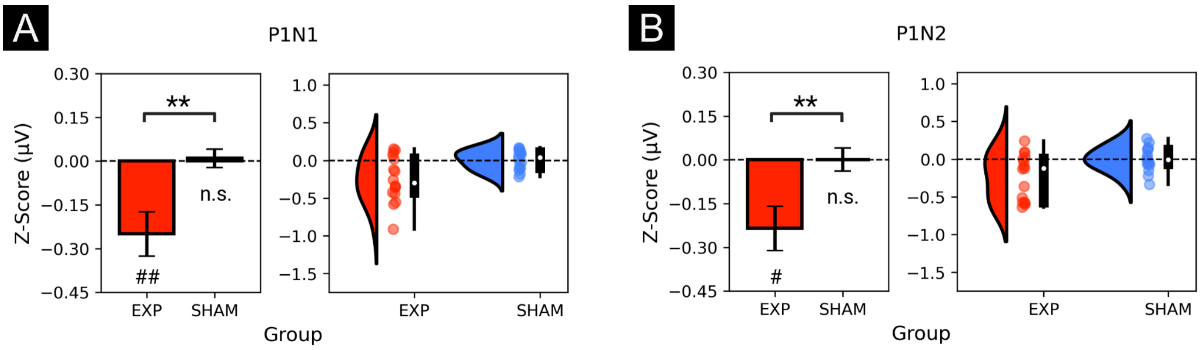

Figure 3-36. *Relative (procedure minus prologue) amplitudes of VEP evoked by control visual stimuli (checkerboard pattern reversal not preceded by single-pulse periorbital current stimulation) applied within each procedure block. (**A**) P1N1 relative peak-to-peak amplitude. (**B**) P1N2 relative peak-to-peak amplitude. Left panels in (A) and (B) present mean Z-scores values with standard error of the mean; right panels depict kernel density estimates of data with scatter plots and box plots. White dots in the box plots represent medians. Statistical significance is marked for the relative VEP amplitude difference from zero as* $^{\#\#}$ *(p-value < 0.01), or* $^{\#}$ *(p-value < 0.05); and by ** (p-value < 0.01) for EXP versus SHAM comparison, highlighting the short-term generalization of current stimulation effects compared to the placebo group.*

When the *control* condition was included in the two-way ANOVA analysis with all the pPCS variants from *procedure* block, the global "Group" effect was preserved for P1N1 and P1N2, along with the lack of "Condition" effects (Table 3-21), indicating that the *control* trials were no different from stimulation trials. Indeed, post-hoc Tukey's tests revealed no significant differences of the relative amplitudes between *control* and any of current stimulation trials (Table 3-22). On the other hand, in a between-group comparison for the *control* condition, the experimental group differed significantly from the placebo group for both peak-to-peak relative amplitudes (M_{diff} = -0.259, t = -2.753, d = -0.973, p-value = 0.006 for P1N1, M_{diff} = -0.236, t = -2.862, d = -1.012, p-value = 0.005 for P1N2).

Table 3-21. *Summary of two-way ANOVA results for the P1N1 and P1N2 relative amplitudes, including the sum of squares, degrees of freedom (df), mean square, F-statistic, p-values, and partial eta-squared (η²) for the main effects (group and condition) and their interaction term (group * condition) with the inclusion of control condition with eight pCS conditions. Amplitude data represented as Z-Scored potential values.*

Relative Amplitude	**Cases**	**Sum of Squares**	**df**	**Mean Square**	**F**	**p-value**	**η²**
P1N1	Group	3.666	1	3.666	51.701	< .001***	0.160
	Condition	0.032	8	0.004	0.057	1.000	0.001
	Group * Condition	0.076	8	0.009	0.133	0.998	0.003
	Residuals	19.145	270	0.071			
P1N2	Group	3.771	1	3.771	69.406	< .001***	0.204
	Condition	0.006	8	0.001	0.014	1.000	0.000
	Group * Condition	0.064	8	0.008	0.147	0.997	0.003
	Residuals	14.668	270	0.054			

*** - p-value < 0.001

Table 3-22. *Mean differences (single-pulse periorbital current stimulation [pCS] condition minus control condition) of relative VEP amplitudes, Cohen's d, t-values, and adjusted p-values from Tukey's post-hoc comparisons between the pCS and control conditions, listed for each pulse condition specified in the second column, for the P1N1 and P1N2 peak-to-peak relative amplitudes.*

Relative Amplitude	**Condition**	**Mean Difference: pCS Condition - *Control***	**Cohen's d**	**t**	**p-value$_{tukey}$**
P1N1	100 ms 100 µA	-0.019	-0.283	-0.071	1.000
	50 ms 100 µA	0.001	0.018	0.004	1.000
	25 ms 100 µA	-0.020	-0.295	-0.074	1.000
	12.5 ms 100 µA	-0.017	-0.253	-0.063	1.000
	100 ms 200 µA	-0.012	-0.178	-0.045	1.000
	50 ms 200 µA	-0.028	-0.414	-0.104	1.000
	25 ms 200 µA	0.003	0.050	0.013	1.000
	12.5 ms 200 µA	-0.021	-0.320	-0.080	1.000
P1N2	100 ms 100 µA	-0.001	-0.013	-0.003	1.000
	50 ms 100 µA	-0.012	-0.201	-0.050	1.000
	25 ms 100 µA	-0.013	-0.222	-0.056	1.000
	12.5 ms 100 µA	-0.010	-0.174	-0.043	1.000
	100 ms 200 µA	-0.009	-0.156	-0.039	1.000
	50 ms 200 µA	-0.011	-0.189	-0.047	1.000
	25 ms 200 µA	-0.010	-0.176	-0.044	1.000
	12.5 ms 200 µA	-0.013	-0.220	-0.055	1.000

Importantly, in the *epilogue* block, where only visual stimulation (CPRs) was applied (without preceding current pulses), VEP peak-to-peak amplitudes were not different from the *prologue* data (Figure 3-37), i.e. their relative amplitudes were not different from zero, as confirmed by the one-sample Wilcoxon test (EXP group P1N1: V = 64.000, p-value = 0.847, r = 0.067; P1N2: V = 50.000, p-value = 0.599, r = -0.167; SHAM group P1N1: V = 87.000, p-value = 0.348, r = 0.279; P1N2: V = 75.000, p-value = 0.744, r = 0.103).

In addition, we performed a one-way ANOVA to test for *epilogue* intergroup differences. Statistical significance was tested, first with Levene's test for equality of variances, which revealed significant differences between groups (F(1, 29) = 5.519, p-value = 0.026), prompting the use of Welch's correction for the one-way ANOVA. The corrected analysis indicated no significant differences between the VEP relative amplitudes from experimental and placebo groups (F(1, 21.659) = 0.052, p-value = 0.822), with an extremely small effect size ($\eta^2 = 0.002$) (Figure 3-37).

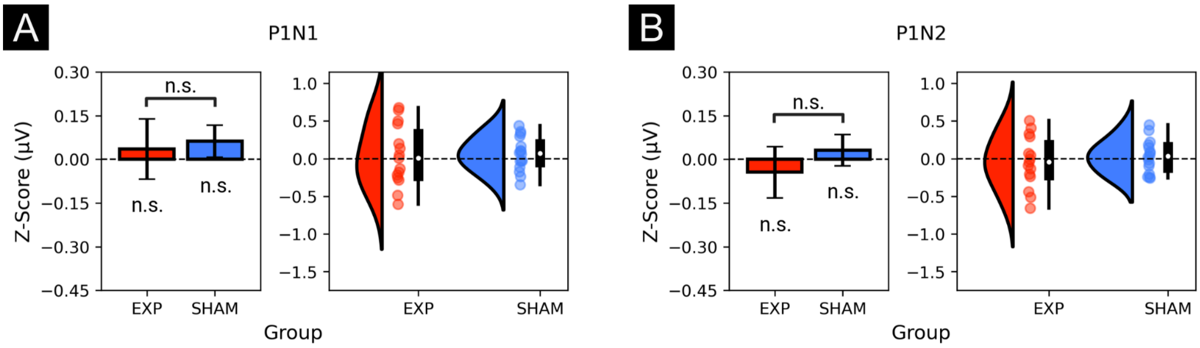

Figure 3-37. *Relative (epilogue minus prologue) VEP amplitudes of VEPs from final (epilogue) experimental block, during which no current stimulation was applied before checkerboard pattern reversal. (**A**) P1N1 relative peak-to-peak amplitude. (**B**) P1N2 relative peak-to-peak amplitude. Left panels in (A) and (B) present mean Z-scores values with standard error of the mean; right panels depict kernel density estimates of data with scatter plots and box plots. White dots in the box plots represent medians. There were no statistically significant differences neither when testing relative amplitudes difference from zero as well as between EXP and SHAM groups.*

Key takeaways:

1. The amplitude of VEP response to *control* visual stimulation, intermingled in a series of paired current + visual stimuli, was influenced (reduced) just as the responses to stimuli directly preceded by pPCS.

2. The lack of differential effects based on pulse characteristics, along with the impact on the sole visual responses suggests that the generalization might have occurred, leading to merging of partial effects related to individual pulse characteristics into a single, time-averaged current stimulation effect.

3. The global, generalized stimulation effect (reduction of VEP amplitude in all the trial types), observed in the *procedure* blocks, did not persist in the final experimental block (*epilogue*, during which the current stimulation was discontinued), emphasizing the transient nature of observed pPCS effects.

Dynamics of VEP Amplitude Changes Between Procedure Blocks

The observations from the experimental group had a larger variance (their distributions were more stretched and flattened as evidenced in Figures 3-34, 3-35, 3-36). Such large variance might have resulted from participant's unequal susceptibility to stimulation, but also from a complex dynamics of VEP amplitude changes between and within *procedure* blocks, which were pooled together in previous analyses. Thus, we measured VEP parameters for each block separately (Figure 3-38) and performed two-way ANOVA including "Group" and "Block" factors (Table 3-23).

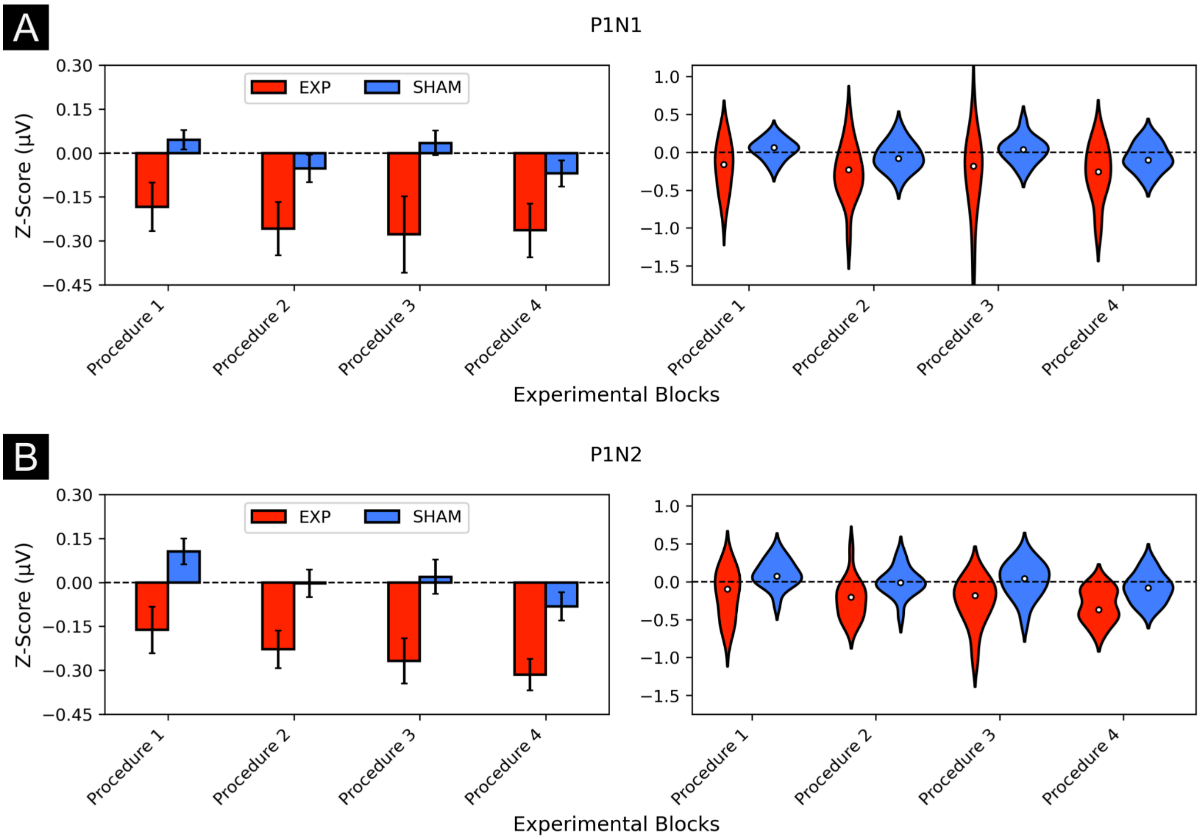

Figure 3-38. *Relative (procedure minus prologue) peak-to-peak P1N1 and P1N2 VEP amplitudes for individual procedure experimental blocks incorporating periorbital current stimulation conditions for the experimental and placebo groups. Left panels present mean Z-scores values with standard error of the mean; right panels depict data distributions using violin plots with kernel density estimates. White dots within the individual violin plots indicate medians.*

Table 3-23. *Two-way (group * block) ANOVA summary for the P1N1 and P1N2 relative amplitudes.*

Relative Amplitude	**Cases**	**Sum of Squares**	**df**	**Mean Square**	**F**	**p-value**	**η²**
P1N1	Group	1.774	1	1.774	18.702	< .001***	0.132
	Block	0.184	3	0.061	0.646	0.587	0.014
	Group * Block	0.069	3	0.023	0.241	0.868	0.005
	Residuals	11.380	120	0.095			
P1N2	Group	2.051	1	2.051	35.004	< .001***	0.214
	Block	0.467	3	0.156	2.657	0.051	0.049
	Group * Block	0.020	3	0.007	0.116	0.950	0.002
	Residuals	7.030	120	0.059			

*** - p-value < 0.001, * - p-value < 0.05

For the P1N1 relative amplitudes (Figure 3-38A), a two-way ANOVA revealed a significant main effect of "Group," with no significant main effect of "Block" or their interaction (Table 3-23). For the P1N2 relative amplitudes (Figure 3-38B), the two-way ANOVA (Table 3-23) showed a significant main effect of "Group" and a trend-level main effect of "Block," suggesting a potential difference in *procedure* effects across experimental blocks. However, the "Group * Block" interaction was not significant, indicating that the progression of the effect over blocks was similar in EXP and SHAM groups.

Table 3-24. *Tukey's post-hoc comparisons for the fixed factor "Block" for the P1N1 and P1N2 relative amplitudes.*

Relative Amplitude	**Block Comparisons**		**Mean Difference**	**t**	**Cohen's d**	**p-value**
P1N1	1	2	0.086	1.116	0.279	0.681
		3	0.053	0.684	0.171	0.903
		4	0.098	1.270	0.317	0.584
	2	3	-0.033	-0.431	-0.108	0.973
		4	0.012	0.154	0.039	0.999
	3	4	0.045	0.585	0.146	0.936
P1N2	1	2	0.088	1.451	0.363	0.470
		3	0.096	1.587	0.397	0.390
		4	0.170	2.816	0.704	0.029*
	2	3	0.008	0.136	0.034	0.999
		4	0.083	1.364	0.341	0.524
	3	4	0.074	1.228	0.307	0.610

* - p-value < 0.05

Post-hoc (Tukey's) comparisons indicated that the global (EXP and SHAM groups) progressive decrease of P1N2 amplitude reached significance for the comparison between block 1 and 4 (Table 3-24). No significant differences were detected for any other blocks neither for P1N2 nor for P1N1 amplitudes (Table 3-24). Also no significant differences were detected between blocks within EXP and SHAM groups (Table 3-25). Finally, the group effect was confirmed within blocks: for P1N1, significant differences between groups were observed in blocks 1 and 3, while blocks 2 and 4 showed trend-level effects; for P1N2, statistically significant differences between groups were observed across all blocks (Table 3-26).

Table 3-25. *Tukey's post-hoc group * block comparisons conditional on group.*

Group	**Relative Amplitude**	**Block Comparisons**		**Mean Difference**	**t**	**Cohen's d**	**p-value$_{\text{tukey}}$**
EXP	P1N1	1	2	0.074	0.681	0.241	0.904
			3	0.095	0.869	0.307	0.821
			4	0.081	0.741	0.262	0.880
		2	3	0.020	0.188	0.066	0.998
			4	0.007	0.060	0.021	1.000
		3	4	-0.014	-0.128	-0.045	0.999
	P1N2	1	2	0.067	0.779	0.275	0.864
			3	0.106	1.234	0.436	0.606
			4	0.153	1.784	0.631	0.286
		2	3	0.039	0.455	0.161	0.968
			4	0.086	1.005	0.355	0.747
		3	4	0.047	0.550	0.194	0.946
SHAM	P1N1	1	2	0.098	0.897	0.317	0.807
			3	0.011	0.099	0.035	1.000
			4	0.115	1.055	0.373	0.717
		2	3	-0.087	-0.798	-0.282	0.855
			4	0.017	0.158	0.056	0.999
		3	4	0.104	0.956	0.338	0.775
	P1N2	1	2	0.109	1.274	0.450	0.581
			3	0.086	1.011	0.357	0.744
			4	0.188	2.198	0.777	0.130
		2	3	-0.023	-0.263	-0.093	0.994
			4	0.079	0.924	0.327	0.792
		3	4	0.102	1.187	0.420	0.636

Table 3-26. *Tukey's post-hoc group * block comparisons conditional on block.*

Relative Amplitude	**Block**	**Mean Difference: EXP - SHAM**	**t**	**Cohen's d**	**p-value$_{tukey}$**
P1N1	1	-0.229	-2.102	-0.743	0.038*
	2	-0.205	-1.887	-0.667	0.062
	3	-0.313	-2.872	-1.015	0.005**
	4	-0.195	-1.788	-0.632	0.076
P1N2	1	-0.268	-3.129	-1.106	0.002**
	2	-0.225	-2.635	-0.931	0.010**
	3	-0.287	-3.353	-1.185	0.001**
	4	-0.232	-2.716	-0.960	0.008**

** - p-value < 0.01, * - p-value < 0.05

The lack of VEP amplitude reduction in the *epilogue* (Figure 3-37) suggested that the stimulation effects, despite the generalization within a 10 minutes *procedure* block, were not persistent enough to survive 3 minute *rest* periods separating consecutive blocks. On the other hand, there was a trend towards a progressive decrease in amplitude of the P1N2 component in successive *procedure* blocks, suggesting that some effects were nonetheless cumulative over time. However, since it was observed in both groups it probably reflected general factors, such as adaptation, rather than a direct result of pPCS.

Given the observed trends, we decided to analyze the dynamics within *procedure* blocks. VEPs from all current stimulation trials of each segment (see Figure 2-9 for a reminder of the experimental procedure scheme) were averaged, and relative amplitudes of peak-to-peak P1N1 and P1N2 components were calculated, as above. Obtained data and their linear regression lines are plotted in Figure 3-39 along the timeline of consecutive segments (i.e. in ~20 second steps). Details regarding regression results are presented in Table 3-27.

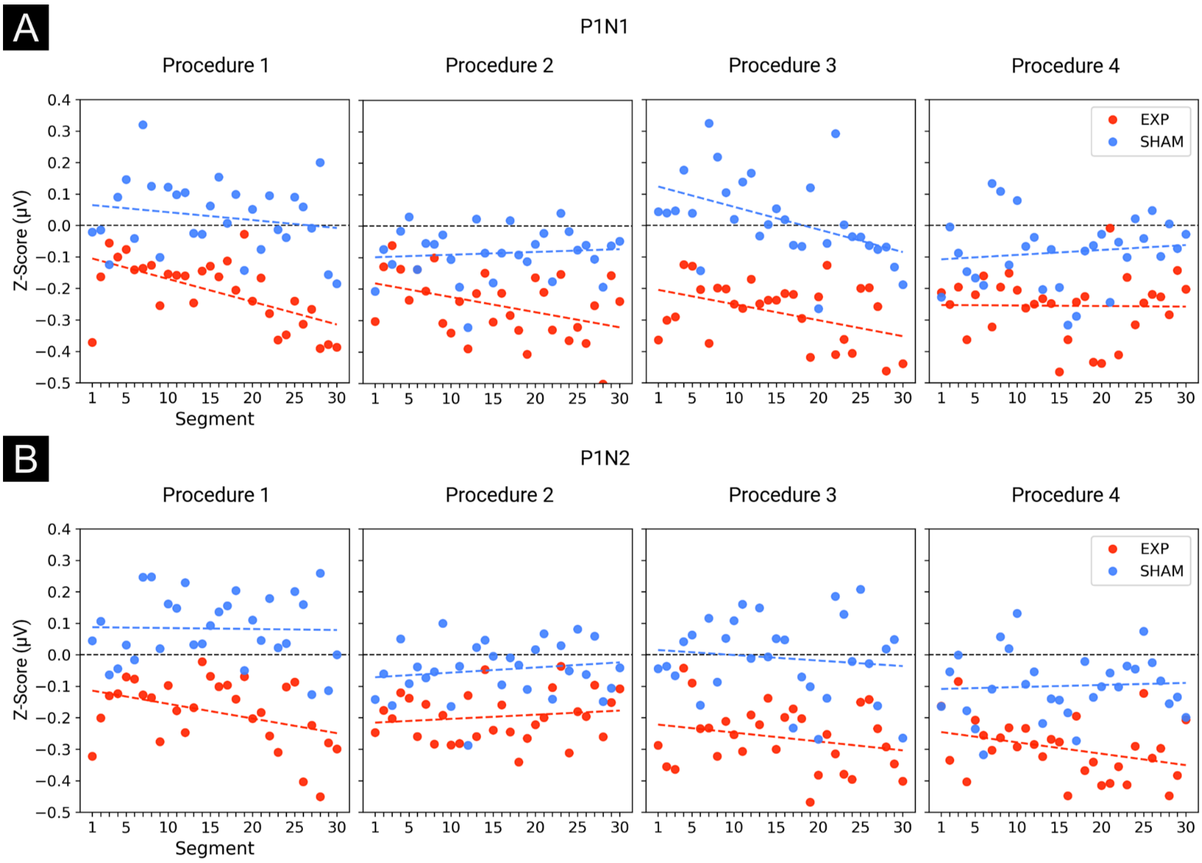

Figure 3-39. *Relative peak-to-peak amplitudes from each segment of four procedure blocks and their linear regression trends. (**A**) P1N1 and (**B**) P1N2. Data points represent averages over 18-second intervals (± 2 seconds), with a 2.25 ± 0.25 second gap due to the exclusion of the "Control" condition, where periorbital current stimulation was not applied before checkerboard pattern reversal in the experimental group. Dashed lines indicate linear regression fit for the respective procedure block.*

Table 3-27. *Summary of linear regression results including slopes, intercepts, and coefficients of determination (R^2) for P1N1 and P1N2 relative peak-to-peak amplitudes across experimental (EXP) and sham (SHAM) groups for individual procedure blocks. Statistical test results and their significance are included (t-test for slope, two-tailed). The y-end value represents the estimated amplitude at the end of each block based on the regression model ("inverted" intercept).*

Relative Amplitude	**Procedure Block**	**Group**	**Slope**	**Intercept**	**y-end**	**R^2**	**t**	**p-value**
P1N1	1	EXP	-0.007	-0.098	-0.315	0.363	-3.992	0.000***
		SHAM	-0.002	0.067	-0.008	0.037	-1.043	0.306
	2	EXP	-0.005	-0.177	-0.322	0.167	-2.370	0.025*
		SHAM	0.001	-0.100	-0.073	0.009	0.510	0.614
	3	EXP	-0.005	-0.200	-0.352	0.178	-2.466	0.020*
		SHAM	-0.007	0.131	-0.085	0.226	-2.856	0.008**
	4	EXP	0.000	-0.253	-0.258	0.000	-0.083	0.934
		SHAM	0.002	-0.109	-0.062	0.015	0.661	0.514
P1N2	1	EXP	-0.005	-0.109	-0.249	0.150	-2.219	0.035*
		SHAM	0.000	0.088	0.079	0.001	-0.131	0.896
	2	EXP	0.001	-0.217	-0.177	0.022	0.796	0.433
		SHAM	0.002	-0.073	-0.024	0.026	0.872	0.391
	3	EXP	-0.003	-0.219	-0.304	0.061	-1.348	0.189
		SHAM	-0.002	0.017	-0.036	0.015	-0.643	0.526
	4	EXP	-0.004	-0.242	-0.351	0.118	-1.934	0.063
		SHAM	0.001	-0.109	-0.089	0.003	0.300	0.766

*** - p-value < 0.001, ** - p-value < 0.01, * - p-value < 0.05

For the relative P1N1 amplitude, the largest decrease in the EXP group was observed during the first block of the procedure. This block exhibited the steepest slope, the greatest difference between the intercept and y-end, and the strongest, most statistically significant R^2 fit (Table 3-27). While decreases in amplitude were also observed in blocks 2 and 3, they were less pronounced compared to block 1. In block 4, the decrease was negligible. These findings suggest a possible weak trend towards partial transfer of the stimulation effect from one block to the next, which diminished in the absence of further current stimulation, as evidenced by the *epilogue* data. Additionally, the negligible decrease observed in block 4 may indicate the beginning of a plateauing effect, where the stimulation's influence reached its maximum and further reductions became minimal.

In the SHAM group, the slopes exhibited greater variability, alternating between negative and positive values for subsequent blocks. Overall relative amplitude trend was negative meaning that, between blocks 1 and 4 intercepts and y-ends decreased, but to lesser extent then in the EXP group (Table 3-26).

For the P1N2 relative amplitudes in the EXP group, the largest decrease was observed in the first block of the procedure, characterized by the steepest slope. The intercepts decreased progressively from block to block; but there was no such clear tendency for slopes, which also did not exhibit a clear plateau in the fourth block, as seen with the P1N1 relative amplitude. Notably, the R^2 value was statistically significant only in the first block, while the regression fit for the remaining three blocks was not significant, likely due to high variability in the data across subsequent segments. In the fourth block, however, the R^2 value was trend-level significant.

In the SHAM group, the slopes for P1N2 relative amplitudes remained close to zero, with regression results being insignificant across all blocks. However, the intercepts showed a continuous decrease across successive blocks, which, unlike in the EXP group, was not accompanied by a corresponding decrease in y-end values.

Key takeaways:

1. The change of VEP amplitude was progressing along the procedure blocks more intensively across earlier procedure blocks for both P1N1 and P1N2 relative amplitudes, with P1N1 effects reaching plateau earlier.
2. Group-specific differences: The experimental group exhibited clear and progressive effects, particularly on P1N1 amplitudes, while the placebo group showed negligible trends for P1N1 and only mild decreases for P1N2 amplitudes, highlighting the distinct impact of experimental conditions, and suggesting the co-occurrence of an adaptive mechanism independent of current stimulation.
3. Amplitude-specific trends: P1N1 amplitudes demonstrated stronger and more consistent within-block amplitude trend compared to P1N2, with higher R^2 values and steeper slopes, whereas P1N2 amplitude showed a potential for the continuous, between blocks decrease of amplitude in the experimental group.

Dynamics of VEP Amplitude Within Epilogue Block

As previously noted, the peak-to-peak VEP amplitudes (P1N1 and P1N2 components) during the *epilogue* were not different from the *prologue* i.e. the relative amplitudes were close to zero in both the experimental (EXP) and placebo (SHAM) groups (see Figure 3-37). To investigate how these amplitudes evolved over time within the *epilogue* block, we performed a linear regression analysis analogous to that described for the procedure blocks, measuring relative amplitudes across the 15 segments constituting the *epilogue*.

The analysis revealed distinct trends for the P1N1 and P1N2 peak-to-peak amplitudes, highlighting differential recovery patterns following the cessation of pPCS (see Figure 3-40 and Table 3-27). For the P1N1 peak-to-peak amplitude in the EXP group, the slope was minimal (0.002), the intercept was near zero (0.011), and the R^2 value was exceptionally low ($R^2 = 0.008$, p-value = 0.753). These findings suggest a stable response with no meaningful change in P1N1 values over the successive segments, indicating that the P1N1 peak-to-peak amplitude had fully returned to its pre-stimulation baseline state. In contrast, the SHAM group showed a larger slope (0.015), a more negative intercept (-0.063), and a moderately strong model fit ($R^2 = 0.430$, p-value = 0.008). This suggests that, unlike the EXP group, there was segmental variability in P1N1 amplitudes in the SHAM group, potentially reflecting non-experimental influences.

For the P1N2 peak-to-peak amplitude, a more dynamic pattern of recovery was observed. In the EXP group, the slope (0.011) and intercept (-0.133) were larger than those for P1N1, and the R^2 value ($R^2 = 0.354$, p-value = 0.019) indicated a stronger linear relationship across segments. These findings suggest a gradual trend towards recovery, with the P1N2 amplitude progressively approaching the pre-stimulation baseline over the course of the *epilogue*. Interestingly, the SHAM group also exhibited a recovery trend, likely reflecting the effects of repetitive visual stimulation alone. The SHAM group had a slightly larger slope (0.016), a less negative intercept (-0.094), and a stronger model fit ($R^2 = 0.413$, p-value = 0.010). These results indicate a comparable recovery trajectory in the SHAM group, though it likely stems from mechanisms unrelated to pPCS.

Taken together, these results demonstrate that while the P1N1 peak-to-peak amplitude in the EXP group returned to baseline with no discernible changes during the *epilogue* block, the P1N2 amplitude exhibited a more prolonged recovery process. The SHAM group, in contrast, showed subtle recovery trends for both components, with greater variability in P1N1 and a more pronounced recovery trajectory for P1N2. These findings highlight the transient and component-specific nature of VEP recovery dynamics and suggest that the cessation of stimulation leads to differential recovery processes, with P1N2 being more susceptible to time-dependent changes following the last *rest* block.

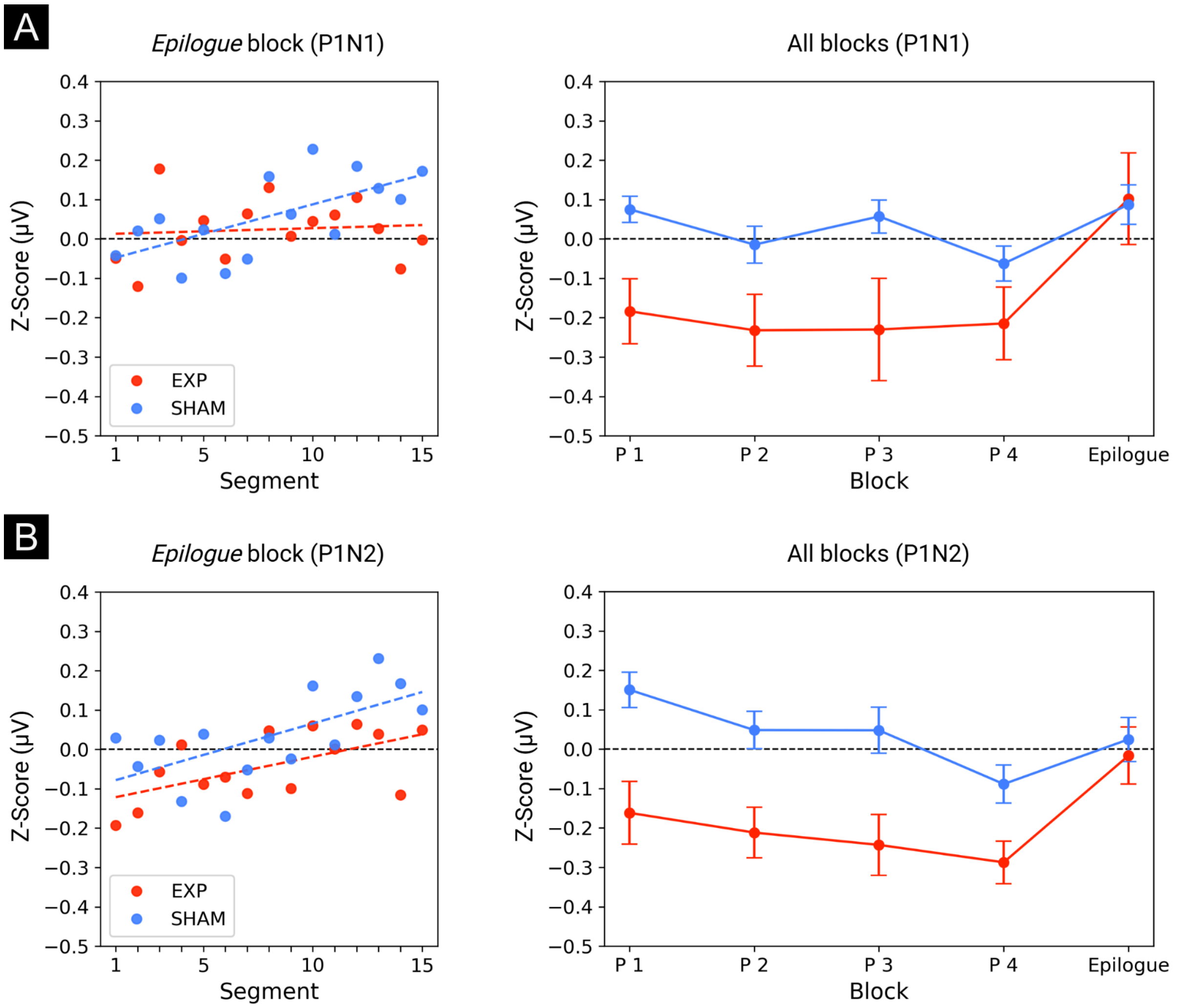

Figure 3-40. *Linear regression trends and block-level averages for P1N1 (**A**) and P1N2 (**B**) peak-to-peak amplitudes. Panel A presents linear regression trends for P1N1 Z-scores under experimental (EXP, red) and placebo (SHAM, blue) groups. The left subplot illustrates the relationship between segment number (independent variable) and P1N1 Z-scores (dependent variable) in the epilogue block. Individual data points represent averaged values for each of the 15 segments, with dashed lines indicating linear regression fits. Although the epilogue block lacked predefined segments (as it included only checkerboard pattern reversal without preceding current stimulation), it was divided into 15 segments, each comprising 8 epochs, averaged into single-point values. Each segment lasted approximately 18 seconds (± 2), and the block's total duration was about 5 minutes, shorter than the procedure blocks (approximately 10 minutes). The right subplot summarizes the average P1N1 Z-scores across all blocks, with error bars indicating the standard error of the mean (SEM). Panel B follows the same structure for P1N2 peak-to-peak amplitudes, displaying segment-level trends in the epilogue block (left) and block-wise averages with SEM across all procedure blocks (right).*

Table 3-27. *Summary of linear regression results including slopes, intercepts, and coefficients of determination (R^2) for P1N1 and P1N2 peak-to-peak amplitudes across experimental (EXP) and sham (SHAM) groups for the last experimental procedure block - epilogue.*

Relative Amplitude	Group	Slope	Intercept	R^2	t	p-value
P1N1	EXP	0.002	0.011	0.008	0.322	0.753
	SHAM	0.015	-0.063	0.430	3.130	0.008**
P1N2	EXP	0.011	-0.133	0.354	2.668	0.019*
	SHAM	0.016	-0.094	0.413	3.022	0.010**

** - p-value < 0.01, * - p-value < 0.05

Key takeaways:

1. Recovery in the *epilogue* block indicates the transient nature of single-pulse pPCS effects, with both P1N1 and P1N2 peak-to-peak amplitudes returning to baseline, and P1N2 demonstrating the most pronounced slope-based recovery.

Summary of the Results

Simulation of Electric Field Induced by Single-Pulse Periorbital Current Stimulation

- **The proper conductivity values.** The default conductivity values provided in the SimNIBS program for simulating the induced electric field are likely inaccurate. We recommend using databases such as the one provided by the Swiss IT'IS Foundation, ensuring that conductivity values are for frequencies not exceeding 1 MHz.

- **Edge effect and its correlates.** The electrode's edge effect is influenced by the current density and the curvature of the electrode edge. Electrodes with sharper curvature or smaller edges produce a more pronounced edge effect, leading to localized intensification of the electric field.

- **Specificity of single-pulse periorbital current stimulation.** The use of small self-adhesive electrodes in single-pulse sinusoidal biphasic periorbital current stimulation achieves nearly half the current density of conventional tDCS protocols, with a several-fold reduction in total charge. This approach ensures greater specificity in targeting the initial visual pathway, preserves effectiveness in stimulating the visual system even at significantly lower current levels, and enables integration with visual stimuli in experimental and rehabilitation paradigms.

- **Periorbital vs. frontal-occipital stimulation.** The periorbital electrode configuration is particularly suited for focusing stimulation on the eyeballs and anterior visual structures, providing localized effects. The frontal-occipital configuration delivers broader stimulation, covering also the optic nerves and occipital cortex.

Responses to Single-Pulse Periorbital Current and LED Stimulation (Study 1)

- **Phosphene detection.** Detection thresholds and latency were influenced by both current amplitude and pulse duration, with shorter pulses necessitating higher amplitudes. A custom three-factor Naka-Rushton model, incorporating total charge, amplitude, and duration, accurately predicted valid response rates for pulses with specific characteristics. The 50 and 100 ms current pulses detection approached the response levels (accuracy and response times) elicited by light stimuli.

- **Evoked potentials.** Effective current pulses (50, 100 ms) elicited occipital activity comparable to visual stimuli, with robust responses observed at the Oz electrode in the 150-300 ms window. Based on the electrophysiological response to LED-like current pulses, it can be assumed that subjects experienced a phosphenic sensation, which was reflected in their behavioral responses.

Effects of Pre-Stimulus Single-Pulse Periorbital Current Stimulation (Study 2)

- **Global stimulation effect.** Pre-stimulus periorbital current stimulation reduced P1N1 and P1N2 VEP relative amplitudes. The effect was consistent across pulse characteristics. The effect diminished during the *epilogue* block, after the cessation of current stimulation in the *epilogue* block, indicating its transient nature.

- **Short-term generalization.** Current stimulation effects generalized during procedure blocks, resulting in similar VEP amplitude reductions in all trials types including control no-stimulation condition.

- **Dynamics between *procedure* blocks.** There was a weak trend for P1N2 relative amplitude to decrease from block to block. Current stimulation effects on P1N1 relative amplitude stabilized earlier than P1N2.

Discussion

Computer Simulations as a Tool for Planning Electrical Brain Stimulation

The aim of this dissertation was to assess the optimal configuration for single-pulse periorbital pulsed current stimulation (pPCS) targeting the initial stages of the visual system, evaluate its impact on visual system activity, and explore its modulation potential. First, a modeling approach was employed to simulate the effects of electrode size, shape, and placement on the distribution and range of the induced electric field. Such methods are increasingly utilized in basic neuroscience research and are gradually being integrated into clinical applications (Haberbosch et al., 2019; Evans et al., 2020; Joshi et al., 2023).

Current Density and Electrode Shape as the Prime Determinant of Edge Effect

The current density at the electrode surface, and in particular the edge effect, can influence the safety and effectiveness of electrical stimulation from a technical and clinical point of view. Excessively high concentration of the electric field at the electrodes' edges can trigger safeguard mechanisms in stimulation devices, interrupting the stimulation protocol. It may also lead to an uneven distribution of the electric field across the stimulated surface, reducing the uniformity and precision of the stimulation. Furthermore, this localized intensification can cause discomfort for the participant, potentially limiting the tolerability and feasibility of the protocol (Minhas et al., 2011).

The edge effect results from the combined impact of boundary conditions (applied potential) and electrode geometry (sharp edges, corners, etc.). These factors determine the local enhancement of the potential gradient, which translates into increased electric field intensity. According to Ohm's law for electrolytes, this stronger electric field drives higher current densities at the edges. Therefore, the phenomenon is a result of coupling between electrode geometry and the conduction equations, rather than a simple cause-effect relationship of "current density → field" or "field → current density" (Miranda et al., 2006; Thielscher et al., 2011; Lavelaine de Maubeuge, 2011; Opitz et al., 2015; Lee et al., 2018).

It was previously suggested that the edge effect was particularly strong at the corners of square electrodes (e.g. Minhas et al., 2011). We thus asked if electrode design could prevent the problem i.e. reduce the edge effect. The results of our simulation consistently showed that edge effects persisted regardless of the electrode shape. Importantly, for small electrodes (standardized to 3 cm² in our example), the differences in edge effect intensity between square and oval shape were negligible, reinforcing the conclusion that the overall current density, rather than geometry, primarily governs edge effects. On the other hand, for larger electrodes, such as sponge-covered rectangular and ellipsoidal types with a 35 cm² surface area, the second determinant of edge effects - electrode curvature - became more evident. Sharper angles in rectangular electrodes led to higher field intensities at corners (as previously shown by Minhas et al., 2011), while ellipsoidal electrodes exhibited a more uniform distribution at the edges, but with more high values. Obviously, any curvature of the electrode shape intensifies edge effects, leading to the lowest values at straight lines of square electrodes with "hot-spots" at their corners, and on average higher values on rounded shapes. Intriguingly, we have not seen the hot-spots on small, square electrodes, probably due to insufficient resolution of computer simulation.

Ultimately, two key aspects should guide the selection of stimulation electrodes: surface area, which determines the overall current density for a given stimulation amplitude, and curvature, which influences its distribution at electrode edges. The ellipsoid (or rounded) electrodes could provide a more uniform edge effect - reducing the risk of participant's adverse sensation due to corner "hot-spots", and ensuring more uniform (and predictable) electric field lines and current density. In conclusion, although localized field intensifications at edges persist regardless of the electrode shape, minimizing edge effects and ensuring participant safety depend primarily on carefully controlling (reducing) current density. These principles should inform the design and selection of electrodes for clinical and research applications (Ambrus et al., 2011; Lee et al., 2010; Kessler et al., 2013).

Electrode Placement as a Determinant of Stimulation Targets

In the conducted computer simulations of the induced electric field (IEF), we investigated two electrode configurations for electrical stimulation of the visual system: (1) a bipolar periorbital setup, and (2) a bipolar frontal-occipital setup. The simulations revealed distinct patterns of electric field magnitude (EFM) and current density magnitude (CDM) distributions, underscoring the influence of electrode placement on the extent, localization and potential therapeutic applications of periorbital current stimulation (pCS) regardless of the characteristics of the stimulation signal.

In the literature we can find few studies describing the range of the electric field induced within close proximity to the eyeballs. However, none of them tested bipolar-transorbital electrode placement analyzed in this thesis. Laakso and Hirata (2013) showed that regardless of the location of the stimulation electrodes on the head, the shunting phenomenon led current paths through the soft tissue towards low resistive eyeballs which worked as a gateway to the brain. The phenomenon was strongest for an electrode pair located at Fpz and Oz, for which the current entered through the eyeballs at such an angle that both the upper eyeballs and the optic nerves should be stimulated for this configuration. This was confirmed by our simulations for electric field magnitude results for the frontal-occipital electrodes' configuration. According to Laakso and Hirata (2013), a substantial portion of injected current should travel via eyeballs even with central transverse electrode montage (T3-T4); the minimal effect was predicted with occipital transverse montage (PO7-PO8).

Another computer simulation was described in the paper by Gall et al. (2016), who used repetitive transorbital alternating current stimulation for the therapy of optic neuropathies. They simulated the current distribution evoked by a stimulation via a single 10 mm diameter circular electrode placed over the eyebrow arch and a reference electrode modeled as the "last axial slice of the neck region" (as in the real application they had the reference on the right arm). The results showed that the IEF had the greatest effect on the upper part of the eyeball and to a lesser extent on the onset of the optic nerve. Proportionally smaller effects on the prefrontal cortex and lower cerebellum and the brainstem were also observed; the latter attributed to the flow towards the return electrode. Despite a different location of the reference electrode, the simulation results for the eyeball have similarities with what we observed for our frontal-occipital configuration - high field values at the top of the eyeball.

Here we confirmed the effectiveness of the single current pulse (applied via two electrodes placed above and below the eye) in inducing a highly localized electric field and current density, concentrated primarily in the anterior-middle segments of the eyeballs. This focused targeting aligns with interventions aimed at modulating early visual processing regions, such as the retina and proximal optic nerve structures. Evidence suggests that such precise electrode positioning can enhance retinal ganglion cell activity or preserve optic nerve function (Gall et al., 2010; Fedorov et al., 2011; Sabel et al., 2011, 2020b) in conditions like optic neuropathy and early glaucoma. Not only it can stimulate neuronal activity but also enhance survival mechanisms like increased IGF-1 production by Müller cells, as was shown in the study on axotomized retinal ganglion cells in rats (Morimoto et al. 2005).

In the frontal-occipital electrodes configuration induced electric field still dominated the eyeballs and optic nerves but also covered the frontal and occipital cortex. Such a setup could support more extensive interventions by engaging both subcortical and cortical sites, thereby leveraging network-level plasticity. Indeed such tES approach was shown to offer potential benefits for complex disorders like cortical visual impairments and post-stroke vision deficits (Sabel et al., 2020b; Elyamany et al., 2021).

The extent of electric field induced in the head tissues is one measure of stimulation range, the other question regards the extent of the effective current density. Our simulations indicated that the distributions of electric field magnitude (EFM) and current density magnitude (CDM) were different for the same stimulation parameters - in particular in the case frontal-occipital electrode position. While EFM patterns indicated the broader spatial reach of frontal-occipital stimulation, CDM remained relatively concentrated near the eyes and optic nerves similarly to bipolar periorbital electrodes' placement. These findings align with the principle that current intensity and field directionality critically depend on electrode montage and tissue conductivities (Klaus and Schutter, 2021; Hunold et al., 2023). Such distinctions highlight the importance of considering both EFM and CFM when designing stimulation protocols, as CDM may more directly correlate with the focus of directed stimulation, whereas EFM reveals the overall "footprint" of the stimulation field in the spatial domain - i.e., showing focal effects versus the broader spread of stimulation (Miranda et al., 2006, 2013; Datta et al., 2008; Opitz et al., 2015).

The simulation of CDM indicated that the "pure" bipolar periorbital stimulation as well as periorbital with occipital reference electrode, both concentrate their impact on the initial stage of visual pathway. Importantly, such localized impact should not preclude the activation of consecutive stages of visual processing, much like visual stimulation with light is not confined to the eyes alone. This expectation was confirmed for the bipolar periorbital current stimulation in our experiment (Study 1) during which participants were able to consciously react to stimulation evoked phosphenes. Phosphenes could of course be also of a cortical origin (Oster, 1970), however we believe that in case of periorbital stimulation focused on the beginning of the visual pathway (eyeballs) they had a retinal genesis, i.e. were induced by the electrical activation of retinal ganglion cell. The modeling approach (our and (Laakso and Hirata, 2013)) confirmed the concentration of the current flow within the eyeball, but there is also an experimental confirmation of this conviction in the invasive study in rats, in which tetrodotoxin (TTX) was infused into eyeballs before transcorneal electrical stimulation (Foik at al. 2015). The blockade of the retinal ganglion cells by TTX resulted in the absence of both – natural VEPs and electrically evoked potential. In this study, the retina was shown to be a necessary medium to evoke EEP not only in eye-eye but also in an eye-neck electrode configuration – the analog of the frontal-occipital configuration for which simulation also indicated the eye region as main focus of induced electric field and peak of current density. Thus, a frontal-occipital configuration may activate the visual pathway mainly via the retina, however thanks to the broader extent of electric field, it may impact other stages of visual processing in a subthreshold way, promoting neuromodulation-related processes across extended neural circuits (To et al., 2018; Antal et al., 2022) and potentially synergize with cognitive retraining exercises, pharmacotherapy, or rehabilitation protocols aimed at higher-order visual processing and perception.

To summarize, the current findings support the notion that electrode positioning should be strategically chosen based on the desired therapeutic or investigative outcome, and tested with a simulation approach – a principle echoed in the literature on electrical stimulation optimization for years (Antal et al., 2022).

Conductivity and its Impact on Electric Field and Current Density Magnitudes

Another important issue during simulation of neuronal activity as well as stimulation effects is the correct software and parameters. Our computer simulations were performed with SimNIBS – a popular and well established open-source software package designed and used for simulating electric fields induced in the human brain by TMS or TCS (original description by Thielscher et al., 2015 was cited 402 times in articles and conference papers). However, we have chosen to use conductivity parameters different from the default values, which we believe to be inappropriate.

The Default Conductivity Values in SimNIBS

The default conductivity values in SimNIBS for white matter (WM), gray matter (GM), cerebrospinal fluid (CSF), bone, and scalp are based on Wagner et al. (2004), with additional values for eyeballs, compact bone, and spongy bone from Opitz et al. (2015), and for blood and muscles from Gabriel et al. (2009). However, discrepancies in these sources raise significant concerns. Wagner et al.'s conductivity values are purportedly derived from earlier works by Geddes and Baker (1967), Geddes (1989), and Holton and Walker (1990). Yet, the 1967 publication provides resistance, not conductivity values, for unrelated tissues, and we could not find "Geddes 1989". Instead, Geddes (1987) includes resistivity values for GM (250 Ohm/cm) and WM (750 Ohm/cm) without sources, which, when converted to conductivity ($\sigma = 1/\rho$), do not match Wagner et al.'s references. Similarly, Holton and Walker (1990) use resistivity values attributed to Geddes and Baker (1967) but derived via unclear methods, also failing to align with values cited by Wagner et al. Consequently, the origins of the reported conductivity values remain unverifiable, casting doubt on their reliability.

Opitz et al. (2015) cited a conductivity value of 0.5 S/m for the eyeball, referencing Gabriel et al. (1996). However, Gabriel et al. did not provide a single conductivity value for the entire eyeball but instead reported various values for its components: cornea (1.05 S/m), lens cortex (0.72 S/m), lens nucleus (0.33 S/m), and retina (1.42 S/m). The origin of the commonly cited 0.5 S/m value remains unclear but may represent an average of the lens cortex and lens nucleus conductivities, yielding 0.525 S/m. Additionally, Gabriel et al. (1996) reported conductivity averages for frequencies up to 100 GHz, which is not appropriate for neuromodulation studies. Beyond 100 MHz, water - the primary source of tissue conductivity - exhibits significant changes in its properties, including a decrease in permittivity and an increase in conductivity, rendering higher-frequency data irrelevant for most biological and stimulation contexts.

Lastly, Gabriel et al. (2009) provide conductivity values for muscle and blood that match the default values in SimNIBS. The reported muscle conductivity of 0.16 S/m corresponds to transverse conductance, with additional values given for 0° (0.15 S/m) and 90° (0.19 S/m), reflecting angle-specific measurements rather than a general, angle-independent value. For blood, the conductivity is listed as 0.6 S/m. However, these values are specific to a narrow frequency range of 40-70 Hz, further limiting their applicability to broader contexts.

From a technical perspective, modern electrical stimulators can generate frequencies up to several hundred kilohertz, with specialized devices reaching into the megahertz range. However, biological tissue properties impose constraints. Above several hundred kilohertz, the capacitive nature of cell membranes reduces stimulation effectiveness as they act more like insulators (McAdams and Jossinet, 1995). Thus, conductivity values for simulations and experiments should focus on frequencies below this threshold.

Neuromodulation therapies typically use frequencies tailored to physiological properties: DBS operates between 130–200 Hz for Parkinson's disease (Benabid et al., 2009), while SCS for chronic pain uses up to 10 kHz to alleviate pain without paresthesia (Baranidharan et al., 2021). Experimental techniques like kilohertz frequency alternating current (KHFAC) blockade employ 5–50 kHz frequencies for reversible nerve inhibition (Kilgore and Bhadra, 2004). Frequencies in the megahertz range are more suitable for tissue heating, such as radiofrequency ablation, rather than neural stimulation due to safety concerns like tissue damage (Diederich, 2005).

Safety limits are critical, as neurons have a maximum firing rate of ~1 kHz, and higher frequencies can lead to significant heating and tissue damage (McCreery et al., 1990). Frequencies exceeding 10 kHz are mostly restricted to non-neural applications, as extremely high frequencies bypass cellular ion channels and fail to induce neural activity (Reilly, 1992). Therefore, frequencies below 10 kHz dominate neuromodulation, while conductivity values up to 1 MHz remain relevant for simulations involving the mammalian nervous system, balancing accuracy and physiological relevance.

The default conductivity values for selected tissues in SimNIBS software appear to have been inappropriately or arbitrarily chosen, without adequate consideration of the complexities of mammalian nerve tissue conductivity or the relevant frequencies for both invasive and non-invasive stimulation. This issue is perpetuated in numerous studies using SimNIBS for simulations and in research addressing tissue conductivity for electric field modeling. While we do not imply any bad intentions, the origin of these default values remains unclear, despite their widespread citation in influential publications.

It is puzzling why these incorrect values have been accepted for so long, particularly given that Saturnino et al. (2019), affiliated with the SimNIBS team, have highlighted how variations in tissue conductivity significantly affect IEF characteristics. This is especially concerning given the extensive reliance on IEF simulations in exploring electrical stimulation for cognitive enhancement, psychiatric treatments, and neurorehabilitation. Accurate conductivity values are critical for individualized assessments of optimal IEF doses, as emphasized by studies such as Haberbosch et al. (2019), Evans et al. (2020), and Joshi et al. (2023).

Given these considerations, we recommend using conductivity values based on reliable data below 1 MHz, such as those provided by the Swiss ITIS Foundation (2024), as a more accurate starting point for simulations.

Conductivity Impact on Electric Field and Current Density Magnitudes

Simulations performed with SimNIBS default conductivity values (not shown in the thesis) compared with those based on Swiss ITIS Foundation (2024) confirmed that the assumed conductivity properties of various tissues exerted a profound influence on EFM and CDM distributions. Lowering the scalp conductivity increased the superficial EFM beneath the electrodes by 151% (from 0.4457 V/m to 1.1187 V/m), indicating stronger field accumulation at the surface and reduced penetration into deeper tissues. Conversely, nerve tissues (e.g. retina in the eyeballs, optic nerves) experienced lower EFM but higher CDM. The optic nerve's EFM declined by 23.9% (0.0134 V/m to 0.0102 V/m), while its CDM nearly doubled, increasing by 105.9% (from 0.0017 A/m^2 to 0.0035 A/m^2), reflecting a more focused and intense current delivery to these neural structures. These patterns highlight the delicate interplay between tissue conductivities and the balance between field spread and current intensity.

The results are important in the light of growing demand for individualized medicine, including individualized dosing strategies in transcranial electrical stimulation. Evans et al. (2020) showed that fixed-dose approaches yield variable IEFs due to anatomical differences, whereas individualized dose strategies (i.e. adjusting input current to anatomy based on computer simulations of IEF) produce more uniform electric fields across individuals. However, to realize the full potential of these individualized approaches, a critical intermediate step involves not only the scanning of individual head anatomy, but also refining the tissue conductivity assumptions. Our findings suggest using standardized references databases - such as those provided by the Swiss ITIS Foundation (2024), however the ideal scenario would be to directly estimate subject-specific conductivities (e.g. via magnetic resonance electrical properties tomography, MR-EPT; Mandija et al., 2021). Another refinement strategy would be to opt for a more detailed segmentation, for example, by dividing the eye into its individual components and assigning specific conductivity values to each (Lee et al., 2021a). The choice depends on the insights we aim to gain regarding the influence of the induced electric field.

Effective Activation of Visual Pathway by Single-Pulse Periorbital Current Stimulation

A phosphene is the phenomenon of perceiving light sensations or flashes of light without actual stimulation of the retina by visible light. It can be triggered by mechanical pressure on the eyeball, electrical stimulation of the visual system, changes in neuronal activity, or magnetic stimulation. In our experiment we monitored behavioral responses to phosphenes to measure the effectiveness of various current stimulation configurations and find the minimal effective current pulse parameters. The data indicated clear perceptual thresholds that depended jointly on pulse duration and amplitude. As expected, the longer was the current pulse and the higher its amplitude, the greater was the chance that the participant would give a response attesting to having experienced phosphene. However the relation was not linear. Shortest pulses (10 ms) produced a few detections only at 300 µA, which is consistent with the notion that transient stimulation requires a higher intensity to surpass the neuronal activation threshold (Legge, 1978). On the other hand, pulses of 50 and 100 ms with an amplitude of 100 µA were already sufficient to generate responses in ~70% of trials. Such a large change in effectiveness was not linearly dependent on the total charge delivered to the RGCs. More specifically, the total charge of a 10 ms 300 µA pulse (1.06 µC) equals to 60% of that of a 50 ms 100 µA pulse (1.77 µC) and 30% of that of a 100 ms 100 µA pulse (3.54 µC). Evidently, then, it is not only the total load delivered to the system that matters, but also the time at which its value is delivered. An estimation based on the custom three-factor Naka-Rushton model indicated that 50 ms 100 µA (about 70% of the maximum behavioral response), should offer a good compromise between increasing the reliability of activation of the visual system activation (and evoking phosphene perception) and minimizing the current pulse intensity.

Unfortunately, directly comparing our results to the existing literature is challenging. Previous studies have examined phosphene thresholds primarily in two distinct contexts: (1) using transcranial magnetic stimulation (TMS) paradigms to assess cortical excitability in relation to stimulation "dose" (e.g. Taylor et al., 2010), thereby producing phosphenes of cortical origin, and (2) employing transcorneal electrical stimulation (TES) to investigate the thresholds of electrically evoked, retinal-origin phosphenes for clinical ophthalmological applications - specifically, to quantitatively assess the level of information transfer from the eye to the cortex in both healthy individuals and those with various ophthalmic conditions (Naycheva et al., 2012). It would therefore be most appropriate to relate our study to this second research, in which 10 ms biphasic pulses with defined amplitudes and durations were applied at specified intervals, effectively creating trains with particular stimulation frequencies. Increasing the frequency of the applied pulses led to a reduction in the amplitude required to elicit phosphenes, pointing to the importance of the accumulation of the current impact within stimulation train/session – exactly as we saw for VEP amplitudes in our Study 2. However, there was no information in (Naycheva et al., 2012) paper about the duration of a train (nor the number of pulses), so the total stimulation time and a resulting accumulated total charge could not be estimated. Thus, while the phosphene detection thresholds reported by Naycheva et al. (2012) (i.e. 109 ± 76 µA for the healthy participants and a slowest, 3 Hz train) seemed to be much lower when compared to our 10 ms pulses, they should rather be compared with the longer ones. For a current pulse amplitude of approximately 100 µA, the three-factor Naka-Rushton model based on our data suggests that stimulation durations of ~42 ms (which would equal to four 10 ms pulses) and ~30 ms (3 x 10 ms pulse) are required to achieve detection rates of 50% and 5%, respectively.

A relationship between longer pulse durations and higher amplitudes with reliable phosphene induction underscores the interplay between total charge, charge density, and temporal summation of neural responses. Intriguingly, the similarity of response rates between 50 ms and 100 ms pulses at higher amplitudes suggests a ceiling effect beyond a certain temporal threshold for single-pulse pCS. Moreover, the above mentioned study (Naycheva et al., 2012) reported inverted-U shape relationship between stimulation frequency (and supposed accumulated stimulus duration) with a peak at 20 Hz. Such a saturation effect likely reflects inherent physiological constraints in membrane depolarization and neuronal firing patterns (Reato et al., 2010; Wischnewski et al., 2023). Our findings indicate that an optimal balance of pulse parameters can yield perceptual outcomes indistinguishable from natural visual stimuli. Although increasing pulse duration beyond 50 ms did not substantially enhance response rates, maintaining sufficient amplitude remained critical for achieving near-ceiling perceptual performance.

There is an important reservation, that the detection of transorbital electrical stimulation might have been based not on actual activation of the visual system (and perception of phosphenes, but instead on the tactile perception at the electrode's site which typically accompanies the stimulus (e.g. Ambrus et al., 2011; Minhas et al., 2011). We strongly believe that it was not the case. First of all, the areas under the electrodes were anesthetized, ruling out or at least limiting tactile sensations. The response latency for the effective, longer and stronger pCS pulses were not not statistically different from those to natural LED stimuli (~300 ms) while reaction times for cutaneous or auditory stimuli are typically much shorter (approximately 100 ms, Woods et al., 2015). Finally, we recorded electrophysiological signals to confirm the activation of the visual cortex. A challenge arose, due to current artifacts in the EEG signal, which made it impossible to analyze the early components, such as the P1 typically occurring around 100 ms after the onset of a visual stimulus. There was however an undisturbed late P2 component of 150-300 ms, commonly associated with the integration of visual stimulus information and with local generators in the occipito-parietal regions (Johannes et al., 1995; Freunberger et al., 2007). This time window was previously utilized to determine the occurrence of a phosphene experience in TMS study (Taylor et al., 2010). The authors concluded that zero activity within this time corresponded to the absence of a phosphene experience. Our results confirm this conclusion as no P2 responses were observed for the 10 ms pulses for which there was practically no phosphene detection. There was also a similarly nonlinear relation between the stimulation parameters and behavioral and electrophysiological responses. It is worth noting that Höffken et al. (2013) identified a significant correlation between individual phosphene thresholds and paired-pulse suppression in central V1, highlighting a meaningful relationship between these measures.

Nonlinear Relationship Between Stimulation Parameters and Behavior and Electrophysiology

It is worth highlighting that our study observed nonlinear responses to pPCS depending on its parameters. This nonlinearity was evident both at the behavioral level, as reflected in valid response rate and valid response time and at the electrophysiological level, as demonstrated by the averaged late P2 component in the 150-300 ms time window. These findings align with research on the intensity-specific effects of tACS, which similarly demonstrate distinctly nonlinear patterns (Zhao et al., 2023). This nonlinear behavior can be further understood through the Naka-Rushton equation (Naka and Rushton, 1966), which effectively models the relationship between stimulus intensity and neural response. The Naka-Rushton framework describes how neural responses increase with stimulus strength but eventually saturate, resulting in reaching a plateau beyond a certain intensity threshold. This model has been widely applied to various physiological responses in the visual system, where it captures the nonlinear dynamics of retinal and cortical responses to increasing light intensity (Anastasi et al., 1993; Binns et al., 2011). Similarly, in the context of pPCS, the observed saturation effect in all three levels, i.e. response accuracy, latency and EEP amplitude, suggests that further increases in stimulation strength may yield minimal improvements in response outcomes (see Figure 3-26, right panel, and Figure 3-31C).

Effects of Pre-Stimulus Single-Pulse Periorbital Current Stimulation

The application of the current pulse before the visual stimulation reduced the peak-to peak amplitudes of VEPs. The effect was independent of the current parameters (amplitude and duration), and applied also to control trials without stimulation intermingled in the series of the stimulated trials. VEP reduction was evident during all four experimental blocks and was gone in the *epilogue* block when visual stimuli were no longer preceded by current pulses.

Paired associative stimulation (PAS) is a neuromodulation technique that relies on timing-dependent plasticity, where the temporal alignment of two stimuli - one peripheral and one cortical - induced potentiation or depression of synaptic connections and, thus, cortical excitability increase or cortical habituation (Classen et al., 2004; Wischnewski and Schutter, 2016). In non-invasieve experimental setting the direct cortical stimulation is achieved by current or magnetic stimulation. Such approach was used in the study by Ranieri et al. (2019), who reported that TMS applied prior to the checkerboard reversal stimulus had an inhibitory effect on VEPs (P1N1 and P1N2 amplitudes), whereas TMS applied after reversal exerted a facilitatory effect (i.e., it reversed habituation trends). Similar effects were observed in our study (to some extent). The pPCS in form of single pulses applied prior to visual stimulus reduced the amplitudes of early VEP components (P1N1 and P1N2), consistent with the inhibitory effects reported by Ranieri and colleagues (2019) for pre-reversal cortical TMS. These inhibitory effects may result from alterations in the excitability state of the visual cortex, demonstrating how pre-stimulus modulation affects subsequent visual processing.

There are however important differences between the studies - our bipolar periorbital pPCS stimulation was focused on the eye and it was predominantly suprathreshold, while TMS pulses were applied directly over visual cortex and were below the phosphene induction threshold. Thus, our experimental paradigm did not follow the typical pattern of PAS, as we actually had two peripheral stimuli – first induced by the electrical, and second by the visual activation of the retina. It reproduced, rather, the paradigm of the paired pulse stimulation (PPS), which also leads to a decrease of a neural response to the second sensory stimulus (e.g. Höffken et al., 2008). PPS is a well established protocol to measure signatures of excitation and inhibition in human subjects. It consists of application of pairs of stimuli in close succession.

Short-Term Generalization of Stimulation Effects

The observed stimulation effects were independent of the stimulation parameters and also “infiltrated” trials with the presentation of a visual stimulus not preceded by the application of a current pulse (i.e., the so-called *control* condition). This short-term generalization of stimulation effects align well with earlier work suggesting that PPS protocols can induce widespread neural adaptation effects, in which the subtle differences between the parameters of individual stimuli blur, the impact averages out, and the effects build up over time (Dinse et al., 2023).

The uniform suppression of P1N1 and P1N2 components across varying pulse characteristics in our experiment may be attributed to mechanisms of temporal integration and generalized neural adaptation. Sequential application of pulses with differing attributes can lead to uniform activation of intracortical inhibitory processes resulting in a generalized suppression response that is independent of specific pulse parameters (Dinse et al., 2023). Additionally, repetitive stimulation patterns with limited recovery time between pulses may induce cortical averaging effects, whereby the brain integrates inputs over time, diminishing sensitivity to parameter variations (Grill-Spector et al., 2006). This phenomenon aligns with findings from paired pulse suppression protocols, which demonstrate that repeated stimulation reduces neural response variability emphasizing global suppression over parameter-specific effects (Rangarajan et al., 2020). This may also explain the observed stimulation effects in the *control* condition, in which the visual stimulus was not preceded by the application of a current pulse. Interestingly, such paired pulse suppression effect diminishes with age, as demonstrated in the somatosensory cortex of rats (David-Jürgens and Dinse, 2010) and in the motor cortex of healthy older adults (Smith et al., 2009), suggesting that the most prominent use of the effect in rehabilitation may be in younger people.

The observed suppression effects align with the concept of paired pulse suppression, wherein shorter temporal intervals between stimuli in PPS protocols lead to stronger suppression of the neural response to the second stimulus. In the visual system, this effect is particularly pronounced for interstimulus intervals (ISIs) below 100 ms (Höffken et al., 2008). This phenomenon is thought to primarily reflect intracortical inhibition mechanisms mediated by GABAergic processes (Wehr and Zador, 2005). To be more specific, intracortical inhibition involves the activation of GABAergic interneurons, which suppress the excitatory activity of pyramidal neurons in the visual cortex. This suppression mechanism ensures that neural circuits are not overstimulated, maintaining a balance between excitation and inhibition (Tremblay et al., 2016). In paired pulse suppression, the first stimulus triggers an inhibitory feedback loop that diminishes the neural response to the second stimulus, particularly at shorter ISIs (Höffken et al., 2008). Studies suggest that such inhibitory dynamics are essential for temporal coding and sensory processing efficiency, allowing the visual system to prioritize novel or temporally distinct stimuli while filtering out redundant or closely timed inputs (Wehr and Zador, 2005).

Delayed Habituation Through Repetitive and Paired Pulse Stimulation

Last but not least, the observed amplitude reduction progressively increased across blocks, as evidenced by a steady decline in P1N1 and P1N2 relative amplitudes, suggesting an ongoing delayed habituation process. In the placebo group, repetitive visual stimulation led to noticeable habituation, evidenced by a progressive decline in P1N1 and P1N2 amplitudes across blocks. In the experimental group, repetitive visual stimulation within a paired pulse paradigm with preceding single pulse pCS resulted in both paired pulse suppression and habituation, as indicated by progressive intensification of the observed paired pulse suppression effects over the course of the experiment. The observed trend is consistent with repetitive stimulation in both PPS (Dinse et al., 2023) and PAS (e.g. Ranieri et al., 2019) protocols.

The paired pulse suppression mechanism, as explained in the previous paragraph, occurs with the consecutive application of two stimuli separated by tens of milliseconds and affects the response to the second stimulus. In contrast, the delayed habituation mechanism arises from the repetitive application of these stimuli, resulting in a progressive reduction in VEP amplitude with successive presentations of visual stimuli over the course of minutes. Notably, shorter intervals between stimuli lead to stronger habituation (Omland et al., 2011). According to Makul'kin and Pedanov (1972), repeated visual stimuli trigger corticofugal impulses that inhibit the activating reticular formation while enhancing the thalamic synchronizing system. This leads to changes in brain function, characterized by a slowing of cortical rhythms and a reduction in evoked potential amplitudes. Additionally, the habituation of VEPs is thought to depend on various "tonic" non-specific and motivational circuits, including brainstem monoaminergic nuclei, ascending thalamocortical loops, and the activity of intracortical inhibitory circuits (Coppola et al., 2013a, 2013b).

In our study, the time interval for checkerboard pattern reversal was 2.25 ± 0.25 seconds. So the frequency was about 0.44 Hz with a range of 0.4 Hz to 0.5 Hz. Omland and colleagues (2011) in a simple paradigm of repetitive visual stimulation noted that the presentation of checkerboard pattern reversals at 3 Hz results in about 30% more intense habituation from block to block than at 1.5 Hz. This suggests that decreasing the temporal distance between presentations in our study could intensify the observed habituation. Moreover, Ranieri and colleagues (2019) showed that delayed habituation also occurs in the PAS paradigm, in which repeated checkerboard pattern reversal presentations are each preceded by the application of a magnetic pulse over the visual cortex. Interestingly, if the magnetic pulse is applied 25 ms after the presentation of a visual stimulus, the habituation process is nullified. Considering that our experiment aligns most closely with the PPS protocol, it is unlikely that applying a current pulse following the checkerboard pattern reversal would produce a similar effect. However, altering the configuration of the stimulation electrodes - such as switching to a frontal-occipital setup or placing the electrodes exclusively over the occipital cortex - might achieve the desired outcome.

Potential in Neurorehabilitation

It is essential to address the potential of single-pulse pCS in clinical use and neurorehabilitation. The potential applications of this approach in the visual system are extensive. It can be utilized to study key parameters such as phosphene detection thresholds and reaction times, allowing for the identification of differences between healthy individuals and those with visual deficits (Taylor et al., 2010, Naycheva et al., 2012). It holds promise for inducing molecular and cellular changes within the eyeballs, such as stimulating the production of trophic factors to support neurorehabilitation in conditions like glaucoma (Morimoto et al., 2005). With adequate pattern of periorbital electrodes, the stimulation effects can be focused in anterior (as in bipolar periorbital montage), upper (frontal-occipital montage) or posterior portion of eyebulb (multielectrode periorbital montage; Sadrzadeh-Afsharazar and Douplik, 2023). This method was already shown to aid in the restoration of visual functions in cases of neuropathy or post-stroke recovery by enhancing neural plasticity along the visual pathway (Silverstein et al., 2019; Sabel et al., 2020b; Joy and Carmichael, 2021; Zhang et al., 2023b).

Recent studies have highlighted the potential of targeted electrical and magnetic stimulation to induce cell-specific plasticity and structural changes at the neuronal level, further underscoring the potential utility of pPCS in neurorehabilitation. Lee et al. (2024) demonstrated that electric field stimulation could entrain neural activity in a cell class-specific manner (Lee et al., 2024), allowing precise modulation of different neural populations. The specificity of cell classes to electric field entrainment is achieved through a combination of subthreshold membrane polarization, which is uniform across cell types, and cell-class-specific excitability properties. Excitatory pyramidal neurons entrain to both slow and fast electric fields, while inhibitory neurons, such as parvalbumin and somatostatin types, primarily respond to high-frequency stimulation. This differentiation is largely dictated by intrinsic firing rates and ion channel properties, which align the temporal dynamics of each cell class with the applied electric field. This finding is particularly relevant to pCS, as it suggests the possibility of tailoring stimulation to activate specific types of neurons within the visual cortex, potentially enhancing rehabilitation outcomes. Similarly, Beros et al. (2024) reported that static magnetic stimulation could induce structural plasticity at the axon initial segment of inhibitory cortical neurons. Such plasticity has significant implications for balancing excitatory and inhibitory dynamics in the visual system, which is critical for restoring function after neural damage. Finally, Iwasa et al. (2024) explored the role of electrical stimulation in enhancing neural repair through stem cell-based interventions. Their findings showed that electrical fields not only modulate the behavior of existing neurons but also influence the integration and function of transplanted stem cells, opening new avenues for neural repair in the visual system. This aligns with the potential of pPCS to act as a complementary approach in regenerative medicine for conditions involving the visual pathway.

Together, these studies illustrate how small-scale and cell-specific approaches, enabled by precise stimulation techniques like single-pulse periorbital pulsed current stimulation, could improve neurorehabilitation. By leveraging targeted plasticity and structural modulation, pPCS has the potential to support both functional recovery and foundational research in visual system dynamics.

Limitations and Challenges

Computer Simulations of the Induced Electric Field

Computer simulations of the IEF for pCS face several limitations. A key challenge lies in determining accurate tissue conductivity values. Standardized conductivity databases, such as those from the Swiss ITIS Foundation (2024), provide a foundation, but individualized estimations (e.g. via MR-EPT) could further improve precision (Mandija et al., 2021). Anatomical variability remains another obstacle; simulations must account for differences in individual head and eye anatomy to ensure consistent IEF patterns. Simplified segmentation approaches, which divide the head into major components, may overlook the nuanced effects of detailed structures, such as individual ocular tissues (Lee et al., 2021a). Further, the interplay between stimulation parameters, such as electrode configuration and pulse duration, and their effects on phosphenes, retinal function, and cortical excitability, needs systematic exploration. Existing evidence, such as from Evans et al. (2020), highlights the value of individualized dosing, but refining computational models is essential to predict behavioral and physiological outcomes reliably. EEG signal simulations also lack clarity on what aspects of the neural signal are removed versus retained after artifact removal, complicating validation efforts. Addressing these limitations through enhanced modeling pipelines, including patient-specific conductivity and structural data, can make pPCS a more personalized and effective tool for research and clinical neurorehabilitation.

Data Analysis in Studies with pPCS

Analyzing data from studies involving pPCS is inherently challenging due to the complexity of removing current-induced artifacts. These artifacts obscure neural signals, making it difficult to interpret the results and evaluate pPCS effects reliably. This is particularly crucial when analyzing neural activity occurring during the application of pPCS. Several approaches to artifact removal have been proposed, each with limitations. Linear filtering methods, such as those described in this study (see Figure 3-29) and a 2020 publication by Żebrowska and colleagues, provide practical solutions but may fail to account for the intricate overlap of artifacts and true neural signals. More advanced nonlinear methods, such as Signal-Space Projection (SSP) used in ACS studies, as described by Vosskuhl et al. (2020), may offer better artifact suppression but require significant adaptation for pPCS applications. Additionally, artifact removal methods inspired by MRI techniques, which model the spatial and temporal characteristics of artifacts, hold promise but demand precise knowledge of artifact sources (Allen et al., 2000), which is difficult to achieve in pPCS.

Fitting Models

The Naka-Rushton model, while effective for describing response saturation, has limitations when applied to current stimulation. It relies on total charge calculations optimized for biphasic sinusoidal impulses, requiring adjustments for other pulse types, such as rectangular or monophasic pulses. Additionally, fitting models often suffer from insufficient data points; sparse matrices of experimental data points are inadequate for capturing complex parameter-response relationships - a data is here a key. The model’s generalizability across different stimulation modalities is also limited without further refinement. Expanding data coverage and tailoring the model to specific stimulation types are essential to improve accuracy and applicability.

Limitations of the Studies Reported in the Thesis and Future Directions

Limitations

Few aspects of the studies reported in the thesis had their additional limitations. In both studies conducted, the number of participants was relatively small for the large spread of measured values. Increasing the sample size could improve the statistical power of the analysis, reduce the impact of outliers, and provide more reliable inference outcomes based on the observed effects, enhancing generalizability of the findings. Furthermore, the paradigm used in the Study 2, which mixed different parameters of current pulses, led to a generalization of stimulation effects, making it impossible to isolate the influence of specific stimulation parameters. To address this, future studies should be conducted using distinct blocks or groups dedicated to different current stimulation strengths and durations. Blocks or groups with short, weak pulses could focus on examining the effects of subthreshold stimulation in modulating VEPs, while those with strong, suprathreshold pulses could explore the level of inhibition within the paired-pulse suppression paradigm.

Future Directions

Future research could focus on several key areas to expand our understanding of pPCS in the form of single pulses and its applications. First, more advanced simulations of the IEF should be conducted, integrating detailed structural data and individualized conductivity values. These simulations should be correlated with neuronal activity observed during pPCS application under specific parameters to improve the precision and predictive power of the models. Second, experimental studies could investigate the effects of applying pPCS during and after a visual stimulus to determine whether it enhances cortical excitability and increases the amplitude of visual responses, as well as whether it will inhibit the process of delayed habituation. Third, the effects of using short segments of alternating current or random noise stimulation in a PPS paradigm, applied both before and after a visual stimulus, should be explored to understand whether longer stimulation protocols differ from single pulse approaches. Finally, the effects of PPS should be translated into clinical applications. For example, single current pulses, short segments of alternating current, or random noise stimulation could be applied at specific temporal intervals relative to diagnostic visual stimuli in computer-based perimetry (e.g., Dzwiniel et al., 2017) to attempt to modify the detection threshold of the diagnostic stimulus. Such an approach could evaluate the potential of pPCS in the neurorehabilitation of basic visual functions, particularly for addressing visual field deficits associated with visual pathway dysfunctions.

Summary and Conclusions

This dissertation explored the feasibility and potential of single-pulse periorbital pulsed current stimulation (pPCS) as a promising neuromodulation method for visual system rehabilitation.

The computational simulations confirmed that periorbital current stimulation (pCS) configurations can effectively stimulate ocular regions while minimizing the total current compared to traditional transcranial electrical stimulation settings. Moreover, simulations demonstrated that current density could be concentrated within the eyeballs, enabling precise modulation. However, the findings also revealed limitations of commonly used simulation tools, such as SimNIBS, which rely on default conductivity values that are arbitrary and incorrect. Instead, reliable sources like the Swiss ITIS Foundation (2024) database or subject-specific conductivity estimations (e.g. MR-EPT) are recommended for accurate simulations. The proposed use of disposable, self-adhesive EMG electrodes can further improve the practicality of pCS by reducing preparation time and ensuring better hygiene.

Behavioral and electrophysiological experiments in Study 1 demonstrated that single-pulse pPCS effectively induced phosphene perception, with a generation threshold observed at a 10 ms 300 µA pulse. The three-factor custom Naka-Rushton model provided valuable insights into the dynamics of single-pulse pPCS responses, including the saturation effect for pulse duration at higher stimulation levels. Behavioral metrics, such as valid response rate and valid response time, were closely correlated with electrophysiological markers, including the P2 late potential. Notably, for 50 and 100 ms pCS pulses, responses plateaued in both behavioral and electrophysiological dimensions, approaching logarithmically but not fully matching the levels elicited by LED flashes.

In Study 2, pre-conditioning electrical pulses applied prior to visual stimuli significantly modulated cortical excitability like in paired pulse stimulation (PPS) and paired associative stimulation (PAS) studies. These pulses reduced early VEP amplitudes (P1N1 and P1N2) induced by checkerboard pattern reversals, demonstrating inhibitory effects. Additionally, the stimulation effects infiltrated trials not directly preceded by single-pulse pPCS, indicating a lasting influence on neural activity beyond immediate stimulation windows. This lingering impact underscores the temporal modulation capabilities of single-pulse pPCS and its potential in shaping cortical responses over extended periods.

The combined findings of this research emphasize the critical role of tailored stimulation parameters in achieving effective neuromodulation. By refining the interplay between stimulation duration, amplitude, and individual variability, single-pulse pPCS offers a novel pathway for visual system rehabilitation. This work not only advances fundamental understanding but also presents a scalable and targeted neuromodulation approach with promising clinical applications.

References

1. Abd Hamid, A. I., Gall, C., Speck, O., Antal, A., & Sabel, B. A. (2015). Effects of alternating current stimulation on the healthy and diseased brain. Frontiers in neuroscience, 9, 391. https://doi.org/10.3389/fnins.2015.00391

2. Agadagba, S. K., Lim, L. W., & Chan, L. L. H. (2023). Advances in transcorneal electrical stimulation: From the eye to the brain. Frontiers in cellular neuroscience, 17, 1134857. https://doi.org/10.3389/fncel.2023.1134857

3. Aldrich, M. S., Alessi, A. G., Beck, R. W., & Gilman, S. (1987). Cortical blindness: etiology, diagnosis, and prognosis. Annals of neurology, 21(2), 149–158. https://doi.org/10.1002/ana.410210207

4. Alekseichuk, I., Wischnewski, M., & Opitz, A. (2022). A minimum effective dose for (transcranial) alternating current stimulation. Brain stimulation, 15(5), 1221–1222. https://doi.org/10.1016/j.brs.2022.08.018

5. Allen, P. J., Josephs, O., & Turner, R. (2000). A method for removing imaging artifact from continuous EEG recorded during functional MRI. NeuroImage, 12(2), 230–239. https://doi.org/10.1006/nimg.2000.0599

6. Ambrus, G. G., Antal, A., & Paulus, W. (2011). Comparing cutaneous perception induced by electrical stimulation using rectangular and round shaped electrodes. Clinical neurophysiology : official journal of the International Federation of Clinical Neurophysiology, 122(4), 803–807. https://doi.org/10.1016/j.clinph.2010.08.023

7. Anastasi, M., Brai, M., Lauricella, M., & Geracitano, R. (1993). Methodological aspects of the application of the Naka-Rushton equation to clinical electroretinogram. Ophthalmic research, 25(3), 145–156. https://doi.org/10.1159/000267283

8. Anastassiou, C. A., Perin, R., Markram, H., & Koch, C. (2011). Ephaptic coupling of cortical neurons. Nature neuroscience, 14(2), 217–223. https://doi.org/10.1038/nn.2727

9. Antal, A., & Herrmann, C. S. (2016). Transcranial Alternating Current and Random Noise Stimulation: Possible Mechanisms. Neural plasticity, 2016, 3616807. https://doi.org/10.1155/2016/3616807

10. Antal, A., & Paulus, W. (2013). Transcranial alternating current stimulation (tACS). Frontiers in human neuroscience, 7, 317. https://doi.org/10.3389/fnhum.2013.00317

11. Antal, A., Alekseichuk, I., Bikson, M., Brockmöller, J., Brunoni, A. R., Chen, R., Cohen, L. G., Dowthwaite, G., Ellrich, J., Flöel, A., Fregni, F., George, M. S., Hamilton, R., Haueisen, J., Herrmann, C. S., Hummel, F. C., Lefaucheur, J. P., Liebetanz, D., Loo, C. K., McCaig, C. D., … Paulus, W. (2017). Low intensity transcranial electric stimulation: Safety, ethical, legal regulatory and application guidelines. Clinical neurophysiology : official journal of the International Federation of Clinical Neurophysiology, 128(9), 1774–1809. https://doi.org/10.1016/j.clinph.2017.06.001

12. Antal, A., Boros, K., Poreisz, C., Chaieb, L., Terney, D., & Paulus, W. (2008). Comparatively weak after-effects of transcranial alternating current stimulation (tACS) on cortical excitability in humans. Brain stimulation, 1(2), 97–105. https://doi.org/10.1016/j.brs.2007.10.001

13. Antal, A., Kincses, T. Z., Nitsche, M. A., & Paulus, W. (2003). Manipulation of phosphene thresholds by transcranial direct current stimulation in man. Experimental brain research, 150(3), 375–378. https://doi.org/10.1007/s00221-003-1459-8

14. Antal, A., Kincses, T. Z., Nitsche, M. A., Bartfai, O., & Paulus, W. (2004). Excitability changes induced in the human primary visual cortex by transcranial direct current stimulation: direct electrophysiological evidence. Investigative ophthalmology & visual science, 45(2), 702–707. https://doi.org/10.1167/iovs.03-0688

15. Antal, A., Luber, B., Brem, A. K., Bikson, M., Brunoni, A. R., Cohen Kadosh, R., Dubljević, V., Fecteau, S., Ferreri, F., Flöel, A., Hallett, M., Hamilton, R. H., Herrmann, C. S., Lavidor, M., Loo, C., Lustenberger, C., Machado, S., Miniussi, C., Moliadze, V., Nitsche, M. A., … Paulus, W. (2022). Non-invasive brain stimulation and neuroenhancement. Clinical neurophysiology practice, 7, 146–165. https://doi.org/10.1016/j.cnp.2022.05.002

16. Antal, A., Nitsche, M. A., & Paulus, W. (2006). Transcranial direct current stimulation and the visual cortex. Brain research bulletin, 68(6), 459–463. https://doi.org/10.1016/j.brainresbull.2005.10.006

17. Arcaro, M. J., McMains, S. A., Singer, B. D., & Kastner, S. (2009). Retinotopic organization of human ventral visual cortex. The Journal of neuroscience : the official journal of the Society for Neuroscience, 29(34), 10638–10652. https://doi.org/10.1523/JNEUROSCI.2807-09.2009

18. Azhdam, A. M., Goldberg, R. A., & Ugradar, S. (2020). In vivo measurement of the human vitreous chamber volume using computed tomography imaging of 100 eyes. Translational Vision Science & Technology, 9(1), 2. https://doi.org/10.1167/tvst.9.1.2

19. Baranidharan, G., Edgar, D., Bretherton, B., Crowther, T., Lalkhen, A. G., Fritz, A. K., & Vajramani, G. (2021). Efficacy and Safety of 10 kHz Spinal Cord Stimulation for the Treatment of Chronic Pain: A Systematic Review and Narrative Synthesis of Real-World Retrospective Studies. Biomedicines, 9(2), 180. https://doi.org/10.3390/biomedicines9020180

20. Başar, E., Başar-Eroglu, C., Karakaş, S., & Schürmann, M. (2001). Gamma, alpha, delta, and theta oscillations govern cognitive processes. International journal of psychophysiology : official journal of the International Organization of Psychophysiology, 39(2-3), 241–248. https://doi.org/10.1016/s0167-8760(00)00145-8

21. Belden C. J. (2002). MR imaging of the globe and optic nerve. Magnetic resonance imaging clinics of North America, 10(4), 663–678. https://doi.org/10.1016/s1064-9689(02)00018-1

22. Benabid, A. L., Chabardes, S., Mitrofanis, J., & Pollak, P. (2009). Deep brain stimulation of the subthalamic nucleus for the treatment of Parkinson's disease. The Lancet. Neurology, 8(1), 67–81. https://doi.org/10.1016/S1474-4422(08)70291-6

23. Beros, J. L., King, E. S., Clarke, D., Jaeschke-Angi, L., Rodger, J., & Tang, A. D. (2024). Static magnetic stimulation induces structural plasticity at the axon initial segment of inhibitory cortical neurons. Scientific reports, 14(1), 1479. https://doi.org/10.1038/s41598-024-51845-7

24. Bestmann, S., & Walsh, V. (2017). Transcranial electrical stimulation. Current biology : CB, 27(23), R1258–R1262. https://doi.org/10.1016/j.cub.2017.11.001

25. Binns, A. M., Mortlock, K. E., & North, R. V. (2011). The relationship between stimulus intensity and response amplitude for the photopic negative response of the flash electroretinogram. Documenta ophthalmologica. Advances in ophthalmology, 122(1), 39–52. https://doi.org/10.1007/s10633-010-9257-7

26. Boije, H., Shirazi Fard, S., Edqvist, P. H., & Hallböök, F. (2016). Horizontal Cells, the Odd Ones Out in the Retina, Give Insights into Development and Disease. Frontiers in neuroanatomy, 10, 77. https://doi.org/10.3389/fnana.2016.00077

27. Bola, M., Gall, C., Moewes, C., Fedorov, A., Hinrichs, H., & Sabel, B. A. (2014). Brain functional connectivity network breakdown and restoration in blindness. Neurology, 83(6), 542–551. https://doi.org/10.1212/WNL.0000000000000672

28. Borucki, D., Rohrer, B., & Tomlinson, S. (2024). Complement propagates visual system pathology following traumatic brain injury. Research square, rs.3.rs-3970621. https://doi.org/10.21203/rs.3.rs-3970621/v1

29. Bosking, W. H., Beauchamp, M. S., & Yoshor, D. (2017). Electrical Stimulation of Visual Cortex: Relevance for the Development of Visual Cortical Prosthetics. Annual review of vision science, 3, 141–166. https://doi.org/10.1146/annurev-vision-111815-114525

30. Bowmaker, J. K., & Dartnall, H. J. (1980). Visual pigments of rods and cones in a human retina. The Journal of physiology, 298, 501–511. https://doi.org/10.1113/jphysiol.1980.sp013097

31. Brignani, D., Ruzzoli, M., Mauri, P., & Miniussi, C. (2013). Is transcranial alternating current stimulation effective in modulating brain oscillations?. PloS one, 8(2), e56589. https://doi.org/10.1371/journal.pone.0056589

32. Buzsáki, G., Anastassiou, C. A., & Koch, C. (2012). The origin of extracellular fields and currents--EEG, ECoG, LFP and spikes. Nature reviews. Neuroscience, 13(6), 407–420. https://doi.org/10.1038/nrn3241

33. Camilleri, R., Pavan, A., & Campana, G. (2016). The application of online transcranial random noise stimulation and perceptual learning in the improvement of visual functions in mild myopia. Neuropsychologia, 89, 225–231. https://doi.org/10.1016/j.neuropsychologia.2016.06.024

34. Camilleri, R., Pavan, A., Ghin, F., Battaglini, L., & Campana, G. (2014). Improvement of uncorrected visual acuity and contrast sensitivity with perceptual learning and transcranial random noise stimulation in individuals with mild myopia. Frontiers in psychology, 5, 1234. https://doi.org/10.3389/fpsyg.2014.01234

35. Campana, G., Camilleri, R., Moret, B., Ghin, F., & Pavan, A. (2016). Opposite effects of high- and low-frequency transcranial random noise stimulation probed with visual motion adaptation. Scientific reports, 6, 38919. https://doi.org/10.1038/srep38919

36. Campana, G., Camilleri, R., Pavan, A., Veronese, A., & Lo Giudice, G. (2014). Improving visual functions in adult amblyopia with combined perceptual training and transcranial random noise stimulation (tRNS): a pilot study. Frontiers in psychology, 5, 1402. https://doi.org/10.3389/fpsyg.2014.01402

37. Carpenter, M. B., & Pierson, R. J. (1973). Pretectal region and the pupillary light reflex. An anatomical analysis in the monkey. The Journal of comparative neurology, 149(3), 271–300. https://doi.org/10.1002/cne.901490302

38. Chaieb, L., Antal, A., & Paulus, W. (2008). Gender-specific modulation of short-term neuroplasticity in the visual cortex induced by transcranial direct current stimulation. Visual neuroscience, 25(1), 77–81. https://doi.org/10.1017/S0952523808080097

39. Cheung, N., Mitchell, P., & Wong, T. Y. (2010). Diabetic retinopathy. Lancet (London, England), 376(9735), 124–136. https://doi.org/10.1016/S0140-6736(09)62124-3

40. Chiang, C. C., Shivacharan, R. S., Wei, X., Gonzalez-Reyes, L. E., & Durand, D. M. (2019). Slow periodic activity in the longitudinal hippocampal slice can self-propagate non-synaptically by a mechanism consistent with ephaptic coupling. The Journal of physiology, 597(1), 249–269. https://doi.org/10.1113/JP276904

41. Chow, A. Y., Chow, V. Y., Packo, K. H., Pollack, J. S., Peyman, G. A., & Schuchard, R. (2004). The artificial silicon retina microchip for the treatment of vision loss from retinitis pigmentosa. Archives of ophthalmology (Chicago, Ill. : 1960), 122(4), 460–469. https://doi.org/10.1001/archopht.122.4.460

42. Classen, J., Wolters, A., Stefan, K., Wycislo, M., Sandbrink, F., Schmidt, A., & Kunesch, E. (2004). Paired associative stimulation. Supplements to Clinical neurophysiology, 57, 563–569.

43. Clayton, M. S., Yeung, N., & Cohen Kadosh, R. (2018). The many characters of visual alpha oscillations. The European journal of neuroscience, 48(7), 2498–2508. https://doi.org/10.1111/ejn.13747

44. Cohen E. D. (2009). Effects of high-level pulse train stimulation on retinal function. Journal of neural engineering, 6(3), 035005. https://doi.org/10.1088/1741-2560/6/3/035005

45. Cohen, M. X. (2014). Analyzing neural time series data: Theory and practice. The MIT Press. https://doi.org/10.7551/mitpress/9609.001.0001

46. Coppola, G., Di Lorenzo, C., Schoenen, J., & Pierelli, F. (2013a). Habituation and sensitization in primary headaches. The journal of headache and pain, 14(1), 65. https://doi.org/10.1186/1129-2377-14-65

47. Coppola, G., Parisi, V., Di Lorenzo, C., Serrao, M., Magis, D., Schoenen, J., & Pierelli, F. (2013b). Lateral inhibition in visual cortex of migraine patients between attacks. The journal of headache and pain, 14(1), 20. https://doi.org/10.1186/1129-2377-14-20

48. Costa, T. L., Hamer, R. D., Nagy, B. V., Barboni, M. T., Gualtieri, M., Boggio, P. S., & Ventura, D. F. (2015). Transcranial direct current stimulation can selectively affect different processing channels in human visual cortex. Experimental brain research, 233(4), 1213–1223. https://doi.org/10.1007/s00221-015-4199-7

49. Dan, Y., & Poo, M. M. (2006). Spike timing-dependent plasticity: from synapse to perception. Physiological reviews, 86(3), 1033–1048. https://doi.org/10.1152/physrev.00030.2005

50. Datta, A., Elwassif, M., Battaglia, F., & Bikson, M. (2008). Transcranial current stimulation focality using disc and ring electrode configurations: FEM analysis. Journal of neural engineering, 5(2), 163–174. https://doi.org/10.1088/1741-2560/5/2/007

51. David-Jürgens, M., & Dinse, H. R. (2010). Effects of aging on paired-pulse behavior of rat somatosensory cortical neurons. Cerebral cortex (New York, N.Y. : 1991), 20(5), 1208–1216. https://doi.org/10.1093/cercor/bhp185

52. de Berker, A. O., Bikson, M., & Bestmann, S. (2013). Predicting the behavioral impact of transcranial direct current stimulation: issues and limitations. Frontiers in human neuroscience, 7, 613. https://doi.org/10.3389/fnhum.2013.00613

53. de Graaf, T. A., Koivisto, M., Jacobs, C., & Sack, A. T. (2014). The chronometry of visual perception: review of occipital TMS masking studies. Neuroscience and biobehavioral reviews, 45, 295–304. https://doi.org/10.1016/j.neubiorev.2014.06.017

54. Delic, N. C., Lyons, J. G., Di Girolamo, N., & Halliday, G. M. (2017). Damaging Effects of Ultraviolet Radiation on the Cornea. Photochemistry and photobiology, 93(4), 920–929. https://doi.org/10.1111/php.12686

55. Di Russo, F., Martínez, A., Sereno, M. I., Pitzalis, S., & Hillyard, S. A. (2002). Cortical sources of the early components of the visual evoked potential. Human brain mapping, 15(2), 95–111. https://doi.org/10.1002/hbm.10010

56. Diederich C. J. (2005). Thermal ablation and high-temperature thermal therapy: overview of technology and clinical implementation. International journal of hyperthermia : the official journal of European Society for Hyperthermic Oncology, North American Hyperthermia Group, 21(8), 745–753. https://doi.org/10.1080/02656730500271692

57. Ding, Z., Li, J., Spiegel, D. P., Chen, Z., Chan, L., Luo, G., Yuan, J., Deng, D., Yu, M., & Thompson, B. (2016). The effect of transcranial direct current stimulation on contrast sensitivity and visual evoked potential amplitude in adults with amblyopia. Scientific reports, 6, 19280. https://doi.org/10.1038/srep19280

58. Dinse, H. R., Höffken, O., & Tegenthoff, M. (2023). Cortical excitability in human somatosensory and visual cortex: implications for plasticity and learning - a minireview. Frontiers in human neuroscience, 17, 1235487. https://doi.org/10.3389/fnhum.2023.1235487

59. Dobelle, W. H., & Mladejovsky, M. G. (1974). Phosphenes produced by electrical stimulation of human occipital cortex, and their application to the development of a prosthesis for the blind. The Journal of physiology, 243(2), 553–576. https://doi.org/10.1113/jphysiol.1974.sp010766

60. Donkor, R., Silva, A. E., Teske, C., Wallis-Duffy, M., Johnson, A. P., & Thompson, B. (2021). Repetitive visual cortex transcranial random noise stimulation in adults with amblyopia. Scientific reports, 11(1), 3029. https://doi.org/10.1038/s41598-020-80843-8

61. Dor, H. (1873). Beiträge zur Electrotherapie der Augenkrankheiten. Albrecht von Graefes Archiv für Klinische und Experimentelle Ophthalmologie, 19, 532.

62. Dzwiniel, P., Gola, M., Wójcik-Gryciuk, A., & Waleszczyk, W. J. (2017). Specvis: Free and open-source software for visual field examination. PloS one, 12(10), e0186224. https://doi.org/10.1371/journal.pone.0186224

63. Einevoll, G. T., Kayser, C., Logothetis, N. K., & Panzeri, S. (2013). Modelling and analysis of local field potentials for studying the function of cortical circuits. Nature reviews. Neuroscience, 14(11), 770–785. https://doi.org/10.1038/nrn3599

64. Elyamany, O., Leicht, G., Herrmann, C. S., & Mulert, C. (2021). Transcranial alternating current stimulation (tACS): from basic mechanisms towards first applications in psychiatry. European archives of psychiatry and clinical neuroscience, 271(1), 135–156. https://doi.org/10.1007/s00406-020-01209-9

65. Enayati, S., Chang, K., Lennikov, A., Yang, M., Lee, C., Ashok, A., Elzaridi, F., Yen, C., Gunes, K., Xie, J., Cho, K. S., Utheim, T. P., & Chen, D. F. (2024). Optimal transcorneal electrical stimulation parameters for preserving photoreceptors in a mouse model of retinitis pigmentosa. Neural regeneration research, 19(11), 2543–2552. https://doi.org/10.4103/1673-5374.392888

66. Euler, T., Haverkamp, S., Schubert, T., & Baden, T. (2014). Retinal bipolar cells: elementary building blocks of vision. Nature reviews. Neuroscience, 15(8), 507–519. https://doi.org/10.1038/nrn3783

67. Evans, C., Bachmann, C., Lee, J. S. A., Gregoriou, E., Ward, N., & Bestmann, S. (2020). Dose-controlled tDCS reduces electric field intensity variability at a cortical target site. Brain stimulation, 13(1), 125–136. https://doi.org/10.1016/j.brs.2019.10.004

68. Fedorov, A., Jobke, S., Bersnev, V., Chibisova, A., Chibisova, Y., Gall, C., & Sabel, B. A. (2011). Restoration of vision after optic nerve lesions with noninvasive transorbital alternating current stimulation: a clinical observational study. Brain stimulation, 4(4), 189–201. https://doi.org/10.1016/j.brs.2011.07.007

69. Felleman, D. J., & Van Essen, D. C. (1991). Distributed hierarchical processing in the primate cerebral cortex. Cerebral cortex (New York, N.Y. : 1991), 1(1), 1–47. https://doi.org/10.1093/cercor/1.1.1-a

70. Fertonani, A., & Miniussi, C. (2017). Transcranial Electrical Stimulation: What We Know and Do Not Know About Mechanisms. The Neuroscientist : a review journal bringing neurobiology, neurology and psychiatry, 23(2), 109–123. https://doi.org/10.1177/1073858416631966

71. Fertonani, A., Pirulli, C., & Miniussi, C. (2011). Random noise stimulation improves neuroplasticity in perceptual learning. The Journal of neuroscience : the official journal of the Society for Neuroscience, 31(43), 15416–15423. https://doi.org/10.1523/JNEUROSCI.2002-11.2011

72. Fitzgerald P. B. (2014). Transcranial pulsed current stimulation: a new way forward?. Clinical neurophysiology : official journal of the International Federation of Clinical Neurophysiology, 125(2), 217–219. https://doi.org/10.1016/j.clinph.2013.10.009

73. Foerster, O. (1929). Beiträge zur Pathophysiologie der Sehbahn und der Sphären. Journal of Psychology and Neurology, 39, 435–463.

74. Foik, A. T., Kublik, E., Sergeeva, E. G., Tatlisumak, T., Rossini, P. M., Sabel, B. A., & Waleszczyk, W. J. (2015). Retinal origin of electrically evoked potentials in response to transcorneal alternating current stimulation in the rat. Investigative ophthalmology & visual science, 56(3), 1711–1718. https://doi.org/10.1167/iovs.14-15617

75. Freitag, S., Hunold, A., Klemm, M., Klee, S., Link, D., Nagel, E., & Haueisen, J. (2019). Pulsed Electrical Stimulation of the Human Eye Enhances Retinal Vessel Reaction to Flickering Light. Frontiers in human neuroscience, 13, 371. https://doi.org/10.3389/fnhum.2019.00371

76. Freunberger, R., Klimesch, W., Doppelmayr, M., & Höller, Y. (2007). Visual P2 component is related to theta phase-locking. Neuroscience letters, 426(3), 181–186. https://doi.org/10.1016/j.neulet.2007.08.062

77. Friedman, D. S., O'Colmain, B. J., Muñoz, B., Tomany, S. C., McCarty, C., de Jong, P. T., Nemesure, B., Mitchell, P., Kempen, J., & Eye Diseases Prevalence Research Group (2004). Prevalence of age-related

macular degeneration in the United States. Archives of ophthalmology (Chicago, Ill. : 1960), 122(4), 564–572. https://doi.org/10.1001/archopht.122.4.564

78. Fujikado, T., Morimoto, T., Matsushita, K., Shimojo, H., Okawa, Y., & Tano, Y. (2006). Effect of transcorneal electrical stimulation in patients with nonarteritic ischemic optic neuropathy or traumatic optic neuropathy. Japanese journal of ophthalmology, 50(3), 266–273. https://doi.org/10.1007/s10384-005-0304-y

79. Fujikado, T., Morimoto, T., Matsushita, K., Shimojo, H., Okawa, Y., & Tano, Y. (2006). Effect of transcorneal electrical stimulation in patients with nonarteritic ischemic optic neuropathy or traumatic optic neuropathy. Japanese journal of ophthalmology, 50(3), 266–273. https://doi.org/10.1007/s10384-005-0304-y

80. Gabriel, C., Peyman, A., & Grant, E. H. (2009). Electrical conductivity of tissue at frequencies below 1 MHz. Physics in medicine and biology, 54(16), 4863–4878. https://doi.org/10.1088/0031-9155/54/16/002

81. Gabriel, S., Lau, R. W., & Gabriel, C. (1996). The dielectric properties of biological tissues: III. Parametric models for the dielectric spectrum of tissues. Physics in medicine and biology, 41(11), 2271–2293. https://doi.org/10.1088/0031-9155/41/11/003

82. Gall, C., Fedorov, A. B., Ernst, L., Borrmann, A., & Sabel, B. A. (2010). Repetitive transorbital alternating current stimulation in optic neuropathy. NeuroRehabilitation, 27(4), 335–341. https://doi.org/10.3233/NRE-2010-0617

83. Gall, C., Schmidt, S., Schittkowski, M. P., Antal, A., Ambrus, G. G., Paulus, W., Dannhauer, M., Michalik, R., Mante, A., Bola, M., Lux, A., Kropf, S., Brandt, S. A., & Sabel, B. A. (2016). Alternating Current Stimulation for Vision Restoration after Optic Nerve Damage: A Randomized Clinical Trial. PloS one, 11(6), e0156134. https://doi.org/10.1371/journal.pone.0156134

84. Gall, C., Sgorzaly, S., Schmidt, S., Brandt, S., Fedorov, A., & Sabel, B. A. (2011). Noninvasive transorbital alternating current stimulation improves subjective visual functioning and vision-related quality of life in optic neuropathy. Brain stimulation, 4(4), 175–188. https://doi.org/10.1016/j.brs.2011.07.003

85. Gamlin, P. D., Zhang, H., & Clarke, R. J. (1995). Luminance neurons in the pretectal olivary nucleus mediate the pupillary light reflex in the rhesus monkey. Experimental brain research, 106(1), 169–176. https://doi.org/10.1007/BF00241367

86. Geddes, L. A. (1987). Optimal stimulus duration for extracranial cortical stimulation. Neurosurgery, 20(1), 94–99.

87. Geddes, L. A., & Baker, L. E. (1967). The specific resistance of biological material--a compendium of data for the biomedical engineer and physiologist. Medical & biological engineering, 5(3), 271–293. https://doi.org/10.1007/BF02474537

88. Gramfort, A., Luessi, M., Larson, E., Engemann, D. A., Strohmeier, D., Brodbeck, C., Goj, R., Jas, M., Brooks, T., Parkkonen, L., & Hämäläinen, M. (2013). MEG and EEG data analysis with MNE-Python. Frontiers in neuroscience, 7, 267. https://doi.org/10.3389/fnins.2013.00267

89. Grill-Spector, K., & Malach, R. (2004). The human visual cortex. Annual review of neuroscience, 27, 649–677. https://doi.org/10.1146/annurev.neuro.27.070203.144220

90. Grossman, N., Bono, D., Dedic, N., Kodandaramaiah, S. B., Rudenko, A., Suk, H. J., Cassara, A. M., Neufeld, E., Kuster, N., Tsai, L. H., Pascual-Leone, A., & Boyden, E. S. (2017). Noninvasive Deep Brain Stimulation via Temporally Interfering Electric Fields. Cell, 169(6), 1029–1041.e16. https://doi.org/10.1016/j.cell.2017.05.024

91. Haberbosch, L., Datta, A., Thomas, C., Jooß, A., Köhn, A., Rönnefarth, M., Scholz, M., Brandt, S. A., & Schmidt, S. (2019). Safety Aspects, Tolerability and Modeling of Retinofugal Alternating Current Stimulation. Frontiers in neuroscience, 13, 783. https://doi.org/10.3389/fnins.2019.00783

92. Hamel C. P. (2007). Cone rod dystrophies. Orphanet journal of rare diseases, 2, 7.

https://doi.org/10.1186/1750-1172-2-7

93. Hameroff S. R. (2007). The brain is both neurocomputer and quantum computer. Cognitive science, 31(6), 1035–1045. https://doi.org/10.1080/03640210701704004

94. Harmony T. (2013). The functional significance of delta oscillations in cognitive processing. Frontiers in integrative neuroscience, 7, 83. https://doi.org/10.3389/fnint.2013.00083

95. Hartong, D. T., Berson, E. L., & Dryja, T. P. (2006). Retinitis pigmentosa. Lancet (London, England), 368(9549), 1795–1809. https://doi.org/10.1016/S0140-6736(06)69740-7

96. Hasgall PA, Di Gennaro F, Baumgartner C, Neufeld E, Lloyd B, Gosselin MC, Payne D, Klingenböck A, Kuster N, "IT'IS Database for thermal and electromagnetic parameters of biological tissues," Version 4.1, Feb 22, 2022, DOI: 10.13099/VIP21000-04-1

97. Hastings, M. H., Maywood, E. S., & Brancaccio, M. (2018). Generation of circadian rhythms in the suprachiasmatic nucleus. Nature reviews. Neuroscience, 19(8), 453–469. https://doi.org/10.1038/s41583-018-0026-z

98. Havlík M. (2017). Missing piece of the puzzle in the science of consciousness: Resting state and endogenous correlates of consciousness. Consciousness and cognition, 49, 70–85. https://doi.org/10.1016/j.concog.2017.01.006

99. Hejtmancik, J. F., Cabrera, P., Chen, Y., M'Hamdi, O., & Nickerson, J. M. (2017). Vision. In P. M. Conn (Ed.), Conn's Translational Neuroscience (pp. 399-438). Academic Press. https://doi.org/10.1016/B978-0-12-802381-5.00019-7

100. Helfrich, R. F., Knepper, H., Nolte, G., Strüber, D., Rach, S., Herrmann, C. S., Schneider, T. R., & Engel, A. K. (2014). Selective modulation of interhemispheric functional connectivity by HD-tACS shapes perception. PLoS biology, 12(12), e1002031. https://doi.org/10.1371/journal.pbio.1002031

101. Hendry, S. H., & Reid, R. C. (2000). The koniocellular pathway in primate vision. Annual review of neuroscience, 23, 127–153. https://doi.org/10.1146/annurev.neuro.23.1.127

102. Herpich, F., Melnick, M. D., Agosta, S., Huxlin, K. R., Tadin, D., & Battelli, L. (2019). Boosting Learning Efficacy with Noninvasive Brain Stimulation in Intact and Brain-Damaged Humans. The Journal of neuroscience : the official journal of the Society for Neuroscience, 39(28), 5551–5561. https://doi.org/10.1523/JNEUROSCI.3248-18.2019

103. Herpich, F., Melnick, M., Huxlin, K., Tadin, D., Agosta, S., & Battelli, L. (2015). Transcranial random noise stimulation enhances visual learning in healthy adults. Journal of Vision, 15(12), 40. https://doi.org/10.1167/15.12.40

104. Herrera-Melendez, A. L., Bajbouj, M., & Aust, S. (2020). Application of Transcranial Direct Current Stimulation in Psychiatry. Neuropsychobiology, 79(6), 372–383. https://doi.org/10.1159/000501227

105. Herreras O. (2016). Local Field Potentials: Myths and Misunderstandings. Frontiers in neural circuits, 10, 101. https://doi.org/10.3389/fncir.2016.00101

106. Herrmann, C. S., Murray, M. M., Ionta, S., Hutt, A., & Lefebvre, J. (2016). Shaping Intrinsic Neural Oscillations with Periodic Stimulation. The Journal of neuroscience : the official journal of the Society for Neuroscience, 36(19), 5328–5337. https://doi.org/10.1523/JNEUROSCI.0236-16.2016

107. Herweg, N. A., Solomon, E. A., & Kahana, M. J. (2020). Theta Oscillations in Human Memory. Trends in cognitive sciences, 24(3), 208–227. https://doi.org/10.1016/j.tics.2019.12.006

108. Hodgkin, A. L., & Huxley, A. F. (1939). Action potentials recorded from inside a nerve fibre. *Nature, 144*(3653), 710–711. https://doi.org/10.1038/144710a0

109. Höffken, O., Grehl, T., Dinse, H. R., Tegenthoff, M., & Bach, M. (2008). Paired-pulse behavior of visually

evoked potentials recorded in human visual cortex using patterned paired-pulse stimulation. Experimental brain research, 188(3), 427–435. https://doi.org/10.1007/s00221-008-1374-0

110. Höffken, O., Lenz, M., Sczesny-Kaiser, M., Dinse, H. R., & Tegenthoff, M. (2013). Phosphene thresholds correlate with paired-pulse suppression of visually evoked potentials. Brain stimulation, 6(2), 118–121. https://doi.org/10.1016/j.brs.2012.02.004

111. Holton, K. S., & Walker, C. F. (1990). Correlation of a magnetic resonance brain image and tissue impedance. In Proceedings of the Twelfth Annual International Conference of the IEEE Engineering in Medicine and Biology Society (pp. 92–93). Philadelphia, PA, USA. https://doi.org/10.1109/IEMBS.1990.690983

112. Hoon, M., Okawa, H., Della Santina, L., & Wong, R. O. (2014). Functional architecture of the retina: development and disease. Progress in retinal and eye research, 42, 44–84. https://doi.org/10.1016/j.preteyeres.2014.06.003

113. Horton, J. C., & Hoyt, W. F. (1991). The representation of the visual field in human striate cortex. A revision of the classic Holmes map. Archives of ophthalmology (Chicago, Ill. : 1960), 109(6), 816–824. https://doi.org/10.1001/archopht.1991.01080060080030

114. Hu, D. N., Simon, J. D., & Sarna, T. (2008). Role of ocular melanin in ophthalmic physiology and pathology. Photochemistry and photobiology, 84(3), 639–644. https://doi.org/10.1111/j.1751-1097.2008.00316.x

115. Hunold, A., Haueisen, J., Nees, F., & Moliadze, V. (2023). Review of individualized current flow modeling studies for transcranial electrical stimulation. Journal of neuroscience research, 101(4), 405–423. https://doi.org/10.1002/jnr.25154

116. Hussey, K. A., Hadyniak, S. E., & Johnston, R. J., Jr (2022). Patterning and Development of Photoreceptors in the Human Retina. Frontiers in cell and developmental biology, 10, 878350. https://doi.org/10.3389/fcell.2022.878350

117. Itzcovich, E., Riani, M., & Sannita, W. G. (2017). Stochastic resonance improves vision in the severely impaired. Scientific reports, 7(1), 12840. https://doi.org/10.1038/s41598-017-12906-2

118. Iwasa, S. N., Liu, X., Naguib, H. E., Kalia, S. K., Popovic, M. R., & Morshead, C. M. (2024). Electrical Stimulation for Stem Cell-Based Neural Repair: Zapping the Field to Action. eNeuro, 11(9), ENEURO.0183-24.2024. https://doi.org/10.1523/ENEURO.0183-24.2024

119. Jaberzadeh, S., Bastani, A., & Zoghi, M. (2014). Anodal transcranial pulsed current stimulation: A novel technique to enhance corticospinal excitability. Clinical neurophysiology : official journal of the International Federation of Clinical Neurophysiology, 125(2), 344–351. https://doi.org/10.1016/j.clinph.2013.08.025

120. Jas, M., Larson, E., Engemann, D. A., Leppäkangas, J., Taulu, S., Hämäläinen, M., & Gramfort, A. (2018). A Reproducible MEG/EEG Group Study With the MNE Software: Recommendations, Quality Assessments, and Good Practices. Frontiers in neuroscience, 12, 530. https://doi.org/10.3389/fnins.2018.00530

121. JASP Team. (2024). JASP (Version 0.19.0) Computer software. Link: https://jasp-stats.org/

122. Javitt D. C. (2015). Meeting overview: Sensory perception and schizophrenia, Lausanne, Switzerland June 31-July 1, 2014. Schizophrenia research. Cognition, 2(2), 42–45. https://doi.org/10.1016/j.scog.2015.04.003

123. Jefferys J. G. (1995). Nonsynaptic modulation of neuronal activity in the brain: electric currents and extracellular ions. Physiological reviews, 75(4), 689–723. https://doi.org/10.1152/physrev.1995.75.4.689

124. Johannes, S., Münte, T. F., Heinze, H. J., & Mangun, G. R. (1995). Luminance and spatial attention effects on early visual processing. Brain research. Cognitive brain research, 2(3), 189–205. https://doi.org/10.1016/0926-6410(95)90008-x

125. John, S. E., Shivdasani, M. N., Williams, C. E., Morley, J. W., Shepherd, R. K., Rathbone, G. D., & Fallon, J. B. (2013). Suprachoroidal electrical stimulation: effects of stimulus pulse parameters on visual cortical responses. Journal of neural engineering, 10(5), 056011. https://doi.org/10.1088/1741-2560/10/5/056011

126. Joshi, R., Murali, S., & Thirugnanasambandam, N. (2023). Behavioral Validation of Individualized Low-Intensity Transcranial Electrical Stimulation (tES) Protocols. eNeuro, 10(12), ENEURO.0374-22.2023. https://doi.org/10.1523/ENEURO.0374-22.2023

127. Joukal, M. (2017). Anatomy of the human visual pathway. In K. Skorkovská (Ed.), Homonymous visual field defects (pp. 1–18). Springer, Cham. https://doi.org/10.1007/978-3-319-52284-5_1

128. Joy, M. T., & Carmichael, S. T. (2021). Encouraging an excitable brain state: mechanisms of brain repair in stroke. Nature reviews. Neuroscience, 22(1), 38–53. https://doi.org/10.1038/s41583-020-00396-7

129. Kaidheim, P. (1977, September 1). Phosphenes. High Times. Retrieved from https://archive.hightimes.com/article/1977/09/01/phosphenes

130. Kamermans, M., & Spekreijse, H. (1999). The feedback pathway from horizontal cells to cones. A mini review with a look ahead. Vision research, 39(15), 2449–2468. https://doi.org/10.1016/s0042-6989(99)00043-7

131. Kanai, R., Chaieb, L., Antal, A., Walsh, V., & Paulus, W. (2008). Frequency-dependent electrical stimulation of the visual cortex. Current biology : CB, 18(23), 1839–1843. https://doi.org/10.1016/j.cub.2008.10.027

132. Karnath, H. O., Ferber, S., & Himmelbach, M. (2001). Spatial awareness is a function of the temporal not the posterior parietal lobe. Nature, 411(6840), 950–953. https://doi.org/10.1038/35082075

133. Kawasaki A. (1999). Physiology, assessment, and disorders of the pupil. Current opinion in ophthalmology, 10(6), 394–400. https://doi.org/10.1097/00055735-199912000-00005

134. Kessler, S. K., Minhas, P., Woods, A. J., Rosen, A., Gorman, C., & Bikson, M. (2013). Dosage considerations for transcranial direct current stimulation in children: a computational modeling study. PloS one, 8(9), e76112. https://doi.org/10.1371/journal.pone.0076112

135. Kilgore, K. L., & Bhadra, N. (2004). Nerve conduction block utilising high-frequency alternating current. Medical & biological engineering & computing, 42(3), 394–406. https://doi.org/10.1007/BF02344716

136. Kim, K. U., Kim, S. H., & An, T. G. (2016). Effect of transcranial direct current stimulation on visual perception function and performance capability of activities of daily living in stroke patients. Journal of physical therapy science, 28(9), 2572–2575. https://doi.org/10.1589/jpts.28.2572

137. Kim, S., Stephenson, M. C., Morris, P. G., & Jackson, S. R. (2014). tDCS-induced alterations in GABA concentration within primary motor cortex predict motor learning and motor memory: a 7 T magnetic resonance spectroscopy study. NeuroImage, 99, 237–243. https://doi.org/10.1016/j.neuroimage.2014.05.070

138. Klaus, J., & Schutter, D. J. L. G. (2021). Electrode montage-dependent intracranial variability in electric fields induced by cerebellar transcranial direct current stimulation. Scientific reports, 11(1), 22183. https://doi.org/10.1038/s41598-021-01755-9

139. Kolb H. (1997). Amacrine cells of the mammalian retina: neurocircuitry and functional roles. Eye (London, England), 11 (Pt 6), 904–923. https://doi.org/10.1038/eye.1997.230

140. Kolster, H., Peeters, R., & Orban, G. A. (2010). The retinotopic organization of the human middle temporal area MT/V5 and its cortical neighbors. The Journal of neuroscience : the official journal of the Society for Neuroscience, 30(29), 9801–9820. https://doi.org/10.1523/JNEUROSCI.2069-10.2010

141. Krames, E. S., Peckham, P. H., Rezai, A., & Aboelsaad, F. (2009). What is neuromodulation? In E. S. Krames, P. H. Peckham, & A. R. Rezai (Eds.), Neuromodulation (pp. 3-8). Academic Press. https://doi.org/10.1016/B978-0-12-374248-3.00002-1

142. Kreutzer, J. S., Agyemang, A. A., Weedon, D., Zasler, N., Oliver, M., Sorensen, A. A., van Wijngaarden, S., & Leahy, E. (2017). The top 100 cited neurorehabilitation papers. NeuroRehabilitation, 40(2), 163–174. https://doi.org/10.3233/NRE-161415

143. Kurimoto, T., Oono, S., Oku, H., Tagami, Y., Kashimoto, R., Takata, M., Okamoto, N., Ikeda, T., & Mimura, O. (2010). Transcorneal electrical stimulation increases chorioretinal blood flow in normal human subjects. Clinical ophthalmology (Auckland, N.Z.), 4, 1441–1446. https://doi.org/10.2147/OPTH.S14573

144. Laakso, I., & Hirata, A. (2013). Computational analysis shows why transcranial alternating current stimulation induces retinal phosphenes. Journal of neural engineering, 10(4), 046009. https://doi.org/10.1088/1741-2560/10/4/046009

145. Lavelaine de Maubeuge, H. (2011). Influence of geometric variables on the current distribution uniformity at the edge of parallel plate electrodes. Electrochimica Acta, 56(28), 10603–10611. https://doi.org/10.1016/j.electacta.2011.06.074

146. Lee, B. B., Martin, P. R., & Grünert, U. (2010). Retinal connectivity and primate vision. Progress in retinal and eye research, 29(6), 622–639. https://doi.org/10.1016/j.preteyeres.2010.08.004

147. Lee, H., Chen, S., Ren, X., Martinez, A., Shutthanandan, V., Vijayakumar, M., Han, K. S., Li, Q., Liu, J., Xu, W., & Zhang, J. G. (2018). Electrode Edge Effects and the Failure Mechanism of Lithium-Metal Batteries. ChemSusChem, 11(21), 3821–3828. https://doi.org/10.1002/cssc.201801445

148. Lee, J. S. A., Bestmann, S., & Evans, C. (2021b). A future of current flow modelling for transcranial electrical stimulation? Current Behavioral Neuroscience Reports, 8(3), 150–159. https://doi.org/10.1007/s40473-021-00238-5

149. Lee, S. Y., Kozalakis, K., Baftizadeh, F., Campagnola, L., Jarsky, T., Koch, C., & Anastassiou, C. A. (2024). Cell class-specific electric field entrainment of neural activity. bioRxiv : the preprint server for biology, 2023.02.14.528526. https://doi.org/10.1101/2023.02.14.528526

150. Lee, S., Park, J., Kwon, J., Kim, D. H., & Im, C. H. (2021a). Multi-channel transorbital electrical stimulation for effective stimulation of posterior retina. Scientific reports, 11(1), 9745. https://doi.org/10.1038/s41598-021-89243-y

151. Lee, W. H., Deng, Z. D., Kim, T. S., Laine, A. F., Lisanby, S. H., & Peterchev, A. V. (2010). Regional electric field induced by electroconvulsive therapy: a finite element simulation study. Annual International Conference of the IEEE Engineering in Medicine and Biology Society. IEEE Engineering in Medicine and Biology Society. Annual International Conference, 2010, 2045–2048. https://doi.org/10.1109/IEMBS.2010.5626553

152. Lefaucheur, J. P., Antal, A., Ayache, S. S., Benninger, D. H., Brunelin, J., Cogiamanian, F., Cotelli, M., De Ridder, D., Ferrucci, R., Langguth, B., Marangolo, P., Mylius, V., Nitsche, M. A., Padberg, F., Palm, U., Poulet, E., Priori, A., Rossi, S., Schecklmann, M., Vanneste, S., … Paulus, W. (2017). Evidence-based guidelines on the therapeutic use of transcranial direct current stimulation (tDCS). Clinical neurophysiology : official journal of the International Federation of Clinical Neurophysiology, 128(1), 56–92. https://doi.org/10.1016/j.clinph.2016.10.087

153. Legge G. E. (1978). Sustained and transient mechanisms in human vision: temporal and spatial properties. Vision research, 18(1), 69–81. https://doi.org/10.1016/0042-6989(78)90079-2

154. Lejoyeux, R., Benillouche, J., Ong, J., Errera, M. H., Rossi, E. A., Singh, S. R., Dansingani, K. K., da Silva, S., Sinha, D., Sahel, J. A., Freund, K. B., Sadda, S. R., Lutty, G. A., & Chhablani, J. (2022). Choriocapillaris: Fundamentals and advancements. Progress in retinal and eye research, 87, 100997. https://doi.org/10.1016/j.preteyeres.2021.100997

155. Li, B., Xie, T., Nawy, S., & Shen, Y. (2024). The development and the genetic diseases of the ciliary body. Cell insight, 3(3), 100162. https://doi.org/10.1016/j.cellin.2024.100162

156. Li, M., Chen, X., Yuan, N., Lu, Y., Liu, Y., Gong, H., Qian, L., Andolina, I. M., Wu, J., Zhang, S., McLoughlin, N., Sun, X., & Wang, W. (2022). Effects of acute high intraocular pressure on red-green and blue-yellow cortical color responses in non-human primates. NeuroImage. Clinical, 35, 103092. https://doi.org/10.1016/j.nicl.2022.103092

157. Liu, X., Huang, H., Snutch, T. P., Cao, P., Wang, L., & Wang, F. (2022). The Superior Colliculus: Cell Types, Connectivity, and Behavior. Neuroscience bulletin, 38(12), 1519–1540. https://doi.org/10.1007/s12264-022-00858-1

158. Longstaff, A. (2002). Krótkie wykłady. Neurobiologia (A. Wróbel, Ed.). Warszawa: Wydawnictwo Naukowe PWN SA. (Original work published in 2000).

159. Luck, S. J. (2014). An introduction to the event-related potential technique (2nd ed.). The MIT Press.

160. Ma, Z., Cao, P., Sun, P., Li, L., Lu, Y., Yan, Y., Chen, Y., & Chai, X. (2014). Optical imaging of visual cortical responses evoked by transcorneal electrical stimulation with different parameters. Investigative ophthalmology & visual science, 55(8), 5320–5331. https://doi.org/10.1167/iovs.14-14600

161. Makul'kin, R. F., & Pedanov, Yu. F. (1972). Physiological mechanisms of habituation of visual evoked potentials. Neurophysiology, 4(4), 416–420.

162. Malekahmad, M., Frazer, A., Zoghi, M., & Jaberzadeh, S. (2024). Transcranial pulsed current stimulation: A scoping review of the current literature on scope, nature, underlying mechanisms, and gaps. Psychophysiology, 61(3), e14521. https://doi.org/10.1111/psyp.14521

163. Mandija, S., Petrov, P. I., Vink, J. J. T., Neggers, S. F. W., & van den Berg, C. A. T. (2021). Brain Tissue Conductivity Measurements with MR-Electrical Properties Tomography: An In Vivo Study. Brain topography, 34(1), 56–63. https://doi.org/10.1007/s10548-020-00813-1

164. Marzbani, H., Marateb, H. R., & Mansourian, M. (2016). Neurofeedback: A Comprehensive Review on System Design, Methodology and Clinical Applications. Basic and clinical neuroscience, 7(2), 143–158. https://doi.org/10.15412/J.BCN.03070208

165. Masland R. H. (2012a). The neuronal organization of the retina. Neuron, 76(2), 266–280. https://doi.org/10.1016/j.neuron.2012.10.002

166. Masland R. H. (2012b). The tasks of amacrine cells. Visual neuroscience, 29(1), 3–9. https://doi.org/10.1017/s0952523811000344

167. Masri, R. A., Grünert, U., & Martin, P. R. (2020). Analysis of Parvocellular and Magnocellular Visual Pathways in Human Retina. The Journal of neuroscience : the official journal of the Society for Neuroscience, 40(42), 8132–8148. https://doi.org/10.1523/JNEUROSCI.1671-20.2020

168. McAdams, E. T., & Jossinet, J. (1995). Tissue impedance: a historical overview. Physiological measurement, 16(3 Suppl A), A1–A13. https://doi.org/10.1088/0967-3334/16/3a/001

169. McConnell Brain Imaging Centre. (2024). Linear ICBM average brain (ICBM152) stereotaxic registration model. Montreal Neurological Institute. https://nist.mni.mcgill.ca/icbm-152lin/

170. McCreery, D. B., Agnew, W. F., Yuen, T. G., & Bullara, L. (1990). Charge density and charge per phase as cofactors in neural injury induced by electrical stimulation. IEEE transactions on bio-medical engineering, 37(10), 996–1001. https://doi.org/10.1109/10.102812

171. Michelson, A. (1927). Studies in optics. University of Chicago Press. Retrieved from https://archive.org/details/in.ernet.dli.2015.86849/page/n11/mode/2up

172. Miller, N. R., Walsh, F. B., & Hoyt, W. F. (Eds.). (2005). Walsh and Hoyt's clinical neuro-ophthalmology (Vol. 1 and Vol. 2). Lippincott Williams & Wilkins.

173. Minhas, P., Datta, A., & Bikson, M. (2011). Cutaneous perception during tDCS: role of electrode shape and

sponge salinity. Clinical neurophysiology : official journal of the International Federation of Clinical Neurophysiology, 122(4), 637–638. https://doi.org/10.1016/j.clinph.2010.09.023

174. Miranda, P. C., Lomarev, M., & Hallett, M. (2006). Modeling the current distribution during transcranial direct current stimulation. Clinical neurophysiology : official journal of the International Federation of Clinical Neurophysiology, 117(7), 1623–1629. https://doi.org/10.1016/j.clinph.2006.04.009

175. Morimoto, T., Fukui, T., Matsushita, K., Okawa, Y., Shimojyo, H., Kusaka, S., Tano, Y., & Fujikado, T. (2006). Evaluation of residual retinal function by pupillary constrictions and phosphenes using transcorneal electrical stimulation in patients with retinal degeneration. Graefe's archive for clinical and experimental ophthalmology = Albrecht von Graefes Archiv fur klinische und experimentelle Ophthalmologie, 244(10), 1283–1292. https://doi.org/10.1007/s00417-006-0260-3

176. Moss, F., Ward, L. M., & Sannita, W. G. (2004). Stochastic resonance and sensory information processing: a tutorial and review of application. Clinical neurophysiology : official journal of the International Federation of Clinical Neurophysiology, 115(2), 267–281. https://doi.org/10.1016/j.clinph.2003.09.014

177. Mure, L. S., Vinberg, F., Hanneken, A., & Panda, S. (2019). Functional diversity of human intrinsically photosensitive retinal ganglion cells. Science (New York, N.Y.), 366(6470), 1251–1255. https://doi.org/10.1126/science.aaz0898

178. Naka, K. I., & Rushton, W. A. (1966). S-potentials from luminosity units in the retina of fish (Cyprinidae). The Journal of physiology, 185(3), 587–599. https://doi.org/10.1113/jphysiol.1966.sp008003

179. Navarro R. (2009). The Optical Design of the Human Eye: a Critical Review. Journal of Optometry, 2(1), 3–18. https://doi.org/10.3921/joptom.2009.3

180. Naycheva, L., Schatz, A., Röck, T., Willmann, G., Messias, A., Bartz-Schmidt, K. U., Zrenner, E., & Gekeler, F. (2012). Phosphene thresholds elicited by transcorneal electrical stimulation in healthy subjects and patients with retinal diseases. Investigative ophthalmology & visual science, 53(12), 7440–7448. https://doi.org/10.1167/iovs.12-9612

181. Naycheva, L., Schatz, A., Röck, T., Willmann, G., Messias, A., Bartz-Schmidt, K. U., Zrenner, E., & Gekeler, F. (2012). Phosphene thresholds elicited by transcorneal electrical stimulation in healthy subjects and patients with retinal diseases. Investigative ophthalmology & visual science, 53(12), 7440–7448. https://doi.org/10.1167/iovs.12-9612

182. Naycheva, L., Schatz, A., Willmann, G., Bartz-Schmidt, K. U., Zrenner, E., Röck, T., & Gekeler, F. (2013). Transcorneal electrical stimulation in patients with retinal artery occlusion: a prospective, randomized, sham-controlled pilot study. Ophthalmology and therapy, 2(1), 25–39. https://doi.org/10.1007/s40123-013-0012-5

183. Nielsen, J. D., Madsen, K. H., Puonti, O., Siebner, H. R., Bauer, C., Madsen, C. G., Saturnino, G. B., & Thielscher, A. (2018). Automatic skull segmentation from MR images for realistic volume conductor models of the head: Assessment of the state-of-the-art. NeuroImage, 174, 587–598. https://doi.org/10.1016/j.neuroimage.2018.03.001

184. Nishida, T., Saika, S., & Morishige, N. (2017). Cornea and sclera: Anatomy and physiology. In M. J. Mannis & E. J. Holland (Eds.), Cornea: Fundamentals, diagnosis and management (4th ed., pp. 1-22). Elsevier.

185. Nitsche, M. A., Fricke, K., Henschke, U., Schlitterlau, A., Liebetanz, D., Lang, N., Henning, S., Tergau, F., & Paulus, W. (2003a). Pharmacological modulation of cortical excitability shifts induced by transcranial direct current stimulation in humans. The Journal of physiology, 553(Pt 1), 293–301. https://doi.org/10.1113/jphysiol.2003.049916

186. Nitsche, M. A., Jaussi, W., Liebetanz, D., Lang, N., Tergau, F., & Paulus, W. (2004). Consolidation of human motor cortical neuroplasticity by D-cycloserine. Neuropsychopharmacology : official publication of the American College of Neuropsychopharmacology, 29(8), 1573–1578. https://doi.org/10.1038/sj.npp.1300517

187. Nitsche, M. A., Liebetanz, D., Lang, N., Antal, A., Tergau, F., & Paulus, W. (2003b). Safety criteria for transcranial direct current stimulation (tDCS) in humans. Clinical neurophysiology: official journal of the International Federation of Clinical Neurophysiology, 114(11), 2220–2223. https://doi.org/10.1016/s1388-2457(03)00235-9

188. Nolte, J. (2012). Mózg człowieka. Tom 2: Anatomia czynnościowa mózgowia (J. Dziewiątkowski, P. Kowiański, & K. M. Majak, Trans.; J. Moryś, Ed.). Wydawnictwo Medyczne Urban & Partner. (Original work published in English)

189. Olma, M. C., Dargie, R. A., Behrens, J. R., Kraft, A., Irlbacher, K., Fahle, M., & Brandt, S. A. (2013). Long-Term Effects of Serial Anodal tDCS on Motion Perception in Subjects with Occipital Stroke Measured in the Unaffected Visual Hemifield. Frontiers in human neuroscience, 7, 314. https://doi.org/10.3389/fnhum.2013.00314

190. Omland, P. M., Nilsen, K. B., & Sand, T. (2011). Habituation measured by pattern reversal visual evoked potentials depends more on check size than reversal rate. Clinical neurophysiology : official journal of the International Federation of Clinical Neurophysiology, 122(9), 1846–1853. https://doi.org/10.1016/j.clinph.2011.02.025

191. Oono, S., Kurimoto, T., Kashimoto, R., Tagami, Y., Okamoto, N., & Mimura, O. (2011). Transcorneal electrical stimulation improves visual function in eyes with branch retinal artery occlusion. Clinical ophthalmology (Auckland, N.Z.), 5, 397–402. https://doi.org/10.2147/OPTH.S17751

192. Opitz, A., Paulus, W., Will, S., Antunes, A., & Thielscher, A. (2015). Determinants of the electric field during transcranial direct current stimulation. NeuroImage, 109, 140–150. https://doi.org/10.1016/j.neuroimage.2015.01.033

193. Oster G. (1970). Phosphenes. Scientific American, 222(2), 82–87. https://doi.org/10.1038/scientificamerican0270-82

194. Ovenseri-Ogbomo, G., & Oduntan, O. (2015). Mechanism of accommodation: A review of theoretical propositions. African Vision and Eye Health, 74, 6. https://doi.org/10.4102/AVEH.V74I1.28

195. Ozeki, N., Shinoda, K., Ohde, H., Ishida, S., & Tsubota, K. (2013). Improvement of visual acuity after transcorneal electrical stimulation in case of Best vitelliform macular dystrophy. Graefe's archive for clinical and experimental ophthalmology = Albrecht von Graefes Archiv fur klinische und experimentelle Ophthalmologie, 251(7), 1867–1870. https://doi.org/10.1007/s00417-013-2341-4

196. Palczewska, G., Vinberg, F., Stremplewski, P., Bircher, M. P., Salom, D., Komar, K., Zhang, J., Cascella, M., Wojtkowski, M., Kefalov, V. J., & Palczewski, K. (2014). Human infrared vision is triggered by two-photon chromophore isomerization. Proceedings of the National Academy of Sciences of the United States of America, 111(50), E5445–E5454. https://doi.org/10.1073/pnas.1410162111

197. Paulus W. (2011). Transcranial electrical stimulation (tES - tDCS; tRNS, tACS) methods. Neuropsychological rehabilitation, 21(5), 602–617. https://doi.org/10.1080/09602011.2011.557292

198. Pavan, A., Ghin, F., Contillo, A., Milesi, C., Campana, G., & Mather, G. (2019). Modulatory mechanisms underlying high-frequency transcranial random noise stimulation (hf-tRNS): A combined stochastic resonance and equivalent noise approach. Brain stimulation, 12(4), 967–977. https://doi.org/10.1016/j.brs.2019.02.018

199. Peters, M. A., Thompson, B., Merabet, L. B., Wu, A. D., & Shams, L. (2013). Anodal tDCS to V1 blocks visual perceptual learning consolidation. Neuropsychologia, 51(7), 1234–1239. https://doi.org/10.1016/j.neuropsychologia.2013.03.013

200. Petzold, A., Fraser, C. L., Abegg, M., Alroughani, R., Alshowaeir, D., Alvarenga, R., Andris, C., Asgari, N., Barnett, Y., Battistella, R., Behbehani, R., Berger, T., Bikbov, M. M., Biotti, D., Biousse, V., Boschi, A., Brazdil, M., Brezhnev, A., Calabresi, P. A., Cordonnier, M., … Plant, G. T. (2022). Diagnosis and classification of optic neuritis. The Lancet. Neurology, 21(12), 1120–1134.

https://doi.org/10.1016/S1474-4422(22)00200-9

201. Plow, E. B., Obretenova, S. N., Fregni, F., Pascual-Leone, A., & Merabet, L. B. (2012a). Comparison of visual field training for hemianopia with active versus sham transcranial direct cortical stimulation. Neurorehabilitation and neural repair, 26(6), 616–626. https://doi.org/10.1177/1545968311431963

202. Plow, E. B., Obretenova, S. N., Halko, M. A., Kenkel, S., Jackson, M. L., Pascual-Leone, A., & Merabet, L. B. (2011). Combining visual rehabilitative training and noninvasive brain stimulation to enhance visual function in patients with hemianopia: a comparative case study. PM & R : the journal of injury, function, and rehabilitation, 3(9), 825–835. https://doi.org/10.1016/j.pmrj.2011.05.026

203. Plow, E. B., Obretenova, S. N., Jackson, M. L., & Merabet, L. B. (2012b). Temporal profile of functional visual rehabilitative outcomes modulated by transcranial direct current stimulation. Neuromodulation : journal of the International Neuromodulation Society, 15(4), 367–373. https://doi.org/10.1111/j.1525-1403.2012.00440.x

204. Potok, W., Post, A., Beliaeva, V., Bächinger, M., Cassarà, A. M., Neufeld, E., Polania, R., Kiper, D., & Wenderoth, N. (2023). Modulation of Visual Contrast Sensitivity with tRNS across the Visual System, Evidence from Stimulation and Simulation. eNeuro, 10(6), ENEURO.0177-22.2023. https://doi.org/10.1523/ENEURO.0177-22.2023

205. Puonti, O., Van Leemput, K., Saturnino, G. B., Siebner, H. R., Madsen, K. H., & Thielscher, A. (2020). Accurate and robust whole-head segmentation from magnetic resonance images for individualized head modeling. NeuroImage, 219, 117044. https://doi.org/10.1016/j.neuroimage.2020.117044

206. Rangarajan, V., Jacques, C., Knight, R. T., Weiner, K. S., & Grill-Spector, K. (2020). Diverse Temporal Dynamics of Repetition Suppression Revealed by Intracranial Recordings in the Human Ventral Temporal Cortex. Cerebral cortex (New York, N.Y. : 1991), 30(11), 5988–6003. https://doi.org/10.1093/cercor/bhaa173

207. Ranieri, F., Coppola, G., Musumeci, G., Capone, F., Di Pino, G., Parisi, V., & Di Lazzaro, V. (2019). Evidence for associative plasticity in the human visual cortex. Brain stimulation, 12(3), 705–713. https://doi.org/10.1016/j.brs.2019.01.021

208. Reato, D., Rahman, A., Bikson, M., & Parra, L. C. (2010). Low-intensity electrical stimulation affects network dynamics by modulating population rate and spike timing. The Journal of neuroscience : the official journal of the Society for Neuroscience, 30(45), 15067–15079. https://doi.org/10.1523/JNEUROSCI.2059-10.2010

209. Reilly, J. P. (1992). Electrical stimulation and electropathology. Cambridge University Press.

210. Reinhart, R. M., Xiao, W., McClenahan, L. J., & Woodman, G. F. (2016). Electrical Stimulation of Visual Cortex Can Immediately Improve Spatial Vision. Current biology : CB, 26(14), 1867–1872. https://doi.org/10.1016/j.cub.2016.05.019

211. Remedios, L., Mabil, P., Flores-Hernández, J., Torres-Ramírez, O., Huidobro, N., Castro, G., Cervantes, L., Tapia, J. A., De la Torre Valdovinos, B., & Manjarrez, E. (2019). Effects of Short-Term Random Noise Electrical Stimulation on Dissociated Pyramidal Neurons from the Cerebral Cortex. Neuroscience, 404, 371–386. https://doi.org/10.1016/j.neuroscience.2019.01.035

212. Research Imaging Institute. (2024). Mango - Multi-image analysis GUI. University of Texas Health Science Center. Retrieved from https://mangoviewer.com/index.html

213. Rockel, A. J., Hiorns, R. W., & Powell, T. P. (1980). The basic uniformity in structure of the neocortex. Brain : a journal of neurology, 103(2), 221–244. https://doi.org/10.1093/brain/103.2.221

214. Rohracher H. (1935). Über subjektive Lichterscheinungen bei Reizung mit Wechselströmen. Z. Sinnesphysiol. 66, 164–181

215. Sabel, B. A., Fedorov, A. B., Naue, N., Borrmann, A., Herrmann, C., & Gall, C. (2011). Non-invasive alternating current stimulation improves vision in optic neuropathy. Restorative neurology and neuroscience,

29(6), 493–505. https://doi.org/10.3233/RNN-2011-0624

216. Sabel, B. A., Gao, Y., & Antal, A. (2020b). Reversibility of visual field defects through induction of brain plasticity: vision restoration, recovery and rehabilitation using alternating current stimulation. Neural regeneration research, 15(10), 1799–1806. https://doi.org/10.4103/1673-5374.280302

217. Sabel, B. A., Thut, G., Haueisen, J., Henrich-Noack, P., Herrmann, C. S., Hunold, A., Kammer, T., Matteo, B., Sergeeva, E. G., Waleszczyk, W., & Antal, A. (2020a). Vision modulation, plasticity and restoration using non-invasive brain stimulation - An IFCN-sponsored review. Clinical neurophysiology : official journal of the International Federation of Clinical Neurophysiology, 131(4), 887–911. https://doi.org/10.1016/j.clinph.2020.01.008

218. Salchow, C., Strohmeier, D., Klee, S., Jannek, D., Schiecke, K., Witte, H., Nehorai, A., & Haueisen, J. (2016). Rod Driven Frequency Entrainment and Resonance Phenomena. Frontiers in human neuroscience, 10, 413. https://doi.org/10.3389/fnhum.2016.00413

219. Santarnecchi, E., Brem, A.-K., Levenbaum, E., Thompson, T., Cohen Kadosh, R., & Pascual-Leone, A. (2015). Enhancing cognition using transcranial electrical stimulation. Current Opinion in Behavioral Sciences, 4, 171–178. https://doi.org/10.1016/j.cobeha.2015.06.003

220. Saturnino, G. B., Thielscher, A., Madsen, K. H., Knösche, T. R., & Weise, K. (2019). A principled approach to conductivity uncertainty analysis in electric field calculations. NeuroImage, 188, 821–834. https://doi.org/10.1016/j.neuroimage.2018.12.053

221. Schalk, G., Brunner, P., Allison, B. Z., Soekadar, S. R., Guan, C., Denison, T., Rickert, J., & Miller, K. J. (2024). Translation of neurotechnologies. Nature Reviews Bioengineering, 2(637-652). https://doi.org/10.1038/s44222-024-00001-1

222. Schatz, A., Röck, T., Naycheva, L., Willmann, G., Wilhelm, B., Peters, T., Bartz-Schmidt, K. U., Zrenner, E., Messias, A., & Gekeler, F. (2011). Transcorneal electrical stimulation for patients with retinitis pigmentosa: a prospective, randomized, sham-controlled exploratory study. Investigative ophthalmology & visual science, 52(7), 4485–4496. https://doi.org/10.1167/iovs.10-6932

223. Schatz, A., Röck, T., Naycheva, L., Willmann, G., Wilhelm, B., Peters, T., Bartz-Schmidt, K. U., Zrenner, E., Messias, A., & Gekeler, F. (2011). Transcorneal electrical stimulation for patients with retinitis pigmentosa: a prospective, randomized, sham-controlled exploratory study. Investigative ophthalmology & visual science, 52(7), 4485–4496. https://doi.org/10.1167/iovs.10-6932

224. Schmolesky, M. T., Wang, Y., Hanes, D. P., Thompson, K. G., Leutgeb, S., Schall, J. D., & Leventhal, A. G. (1998). Signal timing across the macaque visual system. Journal of neurophysiology, 79(6), 3272–3278. https://doi.org/10.1152/jn.1998.79.6.3272

225. Schutter D. J. (2016). Cutaneous retinal activation and neural entrainment in transcranial alternating current stimulation: A systematic review. NeuroImage, 140, 83–88. https://doi.org/10.1016/j.neuroimage.2015.09.067

226. Schutter, D. J., & Hortensius, R. (2010). Retinal origin of phosphenes to transcranial alternating current stimulation. Clinical neurophysiology : official journal of the International Federation of Clinical Neurophysiology, 121(7), 1080–1084. https://doi.org/10.1016/j.clinph.2009.10.038

227. Schwab, B. C., Misselhorn, J., & Engel, A. K. (2019). Modulation of large-scale cortical coupling by transcranial alternating current stimulation. Brain stimulation, 12(5), 1187–1196. https://doi.org/10.1016/j.brs.2019.04.013

228. Schwiedrzik C. M. (2009). Retina or visual cortex? The site of phosphene induction by transcranial alternating current stimulation. Frontiers in integrative neuroscience, 3, 6. https://doi.org/10.3389/neuro.07.006.2009

229. Sehic, A., Guo, S., Cho, K. S., Corraya, R. M., Chen, D. F., & Utheim, T. P. (2016). Electrical Stimulation as a Means for Improving Vision. The American journal of pathology, 186(11), 2783–2797.

https://doi.org/10.1016/j.ajpath.2016.07.017

230. Senkowski, D., & Engel, A. K. (2024). Multi-timescale neural dynamics for multisensory integration. Nature reviews. Neuroscience, 25(9), 625–642. https://doi.org/10.1038/s41583-024-00845-7

231. Silverstein, J., Cortes, M., Tsagaris, K. Z., Climent, A., Gerber, L. M., Oromendia, C., Fonzetti, P., Ratan, R. R., Kitago, T., Iacoboni, M., Wu, A., Dobkin, B., & Edwards, D. J. (2019). Paired Associative Stimulation as a Tool to Assess Plasticity Enhancers in Chronic Stroke. Frontiers in neuroscience, 13, 792. https://doi.org/10.3389/fnins.2019.00792

232. Smith, A. E., Ridding, M. C., Higgins, R. D., Wittert, G. A., & Pitcher, J. B. (2009). Age-related changes in short-latency motor cortex inhibition. Experimental brain research, 198(4), 489–500. https://doi.org/10.1007/s00221-009-1945-8

233. Snell, R. S., & Lemp, M. A. (1998). Clinical anatomy of the eye. Blackwell Science Ltd. https://doi.org/10.1002/9781118690987

234. Spiegel, D. P., Hansen, B. C., Byblow, W. D., & Thompson, B. (2012). Anodal transcranial direct current stimulation reduces psychophysically measured surround suppression in the human visual cortex. PloS one, 7(5), e36220. https://doi.org/10.1371/journal.pone.0036220

235. Stett, A., Schatz, A., Gekeler, F., & Franklin, J. (2023). Transcorneal Electrical Stimulation Dose-Dependently Slows the Visual Field Loss in Retinitis Pigmentosa. Translational vision science & technology, 12(2), 29. https://doi.org/10.1167/tvst.12.2.29

236. Strüber, D., Rach, S., Neuling, T., & Herrmann, C. S. (2015). On the possible role of stimulation duration for after-effects of transcranial alternating current stimulation. Frontiers in cellular neuroscience, 9, 311. https://doi.org/10.3389/fncel.2015.00311

237. Sun, P., Li, H., Lu, Z., Su, X., Ma, Z., Chen, J., Li, L., Zhou, C., Chen, Y., & Chai, X. (2018). Comparison of cortical responses to the activation of retina by visual stimulation and transcorneal electrical stimulation. Brain stimulation, 11(4), 667–675. https://doi.org/10.1016/j.brs.2018.02.009

238. Swiss ITIS Foundation. (2024). Tissue properties: Low frequency conductivity (up to 1 MHz). Swiss ITIS Foundation. https://itis.swiss/virtual-population/tissue-properties/database/low-frequency-conductivity/

239. Tallon-Baudry C. (2003). Oscillatory synchrony and human visual cognition. Journal of physiology, Paris, 97(2-3), 355–363. https://doi.org/10.1016/j.jphysparis.2003.09.009

240. Tallon-Baudry C. (2009). The roles of gamma-band oscillatory synchrony in human visual cognition. Frontiers in bioscience (Landmark edition), 14(1), 321–332. https://doi.org/10.2741/3246

241. Taylor, H. R., West, S. K., Rosenthal, F. S., Muñoz, B., Newland, H. S., Abbey, H., & Emmett, E. A. (1988). Effect of ultraviolet radiation on cataract formation. The New England journal of medicine, 319(22), 1429–1433. https://doi.org/10.1056/NEJM198812013192201

242. Taylor, P. C., Walsh, V., & Eimer, M. (2010). The neural signature of phosphene perception. Human brain mapping, 31(9), 1408–1417. https://doi.org/10.1002/hbm.20941

243. Thielscher, A., Antunes, A., & Saturnino, G. B. (2015). Field modeling for transcranial magnetic stimulation: A useful tool to understand the physiological effects of TMS?. Annual International Conference of the IEEE Engineering in Medicine and Biology Society. IEEE Engineering in Medicine and Biology Society. Annual International Conference, 2015, 222–225. https://doi.org/10.1109/EMBC.2015.7318340

244. Thielscher, A., Opitz, A., & Windhoff, M. (2011). Impact of the gyral geometry on the electric field induced by transcranial magnetic stimulation. NeuroImage, 54(1), 234–243. https://doi.org/10.1016/j.neuroimage.2010.07.061

245. To, W. T., De Ridder, D., Hart, J., Jr, & Vanneste, S. (2018). Changing Brain Networks Through Non-invasive Neuromodulation. Frontiers in human neuroscience, 12, 128.

https://doi.org/10.3389/fnhum.2018.00128

246. Tong F. (2003). Primary visual cortex and visual awareness. Nature reviews. Neuroscience, 4(3), 219–229. https://doi.org/10.1038/nrn1055

247. Tootell, R. B., Hadjikhani, N. K., Vanduffel, W., Liu, A. K., Mendola, J. D., Sereno, M. I., & Dale, A. M. (1998). Functional analysis of primary visual cortex (V1) in humans. Proceedings of the National Academy of Sciences of the United States of America, 95(3), 811–817. https://doi.org/10.1073/pnas.95.3.811

248. Tremblay, R., Lee, S., & Rudy, B. (2016). GABAergic Interneurons in the Neocortex: From Cellular Properties to Circuits. Neuron, 91(2), 260–292. https://doi.org/10.1016/j.neuron.2016.06.033

249. van der Groen, O., & Wenderoth, N. (2016). Transcranial Random Noise Stimulation of Visual Cortex: Stochastic Resonance Enhances Central Mechanisms of Perception. The Journal of neuroscience : the official journal of the Society for Neuroscience, 36(19), 5289–5298. https://doi.org/10.1523/JNEUROSCI.4519-15.2016

250. van der Groen, O., Potok, W., Wenderoth, N., Edwards, G., Mattingley, J. B., & Edwards, D. (2022). Using noise for the better: The effects of transcranial random noise stimulation on the brain and behavior. Neuroscience and biobehavioral reviews, 138, 104702. https://doi.org/10.1016/j.neubiorev.2022.104702

251. van Koningsbruggen, M. G., Ficarella, S. C., Battelli, L., & Hickey, C. (2016). Transcranial random-noise stimulation of visual cortex potentiates value-driven attentional capture. Social cognitive and affective neuroscience, 11(9), 1481–1488. https://doi.org/10.1093/scan/nsw056

252. Vöröslakos, M., Takeuchi, Y., Brinyiczki, K., Zombori, T., Oliva, A., Fernández-Ruiz, A., Kozák, G., Kincses, Z. T., Iványi, B., Buzsáki, G., & Berényi, A. (2018). Direct effects of transcranial electric stimulation on brain circuits in rats and humans. Nature communications, 9(1), 483. https://doi.org/10.1038/s41467-018-02928-3

253. Vosskuhl, J., Mutanen, T. P., Neuling, T., Ilmoniemi, R. J., & Herrmann, C. S. (2020). Signal-Space Projection Suppresses the tACS Artifact in EEG Recordings. Frontiers in human neuroscience, 14, 536070. https://doi.org/10.3389/fnhum.2020.536070

254. Wagner, T. A., Zahn, M., Grodzinsky, A. J., & Pascual-Leone, A. (2004). Three-dimensional head model simulation of transcranial magnetic stimulation. IEEE transactions on bio-medical engineering, 51(9), 1586–1598. https://doi.org/10.1109/TBME.2004.827925

255. Wehr, M., & Zador, A. M. (2005). Synaptic mechanisms of forward suppression in rat auditory cortex. Neuron, 47(3), 437–445. https://doi.org/10.1016/j.neuron.2005.06.009

256. Weinreb, R. N., Aung, T., & Medeiros, F. A. (2014). The pathophysiology and treatment of glaucoma: a review. JAMA, 311(18), 1901–1911. https://doi.org/10.1001/jama.2014.3192

257. Weinrich, C. A., Brittain, J. S., Nowak, M., Salimi-Khorshidi, R., Brown, P., & Stagg, C. J. (2017). Modulation of Long-Range Connectivity Patterns via Frequency-Specific Stimulation of Human Cortex. Current biology : CB, 27(19), 3061–3068.e3. https://doi.org/10.1016/j.cub.2017.08.075

258. Weyand T. G. (2016). The multifunctional lateral geniculate nucleus. Reviews in the neurosciences, 27(2), 135–157. https://doi.org/10.1515/revneuro-2015-0018

259. Winawer, J., & Witthoft, N. (2015). Human V4 and ventral occipital retinotopic maps. Visual neuroscience, 32, E020. https://doi.org/10.1017/S0952523815000176

260. Windhoff, M., Opitz, A., & Thielscher, A. (2013). Electric field calculations in brain stimulation based on finite elements: an optimized processing pipeline for the generation and usage of accurate individual head models. Human brain mapping, 34(4), 923–935. https://doi.org/10.1002/hbm.21479

261. Wischnewski, M., Alekseichuk, I., & Opitz, A. (2023). Neurocognitive, physiological, and biophysical effects of transcranial alternating current stimulation. Trends in cognitive sciences, 27(2), 189–205.

https://doi.org/10.1016/j.tics.2022.11.013

262. Woods, D. L., Wyma, J. M., Yund, E. W., Herron, T. J., & Reed, B. (2015). Factors influencing the latency of simple reaction time. Frontiers in human neuroscience, 9, 131. https://doi.org/10.3389/fnhum.2015.00131

263. Wróbel A. (2000). Beta activity: a carrier for visual attention. Acta neurobiologiae experimentalis, 60(2), 247–260. https://doi.org/10.55782/ane-2000-1344

264. Xie, J., Wang, G. J., Yow, L., Humayun, M. S., Weiland, J. D., Cela, C. J., Jadvar, H., Lazzi, G., Dhrami-Gavazi, E., & Tsang, S. H. (2012). Preservation of retinotopic map in retinal degeneration. Experimental eye research, 98, 88–96. https://doi.org/10.1016/j.exer.2012.03.017

265. Xie, J., Wang, G. J., Yow, L., J Cela, C., Humayun, M. S., Weiland, J. D., Lazzi, G., & Jadvar, H. (2011). Modeling and percept of transcorneal electrical stimulation in humans. IEEE transactions on bio-medical engineering, 58(7), 1932–1939. https://doi.org/10.1109/TBME.2010.2087378

266. Yan, W., Peng, Y. R., van Zyl, T., Regev, A., Shekhar, K., Juric, D., & Sanes, J. R. (2020). Cell Atlas of The Human Fovea and Peripheral Retina. Scientific reports, 10(1), 9802. https://doi.org/10.1038/s41598-020-66092-9

267. Ye, Z., & Hang Chan, L. L. (2023). Effect of the Aperiodic Electrical Stimulation on the Visual Cortical Neuronal Response. Annual International Conference of the IEEE Engineering in Medicine and Biology Society. IEEE Engineering in Medicine and Biology Society. Annual International Conference, 2023, 1–4. https://doi.org/10.1109/EMBC40787.2023.10341193

268. Yücel, Y. H., Zhang, Q., Weinreb, R. N., Kaufman, P. L., & Gupta, N. (2003). Effects of retinal ganglion cell loss on magno-, parvo-, koniocellular pathways in the lateral geniculate nucleus and visual cortex in glaucoma. Progress in retinal and eye research, 22(4), 465–481. https://doi.org/10.1016/s1350-9462(03)00026-0

269. Yuen, T. G., Agnew, W. F., Bullara, L. A., Jacques, S., & McCreery, D. B. (1981). Histological evaluation of neural damage from electrical stimulation: considerations for the selection of parameters for clinical application. Neurosurgery, 9(3), 292–299.

270. Zaehle, T., Rach, S., & Herrmann, C. S. (2010). Transcranial alternating current stimulation enhances individual alpha activity in human EEG. PloS one, 5(11), e13766. https://doi.org/10.1371/journal.pone.0013766

271. Zhang, G., Wei, Q., Lu, L., Lin, A. L., & Qu, C. (2023a). The evolution of mechanism of accommodation and a novel hypothesis. Graefe's archive for clinical and experimental ophthalmology = Albrecht von Graefes Archiv fur klinische und experimentelle Ophthalmologie, 261(11), 3083–3095. https://doi.org/10.1007/s00417-023-06045-w

272. Zhang, J. P., Xing, X. X., Zheng, M. X., Wu, J. J., Xue, X., Li, Y. L., Hua, X. Y., Ma, S. J., & Xu, J. G. (2023b). Effects of cortico-cortical paired associative stimulation based on multisensory integration to brain network connectivity in stroke patients: study protocol for a randomized doubled blind clinical trial. BMC neurology, 23(1), 176. https://doi.org/10.1186/s12883-023-03218-2

273. Zhao, Z., Shirinpour, S., Tran, H., Wischnewski, M., & Opitz, A. (2023). Intensity- and frequency-specific effects of transcranial alternating current stimulation are explained by network dynamics. bioRxiv : the preprint server for biology, 2023.05.19.541493. https://doi.org/10.1101/2023.05.19.541493

274. Żebrowska, M., Dzwiniel, P., & Waleszczyk, W. J. (2020). Removal of the Sinusoidal Transorbital Alternating Current Stimulation Artifact From Simultaneous EEG Recordings: Effects of Simple Moving Average Parameters. Frontiers in neuroscience, 14, 735. https://doi.org/10.3389/fnins.2020.00735

Author's Scientific Publications

1. Raciborska, I., **Dzwiniel**, **P**., Kordecka, K., Posłuszny, A., Waleszczyk, W., & Wróbel, A. (2024). Optical imaging of the intrinsic signal as a tool to characterize orientation sensitivity in the primary visual cortex of the young mouse. *Acta neurobiologiae experimentalis*, *84*(1), 1–25. https://doi.org/10.55782/ane-2024-2397

2. Żebrowska, M., **Dzwiniel**, **P**., & Waleszczyk, W. J. (2020). Removal of the Sinusoidal Transorbital Alternating Current Stimulation Artifact From Simultaneous EEG Recordings: Effects of Simple Moving Average Parameters. *Frontiers in neuroscience*, *14*, 735. https://doi.org/10.3389/fnins.2020.00735

3. **Dzwiniel**, **P**., Gola, M., Wójcik-Gryciuk, A., & Waleszczyk, W. J. (2017). Specvis: Free and open-source software for visual field examination. *PloS one*, *12*(10), e0186224. https://doi.org/10.1371/journal.pone.0186224

4. Brzostek, A., & **Dzwiniel**, **P**. (2012). Jak neurobiologiczne mechanizmy leżące u podstaw powstawania rytmu korelują z istnieniem stanów świadomości? *Młoda Psychologia, 1*, 493–502. Liberi Libri.

Corrigenda

to the doctoral dissertation

Modulation of Visual Information Processing in the Human Nervous System Using Non-Invasive Electrical Stimulation

Piotr Dzwiniel

Supervisor
Ewa Kublik, Ph.D., D.Sc.

Warsaw, 2025

Contents

Revised formulas

Page 62, line 6

before	after
$Q_{area} = \frac{I_{RMS} \times t_{half-phase}}{A}$	$Q_{pulse} = 2 \cdot \int_{0}^{t_{half-phase}} I_{peak} \cdot sin(2\pi f t)dt = \frac{2I_{peak}}{\pi f}$
	$Q_{area} = Q_{pulse} \div A$

Rationale: The initially applied method of charge calculation, based on the root mean square (RMS), reflects the effective value but does not account for the actual charge flow during the duration of a sinusoidal pulse. The revised approach integrates the pulse function over time, providing a more accurate representation of total charge (see Corrigendum Table 1).

Page 66, line 33; page 67, line 4

before	$\sigma_{eyeballs} = \frac{(W_{vitreous\ humor} \times \sigma_{vitreous\ humor}) + (W_{other} \times \sigma_{other})}{2}$
	$\sigma_{eyeballs} = \frac{(0.8 \times 2.16\ S/m) + (0.2 \times 0.6835\ S/m)}{2} = 0.9323\ S/m$
after	$\sigma_{eyeballs} = (W_{vitreous\ humor} \times \sigma_{vitreous\ humor}) + (W_{other} \times \sigma_{other})$
	$\sigma_{eyeballs} = (0.8 \times 2.16\ S/m) + (0.2 \times 0.6835\ S/m) = 1.8647\ S/m$

Rationale: Correction of a weighted average equation. Incorporating this change resulted in an increase (x2) of eyeballs conductivity and subtle changes in modeling results (see Tables and updated Figures below).

Page 83, line 6

before	after
$f(d, A) = r_{max} + r_{base}\left(\frac{Q(d,A)^{n}}{Q(d,A)^{n} + \sigma_{Q}^{n}}\right)$	$f(d, A) = r_{base} + r_{max}\left(\frac{Q(d,A)^{n}}{Q(d,A)^{n} + \sigma_{Q}^{n}}\right)$

Rationale: Swapping the r_{max} and r_{base} parameters.

Page 126, line 20

before	$f(d, A) = r_{max} + r_{base}\left(\frac{Q(d,A)^{n}}{Q(d,A)^{n} + \sigma_{Q}^{n}}\right)\left(\frac{A^{m}}{A^{m} + \sigma_{A}^{m}}\right)\left(\frac{\delta^{p}}{\delta^{p} + d^{p}}\right)$
after	$f(d, A) = r_{base} + r_{max}\left(\frac{Q(d,A)^{n}}{Q(d,A)^{n} + \sigma_{Q}^{n}}\right)\left(\frac{A^{m}}{A^{m} + \sigma_{A}^{m}}\right)\left(\frac{\delta^{p}}{\delta^{p} + d^{p}}\right)$

Rationale: Swapping the r_{max} and r_{base} parameters.

Page 105, line 27

before	after
$I_{total} = \sum_{i=1}^{N_{vox}} I_{vox} = \sum_{i=1}^{N_{vox}} \left(magnJ_i \times A_{vox} \right)$	The I_{total} measure and it's formula has been removed from the dissertation.

Rationale: The introduction of the I_{total} measure, which sums current flowing through all voxels of a given anatomical structure, was intended as a practical way to highlight the relationship between a structure's size and the total amount of current passing through it. The aim was to draw attention to the fact that large structures (e.g., scalp), even with low current density, could conduct equal or greater total current compared to smaller regions with high current density (e.g., the eyeballs). However, the I_{total} measure lacks physical justification - it is based on summing absolute current values and does not account for the directionality of the current density vector or charge conservation. As a result, it leads to mathematical overaccumulation and obscures the distinction between real current flow and geometric accumulation of density. For this reason, the corrigendum removes this measure from further use. In its place, the number of voxels comprising each structure/ROI is reported, which allows for better normalization of average EFM and CDM values to the actual volume of the analyzed region, reducing the risk of overinterpretation and exaggeration of regional significance or the current flowing through it.

The source code, reflecting changes of the equations, is available at: https://github.com/piotrdzwiniel/nencki_phd/tree/master/src/corrigenda.

Revised values

This section presents the recalculated results after corrections to the above formulas were implemented. The updated computations include values of total charge for current pulses, parameters and predictions of the Naka-Rushton models, as well as values of the induced electric field. The corrected values have also been incorporated into the subsequent sections dedicated to text, tables, and figures in the dissertation.

Corrigendum Table 1. *Comparison of total charge (Q_{pulse}) values for pulses of specified duration and amplitude, calculated using the root mean square (RMS, before correction) and integral-based (after) methods.*

Pulse Parameters	**Before**	**After**	**Difference (%)**
10 ms 100 μA	0.3536 μC	0.3183 μC	9.98
10 ms 200 μA	0.7071 μC	0.6366 μC	9.97
10 ms 300 μA	1.0607 μC	0.9549 μC	9.97
50 ms 100 μA	1.7678 μC	1.5915 μC	9.97
50 ms 200 μA	3.5355 μC	3.1831 μC	9.97
50 ms 300 μA	5.3033 μC	4.7746 μC	9.97
100 ms 100 μA	3.5355 μC	3.1831 μC	9.97
100 ms 200 μA	7.0711 μC	6.3662 μC	9.97
100 ms 300 μA	10.6066 μC	9.5493 μC	9.97

Corrigendum Table 2. *Comparison of Naka-Rushton model parameter estimates obtained with initially used RMS-based (before) versus updated integral-based (after) pulse charge calculations. The table includes results from one-dimensional (1D) and three-dimensional (3D) model fits for behavioral data from the first study, and three-dimensional model fits for EEG data from the second study.*

Param.	**Description**	**1D First Study**		**3D First Study**		**3D Second Study**	
		Before	**After**	**Before**	**After**	**Before**	**After**
r_max	Maximum response level, representing the upper bound of the model (asymptote).	89.7117	89.8717	148.1112	191.3033	93.3224	90.6216
sigma_Q	Half-saturation constant for total charge (Q); the charge level at which the response reaches 50% of r_max.	1.5385	1.3851	7.9801	1.2701	4.7580	0.8913
n	Hill coefficient for total charge; controls the steepness of the response curve related to total charge.	7.9742	7.9743	11.1811	11.1827	1.4026	4.3575
sigma_A	Half-saturation constant for pulse amplitude (A); the amplitude level at which the response reaches 50% of r_max.	N/A	N/A	65.5224	65.5224	93.6687	82.0661
m	Hill coefficient for amplitude; controls the steepness of the response curve related to amplitude.	N/A	N/A	2.7862	2.7862	20.2654	3.7853
delta	Scaling constant for duration effectiveness.	N/A	N/A	0.0048	57.7021	15.0085	19.8739
p	Hill coefficient for duration effectiveness; controls how duration influences the response.	N/A	N/A	-0.064	-0.0452	-2.3460	-1.7789
r_base	Baseline response (minimum response level); the lowest possible response level when stimulation is minimal.	0.5590	0.5591	0.8596	0.8596	-5.4768	-0.3437
R^2	Goodness of fit	0.9797	0.9797	1.0000	1.0000	0.9948	0.9952

Corrigendum Table 3. *Predicted pulse durations (in ms) required to reach selected phosphene detection levels for specific current amplitudes. Results are based on the* ***one- and three-dimensional Naka-Rushton model*** *fitted to behavioral data from the first study. Values are shown for RMS-based (before) and updated integration-based (after) charge calculations.*

Detection Level	**Pulse amplitude (μA)**	**Duration (ms)**			
		One-dimensional Naka-Rushton model		*Three-dimensional Naka-Rushton model*	
		Before	**After**	**Before**	**After**
90%	300	28.54	28.54	18.37	18.35
90%	200	42.42	42.42	29.86	29.84
90%	100	83.24	83.24	NaN	NaN
50%	300	14.99	14.99	13.6	13.60
50%	200	22.31	22.31	20.26	20.26
50%	100	43.70	43.70	41.54	41.54
5%	300	10.06	10.06	10.15	10.15
5%	200	14.98	14.98	15.25	15.25
5%	100	29.48	29.48	30.42	30.42

Corrigendum Table 4. *Predicted pulse durations (in ms) required to reach P2 amplitude level, defined as 75%, 50% or 10% of the response evoked by a visual stimulus (LED), for specific current amplitudes. Results are based on the* ***three-dimensional Naka-Rushton*** *model fitted to EEG data from the second study. Values are shown for both RMS-based (before) and updated integration-based (after) charge calculations.*

Percent of Response to Visual Stimulus	Amplitude (μA)	Duration (ms)	
		Before	After
75%	300		50.12
75%	200		55.76
75%	100		NaN
50%	300	22.93	23.32
50%	200	26.36	25.84
50%	100	51.32	51.99
10%	300	10.13	NaN
10%	200	11.36	12.60
10%	100	15.91	22.41

Corrigendum Table 5. *Maximum EFM and CDM values in selected regions of interest (ROIs) before and after the correction of eye conductivity values for the "periorbital" electrode montage. The values are presented for both surface simulation outputs (mesh; .msh files) and data exported to the voxel format (voxel; NIfTI files). For each method and format, values before and after the correction are shown, along with the corresponding percent change.*

ROI	Measure	Before		After		Difference (%)	
		msh (mesh)	nii (voxel)	msh (mesh)	nii (voxel)	msh (mesh)	nii (voxel)
Scalp	EFM	1.7667	1.1187	1.7876	1.1292	1.1864	0.9404
	CDM	0.3445	0.2182	0.3486	0.2202	1.1864	0.9397
Eyeballs	EFM	0.0844	0.0779	0.0482	0.0444	-42.8830	-43.0222
	CDM	0.0787	0.0726	0.0899	0.0828	14.2954	14.0102
GM	EFM	0.0225	N/A	0.0220	N/A	-2.5640	N/A
	CDM	0.0094	N/A	0.0092	N/A	-2.5640	N/A
WM	EFM	0.0749	N/A	0.0704	N/A	-5.8939	N/A
	CDM	0.0260	N/A	0.0245	N/A	-5.8938	N/A
Optic Nerve	EFM	N/A	0.0375	N/A	0.0352	N/A	-6.1050
	CDM	N/A	0.0131	N/A	0.0123	N/A	-6.0536
Rest of the Brain	EFM	N/A	0.0244	N/A	0.0186	N/A	-24.0066
	CDM	N/A	0.0085	N/A	0.0078	N/A	-8.5882

Corrigendum Table 6. *Volumetric statistics of electric field magnitude (EFM) in selected regions of interest (ROIs) after correction of eyeball conductivity for the "periorbital" electrode configuration. The table represents a corrected version of* ***Table 3-1****, supplemented with the column “% Change”, which indicates the percentage change in mean EFM values after correction relative to the values before correction.*

Volume	Electric Field Magnitude [V/m]					Voxel Count
	Mean	Difference (%)	SD	Max	Min	
Scalp	0.0047	-1.6842	0.0255	1.1292	0.0000	1.22E+07
Eyeballs	0.0281	-42.5971	0.0061	0.0444	0.0145	17542
Optic Nerve	0.0092	-9.8522	0.0035	0.0352	0.0047	1637
Rest of the Brain	0.0034	-2.6087	0.0018	0.0186	0.0000	1638915

Corrigendum Table 7. *Volumetric statistics of current density magnitude (CDM) in selected regions of interest (ROIs) after correction of eyeball conductivity for the "periorbital" electrode configuration. The table represents a corrected version of* ***Table 3-2****, supplemented with the column "% Change", which indicates the percentage change in mean CDM values after correction relative to the values before correction.*

Volume	**Current Density Magnitude [A/m2]**					**Voxel Count**
	Mean	**Difference (%)**	**SD**	**Max**	**Min**	
Scalp	0.0009	-2.1505	0.0050	0.2202	0.0000	1.22E+07
Eyeballs	0.0524	14.8782	0.0113	0.0828	0.0061	17542
Optic Nerve	0.0032	-9.9150	0.0012	0.0123	0.0016	1637
Rest of the Brain	0.0013	-3.0075	0.0007	0.0078	0.0000	1638915

Corrigendum Table 8. *Maximum EFM and CDM values in selected regions of interest (ROIs) before and after the correction of eye conductivity values for the "frontal-occipital" electrode montage. The values are presented for both surface simulation outputs (mesh; .msh files) and data exported to the voxel format (voxel; NIfTI files). For each method and format, values before and after the correction are shown, along with the corresponding percent change.*

ROI	**Measure**	**Before**		**After**		**Difference (%)**	
		msh (mesh)	**nii (voxel)**	**msh (mesh)**	**nii (voxel)**	**msh (mesh)**	**nii (voxel)**
Scalp	EFM	1.6173	1.0695	1.6223	1.0726	0.3092	0.2955
	CDM	0.3154	0.2086	0.3163	0.2092	0.3095	0.2925
Eyeballs	EFM	0.0797	0.0936	0.0443	0.1041	-44.3525	11.2667
	CDM	0.0743	0.0688	0.0827	0.0772	11.3548	12.1820
GM	EFM	0.0666	N/A	0.0673	N/A	1.0031	N/A
	CDM	0.0279	N/A	0.0282	N/A	1.0029	N/A
WM	EFM	0.2389	N/A	0.2445	N/A	2.3567	N/A
	CDM	0.0831	N/A	0.0851	N/A	2.3571	N/A
Optic Nerve	EFM	N/A	0.1462	N/A	0.1493	N/A	2.1269
	CDM	N/A	0.0509	N/A	0.0520	N/A	2.1423
Rest of the Brain	EFM	N/A	0.0951	N/A	0.1076	N/A	13.1413
	CDM	N/A	0.0331	N/A	0.0375	N/A	13.1420

Corrigendum Table 9. *Volumetric statistics of electric field magnitude (EFM) in selected regions of interest (ROIs) after correction of eyeball conductivity for the "frontal-occipital" electrode configuration. The table represents a corrected version of* ***Table 3-3****, supplemented with the column "% Change", which indicates the percentage change in mean EFM values after correction relative to the values before correction.*

Volume	**Electric Field Magnitude [V/m]**					**Voxel Count**
	Mean	**Difference (%)**	**SD**	**Max**	**Min**	
Scalp	0.0062	0.0000	0.0253	1.0726	0.0000	1.22E+07
Eyeballs	0.0198	-43.8244	0.0054	0.1041	0.0098	17542
Optic Nerve	0.0414	1.7949	0.0294	0.1493	0.0067	1637
Rest of the Brain	0.0096	-0.3115	0.0022	0.1076	0.0000	1638915

Corrigendum Table 10. *Volumetric statistics of current density magnitude (CDM) in selected regions of interest (ROIs) after correction of eyeball conductivity for the "frontal-occipital" electrode configuration. The table represents a corrected version of* ***Table 3-4****, supplemented with the column "% Change", which indicates the percentage change in mean CDM values after correction relative to the values before correction.*

Volume	**Current Density Magnitude [A/m2]**					**Voxel Count**
	Mean	**% Change**	**SD**	**Max**	**Min**	
Scalp	0.0012	0.0000	0.0049	0.2092	0.0000	1.22E+07
Eyeballs	0.0370	12.4012	0.0100	0.0772	0.0182	17542
Optic Nerve	0.0144	1.8375	0.0102	0.0520	0.0023	1637
Rest of the Brain	0.0037	-0.2703	0.0009	0.0375	0.0000	1638915

Text revisions

The result description in the text also requires few corrections i.e. introduction of revised values:

Page	**Line**	**Before**	**After**
7	9	…**stężenia** indukowanego pola elektrycznego…	…**natężenia** indukowanego pola elektrycznego…
9		gamma-aminobutyric acid (neurotransmitter)	gamma-aminobutyric acid
62	16	…determined to be **1.77** μC. When distributed over an electrode area of 3 cm^2, the total charge per unit area is approximately **0.59** μC/cm^2…	…determined to be **1.59** μC. When distributed over an electrode area of 3 cm^2, the total charge per unit area is approximately **0.53** μC/cm^2…
62	26	…(**0.00448** C/cm^2 vs. 0.022 C/cm^2).	…(**0.00804** C/cm^2 vs. 0.022 C/cm^2).
66	28	…a value of **0.9323** S/m for the eyeballs parameter. This is almost **double** the default value in SimNIBS software, which is 0.5 S/m.	…a value of **1.8646 S/m** for the eyeballs parameter. This **is** almost **four times higher** than the default value in SimNIBS software, which is 0.5 S/m.
96	13	…the maximum electric field magnitude (EFM) value for the ellipsoidal electrode was **1.7609 V/m^2**, as compared to **1.7667** V/m for the rectangular electrode.	…the maximum electric field magnitude (EFM) value for the ellipsoidal electrode was **1.7680 V/m**, as compared to **1.7876** V/m for the rectangular electrode.
96	20	…(KS = **0.389**, p-value = **0.332**).	…(KS = **0.064**, p-value = **0.213**).
97	1	…observed for the ellipsoidal electrode (**1.7609** V/m), …	…observed for the ellipsoidal electrode (**1.7680** V/m), …
97	16	…(KS = **0.109**, p-value = **0.003**).	…(KS = **0.090**, p-value = **0.025**).
97	17	For the **0.6-1.0 range**, [...] (**KS = 0.638**, **p-value = 0.010**).	For the **0.5-1.0 range**, [...] (**KS = 0.412**, **p-value = 0.002**).
99	9	The maximum field values were **0.786** V/m and **0.755** V/m for the rectangular and ellipsoid electrodes, respectively **- 2.25** and **2.33** times lower than those observed with smaller electrodes of corresponding shapes.	The maximum field values were **0.700** V/m and **0.869** V/m for the rectangular and ellipsoid electrodes, respectively **- 2.55** and **2.03** times lower than those observed with smaller electrodes of corresponding shapes.

99	15	…(KS = **0.128**, p-value < **0.001**; [...]).	…(KS = **0.136**, **p-value < 0.001**; [...]).
99	16	…range (**0.5-1.0**), [...] (KS = **0.393**, p-value = **0.009**)...	…range (**0.4-1.0**), [...] (KS = **0.317**, p-value = **0.007**)...
102	20	The value observed on the surface of the eyeballs was **0.0844** V/m; **0.0749** V/m in the white matter of the optic nerve and as low as **0.0225** V/m was noted in the gray matter in the anterior cortical region.	The value observed on the surface of the eyeballs was **0.0482** V/m; **0.0704** V/m in the white matter of the optic nerve and as low as **0.0220** V/m was noted in the gray matter in the anterior cortical region.
104	16	…**1.1187** V/m, [...] **14** times higher [...] (**0.0779** V/m).	…**1.1292** V/m, [...] **25** times higher [...] (**0.0444** V/m).
104	17	…**6.96**%...	…**3.93**%...
104	21	…**93**%...	…**96**%...
105	2	…the maximum EFM in the optic nerve reaching only **0.0375** V/m - equivalent to **3.35**% of the scalp maximum…	…the maximum EFM in the optic nerve reaching only **0.0352** V/m - equivalent to **3.12**% of the scalp maximum…
105	3	For the rest of the brain volume the maximum EFM was **0.0244** V/m, or **2.18**% of the scalp maximum…	For the rest of the brain volume the maximum EFM was **0.0186** V/m, or **1.65**% of the scalp maximum…
105	11	…(**0.0489** V/m).	…(**0.0281** V/m).
105	11	This value is nearly **five** times greater than the average EFM in the optic nerve (**0.0102** V/m) and almost **14** times higher than the average EFM in the rest of the brain (**0.0035** V/m). It is also **ten** times greater than the average EFM in the scalp (**0.0048** V/m).	This value is nearly **three** times greater than the average EFM in the optic nerve (**0.0092** V/m) and **8** times higher than the average EFM in the rest of the brain (**0.0034 V/m**). It is also **six** times greater than the average EFM in the scalp (**0.0047** V/m).
106	18	…the maximum CDM on the skin was only **three** times higher than in the eyeballs, measuring **0.2182** A/m^2 for the scalp and **0.0726** A/m^2 for the eyeballs…	…the maximum CDM on the skin was only **2.5** times higher than in the eyeballs, measuring **0.2202** A/m^2 for the scalp and **0.0828** A/m^2 for the eyeballs…
107	1	…**0.0131** A/m^2…	…**0.0123** A/m^2…
107	2	…**0.0085** A/m^2 [...] **0.0456** A/m^2…	…**0.0078** A/m^2 [...] **0.0524** A/m^2…
107	4	…**0.0035** A/m^2…	…**0.0032** A/m^2…
107	5	…**51** times lower…	…**58** times lower…
109	15	…(**1.6173** V/m)...	…(**1.6223** V/m)...
109	16	…**20** times higher…	…**37** times higher…
109	17	…**0.0797** V/m…	…**0.0443** V/m…
109	18	…**0.2389** V/m…	…**0.2445** V/m…
109	19	…**6.8** times lower [...] **3** times higher…	…**6.6** times lower [...] **5.5** times higher…
109	21	…**0.0666** V/m…	…**0.0673** V/m…

111	1	…**0.0407** V/m…	…**0.0414** V/m…
111	2	…**0.1462** V/m…	…**0.1493** V/m…
111	5	…**1.0695** V/m…	…**1.0726** V/m…
111	7	…**0.0353** V/m…	…**0.0198** V/m…
111	8	…**0.0936** V/m…	…**0.1041** V/m…
111	11	…**0.0951** V/m…	…**0.1076** V/m…
112	13	…Figure **47**…	…Figure **3-18**…
113	12	…**0.2086** A/m^2…	…**0.2092** A/m^2…
113	13	…**0.0329** A/m^2…	…**0.0370** A/m^2…
113	14	…**0.0688** A/m^2…	…**0.0772** A/m^2…
113	15	…**0.0142** A/m^2…	…**0.0144** A/m^2…
113	16	…**0.0509** A/m^2…	…**0.0520** A/m^2…
113	19	…**0.0331** A/m^2…	…**0.0375** A/m^2…
115	13	…**1.7667** V/m [...] **1.6173** V/m…	…**1.7876** V/m [...] **1.6223** V/m…
115	17	…(**0.2389** V/m) [...] (**0.0666 V/m**)...	…(**0.2445** V/m) [...] (**0.0673** V/m)...
115	19	…(**0.0844** V/m) [...] **0.0797** V/m…	…(**0.0482** V/m) [...] **0.0443** V/m…
117	11	…**0.3445** A/m^2 [...] **0.3154** A/m^2…	…**0.3486** A/m^2 [...] **0.3163** A/m^2…
117	15	…(**0.0787** A/m^2) [...] **0.0743** A/m^2…	…(**0.0899** A/m^2) [...] **0.0827** A/m^2…
117	17	…(**0.0831** A/m^2) [...] (**0.0279** A/m^2)...	…(**0.0851** A/m^2) [...] (**0.0282 A/**m^2)...
119	14	…KS statistic of **0.4775**…	…KS statistic of **0.5219**…
119	16	…KS statistic of **0.6005**…	…KS statistic of **0.6872**…
120	1	…KS statistic of **0.8987**…	…KS statistic of **0.9066**…
120	15	…KS test statistic was **0.4776**…	…KS test statistic was **0.5219**…
120	16	…KS statistic of **0.6005**…	…KS statistic of **0.6872**…
120	17	…KS statistic of **0.8970**…	…KS statistic of **0.9048**…
124	7	…F(9, **70597**) = 2152.22…	…F(9, **70.597**) = 2152.22…
125	16	For 90% responses, the differences were more pronounced, with the three-factor model predicting **18.37** ms for 300 µA (a reduction of **35.63**%) and **29.86** ms for 200 µA (a reduction of **29.63**%).	For 90% responses, the differences were more pronounced, with the three-factor model predicting **18.35** ms for 300 µA (a reduction of **35.70**%) and **29.84** ms for 200 µA (a reduction of **29.66**%).
139	36	…Figure 3-**30**C…	…Figure 3-**28**C…

145	8	…goodness-of-fit R^2 of **0.9948** and an average absolute difference between the actual and predicted values of only **2.22**%.	…goodness-of-fit R^2 of **0.9952** and an average absolute difference between the actual and predicted values of only **1.64**%.
145	14	To achieve a modeled response of 50%, the required pulse durations were **51.32** ms for 100 μA, **26.36** ms for 200 μA, and **22.93** ms for 300 μA.	To achieve a modeled response of 50%, the required pulse durations were **51.99** ms for 100 μA, **25.84** ms for 200 μA, and **23.32** ms for 300 μA.
145	15	For a modeled response of 10%, [...] **15.91** ms for 100 μA, **11.36** ms for 200 μA, and **10.13 ms** for 300 μA.	For a modeled response of 10%, [...] **22.41** ms for 100 μA, **12.69** ms for 200 μA, and **NaN** for 300 μ.
146	21	…**2.22**%...	…**1.64**%...
180	22	…Figure 3-2**6**…	…Figure 3-2**5**…

Revised tables

Page 68, line 1, Table 2-1
Description of changes: the value in the "Eye" row and "Swiss ITIS Foundation" column has been updated to 1.8647 S/m, reflecting the corrected result of the formula used to calculate ocular conductivity.

Page 104, line 1, Table 3-1
Description of changes: Revised values reflecting the updated eye conductivity and the removal of the "Sum" column.

Volume	Electric Field Magnitude [V/m]				Voxel Count
	Mean	SD	Max	Min	
Scalp	0.0047	0.0255	1.1292	0.0000	12,220,000
Eyeballs	0.0281	0.0061	0.0444	0.0145	17,542
Optic Nerve	0.0092	0.0035	0.0352	0.0047	1,637
Rest of the Brain	0.0034	0.0018	0.0186	0.0000	1,638,915

Page 107, line 11, Table 3-2
Description of changes: Revised values reflecting the updated eye conductivity and the removal of the "I_{total}" column.

Volume	Current Density Magnitude [A/m^2]				Voxel Count
	Mean	SD	Max	Min	
Scalp	0.0009	0.0050	0.2202	0.0000	12,220,000
Eyeballs	0.0524	0.0113	0.0828	0.0061	17,542
Optic Nerve	0.0032	0.0012	0.0123	0.0016	1,637
Rest of the Brain	0.0013	0.0007	0.0078	0.0000	1,638,915

Page 111, line 14, Table 3-3
Description of changes: Revised values reflecting the updated eye conductivity and the removal of the "Sum" column.

Volume	**Electric Field Magnitude [V/m]**				**Voxel Count**
	Mean	**SD**	**Max**	**Min**	
Scalp	0.0062	0.0253	1.0726	0.0000	12,220,000
Eyeballs	0.0198	0.0054	0.1041	0.0098	17,542
Optic Nerve	0.0414	0.0294	0.1462	0.0067	1,637
Rest of the Brain	0.0096	0.0022	0.1076	0.0000	1,638,915

Page 114, line 4, Table 3-4
Description of changes: Revised values reflecting the updated eye conductivity and the removal of the "I_{total}" column.

Volume	**Current Density Magnitude [A/m^2]**				**Voxel Count**
	Mean	**SD**	**Max**	**Min**	
Scalp	0.0012	0.0049	0.2092	0.0000	12,220,000
Eyeballs	0.0370	0.0100	0.0772	0.0182	17,542
Optic Nerve	0.0144	0.0102	0.0520	0.0023	1,637
Rest of the Brain	0.0037	0.0009	0.0375	0.0000	1,638,915

Page 116, line 11, Table 3-5
Description of changes: Revised values reflecting the updated eye conductivity.

Configuration	**Surface**			
	Scalp	**Eyeballs**	**WM**	**GM**
Periorbital	1.7876	0.0482	0.0704	0.0220
Frontal-Occipital	1.6223	0.0443	0.2445	0.0673

Page 118, line 1, Table 3-6
Description of changes: Revised values reflecting the updated eye conductivity.

Configuration	**Surface**			
	Scalp	**Eyeballs**	**WM**	**GM**
Periorbital	0.3486	0.0899	0.0245	0.0092
Frontal-Occipital	0.3163	0.0827	0.0851	0.0282

Page 129, line 12, Table 3-9
Description of changes: Modifications in the calculation of total pulse charge led to adjustments in model parameters (Corrigendum Table 2), but not in predicted values of valid response rates (%).

Page 146, line 1, Table 3-16

Description of changes: Modifications in the calculation of total pulse charge led to adjustments in model parameters (Corrigendum Table 2) and in the predicted values.

Values	**Trial Type**								
	10 ms 100 µA	**10 ms 200 µA**	**10 ms 300 µA**	**50 ms 100 µA**	**50 ms 200 µA**	**50 ms 300 µA**	**100 ms 100 µA**	**100 ms 200 µA**	**100 ms 300 µA**
Predictions	-0.19	3.40	11.42	47.37	72.77	74.96	57.65	82.57	84.80
Actual	0.00	3.10	11.51	47.75	69.00	78.38	57.34	85.90	81.77
Difference	-0.19	0.3	-0.09	-0.38	3.76	-3.41	0.31	-3.33	3.03

average absolute difference = 1.64; goodness of fit (R^2) = 0.9952

Revised figures

Figure 3-26

Due to an editorial oversight, the figure numbering in *Results* skips Figure 3-26 - the numbering goes from Figure 3-25 directly to Figure 3-27. No figure is actually missing; the issue is limited to the numbering only.

Page 91, line 12, Figure 3-1

Description of changes: Revised figure reflecting the use of integration-based instead of RMS-based pulse total charge calculations.

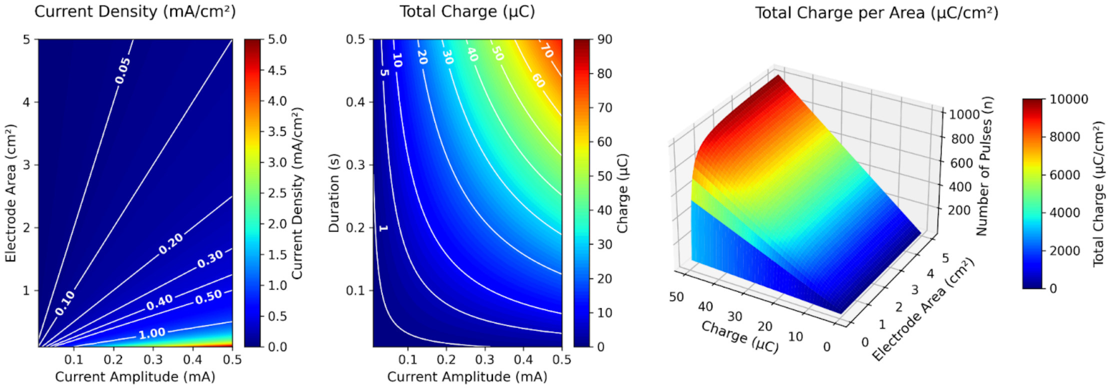

Page 95, line 1, Figure 3-4

Description of changes: Revised figure reflecting the updated eye conductivity. Adjusted Y-axis limits.

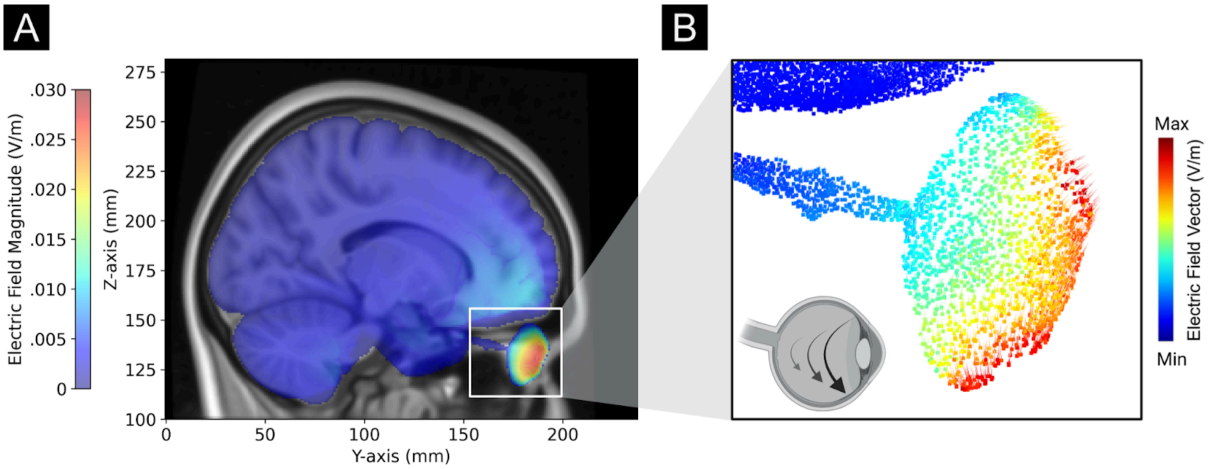

Page 96, line 22, Figure 3-5
Description of changes: Revised figure reflecting the updated eye conductivity. Adjusted Y-axis limits.

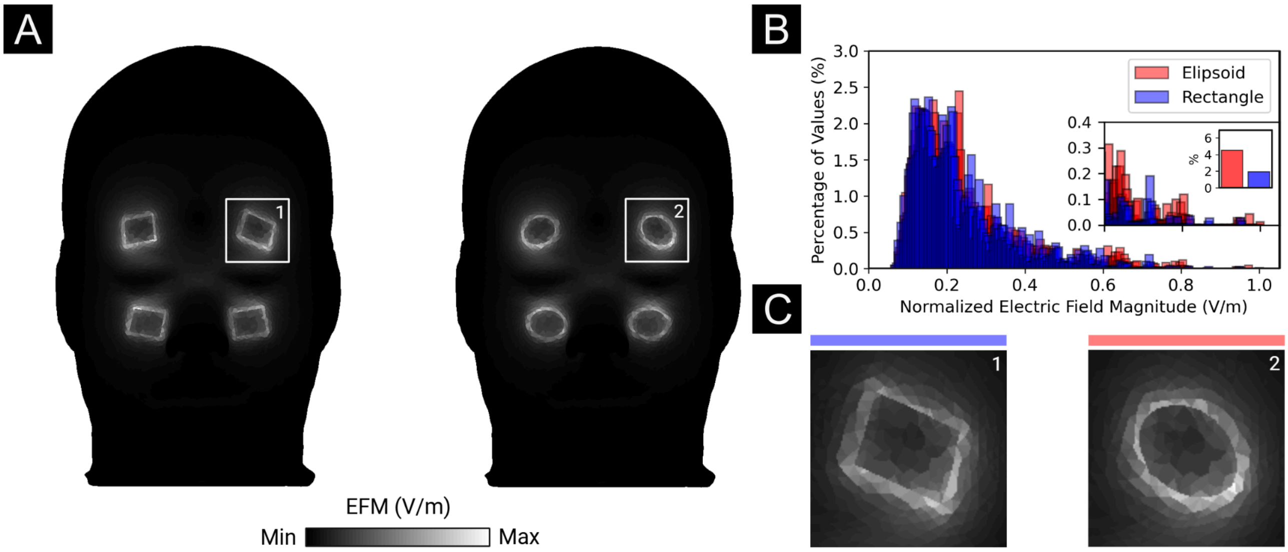

Page 97, line 20, Figure 3-6
Description of changes: Revised figure reflecting the updated eye conductivity. Adjusted Y-axis limits.

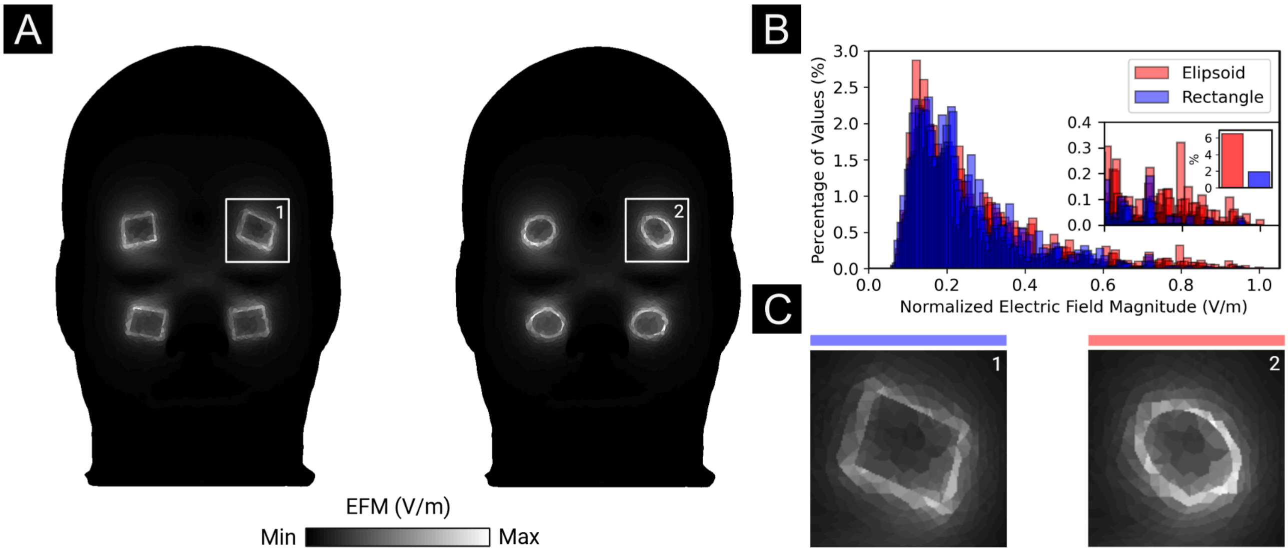

Page 98, line 4, Figure 3-7
Description of changes: Revised figure reflecting the updated eye conductivity.

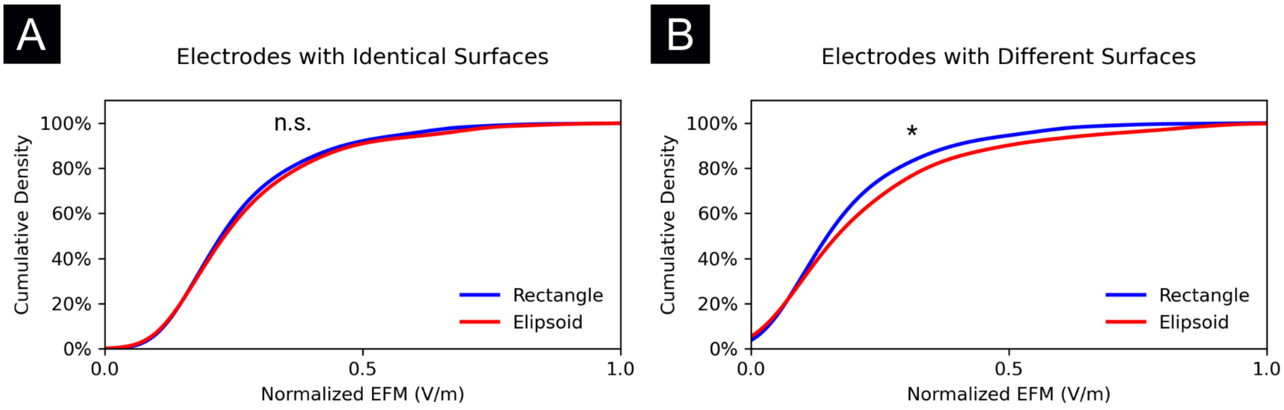

Page 99, line 1, Figure 3-8
Description of changes: Revised figure reflecting the updated eye conductivity.

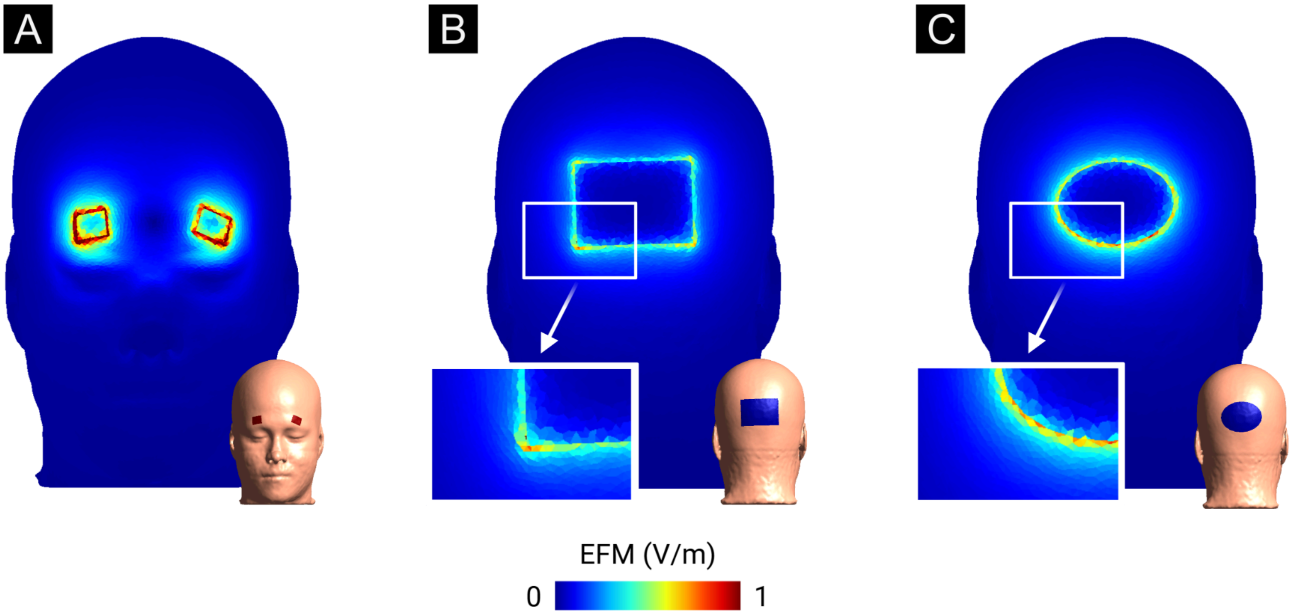

Page 100, line 1, Figure 3-9
Description of changes: Revised figure reflecting the updated eye conductivity. Adjusted Y-axis limits.

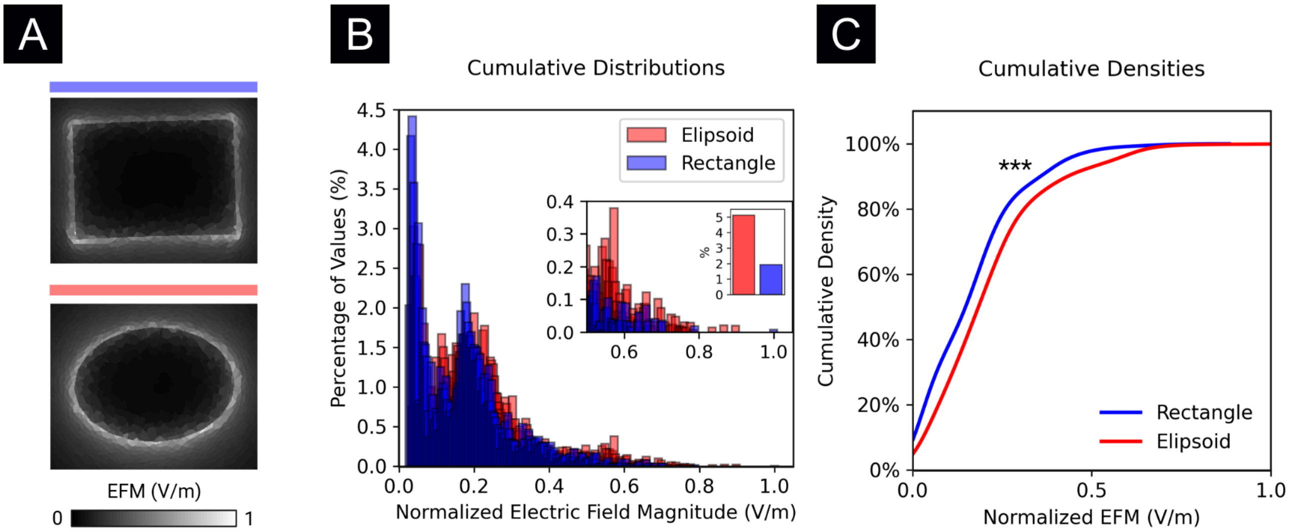

Page 102, line 8, Figure 3-10
Description of changes: Revised figure reflecting the updated eye conductivity.

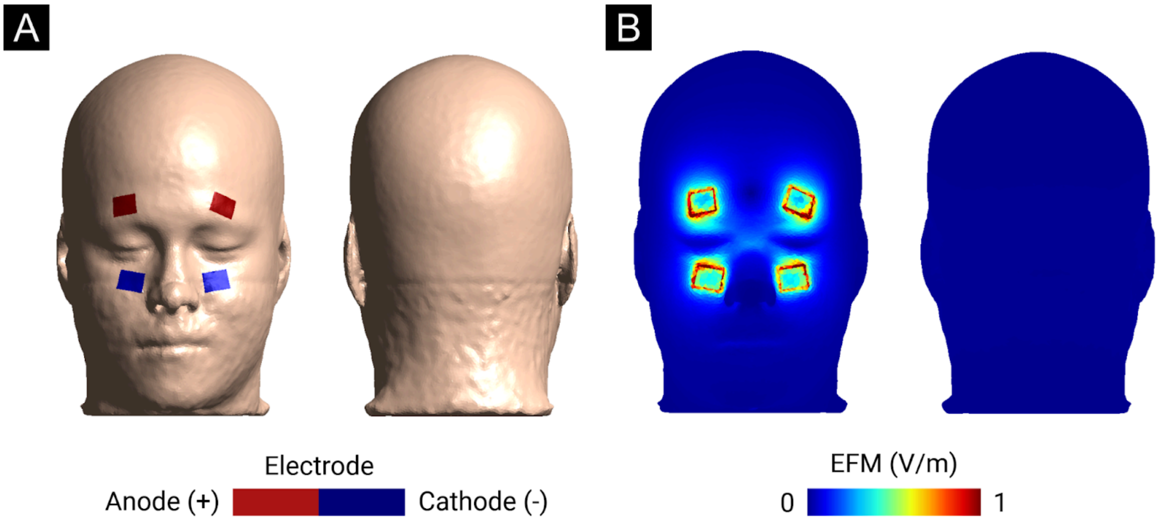

Page 103, line 1, Figure 3-11
Description of changes: Revised figure reflecting the updated eye conductivity.

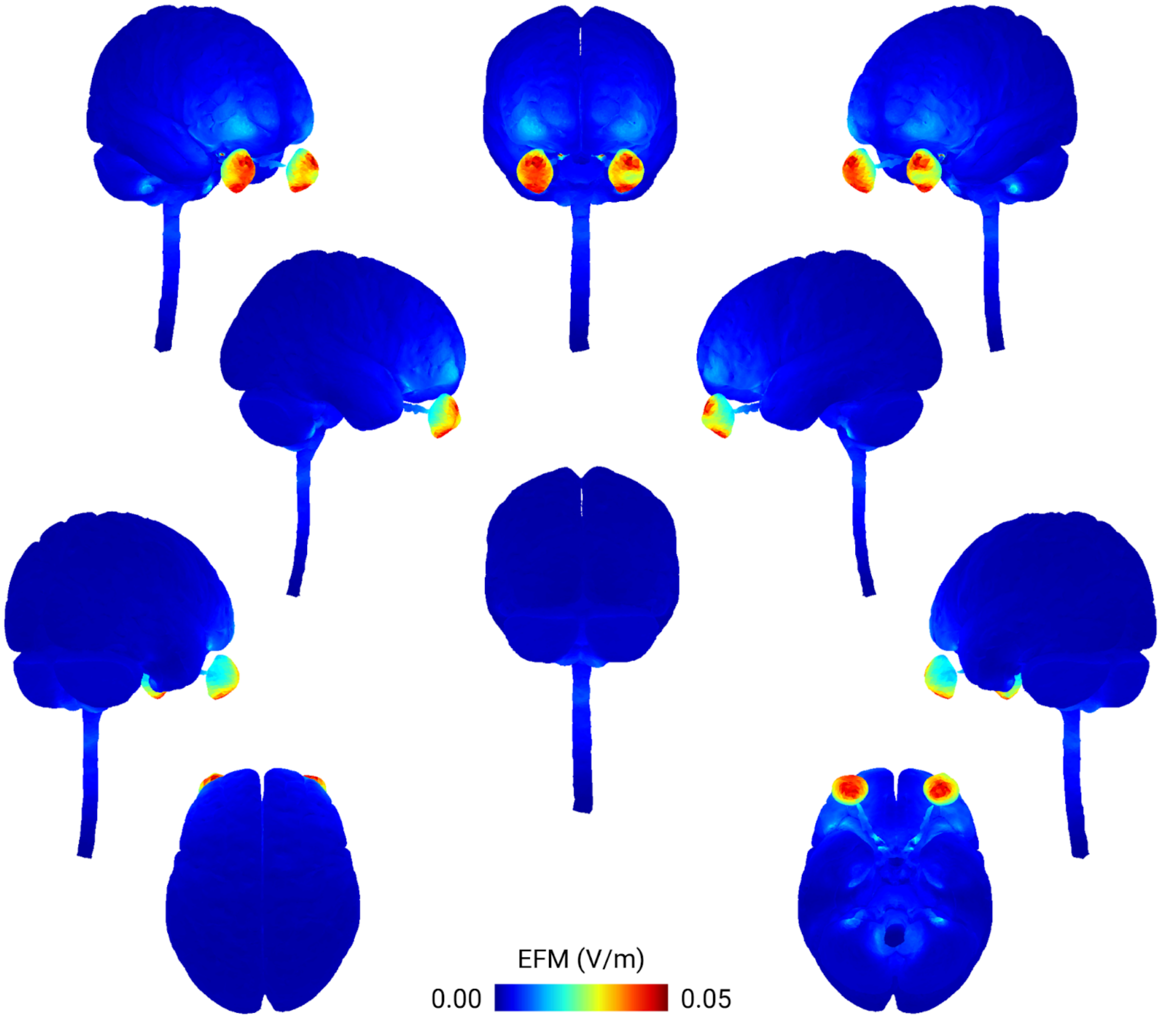

Page 104, line 8, Figure 3-12
Description of changes: Revised figure reflecting the updated eye conductivity and the removal of the “Total Electric Field Across Volumes” panel.

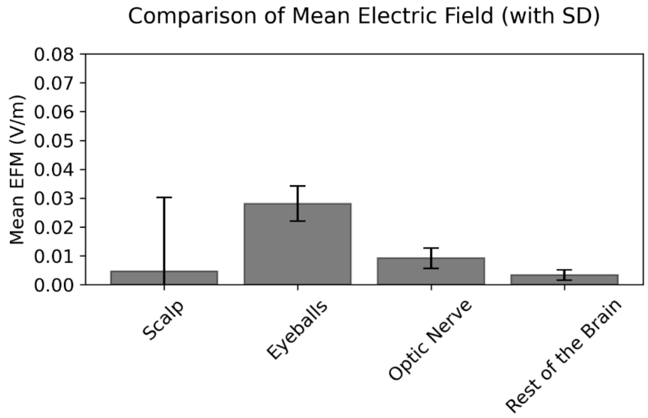

Page 106, line 6, Figure 3-13
Description of changes: Revised figure reflecting the updated eye conductivity.

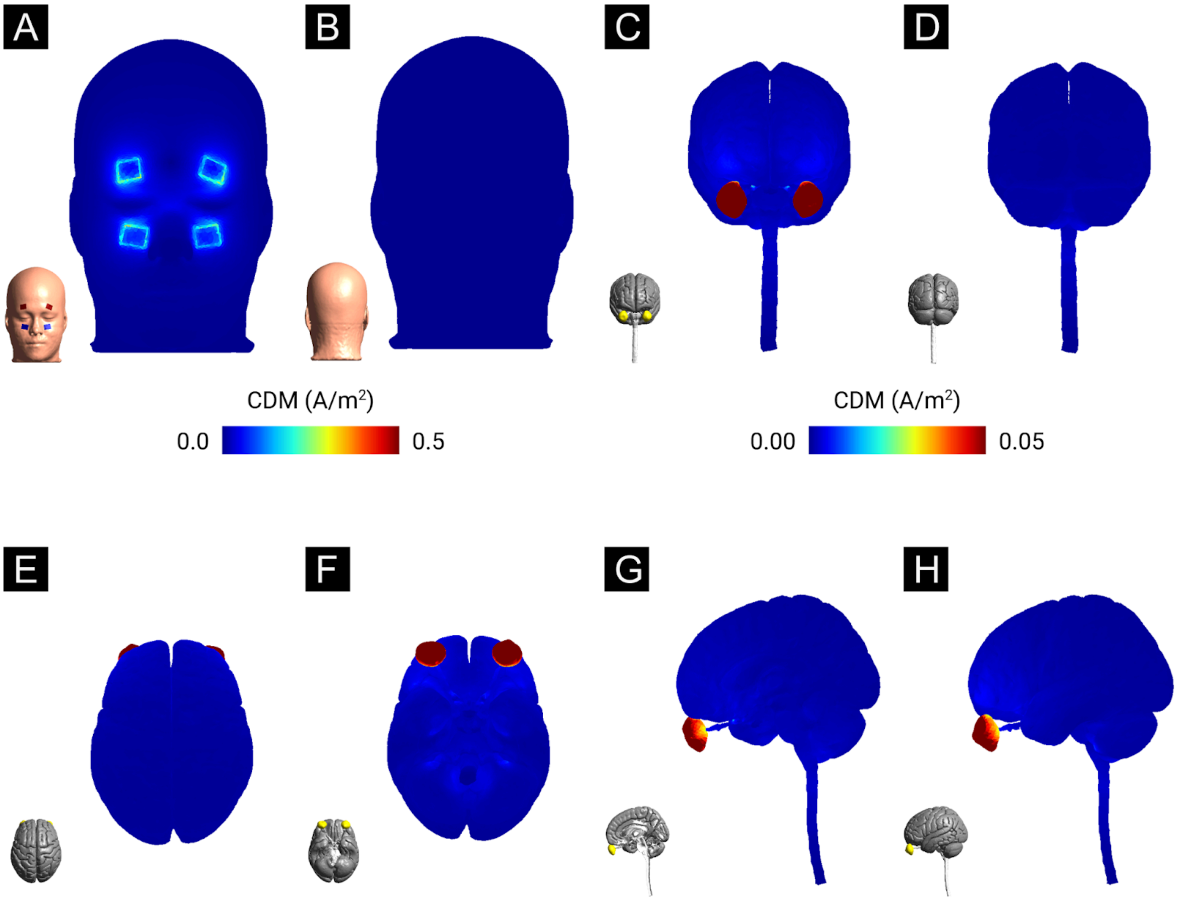

Page 108, line 1, Figure 3-14

Description of changes: Revised figure reflecting the updated eye conductivity and the removal of the “Total Current Across Volumes” panel. Adjusted Y-axis limits.

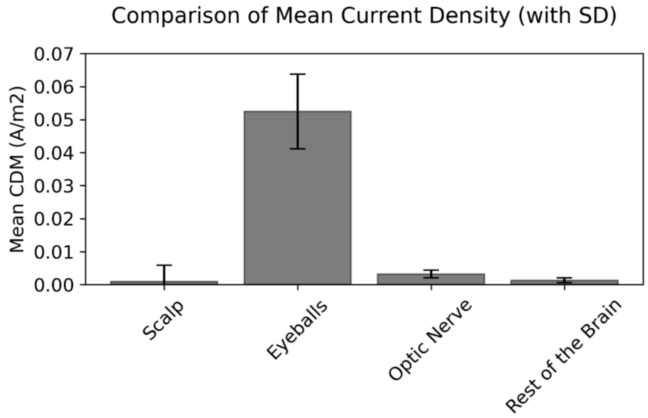

Page 109, line 1, Figure 3-15

Description of changes: Revised figure reflecting the updated eye conductivity.

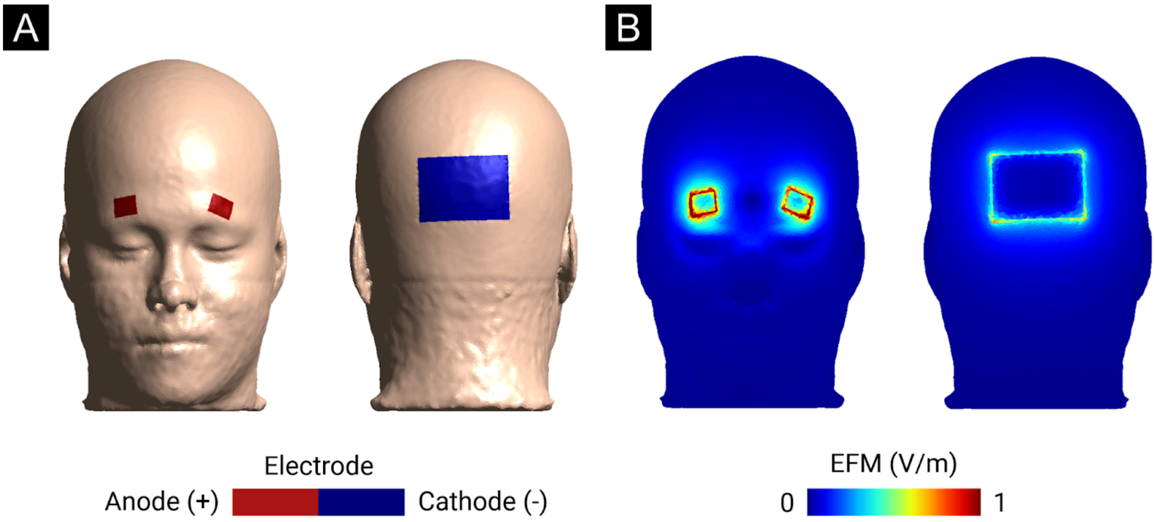

Page 110, line 7, Figure 3-16
Description of changes: Revised figure reflecting the updated eye conductivity.

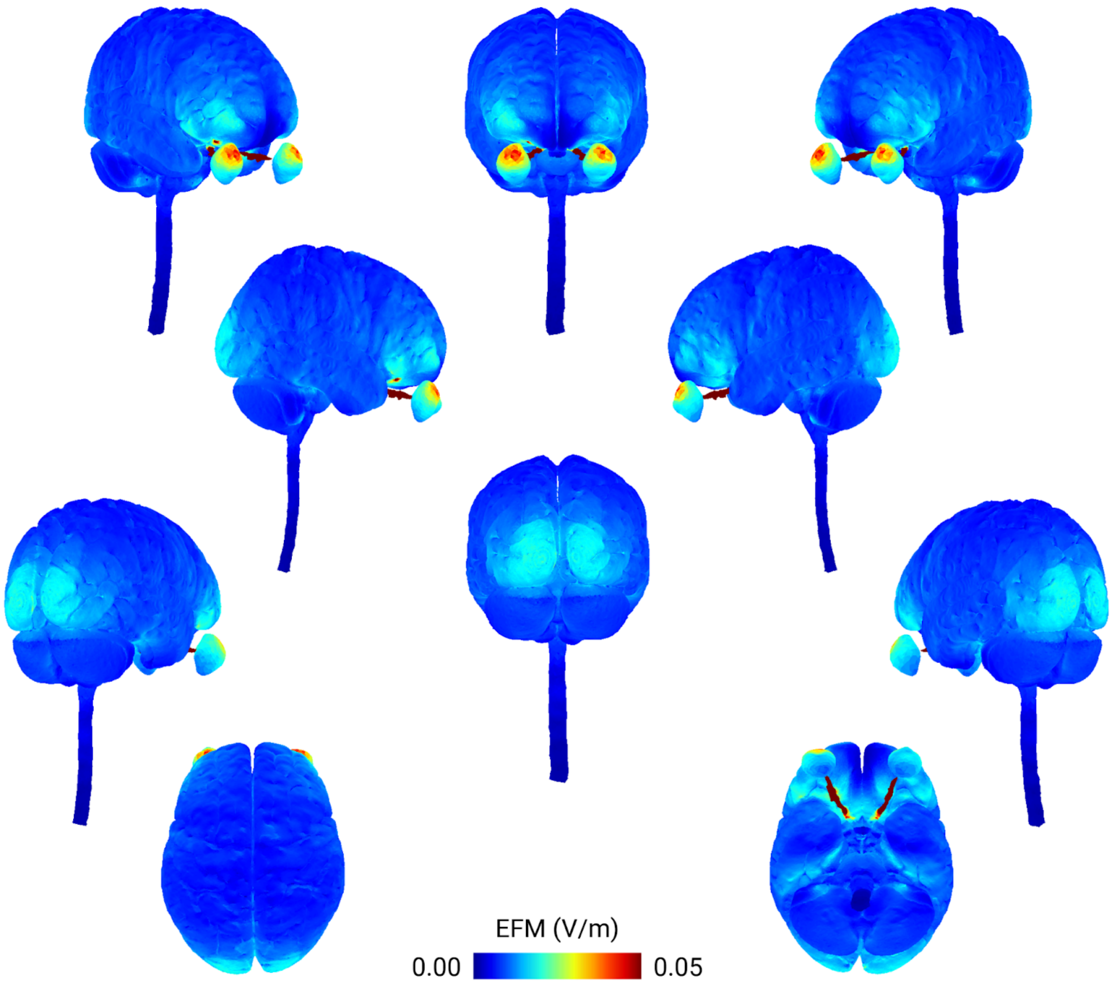

Page 112, line 6, Figure 3-17
Description of changes: Revised figure reflecting the updated eye conductivity and the removal of the “Total Electric Field Across Volumes” panel.

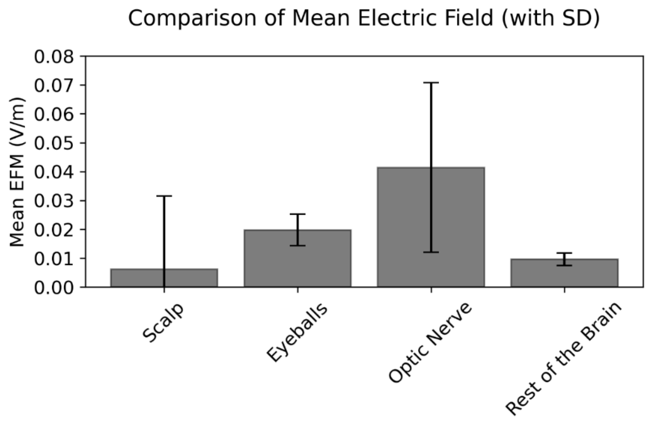

Page 113, line 1, Figure 3-18
Description of changes: Revised figure reflecting the updated eye conductivity.

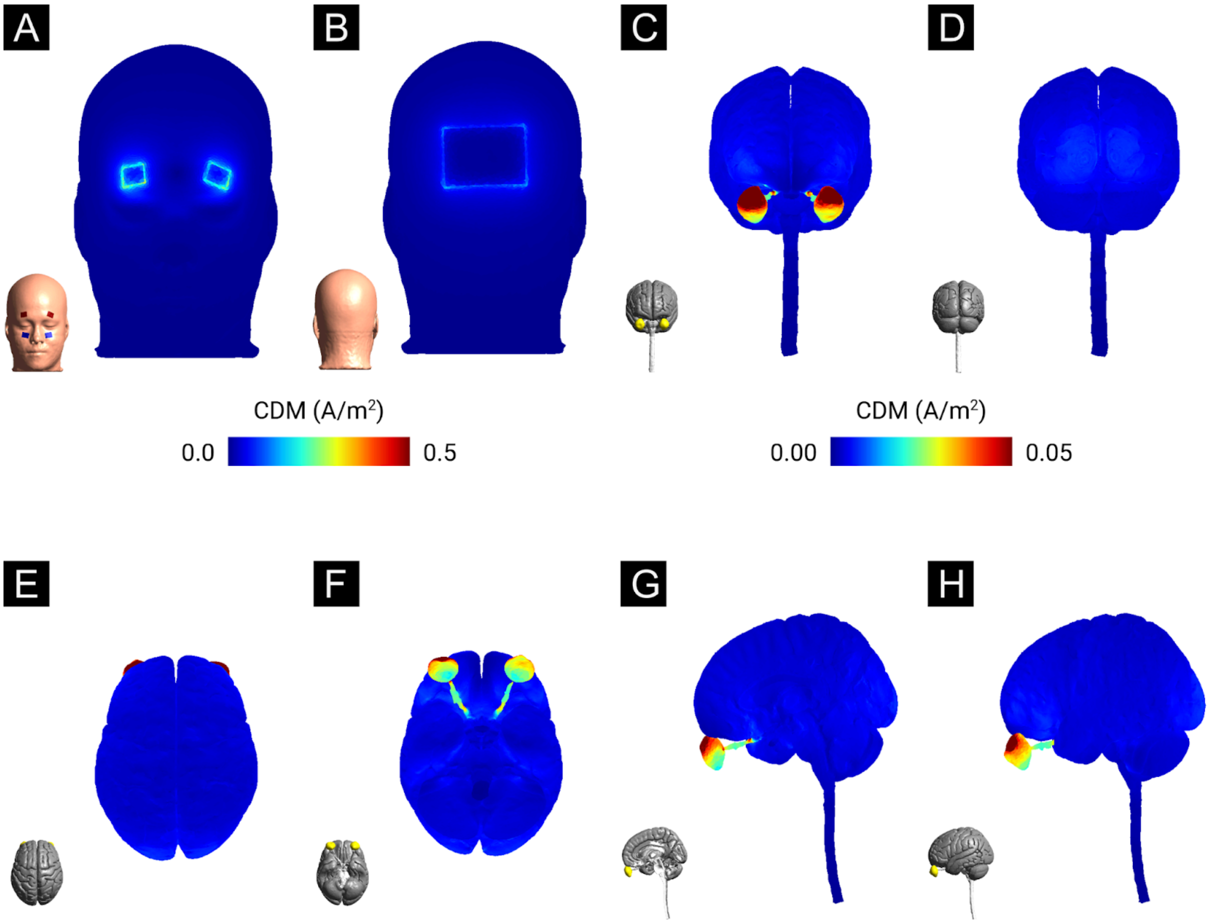

Page 115, line 1, Figure 3-19
Description of changes: Revised figure reflecting the updated eye conductivity and the removal of the “Total Current Across Volumes” panel.

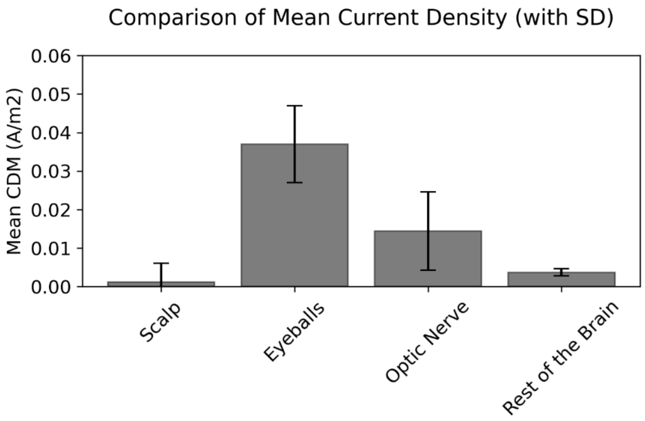

Page 117, line 1, Figure 3-20

Description of changes: Revised figure reflecting the updated eye conductivity. Adjusted Y-axis limits. Corrected reference to Figure 3-4A.

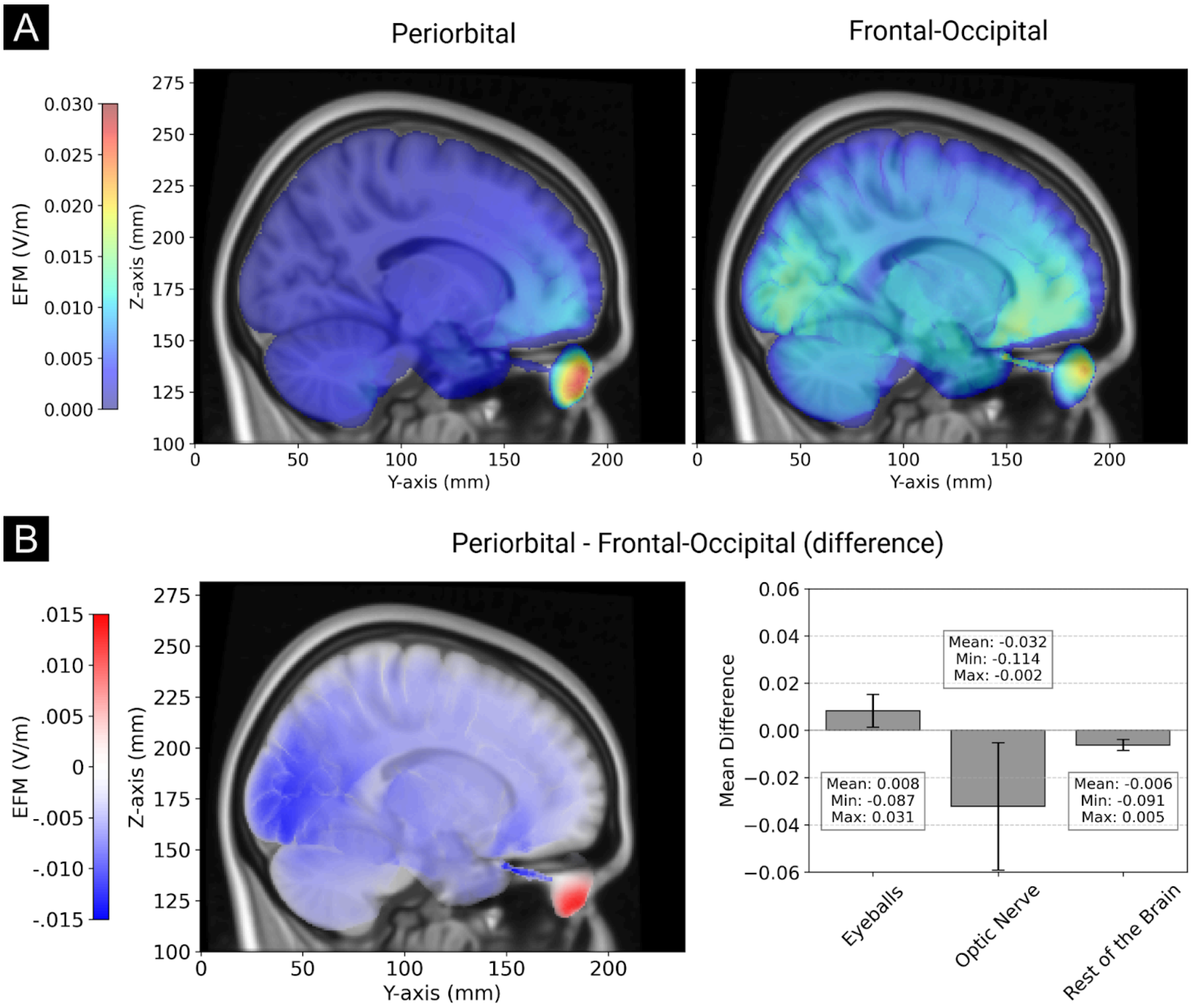

Page 119, line 1, Figure 3-21

Description of changes: Revised figure reflecting the updated eye conductivity. Adjusted Y-axis limits.

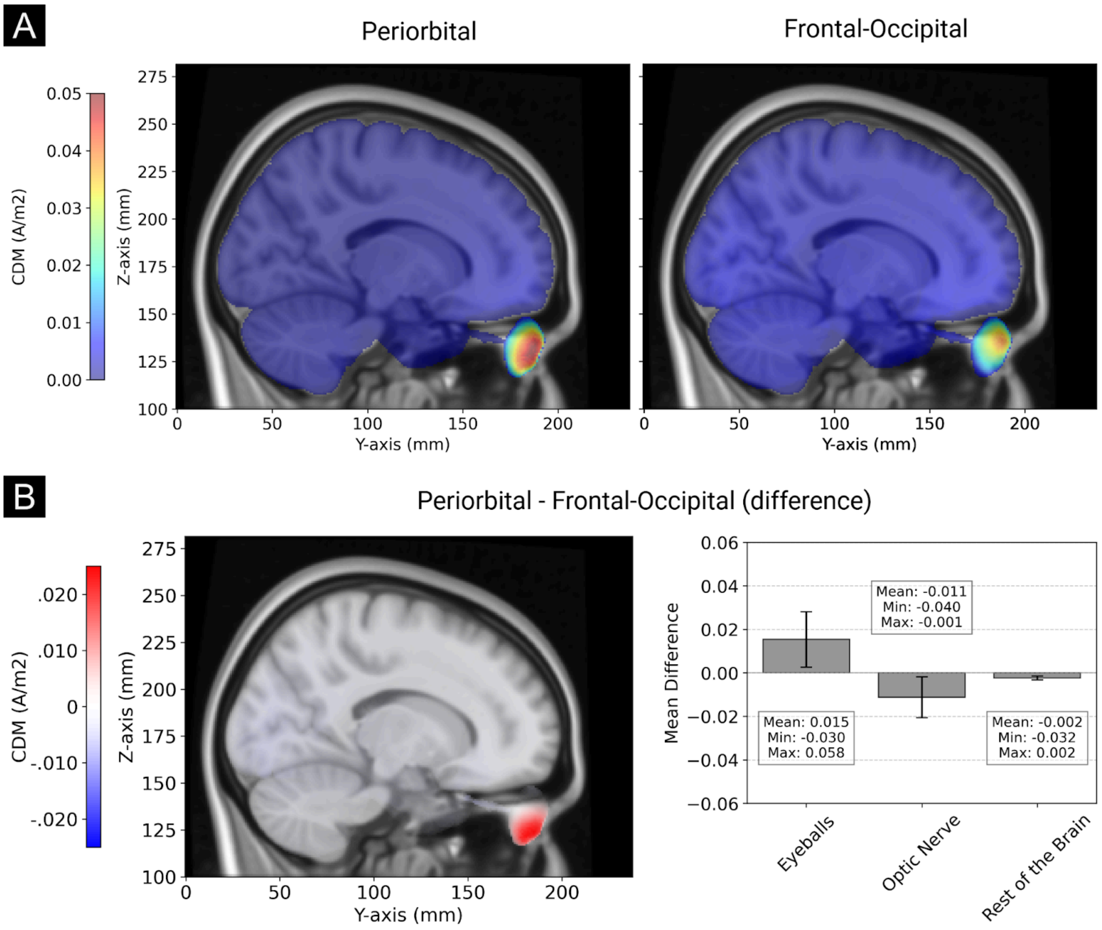

Page 120, line 4, Figure 3-22

Description of changes: Revised figure reflecting the updated eye conductivity.

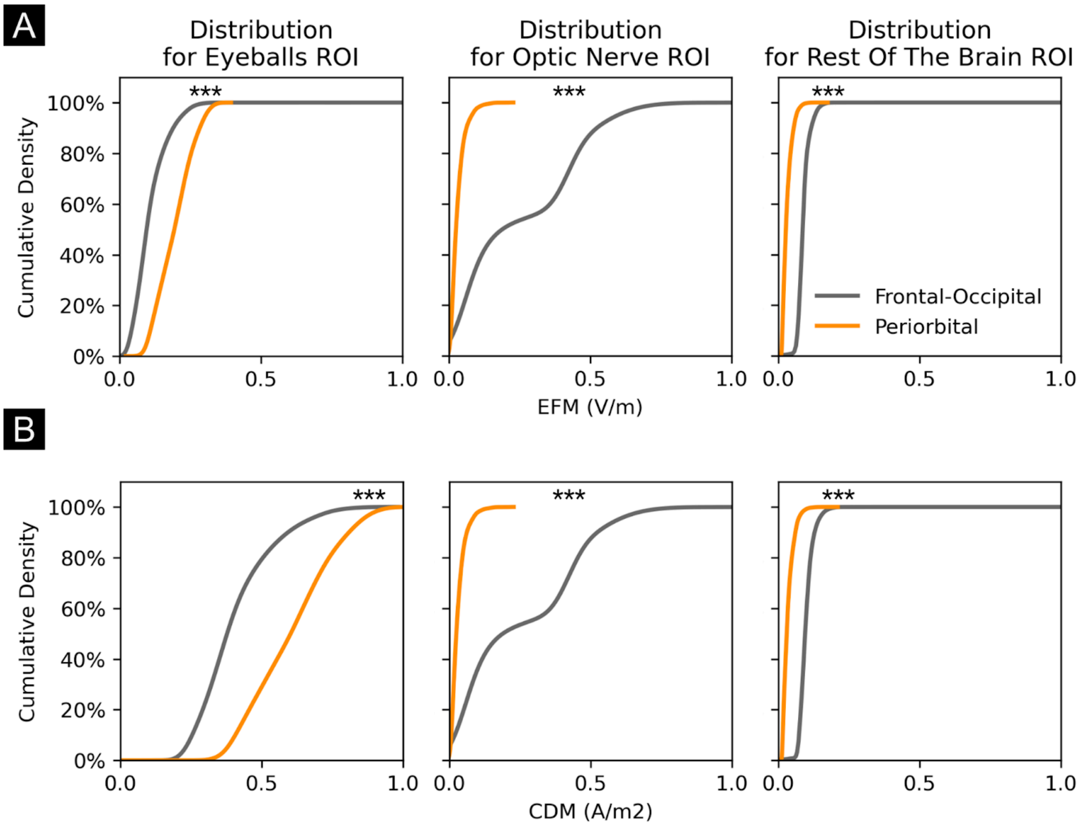

Page 129, line 1, Figure 3-25

Description of changes: Revised figure reflecting the use of integration-based instead of RMS-based pulse total charge calculations.

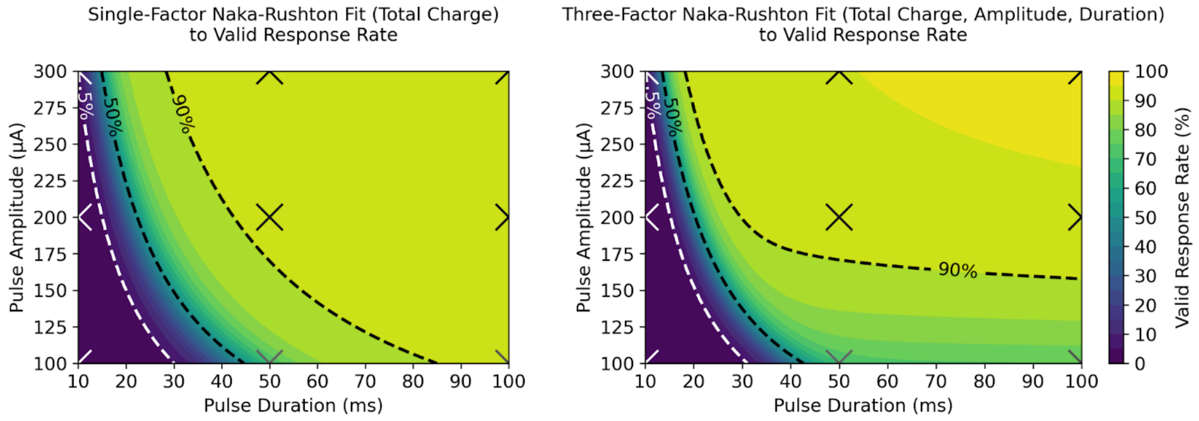

Page 144, line 9, Figure 3-31C

Description of changes: Revised figure reflecting the use of integration-based instead of RMS-based pulse total charge calculations.

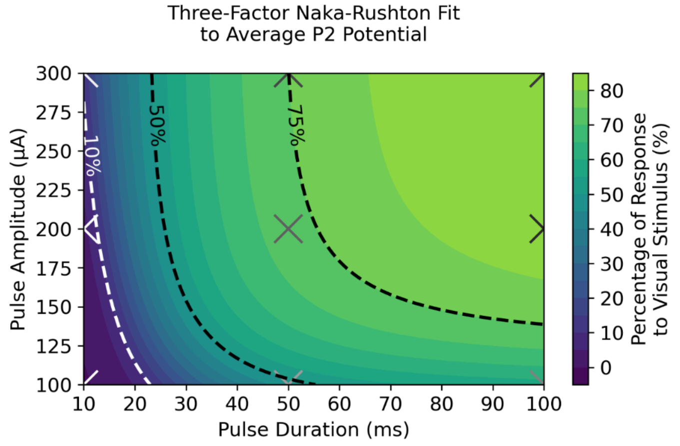

Revised abbreviations

The missing expansions of the abbreviations are provided below.

ADL	activities of daily living
CNS	central nervous system
CNTF	ciliary nerve trophic factor
DCS	direct current stimulation
FGF	fibroblast growth factor
GS	glutamine synthetase
IGF-1	insulin-like growth factor 1
PG	primary microglia
RNS	random noise stimulation
TNF-α	tumor necrosis factor-α